

DTIC FILE COPY

AD-A215 758



DTIC
ELECTE
DEC 27 1989
S D CS D

SIGNALS OF FINITE AMPLITUDE

DISSERTATION

Wayne P. Chepren
Captain, USAF

AFIT/DS/ENY/89-2

DISTRIBUTION STATEMENT A

Approved for public release
Distribution Unlimited

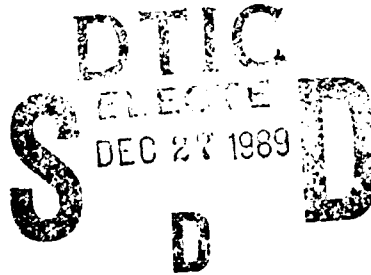
DEPARTMENT OF THE AIR FORCE
AIR UNIVERSITY

AIR FORCE INSTITUTE OF TECHNOLOGY

Wright-Patterson Air Force Base, Ohio

89 12 26 143

AFIT/DS/ENY/89-2



FLUID TRANSMISSION LINE DYNAMICS FOR
SIGNALS OF FINITE AMPLITUDE

DISSERTATION

Wayne P. Chepren
Captain, USAF

AFIT/DS/ENY/89-2

Approved for public release; distribution unlimited

FLUID TRANSMISSION LINE DYNAMICS FOR SIGNALS OF FINITE AMPLITUDE

DISSERTATION

Presented to the Faculty of the School of Engineering
of the Air Force Institute of Technology

Air University

In Partial Fulfillment of the
Requirements for the Degree of
Doctor of Philosophy

Wayne P. Chepren, B.S., M.S.
Captain, USAF

December 1989

Accession #	
NTIS	
DTIC	
Unannounced	
J. M. A. N.	
By	
Date	
Dist	
A-1	

FLUID TRANSMISSION LINE

DYNAMICS FOR SIGNALS

OF FINITE AMPLITUDE

by

Wayne P. Chepren, B.S., M.S.
Captain, USAF

Approved:

W.E. Frank 8 Dec 1989
Chairman

John Jones Jr. 8 Dec 1989

Alvin W. Z... 8 Dec 1989

James E. Hitchcock 8 Dec 1989

Philip J. Bern 11 Dec 1989

Accepted:

Robert A. Caber 11 Dec 89

Preface

The purpose of this study was to determine the significance of deviations from linearity for finite-amplitude signals propagating in fluid transmission lines. The application of this model is to help determine when linear models of fluid transmission-line transient behavior are no longer applicable.

The potential use of this model as an aid in the design of complex pneumatic systems requires that it run on the moderately powerful computers readily available to the design engineer. To this end, the finite-difference model was constructed to keep computer resource requirements to a minimum. As a design aid, the finite-difference model is intended to supply data by which a much simpler, modal model, in state-space format, can be tuned to reflect the important features of nonlinear behavior predicted by the finite-difference model. The modal model, tuned to reflect the finite-difference results, would allow accounting of the nonlinear effects in the design of complex fluid systems containing long transmission lines.

Completion of this study would not have been possible without the understanding and assistance of my doctoral committee chairman, Dr M. E. Franke. I am also indebted to my friend, Kim Turney, who provided much of the support that helped me complete this work.

Wayne P. Chepren

Table of Contents

	Page
Preface	ii
List of Figures	v
List of Tables	xi
Notation.	xiii
Abstract	xviii
I. Introduction	1
Background	2
Previous Investigations	4
Objective	7
Approach	9
Organization of Thesis	9
II. Damped-Wave Equations	11
Approximation of Friction and Heat Transfer Terms	14
III. Damping Functions.	20
Models for Viscous Losses in Transient Turbulent Flow.	20
Steady-State Pressure and Velocity Fields	29
IV. Numerical Scheme	37
Two-Step Lax-Wendroff Method	37
V. Lumped-Parameter Representation of Transmission Lines. .	62
Lumped-Parameter Models of Fluid Transmission Lines	62
Simplified Equations for Solution by Normal Modes	63
Modal Superposition	65
VI. Numerical Results	79
Summary of Figures	79
Semi-infinite Line Simulation	81
Lines of Finite Length	139
Results Using Modal Superposition	170
VII. Conclusions and Suggestions for Further Research . . .	191

Conclusions	191
Suggestions for Further Research.	197
Appendix A: Transient Solutions Using the Brown-Nichols Model	201
Appendix B: Derivation of Damped Wave Equations	208
Appendix C: Velocity Profile Approximation by Piecewise Defined Polynomials	221
Appendix D: Unsteady Turbulent Friction Model	231
Appendix E: Development of Modal Superposition	239
Bibliography	249
Vita.	256

List of Figures

Figure	Page
1. Partitioning of Flow	12
2. Annular and Cylindrical Flow Partitions	34
3. Magnitude of Amplification Factor for Two-Step Lax-Wendroff Method	42
4. Relative Phase Error for Two-Step Lax-Wendroff Method	43
5. Magnitude of Amplification Factor for Upstream (SCM) Method	54
6. Relative Phase Error for Upstream (SCM) Method	55
7. Magnitude of Amplification Factor for Moretti λ Differencing Method	56
8. Relative Phase Error for Moretti λ Differencing Method	57
9. Magnitude of Amplification Factor for Upwind (Gabutti) Method.	58
10. Relative Phase Error for Upwind (Gabutti) Method	59
11. Bond Graph for Eqs (106) and (107) with Pressure Inputs	71
12. Bond Graph for Mixed Pressure and Flow Inputs	72
13. Equivalent Circuit of an Infinitesimal Portion of Uniform Transmission Line in Time Domain	74
14. Single Trapezoidal Pulse Traveling to Right, Nonlinear Results, No Damping	87
15. Time History of Single Trapezoidal Pulse at 0, 10, 20 ft, Nonlinear Results, No Damping	89
16. Single Trapezoidal Pulse Traveling to Right, Linear Results, No Damping	90
17. Time History of Single Trapezoidal Pulse at 0, 10, 20 ft, Linear Results, No Damping	91

18.	Comparison of Linear (Fig.16) and Nonlinear (Fig. 15) Results for Trapezoidal Pulse, No Damping, 200 Grid Points	92
19.	Single Positive Half-Sinusoidal Pulse Traveling to Right, Nonlinear Results, No Damping	94
20.	Time History of Single Positive Half-Sinusoidal Pulse at 0, 10, 20 ft, Nonlinear Results, No Damping	95
21.	Single Positive Half-Sinusoidal Pulse Traveling to Right, Linear Results, No Damping	96
22.	Time History of Single Sinusoidal Pulse at 0, 10, 20 ft., Linear Results, No Damping, 200 Grid Points	97
23.	Single Trapezoidal Pulse, Nonlinear Results, No Damping, Filtering Algorithm Applied, 200 Grid Points	99
24.	Single Trapezoidal Pulse, Nonlinear Results, Steady Friction, 200 Grid Points	101
25.	Single Trapezoidal Pulse, Linear Results, Steady Friction	102
26.	Single Trapezoidal Pulse, Nonlinear Results, Unsteady Friction	104
27.	Single Trapezoidal Pulse, Linear Results, Unsteady Friction	105
28.	Single Trapezoidal Pulse, Comparison of Linear (Fig. 27) and Nonlinear (Fig. 26) Results	106
29.	Single Trapezoidal Pulse, Comparison of Steady (Fig. 24) and Unsteady (Fig. 26) Friction, Nonlinear	108
30.	Single Trapezoidal Pulse, Comparison of Steady (Fig. 25) and Unsteady (Fig. 27) Friction, Linear	109
31.	Single Trapezoidal Pulse, Nonlinear Results, Combined Unsteady Friction and Heat Transfer	110
32.	Single Trapezoidal Pulse, Linear Results, Combined Unsteady Friction and Heat Transfer	111
33.	Single Trapezoidal Pulse, Comparison of Linear (Fig. 32) and Nonlinear (Fig. 31) Results, Combined Unsteady Friction and Heat Transfer	112

34.	Single Trapezoidal Pulse, Comparison of Unsteady Friction (Fig. 26) and Combined Unsteady Friction and Heat Transfer (Fig. 31), Nonlinear Results	114
35.	Single Trapezoidal Pulse, Comparison of Unsteady Friction (Fig. 27) and Combined Unsteady Friction and Heat Transfer (Fig. 32), Linear Results	115
36.	Single Trapezoidal Pulse, Comparison of Steady Friction (Fig. 24) and Combined Unsteady Friction and Heat Transfer (Fig. 31), Nonlinear Results	117
37.	Terminated Ramp, Nonlinear Results, Unsteady Friction	118
38.	Terminated Ramp, Linear Results, Unsteady Friction	119
39.	Terminated Ramp, Nonlinear Results, Combined Unsteady Friction and Heat Transfer	120
40.	Terminated Ramp, Linear Results, Combined Unsteady Friction and Heat Transfer	121
41.	Terminated Ramp, Comparison of Linear and Nonlinear Results	123
42.	Terminated Ramp, Comparison of Linear and Nonlinear Results, Time History	124
43.	Terminated Ramp, Comparison of Unsteady Friction and Combined Unsteady Friction and Heat Transfer	125
44.	Terminated Ramp, Comparison of Unsteady Friction and Combined Unsteady Friction and Heat Transfer, Time History	126
45.	Single Positive Half-Sinusoidal Pulse Traveling to Right, Nonlinear Results	128
46.	Single Sinusoidal Pulse Traveling to Right, Linear Results	129
47.	Single Positive Half-Sinusoidal Pulse Traveling to Right, Comparison of Linear (Fig. 45) and Nonlinear (Fig. 46) Results, Combined Unsteady Friction and Heat Transfer	131
48.	Single Sinusoidal Pulse, Comparison of Linear and Nonlinear Results, Combined Unsteady Friction and Heat Transfer, Time History	132

49.	Single Positive Half-Sinusoidal Pulse, Convergence of Linear and Nonlinear Results for Sufficiently Small Amplitude	133
50.	Single Trapezoidal Pulse, Comparison of Laminar (Fig. 27) and Turbulent Unsteady Friction	135
51.	Trapezoidal Pulse, Comparison of Two Different Sets of Flow Interval Boundary Locations	136
52.	Instantaneous Velocity Profiles Produced by Passage of Terminated Ramp Input Signal	138
53.	Finite Length Transmission Line Configurations	140
54..	Transient Response for Blocked 5 ft, 0.170 in ID Line, Linear Results, Terminated Ramp Input	141
55.	Transient Response for Blocked 5 ft, 0.170 in ID Line, Linear Results, Terminated Ramp Input	142
56.	Comparison of Linear and Nonlinear Response to 2.0 psi Terminated Ramp in 5 ft, 0.170 in ID Blocked Line	143
57.	1.0 psi Terminated Ramp Input in 5 ft, 0.170 in ID Volume Terminated Line	144
58.	Transient Velocity Response, 1.0 psi Terminated Ramp Input in 5 ft, 0.170 in ID Volume Terminated Line, $V_C = 0.5 \quad V_L$	146
59.	Transient Velocity Response, 1.0 psi Terminated Ramp Input in 5 ft, 0.170 in ID Volume Terminated Line, $V_C = 0.5 \quad V_L$	147
60.	Transient Velocity Response, 1.0 psi Terminated Ramp Input in 5 ft, 0.170 in ID Volume Terminated Line, $V_C = 1.0 \quad V_L$	148
61.	Transient Velocity Response, 1.0 psi Terminated Ramp Input in 5 ft, 0.170 in ID Volume Terminated Line, $V_C = 1.0 \quad V_L$	149
62.	Comparison of Linear and Nonlinear Results for 0.25 psi Terminated Ramp Input to 5 ft, 0.170 in ID Open Line	150
63.	Transient Velocity Response, 1.0 psi Terminated Ramp Input in 5 ft, 0.170 in ID Open Line, Linear Results	151

64.	Transient Velocity Response, 1.0 psi Terminated Ramp Input in 5 ft, 0.170 in ID Open Line, Linear Results .	152
65.	Transient Velocity Response, 2.0 psi Terminated Ramp Input in 5 ft, 0.170 in ID Open Line, Linear Results .	154
66.	Transient Velocity Response, 2.0 psi Terminated Ramp Input in 5 ft, 0.170 in ID Open Line, Linear Results .	155
67.	Comparison of Inlet Velocity Response for Blocked and Open 5 ft, 0.170 in ID Lines, 1.0 psi Terminated Ramp, Linear Results	156
68.	Comparison of Inlet Velocity Response for Blocked and Open 5 ft, 0.170 in ID Lines, 2.0 psi Terminated Ramp, Linear	157
69.	Velocity Profile for Steady Flow from Piecewise Defined Polynomials	159
70.	Response of Oil-Filled Line with 0.42 fps Flow Velocity to Sudden Closure of Upstream Valve	169
71.	1.0 psi Terminated Ramp Input in 5 ft, 0.170 in ID Blocked Line, Modal Superposition Results	172
72.	1.0 psi Terminated Ramp Input in 5 ft, 0.170 in ID Blocked Line, Modal Superposition Results	173
73.	1.0 psi Terminated Ramp Input in 5 ft, 0.170 in ID Blocked Line, Modal Superposition Results	174
74.	1.0 psi Terminated Ramp Input in 5 ft, 0.170 in ID Blocked Line, Comparison of Modal Superposition Results	175
75.	1.0 psi Terminated Ramp Input in 5 ft, 0.170 in ID Blocked Line, Modal Superposition Results for 6 Modes	177
76.	1.0 psi Terminated Ramp Input in 5 ft, 0.170 in ID Blocked Line, Modal Superposition Results for 10 Modes	178
77.	1.0 psi Terminated Ramp Input in 5 ft, 0.170 in ID Blocked Line, Modal Superposition Results for 15 Modes	179
78.	1.0 psi Terminated Ramp Input in 5 ft, 0.170 in ID Blocked Line, Modal Superposition Results for 20 Modes	180

79.	Transient Response at Exit to Volume, 1.0 psi Terminated Ramp Input in 5 ft, 0.170 in ID Volume Terminated Line, $V_c = V_L$	181
80.	Transient Velocity Response at Line Inlet, 1.0 psi Terminated Ramp Input in 5 ft, 0.170 in ID Volume Terminated Line, $V_c = V_L$	182
81.	Transient Velocity Response at Line Exit to Volume, 1.0 psi Terminated Ramp Input in 5 ft, 0.170 in ID Volume Terminated Line, $V_c = V_L$	183
82.	Transient Response in One Leg of Branched Line, 1.0 psi Terminated Ramp Input in 5 ft, 0.170 in ID, Blocked Branches, Line 2	185
83.	Transient Velocity Response at Line Inlet, 1.0 psi Terminated Ramp Input in 5 ft, 0.170 in ID Open Line	187
84.	Transient Velocity Response at Line Exit, 1.0 psi Terminated Ramp Input in 5 ft, 0.170 in ID Open Line	188
85.	Transient Velocity Response at Line Inlet, 0.25 psi Terminated Ramp Input in 5 ft, 0.170 in ID Open Line	189
86.	Transient Velocity Response at Line Exit, 0.25 psi Terminated Ramp Input in 5 ft, 0.170 in ID Open Line	190
87.	Transmission Line Transient Measurement Instrumentation	197
A.1.	Equivalent Circuit of an Infinitesimal Portion of Uniform Transmission Line in Time Domain	202
B.1.	Partitioning of Flow	216
E.1.	Bond Graph for Equations (E.16) and (E.17) with Flow Inputs at Each End	243
E.2.	Bond Graph for Equations (E.16) and (E.17) with Mixed Pressure and Flow Inputs	244

List of Tables

Table	Page
1. Transmission Line Literature Summary	8
2. Classification of Turbulence Models	22
3. Inertia, Capacitance, and Resistance Parameters, Pressure Input	68
4. Definition of Terms in Modal State Equations	70
5. Transmission Line configurations Analyzed with Finite-Difference Model	79
6. Input Signal and Line Characteristics for Figures 14-52	80
7. Summary of Figures	82
8. One-Dimensional Pressures and Velocities for Laminar Flow	160
9. Comparison of Analytical and Polynomial Velocities for Laminar Flow	162
10. Comparison of Velocity Gradient for Laminar Flow	163
11. Dimensionless Values of Averaged Velocity Functions for Laminar Flow	163
12. Comparison of Radial Velocity Profile for Laminar Flow	164
13. Comparison of Radial Velocity Profile for Laminar Flow	164
14. One-Dimensional Pressures and Velocities for Turbulent Flow	165
15. One-Dimensional Pressures and Velocities for Turbulent Flow	165
16. One-Dimensional Pressures and Velocities for Turbulent Flow	166
17. Values of Averaged Velocity Functions for Turbulent Flow	167
18. Oil Filled Line	168
E.1. Inertia, Capacitance, and Resistance Parameters	245

E.2.	Inertia, Capacitance, and Resistance Parameters	247
E.3.	Inertia, Capacitance, and Resistance Parameters	247

Notation

a	fluid line radius
$A, \Delta A$	cross-sectional area of fluid line
ΔA_n	area of flow interval in fluid line
A	coefficient matrix of damped-wave equations
a_n, b_n, c_n, d_n	coefficients of piecewise continuous polynomials
c	adiabatic speed of sound
c_p	specific heat at constant pressure
C	capacitance
D	fluid line diameter
e	effort variable
\mathbf{e}	vector of effort variables
f	Darcy-Weisbach friction factor, flow variable
\mathbf{f}	vector of flow variables
F	viscous damping function
\mathbf{F}	vector of damping functions
G	conductance
H	heat transfer damping function
I	inertance
I_n	designation of individual flow intervals over cross section of fluid line
\mathbf{I}	identity matrix
k	thermal conductivity coefficient
k_B	bulk modulus

k_T	sum of molecular and turbulent thermal conductivity coefficients
l	length scale characteristic of turbulent flow
l_n	effective interaction distance between eddies
L	length of fluid line
M	number of flow intervals over cross section of fluid line
p	pressure, generalized momentum coordinate
\mathbf{p}	vector of generalized momentum coordinates
Pr	Prandtl number
q_r	heat transfer in radial direction
\mathbf{q}	generalized displacement vector
\mathbf{q}	vector of p, u_1, u_2, \dots, u_M , vector of generalized displacements
Q	volumetric flow
r	radial distance measured from centerline
r_n	radial location of flow interval boundary
R	gas constant, resistance
Re	Reynolds number
T	temperature
T_n	value of averaged temperature function in flow interval n
t	time
\mathbf{T}^{-1}	matrix with columns composed of left eigenvectors of \mathbf{A}
u	fluid axial velocity
u_n	value of averaged velocity function in flow interval
u_*	friction velocity

u_τ	friction velocity calculated using τ_τ
U	average velocity used in calculating Δp with Darcy-Weisbach friction factor
x	axial coordinate
y	vertical distance above flat plate, vertical distance from pipe wall
Y	admittance
Z	impedance
Z_c	characteristic impedance
Z_L	load impedance
γ	ratio of specific heats
Γ	propagation operator
δ	Dirac delta function, $r_n - r_{n-1}$
ϵ	dissipation of turbulent kinetic energy, roundoff error
κ	von Kármán mixing length constant
λ	eigenvalue
$[\Lambda_A]$	diagonal matrix of eigenvalues of λ
ρ	fluid density
ρ_c	spectral density
ρ_w	fluid density at wall
μ	viscosity
μ_T	sum of molecular and eddy viscosities
ν	Courant number
τ_c	time constant governing change in turbulent kinetic energy
τ_{xr}	axial shear stress

τ_T	sum of laminar and turbulent axial shear stresses
τ_w	axial shear stress at wall of fluid line
τ_s	shear stress at outer edge of Stokes layer
ϕ	phase angle
ω	frequency

Superscripts

n	value at time $n\Delta t$, nth step in iteration
'	fluctuating quantities for mass-weighted-averaging
"	fluctuating quantities for conventional time averaging
*	dimensionless value
-	time average, value obtained from predictor of predictor-corrector numerical method
~	mass weighted average

Subscripts

a	adiabatic value
av	average over cross section of flow
c	value at centerline
e	exact solution, input variable
n	value at flow interval boundary, averaged value in flow interval bounded by r_n and r_{n-1}
o	original conditions
r	in radial direction
s	value at outer edge of Stokes' layer, output variable
t	derivative with respect to time

T	total
Turb	value of coefficient due to presence of turbulence
W	value at wall
x	derivative with respect to axial coordinate, in axial direction
0	value at $x = 0$
L	value at $x = L$
θ	in circumferential direction

ABSTRACT

The transient response of a straight, cylindrical, fluid transmission line to a finite-amplitude pressure input is studied numerically to identify deviations from linear behavior. A nonlinear, finite-difference method is developed to predict the changes in the shape of a pressure wave as it propagates. The finite-difference algorithm is also applied to a linearized version of the governing equations to generate a basis against which to identify nonlinear behavior. The finite-difference method accounts for viscous losses and heat transfer. An algebraic model for calculating eddy-viscosity in transient turbulent flows is included.

Numerical simulations of a semi-infinite transmission line are performed using trapezoidal and half-sinusoidal pulses as well as a terminated-ramp as input pressure signal waveforms. Significant differences between linear and nonlinear results are found, even for input signals with maximum pressures less than two percent of the initial, undisturbed pressure.

Results are also obtained for lines of finite length with a blocked, volume terminated, or open end, opposite the end where the input signal is applied. The transient response to a terminated-ramp input pressure waveform is studied for this case. Good agreement with published results is obtained.

An engineering model is developed using the method of modal superposition. The modal model is modified to include frequency-dependent parameters for viscous and heat transfer losses. Results produced by the modal model for finite-length lines agree well with results from the finite-difference model and published data. All features present in the transient pressure and velocity waveforms produced at each end of the simulated transmission line by the finite-difference model are closely tracked by the modal model results.

FLUID TRANSMISSION LINE DYNAMICS FOR SIGNALS OF FINITE AMPLITUDE

I. Introduction

Transmission lines are often present in hydraulic or pneumatic control and pressure measurement systems. These lines affect the dynamics of system components by imposing loads on components the lines connect. The effect of the imposed loads must be considered in order to predict the overall system response to applied signals.

Simple analyses of these systems allow transmission lines to be treated as lumped-parameter components; however, a line must be considered as a distributed-parameter component to accurately predict responses to applied signals containing frequency components with wavelengths significantly smaller than the length of the transmission line. The properties of the transmission line are then considered to act on the signal continuously as it travels through the line.

The design of fluid control systems may require accurate portrayal of nonlinear effects in long transmission lines to determine the input signal shape needed to produce a desired control action. Accurate fluid control in the presence of signals of finite amplitude requires an understanding of how nonlinear effects act to alter the signal waveform. The behavior of a fluid transmission line treated as a distributed-parameter component can be described by the Navier-Stokes equations. Numerical solution of these equations will accurately predict transients produced by signals of finite amplitude. However,

numerical solution is expensive with respect to computer resources, requiring several hours on a supercomputer performing millions of operations per second to produce a solution. Designers of fluid systems do not always have ready access to these computers and must rely on much slower machines. A finite-difference model requiring only modest computer resources and based on the simplified Navier-Stokes equations would be useful to fluid system designers.

Despite the availability of a finite-difference model capable of running on computers easily accessible to designers, a simplified lumped parameter model capable of interfacing with standard techniques used in system design is also needed. Numerical solution of the partial differential equations governing fluid flow results in an overwhelming amount of data that can be cumbersome and expensive to apply to complex fluid systems. Lumped-parameter models have been used for many years to calculate the transient response of structures to suddenly applied or nonperiodic loads. These techniques are based on modal superposition which is mathematically valid for linear systems only. However, modifications to modal superposition that account for nonlinear effects in structures have produced good results in some cases (47:72). Additionally, state-space analyses of physical systems have relied on describing functions to modify linear models to account for nonlinear effects in transient solutions.

Background

Accurate predictions of the transient behavior of the fluid systems have been obtained using modal approximations to invert the

well-developed small laminar disturbance (SLD) models from the Laplace domain to the time domain (24). Due to the linear nature of the SLD models, the modal approximations cannot be modified to deal with a turbulent mean flow, signals of finite amplitude, or transmission line terminations with complicated nonlinear behavior. Other transient solutions based on a SLD model suffer from similar drawbacks (5:78; 7; 30).

A simplified engineering model capable of predicting the effects of finite-amplitude signals and viscous losses for transient turbulent flow in fluid transmission lines should be useful in pneumatic system design. This engineering model should be compatible with standard, control-system analysis and design techniques. It should also require only a minimum of empirical information to model transmission-line response and be compatible with ordinary differential equations used to describe other system components. Such a model could be developed from solutions generated with a finite-difference model. The engineering model will then contain parameters whose values are adjusted to give its solutions the same important characteristics as solutions produced by the computer intensive finite-difference model. The adjustable parameters of the engineering model allow the information obtained with the f'nite-difference model to be compressed into a convenient format.

Ideally, results of the numerical model obtained for a small number of cases could be used to modify the engineering model for a wide range of signals and system configurations. Although the need for actual system construction and testing will never be eliminated, the finite-difference and engineering models used together in the early stages of design should result in a prototype fluid system with

improved performance. Less redesign and rework of the fluid system during prototype testing would be required to achieve desired performance.

Previous Investigations

Propagation of sinusoidal signals through fluid transmission lines with no established mean flow has been studied by numerous investigators using frequency-domain techniques (26; 29; 49; 55). The assumption of a SLD allows the continuity, momentum, energy, and state equations to be greatly simplified and solved to produce explicit expressions for distributed friction and heat transfer losses as a function of frequency. These frequency-domain models can be inverted from the Laplace domain to the time domain to obtain the transient response to the simple cases of impulse and step inputs (7). Methods to obtain the transient response for a suddenly applied sinusoidal signal (28) as well as the approximate response for an arbitrary signal (30) were developed assuming a small laminar disturbance.

Two other approaches that rely on frequency-domain models to obtain the transient response to an arbitrary signal are the frequency response conversion method (33; 76; 77; 78; 79; 80; 81) and the Fast Fourier Transform (FFT) method (71). Frequency response conversion is the direct conversion of the exact frequency response model for terminated transmission lines into the transient response (33:3). The fast Fourier transform method calculates the effect of the transmission line on each frequency component of the transformed signal and then reconstructs the signal from the modified frequency components.

Methods to incorporate the effects of laminar mean flow into SLD models in the frequency domain have been developed by various authors (5; 51; 52). In this case the signal is imposed on an otherwise steady laminar flow. The more complex problem of accounting for the effects of turbulent mean flow in the SLD models has also been addressed (9; 19; 34; 43; 44). Viscous losses in transient turbulent flow have also been modeled (74). In addition, approximations to the transmission line transfer function as well as the complicated impedance and admittance expressions have been made (25; 50) allowing the transient response for a variety of input signals to be easily calculated.

With the exception of the FFT method (71) and the block diagram reduction method (30) the transient response for arbitrary signals cannot be obtained from the SLD models. Additionally, the use of SLD models requires line terminations to behave in a linear fashion. Numerical techniques such as the method of characteristics and finite-difference methods can be applied to overcome these limitations.

The method of characteristics is a numerical method long used for the solution of transient flow in pipelines (1; 64:20). This method has also been applied to systems with finite-amplitude signals in compressible fluids (3; 41; 60). A one-dimensional finite-difference solution retaining the convective terms in the governing equations has also been presented (19). In this method, and the method of characteristics, the viscous losses are calculated using the Darcy-Weisbach friction factor developed for steady flow. It has been shown that use of friction factors developed for steady flow significantly underestimates the attenuation of a propagating signal (23:6; 74:866). The method of characteristics has been adapted to

handle viscous losses in transient flow by developing forcing functions based on earlier frequency domain friction models (9; 82). This method works well for lines with laminar mean flow and for a limited range of turbulent mean flows (69).

Solutions of the full Navier-Stokes equations and of the axisymmetric equations for pulsed, turbulent pipe flow have been obtained (35; 54). These numerical approaches provide detailed information on the transient behavior of the flow, however a large number of grid points in the radial direction is required to accurately represent the boundary-layer phenomena (70:588).

A significant reduction in the number of grid points may be realized by simplifying the Navier-Stokes equations to produce a set of equations that treat heat transfer and friction terms as forcing functions (70). By using piecewise defined polynomials to approximate velocity and temperature profiles, the number of mesh points needed to approximate the friction and heat transfer forcing functions is significantly decreased. The availability of the velocity and temperature profiles from the polynomials allows the use of Boussinesq-type friction models to calculate the values of the damping functions.

A numerical method that uses modal superposition to predict the transient response of a transmission line has also been presented (31; 40). Modal superposition removes spatial dependence, producing a system of ordinary differential equations compatible with standard methods of system analysis.

The studies discussed above are categorized in Table 1 according to the solution method provided by the model. A more detailed summary

of the frequency-domain models has been presented by Goodson and Leonard (22).

Objective

The intent of this study is to determine the importance of nonlinear effects in the transient response of a fluid transmission line for signals of finite amplitude. An explicit, nonconservative, finite-difference model accounting for nonlinear effects as well as viscous and heat transfer losses in transient flow is developed. The model has provisions for both laminar and turbulent viscous losses and heat transfer in addition to provisions for a mean flow. The transient response of blocked, open, and volume-terminated transmission lines is examined to identify nonlinear effects and assess limitations of the finite-difference model for this application. A linear version of this model is also developed to compare linear and nonlinear transmission line behavior. The relative importance of viscous and heat transfer losses is also examined. The finite-difference model is developed to minimize the computational capability required. The intent is to allow the finite-difference model developed in the present study to run on computers of modest capability and find use as a fluid system design tool.

An engineering model suitable for use with the state-space method of dynamic system analysis is also developed. This model allows the influence of the transmission line to be accounted for in the transient response for a complete fluid system.

TABLE 1

Transmission Line Literature Summary

Frequency domain solutions	Inversion of frequency domain models to get transient solution
Iberall (1950) Rohmann and Grogan (1957) Nichols (1961) Brown (1962) Karam and Franke (1967)	Brown (1962) Kantola (1971) Karam (1972) Karam and Leonard (1973)
Frequency response conversion	Fast Fourier transform method
Katz (1976) Yoshioka (1983)	Tsang et al (1984)
Frequency domain friction models incorporating effects of throughflow	Approximations to transfer matrix and impedance terms
Brown et al (1969) Orner (1969) Wood and Funk (1970) Mercier and Wright (1973) Katz et al (1974) Braden (1973) Margolis and Brown (1975) Pletcher (1979) Brown (1981)	Oldenburger (1964) Hullender, Woods, and Hsu (1983)
Method of characteristics	Method of characteristics with unsteady friction
Benson et al (1964) Manning (1968) Sandoz (1973)	Zielke (1968)
Numerical approaches (Two or three dimensional)	One dimensional numerical method
Tsao (1968) Kirmse (1979) Reddy et al (1985)	Funk and Robe (1970)

Approach

The finite-difference model will be based on the approach described by Tsao (70). The governing equations are simplified and expressed in what Tsao calls damped-wave-propagation equations (70:589). These damped-wave equations, as they will be called in this study, will then be solved using the Gabutti finite-difference algorithm (2:294; 21) with an algebraic turbulence model for viscous losses in transient turbulent flow that approximates the apparent viscosity at turbulent Reynolds numbers. An algorithm for generating the pressure and velocity fields for an established mean flow for use with the finite-difference model is also developed. The modal superposition method described by Karnopp (31) and Lebrun (40) is used to develop a linear engineering model.

Organization of Thesis

The complete Navier-Stokes equations are reduced to a simplified form in Chapter II using the well-known transmission line assumptions. Following Tsao, the simplified equations and an equation of state are combined to produce a system of nonlinear equations, called damped-wave equations (70). The use of piecewise defined polynomial approximations of the velocity and temperature profiles is introduced and applied to the solution of the damped-wave equations.

Damping functions that are used with the damped-wave equations and the piecewise polynomial approximations developed in Chapter II are presented in Chapter III. Development of a relatively simple,

algebraic turbulence model suitable for transient flows and a method which calculates the initial pressure and velocity field for a turbulent or laminar mean flow are also shown in Chapter III. The Gabutti numerical algorithm used to solve the damped-wave equations is discussed in Chapter IV. Features of other numerical methods are also discussed and compared to those of the Gabutti algorithm.

An engineering model based on modal superposition and electromagnetic transmission line theory is developed to approximate the finite-difference solution of the damped-wave equations in Chapter V. A method for determining the modal parameters from linear transmission line theory is described.

Numerical results from both models are presented and discussed in Chapter VI. Results are also compared with results from past studies where possible.

Chapter VII contains conclusions and recommendations for further studies.

II. Damped Wave Equations

A finite-difference model capable of accurately representing the dynamic response of a fluid transmission line to flow and pressure disturbances applied at the ends of the line is developed in this study. This numerical method must account for nonlinear effects due to finite-amplitude signals, effects due to the presence of an initial turbulent or laminar mean flow, and both laminar or turbulent viscous losses and heat transfer. The development of this finite-difference model can be separated into three steps; simplification of the axisymmetric Navier-Stokes equations into a manageable form, development of suitable expressions for viscous losses and heat transfer, and selection and application of the numerical algorithm to be used to solve the system of equations resulting from the first two steps. This chapter describes the first step in development of the finite-difference model.

The simple geometry of a cylindrical transmission line allows assumptions that greatly simplify the Navier-Stokes equations. Following common practice, the term Navier-Stokes will include the continuity and energy equations as well as the components of the viscous momentum equations.

The following assumptions can be made for the transmission line shown in Figure 1.

1. The transmission line is rigid, circular in cross section, and has constant cross-sectional area.
2. The gas behaves ideally. Liquids are assumed to be barotropic

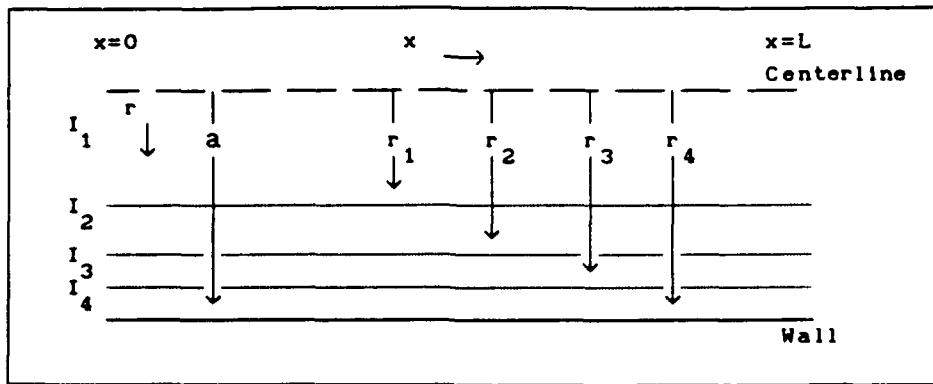


Fig. 1. Partitioning of Flow into Four Intervals

($\rho = \rho(p)$) with fluid properties such as the speed of sound and the ratio of specific heats assumed continuous.

3. The mean flow is fully developed laminar or turbulent flow.
4. The time varying pressure is uniform across any given cross section of the line.
5. The flow is at all times parallel to the axis of the line. This means that velocity components in the θ and r directions have zero magnitude.
6. The transmission line walls are isothermal.
7. The length of the transmission line is much greater than the radius. This allows the end effects and higher mode propagation to be neglected.
8. The bulk viscosity is assumed to be zero and the fluid undergoes no relaxation.
9. There are no significant body forces acting on the fluid.

A set of nonlinear, damped-wave equations may be obtained following a procedure similar to that used by Tsao (70). The

nonlinear, damped-wave equations with the convective terms retained are shown below. Details of the development of these equations are shown in Appendix B:

$$\frac{\partial u}{\partial t} + \frac{c^2}{\gamma} \frac{\partial(\text{Ln}[p])}{\partial x} + u \frac{\partial u}{\partial x} = \frac{c^2}{p\gamma} \frac{1}{r} \frac{\partial}{\partial r} [r(\tau_{xr} + \overline{\rho u v})] \quad (1)$$

$$\frac{\partial(\text{Ln}[p])}{\partial t} + \gamma \frac{\partial u}{\partial x} + u \frac{\partial(\text{Ln}[p])}{\partial x} = - \frac{(\gamma-1)}{p} \frac{1}{r} \frac{\partial}{\partial r} [r(q_r + \overline{\rho v c_p T})] \quad (2)$$

The right-hand side of Eq (1) represents the viscous losses while the corresponding term in Eq (2) represents losses due to heat transfer. All variables in Eqs (1) and (2) are time averaged except where noted by primes. Primes denote values that fluctuate about the average. The set of initial and boundary conditions are

$$\begin{aligned} p &= f(x), \quad u = g(x, r), \quad T - T_w = 0 & t < 0, \quad 0 \leq x \leq L, \quad 0 \leq r \leq a \\ (p)_{x=0} &= f(t), \quad \text{or } (u)_{x=0} = f(r, t) & 0 \leq t, \quad 0 \leq r \leq a \\ (u)_{x=L} &= g(r, t) \quad \text{or } (p)_{x=L} = f(t) & 0 \leq t, \quad 0 \leq r \leq a \\ \left(\frac{\partial u}{\partial r} \right)_{r=0} &= \left(\frac{\partial T}{\partial r} \right)_{r=0} = 0 & 0 \leq t, \quad 0 \leq x \leq L \\ (u)_{r=a} &= (T - T_w)_{r=a} = 0 & 0 \leq t, \quad 0 \leq x \leq L \end{aligned}$$

The above equations are nondimensionalized using the groupings shown below:

$$u^* = \frac{u}{c_0}, \quad p^* = \frac{p}{\rho_0 c_0^2}, \quad x^* = \frac{x}{L}, \quad t^* = t \frac{c_0}{L}, \quad T^* = \frac{T}{T_w}, \quad r^* = \frac{r}{a}$$

Approximation of Friction and Heat Transfer Terms

Before doing any further work with the damped-wave equations, it is necessary to develop a means of specifying the right-hand side of Eqs (1) and (2). These expressions will be referred to as damping functions, since they represent attenuation resulting from viscous and heat transfer losses. The method proposed by Tsao uses averaged velocity and temperature functions as a means of approximating these damping functions (70:591). A conventional differencing scheme requires a very fine mesh near the pipe wall in the radial direction to represent accurately the behavior of the velocity profile in the boundary layer. The averaged velocity and temperature functions in conjunction with piecewise defined polynomials are used to generate approximate velocity and temperature profiles over the cross section, significantly reducing the number of mesh points required in the radial direction.

The cross section of the transmission line is partitioned into M flow intervals as shown in Figure 1. The locations of the interval boundaries with respect to the centerline are denoted as $0 = r_0 < r_1 < r_2 < \dots < r_M = a$ where a is the internal radius of the transmission line. The area of the annular region formed between r_{n-1} and r_n is denoted by ΔA_n and is defined as $\Delta A_n = \pi (r_n^2 - r_{n-1}^2)$ where $n = 1, 2, \dots, M$. The averaged temperature and averaged velocity functions are defined as

$$T_n(x, t) = \frac{1}{\Delta A_n} \int_{r_{n-1}}^{r_n} T(x, r, t) 2\pi r dr \quad (3)$$

$$u_n(x, t) = \frac{1}{\Delta A_n} \int_{r_{n-1}}^{r_n} u(x, r, t) 2\pi r dr \quad (4)$$

These averaged functions are then incorporated into the damped-wave equations to produce a set of simultaneous, one-dimensional, partial differential equations:

$$\frac{\partial u_n}{\partial t} + \frac{c^2}{\gamma} \frac{\partial(\ln[p])}{\partial x} + u_n \frac{\partial u_n}{\partial x} = \frac{2\pi c^2}{\gamma p \Delta A_n} \left[(\mu_T)_{r=r_n} r_n \left(\frac{\partial u}{\partial r} \right)_{r=r_n} - (\mu_T)_{r=r_{n-1}} r_{n-1} \left(\frac{\partial u}{\partial r} \right)_{r=r_{n-1}} \right] \quad (5)$$

$$n = 1, 2, \dots, M$$

$$\frac{\partial(\ln[p])}{\partial t} + u_{av} \frac{\partial(\ln[p])}{\partial x} + \gamma \frac{\partial u_{av}}{\partial x} = \frac{2(\gamma - 1)}{a p} k_T \left(\frac{\partial T}{\partial r} \right)_{r=a} \quad (6)$$

where $u_{av} = \frac{1}{\Delta A} \int_0^a u 2\pi r dr$ and $\Delta A = \int_0^a 2\pi r dr$, and μ_T and k_T are the total fluid viscosity and thermal conductivity, respectively. Total fluid viscosity is understood to be the sum of the molecular fluid properties and the apparent fluid properties due to turbulence. μ_T and k_T are found using a suitable turbulent viscosity model that will be described in the next chapter. The groupings shown below are used to nondimensionalize μ_T and k_T :

$$k_T^* = k_T \left(\frac{T_w L}{c_0 p_0 a^2} \right), \quad \mu_T^* = \mu_T \left(\frac{c_0 L}{g_c p_0 a^2} \right);$$

The energy equation, in terms of averaged variables, is written as

$$\frac{\partial T_n}{\partial t} + u_n \frac{\partial T_n}{\partial x} - \frac{c^2}{\gamma c_p} \frac{\partial}{\partial t} (\ln[p]) - \frac{c^2}{\gamma c_p} u_n \frac{\partial (\ln[p])}{\partial x} =$$

$$\frac{2c^2}{\gamma c_p (r_n^2 - r_{n-1}^2)} \left[r_n k_T(r_n) \left(\frac{\partial T}{\partial r} \right)_{r=r_n} - r_{n-1} k_T(r_{n-1}) \left(\frac{\partial T}{\partial r} \right)_{r=r_{n-1}} \right] \quad (7)$$

$n = 1, 2, \dots, M$

The terms $\frac{\partial (\ln[p])}{\partial t}$ and u_n , required to numerically solve the energy equation, are obtained from solution of the damped-wave equations.

The derivatives of velocity and temperature at the interval boundaries are necessary to calculate values for the right-hand side of Eqs (5) through (7). Tsao describes a method for reconstructing these profiles (70:595). The reconstruction uses piecewise polynomials and the values of the averaged variables u_n and T_n in a manner similar to a cubic spline function to approximate the velocity and temperature profiles.

Let each interval be denoted by I_n with $n = 1, 2, \dots, M$ as shown in Figure 1. In each interval, the velocity is approximated by a polynomial (70:591):

$$u(x, r, t) \approx \begin{cases} P_1(x, r, t) = a_1 + b_1 r + c_1 r^2 & r \in I_1 \\ P_n(x, r, t) = a_n + b_n (r - r_{n-1}) + c_n (r - r_{n-1})^2 + d_n (r - r_{n-1})^3 & r \in I_n, \quad n = 1, 2, \dots, M \end{cases} \quad (8)$$

Equation (8) has $4M-1$ unknown coefficients which require $4M-1$ linearly independent equations to determine. The value for the averaged velocity in each interval is known from the initial conditions

or from the solution of Eq (5) at each time step. The definition of averaged velocity shown in Eq (5) is applied to Eq (8) and used with the known values of averaged velocity to provide M independent equations. Each piecewise polynomial as well as its first and second derivatives are required to be continuous at each boundary between intervals. This provides an additional 3M-3 independent equations. Two more equations result from the assumptions of no slip at the wall and axisymmetric flow where $u|_{r=a}$ and $\frac{\partial u}{\partial r}|_{r=0}$ are zero, respectively. Each of the 4M-1 unknowns in the polynomials is determined at each time step from a set of recursion relationships resulting from the application of these conditions. The procedure for determining these recursion relationships is shown in detail in Appendix C. The recursion relations are used to produce a system of equations in terms of the coefficients c_n and d_M of Eq (8). Solution of this system of equations allows reconstruction of the velocity profiles and gradients:

$$\begin{bmatrix} c_2 \\ c_3 \\ \vdots \\ \vdots \\ c_M \\ d_M \end{bmatrix} = \begin{bmatrix} l_{1,1} & l_{1,2} & & l_{1,M-1} & l_{1,M} \\ l_{2,1} & l_{2,2} & & l_{2,M-1} & l_{2,M} \\ \cdot & \cdot & & \cdot & \cdot \\ \cdot & \cdot & \cdot \cdot \cdot & \cdot & \cdot \\ \cdot & \cdot & & \cdot & \cdot \\ l_{M-1,1} & l_{M-1,2} & & l_{M-1,M-1} & l_{M-1,M} \\ l_{M,1} & l_{M,2} & & l_{M,M-1} & l_{M,M} \end{bmatrix}^{-1} \begin{bmatrix} u_1 \\ u_2 \\ \cdot \\ \cdot \\ u_{M-1} \\ u_M \end{bmatrix} \quad (9)$$

The elements $l_{i,j}$ of Eq (9) are constants determined by the locations of the interval boundaries r_n .

Temperature profiles are determined in the same manner except that the profile of $T - T_w$ is found instead of the actual temperature

profile, with $T - T_w$ replacing u and $T_n - T_w$ replacing u_n in Eqs (8) and (9). T_w is the wall temperature of the transmission line and remains constant. The field of values of u_n is provided by the numerical solution of Eqs (5) through (7) from which Eq (9) produces values of c_n and d_n at each time step. These values are substituted into the recursion relationships for a_n , b_n , and d_n (found in Appendix C), allowing $\frac{\partial}{\partial r} u(j\Delta x, r, t)$ to be determined from Eq (8). Values of the velocity gradients at $r = r_n$ are used to evaluate the right-hand side of Eq (5). This entire sequence is repeated at each time step throughout the numerical solution of Eqs (5) through (7). In exactly the same manner, $\frac{\partial}{\partial r} T(j\Delta x, r, t)$ is evaluated from values of $T_n - T_w$ produced by the numerical solution. The right-hand sides of Eqs (6) and (7) are then evaluated. This procedure must include an additional step when the flow is turbulent. Expressions for the total viscosity μ_T and the total thermal conductivity k_T must be evaluated at each time step.

The use of piecewise defined polynomials to approximate the velocity and temperature profiles and gradients is very similar to cubic spline interpolation. Cubic spline interpolation provides a good approximation of slopes which has made it popular as a means of numerical differentiation.

A linearized set of equations obtained from the Navier-Stokes equations was presented by Tsao (70:589). Using these equations and proceeding as described in Appendix B, the following equations are obtained:

$$\frac{\partial u_n}{\partial t} + \frac{c^2}{\gamma} \frac{\partial (\ln[p])}{\partial x} =$$

$$\frac{2\pi c^2}{\gamma p \Delta A_n} \left[(\mu_T)_{r=r_n} r_n \left(\frac{\partial u}{\partial r} \right)_{r=r_n} - (\mu_T)_{r=r_{n-1}} r_{n-1} \left(\frac{\partial u}{\partial r} \right)_{r=r_{n-1}} \right]$$

$$n = 1, 2, \dots, M \quad (10)$$

$$\frac{\partial (\ln[p])}{\partial t} + \gamma \frac{\partial u_{av}}{\partial x} = \frac{2(\gamma - 1)}{a p} k_T \left(\frac{\partial T}{\partial r} \right)_{r=a} \quad (11)$$

$$\frac{\partial T_n}{\partial t} + \frac{c^2}{\gamma c_p} \frac{\partial (\ln[p])}{\partial t} =$$

$$\frac{2c^2}{\gamma c_p p (r_n^2 - r_{n-1}^2)} \left[r_n k_T(r_n) \left(\frac{\partial T}{\partial r} \right)_{r=r_n} - r_{n-1} k_T(r_{n-1}) \left(\frac{\partial T}{\partial r} \right)_{r=r_{n-1}} \right]$$

$$n = 1, 2, \dots, M \quad (12)$$

These equations are in the same format as Eqs (5) through (7). The numerical solutions of both sets of equations will be compared in Chapter VI to identify nonlinear effects.

III. Damping Functions

Model for Viscous Losses in Transient Turbulent Flow

Data on the transient turbulent flows under consideration in this study is very limited. As a result, no criteria are available on which to base selection of a turbulent viscosity model. A simple, algebraic model to approximate of the effect of viscous losses due to turbulence in the solution of the equations developed in Chapter II will be discussed in this chapter.

Systems of interest in this study include the presence of a mean flow. This is a steady, fully-developed flow assumed to be in existence before application of any signal. Determination of the initial velocity field for a mean flow would normally require continuing the numerical solution of the damped-wave equations developed in the previous chapter until steady state is reached. An algebraic method using the turbulent viscosity model to generate a velocity field for use as an initial condition will be developed in this chapter.

Expressions for the total viscosity μ_T and the total thermal conductivity k_T are needed to solve Eqs (5) through (7) and (10) through (12). For the case of laminar flow, μ_T and k_T are identical to μ and k respectively. The presence of turbulence complicates the problem significantly.

Viscous effects resulting from turbulent flow are often treated in a quasi-steady manner when numerical techniques such as the method of

characteristics are applied to fluid transmission line problems. In this case, viscous forces are calculated using expressions valid only for fully developed velocity profiles. In the quasi-steady approximation, the friction force is usually expressed as $\Delta p = \frac{\rho V^2 f L}{2 D}$ where f is the Darcy-Weisbach friction factor and is calculated as a function of the Reynolds number. Examples of this approach are numerous (3:117; 16:9; 75:18).

The effectiveness of this quasi-steady approach for representing viscous effects resulting from turbulent flow has been questioned. For example, Wood and Funk found that, for the extreme case of pressure wave propagation in a tube, the quasi-steady approximation fails to predict the true attenuation of the wave (74:866). They use waterhammer caused by sudden valve closure as an example and show that the large reverse pressure gradient reverses the flow near the wall, producing significant dissipation. This dissipation decreases the magnitude of the wave more than a quasi-steady calculation would indicate.

Expressions for viscous losses in transient flow of liquids based upon the frequency dependent laminar friction models discussed in Chapter I have been developed for laminar flows (82) and modified for a limited range of turbulent flows (69). These techniques use weighting functions to calculate damping based on the time rate of change of the average velocity and the velocity history. This method works well for laminar flows and when steady, turbulent, mean flows are present. The methods of Zielke (82) and Trikha (69), however, are one dimensional and provide no means to calculate viscous losses from transient turbulent flow.

The equations developed in Chapter II produce two-dimensional velocity and temperature profiles which allow the use of Boussinesq-type eddy viscosity models to predict the viscous and heat transfer losses on disturbances traveling through the transmission line. A variety of eddy viscosity models commonly used in numerical methods may be employed to calculate values for μ_T and k_T .

Lauder defines a turbulence model as a set of differential or algebraic equations whose solution enables certain features of turbulent flow to be predicted. Classifications of turbulence models, as described by Launder (39), are shown in Table 2.

Table 2
Classification of Turbulence Models (39:417)

<u>Type</u> <u>of Model</u>	<u>Number of</u> <u>Transport Eqs.</u>	<u>Dependent Turbulent</u> <u>Variables</u>
Mixing Length/ Eddy viscosity	0	—
Bradshaw's Method (also Nee and Kovaszny)	1	k
Two equation Viscosity Model	2	k, ϵ or equivalent
Stress Transport Model	5-7	$\overline{u_i u_j}$, ϵ
Third Order Closure	9-17	$\overline{u_i u_j}$, $\overline{u_i u_j u_k}$, ϵ

Boussinesq suggested that an apparent scalar eddy viscosity might relate turbulent shearing stresses to the rate of mean stress (61:189). Using an analogy with the kinetic theory by which the molecular viscosity for gases has been calculated, the turbulent viscosity is modeled as $\mu_{\text{Turb}} = \rho v_{\text{Turb}} \ell$ where v_{Turb} and ℓ are characteristic velocity and length scales for turbulence, respectively (2:221). The first three models listed in Table 2 provide a means to solve for v_{Turb} and ℓ . The remaining two models are solved for the Reynolds stresses directly but require the solution of several simultaneous, differential equations. The averaged velocity functions developed in Chapter II allow the use of one of the first three types of turbulence models shown in Table 2 to obtain the values of eddy viscosity.

Eddy viscosity models were first developed for steady flow applications. The goal of these models is to find a relationship $\tau_{\text{Turb}} = \overline{-\rho uv} = f(x, r, u, p)$ that will faithfully reproduce the solid curve through the data on the universal wall plot for steady, turbulent boundary layers on smooth, solid surfaces. From an analogy with laminar flow, the eddy viscosity formulation of Boussinesq has the form (73:559)

$$\tau_{\text{Turb}} = \overline{-\rho uv} = \mu_{\text{Turb}} \frac{\partial u}{\partial y} \quad (13)$$

Prandtl suggested the mixing length formulation (73:469)

$$\tau_{\text{Turb}} = \overline{-\rho uv} = \rho \ell_m^2 \left| \frac{\partial u}{\partial y} \right| \frac{\partial u}{\partial y} \quad (14)$$

where l_e is some effective interaction distance between eddies. The eddy viscosity and the mixing length formulations are essentially equivalent since we may write from Eqs (13) and (14) as

$$\mu_{\text{Turb}} = \rho l_e^2 \left| \frac{\partial u}{\partial y} \right| \quad (15)$$

It is important to note that the turbulent viscosity, μ_{Turb} , must be expected to depend on the state of the flow and not just the state of the fluid.

The approach above is known as a gradient transport formulation and produces $\tau_{\text{Turb}} = 0$ where the velocity profile has zero slope. Due to the symmetry of the flows considered in this study, there is no net momentum transfer across the centerline and the gradient transport formulation applies. Schetz points out that experiments with high-velocity injection into a turbulent boundary layer through an upstream slot in the wall indicate that a nonzero, turbulent shear stress may exist at local maxima or minima in the velocity profile (61:176). However, theoretical and experimental studies of pulse propagation in pipe flow show that local maxima or minima, other than at the centerline, occur very close to the wall where the molecular viscosity is dominant (63:83; 70:594-595; 74:867). As a result, the gradient transport formulation should provide reasonable accuracy for the simple geometry and rigid, nonporous walls of the transmission lines in this study.

Turbulence models based on differential equations, such as the method of Bradshaw et al. (6) and two-equation models, require the

solution of differential equations in addition to the governing equations to determine a value for the eddy viscosity. This translates into a significant amount of computer time in addition to that required to solve the governing equations. Schetz (61:208) shows that formulations based on turbulent kinetic energy such as that of Bradshaw et al. (6) are equivalent to the algebraic mixing length or eddy viscosity methods for steady flow in the wall region. Since the predominant dynamic shear region is always very close to the wall in transient flow in transmission lines (63:84; 70:595; 74:866), use of the much simpler algebraic mixing length/eddy viscosity turbulence models for this study is justified on this basis. Anderson, Tannehill, and Pletcher (2:226) point out that algebraic models have accumulated an impressive record of good performance for simple flows and can be modified for simple compressible flow applications. The steady-flow algebraic eddy viscosity model developed by Van Driest was modified by Telionis (65) to account for transient flow. Lack of data on transient turbulent flow makes development of criteria for selecting a turbulent viscosity model impossible. As a result, the algebraic model described by Telionis will be used to calculate turbulent viscosity in this study.

The steady-state turbulent viscosity model of Van Driest is used as a point of departure for developing a model capable of describing eddy viscosity in transient turbulent flow. The steady-state model of Van Driest is shown below (73:477):

$$\mu_T = \rho \kappa^2 \left[1 - \exp \left(\frac{-y u_*}{26\nu} \right) \right]^2 y^2 \left| \frac{\partial u}{\partial y} \right| \quad (16)$$

where $u_* = \sqrt{\frac{\tau_w}{\rho}}$.

This eddy viscosity model is valid for steady flow but can be modified to include transient changes in the local axial pressure gradient and velocity. Cebeci accounts for unsteady effects by using τ_s instead of τ_w in the calculation of u_* (12:2153). τ_s is the shear stress evaluated at the edge of the viscous sublayer rather than at the wall. τ_s is obtained by solving Eq (17) which is the momentum equation for steady flow in the immediate vicinity of the wall. Cebeci justifies this modification on the physical grounds that the random velocity fluctuations, damped according to the mechanism of the Stokes layer, do not extend all the way to the wall but disappear at the viscous sublayer:

$$\frac{\partial \tau_s}{\partial y} = \frac{\partial p}{\partial x} \quad (17)$$

Telionis recommends the unsteady velocity term be included in the approximation of the momentum equation by modifying Eq (17) (66:233; 77:470):

$$\rho \frac{\partial u}{\partial t} = - \frac{\partial p}{\partial x} + \frac{\partial \tau_s}{\partial y} \quad (18)$$

τ_s is found by integrating from the wall to to the edge of the viscous sublayer:

$$\tau_s = \frac{1}{r_s} \left[a \tau_w + (r_s - a) \frac{\partial p}{\partial x} + \rho_w \int_{r_s}^a \frac{\partial u}{\partial t} r \, dr \right] \quad (19)$$

A more detailed development of the eddy viscosity model is presented in Appendix D.

White (73:471) describes a three-layer concept for boundary layers. There is an inner layer where viscous shear dominates, an outer layer where turbulent shear dominates and an overlap layer where both types of shear are important. The eddy viscosity model of Clauser is usually assumed to hold in the outer layer for flat plate flow (73:478):

$$\epsilon_0 = \rho \kappa_2 U_c \delta^* \quad (20)$$

where $\kappa_2 = 0.0168$ and δ^* is the displacement thickness. White (73:473) points out that the outer layer is commonly neglected in pipe flow. The outer layer has little effect on the analysis and the lack of intermittence in duct flow produces greatly increased turbulence at the centerline as compared to flow over a flat plate. As a result, Eq (19) will be used to calculate eddy viscosity from the wall through the inner and overlap layers to the centerline of the transmission line. No special expression will be used for the outer layer.

The modification to the eddy viscosity model of Van Driest suggested by Telionis (65) was developed primarily for low-frequency oscillating flow. Pressure disturbances examined with the finite-difference model in this study are not periodic and may contain frequency components significantly higher than the 10 - 50 Hz range for which the Telionis model was intended.

Studies of pulsating flow make reference to a frozen viscosity in

which the frequency of the signal is much higher than the mean turnover time of the turbulent eddies (11:682, 54:211). As a result, the eddies do not have time to reach a new equilibrium and the change in eddy viscosity is quite small. Brown characterizes this frozen viscosity by a relaxation time constant, which is the time it takes a fluid particle near the wall to travel a distance over which its deviation of turbulence level from its equilibrium level is reduced to e^{-1} of its initial value (11:686). This time constant is somewhat arbitrarily assumed to equal the time it takes a particle to travel 110 times the boundary layer momentum thickness. Brown points out that the lag in the establishment of turbulence is more important for most problems than the change in the velocity profile due to the dynamic effects (11:686). He further states that the lag becomes vastly more important for large disturbances than for small disturbances.

The effect of a lag in the establishment of turbulence in the solution of the equations developed in Chapter II could be incorporated by treating the changes in eddy viscosity like the response of a first-order system where the change in eddy viscosity lags the change in velocity by a time constant τ_c . Incorporating a first-order lag function into the unsteady, eddy-viscosity model is straightforward. The ordinary differential equation, $(\tau_c \frac{\partial}{\partial t} + 1) \mu_{lag} = K \mu_T$, is solved numerically for μ_{lag} with μ_T supplied by the eddy-viscosity model. μ_{lag} is then used in place of μ_T in Eqs (5) through (7). First-order behavior of eddy viscosity could be expected to significantly influence the waveform of the signal. In fact, Brown made an analogous modification to his frequency dependent model to account for eddy viscosity in turbulent periodic flow. The

steady-state, eddy-viscosity profile is multiplied by an empirically-determined complex function of frequency (10).

Unfortunately, values of τ_c and K could not be calculated for use in this study, since no data on unsteady turbulence resulting from pulses or arbitrary disturbances was found. As a result, no provision for relaxation of the eddy viscosity will be made in this study although it is recognized that the effects of relaxation can be important.

Steady-State Pressure and Velocity Fields

Relationships among the various coefficients in the polynomials used to approximate the velocity profiles were derived in Chapter II. These relationships provide a means to deduce an initial steady-state velocity profile of an established mean throughflow without carrying out the numerical solution of the governing equations to steady state.

The mean flow is caused by a difference in pressure between opposite ends of the transmission line at time $t < 0$. With the initial value of the pressure known at each end of the line, the steady-state average velocity for compressible flow in the line is found from the one-dimensional equations governing isothermal, compressible flow through a pipe (4:100):

$$u_0^2 = \frac{\left(\frac{p_0}{\rho_0} \right) \left[1 - \left(\frac{p_L}{p_0} \right)^2 \right]}{\frac{f L}{D} - \ln \left(\frac{p_L}{p_0} \right)^2} \quad (21)$$

The subscript 0 denotes the end of the line with the higher pressure

while the subscript L denotes the low-pressure end. The average velocity of the mean flow considered in this study will always be significantly less than the speed of sound. Isothermal behavior of the fluid is assumed for the mean flow since the mean velocity is low and the length of the transmission line is much greater than its radius. As a result, the isothermal equation is used to predict the mean velocity. The Darcy-Weisbach friction factor, f , is calculated as a function of Reynolds number as follows:

$$\text{Laminar Flow} \quad f = \frac{64}{R_e} \quad (22)$$

$$\text{Turbulent Flow} \quad f = \left[1.14 - 2 \log_{10} \left(\frac{21.25}{R_e^{0.9}} \right) \right]^{-2} \quad (23)$$

where $R_e = \frac{u_0 D \rho}{\mu}$ (4:50). Equation (21) cannot be solved for u_0 in closed form since f is a function of the unknown u_0 and an iterative solution of Eqs (21) and (22) or (21) and (23) for laminar or turbulent throughflow, respectively, is required. Newton's method is used to solve these equation pairs for u_0 :

$$u_0^{n+1} = u_0^n - \frac{g(u_0^n)}{\frac{dg}{du_0}} \quad (24)$$

The function $g(u_0^n)$ is obtained from Eq (21):

$$g(u_0) = \frac{\left(\frac{p_0}{\rho_0}\right) \left[1 - \left(\frac{p_L}{p_0}\right)^2 \right]}{\frac{f L}{D} - \ln \left(\frac{p_L}{p_0}\right)^2} - u_0^2 \quad (25)$$

The first derivative of Eq (25) with respect to u_0 is

$$\frac{dg}{du_0} = \left(\frac{p_0}{\rho_0}\right) \left[1 - \left(\frac{p_L}{p_0}\right)^2 \right] \left[\frac{f L}{D} - \ln \left(\frac{p_L}{p_0}\right)^2 \right]^{-2} \frac{L}{D} \frac{\partial f}{\partial u_0} - 2 u_0 \quad (26)$$

The derivative of the friction factor is easily found for both laminar and turbulent flow:

$$\text{Laminar} \quad \frac{\partial f}{\partial u_0} = - \frac{f}{u_0} \quad (27)$$

$$\text{Turbulent} \quad \frac{\partial f}{\partial u_0} = \frac{- 3.6 f^{3/2} \log(e)}{u_0} \quad (28)$$

Iteration is used to find u_0 from Eqs (24) through (28).

Once u_0 has been determined from the known values of p_0 and p_L , the pressures at each grid point along the interior of the line are found. Equation (21) must, again, be solved by iteration but this time for pressures at each interior point x_j , with u_0 and f known. The functions needed for Newton's method in this case are

$$g(p_{x_j}) = \frac{\left(\frac{p_0}{\rho_0}\right) \left[1 - \left(\frac{p_{x_j}}{p_0}\right)^2 \right]}{\frac{f x_j}{D} - \ln \left(\frac{p_{x_j}}{p_0}\right)^2} - u_0^2 \quad (29)$$

$$\frac{dg}{dp_{x_j}} = -\frac{2}{\rho_0} \left\{ \left[\frac{p_0}{p_{x_j}} - \frac{p_{x_j}}{p_0} \right] \left[\frac{f x_j}{D} - \ln \left(\frac{p_{x_j}}{p_0}\right)^2 \right]^{-2} + \frac{p_{x_j}}{p_0} \left[\frac{f x_j}{D} - \ln \left(\frac{p_{x_j}}{p_0}\right)^2 \right]^{-1} \right\} \quad (30)$$

Values of average velocity at each grid point along the line are found from the corresponding pressure value at that point:

$$u_{x_j} = u_0 \frac{p_0}{p_{x_j}} \quad (31)$$

The average mean velocity and pressure fields for a steady, mean flow are used to find steady-state values of the averaged velocity function in each flow interval. The same eddy viscosity model developed earlier in this section must be used to obtain steady-state values of the averaged velocities at the required locations along the line. The use of empirical expressions for the steady-state velocity profile produces an initial velocity field significantly different from what would be obtained from the numerical solution of the governing equations carried out until steady state is reached. The use of this incompatible field as a set of initial conditions causes the numerical solution to change significantly with time in the absence of an input

signal. This drift, under steady-state conditions, would show up as an error in the numerical solution when a signal is present.

The relations for obtaining the coefficients of the polynomials described in Chapter II provide the means to obtain an initial velocity field compatible with Eqs (5) and (6) or (10) and (11). The key to this procedure is recognizing that the value of the forcing function F_n is the same at the boundary of each flow interval for steady flow. The expression for F_n developed in Chapter II is shown below:

$$F_n = \frac{2\pi c^2}{\gamma p \Delta A_n} \left[(\mu_T)_{r=r_n} r_n \left(\frac{\partial u}{\partial r} \right)_{r=r_n} - (\mu_T)_{r=r_{n-1}} r_{n-1} \left(\frac{\partial u}{\partial r} \right)_{r=r_{n-1}} \right] \quad (32)$$

Values of F_n that differ from boundary to boundary would signify a net change in momentum inside each flow interval which is characteristic of an evolving flow. Equal values of F_n at each interval boundary also imply that the value of F_n at each boundary is equal to the value of F_H at the wall. The value for F_n in the case of an annular section is zero for steady flow when calculated as shown in Eq (32), since the momentum entering the interval balances that leaving. Figure 2 shows the flow cross section partitioned into both annular and cylindrical regions.

Equation (32) may be written at each cylindrical boundary as

$$F_n = \frac{2 c^2}{\gamma p r_n} (\mu_T)_{r=r_n} \left(\frac{\partial u}{\partial r} \right)_{r=r_n} \quad (33)$$

Note that this is Eq (32) with r_{n-1} equal to zero. For F_n in Eq (32) to be zero for the annular sections, the value of F_n in Eq (33) must be

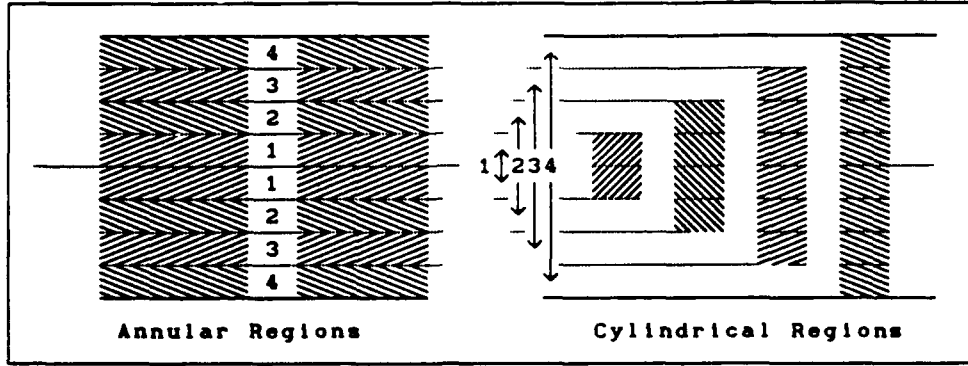


Fig. 2. Annular and Cylindrical Flow Partitions

the same at each interval boundary. The value of F_H at the wall is determined from the value of the mean velocity (4:42):

$$\tau_w = \frac{\rho u^2 f}{8} = \mu \left. \frac{\partial u}{\partial r} \right|_{r=a} \quad (34)$$

This equation is easily solved for $\left. \frac{\partial u}{\partial r} \right|_{r=a}$ to produce

$$\left. \frac{\partial u}{\partial r} \right|_{r=a} = \frac{\rho u^2 f}{8\mu} \quad (35)$$

The result of Eq (35) is used in Eq (33) to calculate the value of F_H . At the wall, μ_T is always equal to μ . At the interval boundaries away from the wall, however, μ_T , as described earlier in this chapter, depends on the velocity gradient $\left. \frac{\partial u}{\partial r} \right|_{r=r_n}$ which must be found by iteration. A first approximation of $\left. \frac{\partial u}{\partial r} \right|_{r=r_n}$ is obtained assuming $\mu_T = \mu$ and solving Eq (33):

$$\left(\frac{\partial u}{\partial r}\right)_{r=r_n} = \frac{F_n \gamma p r_n}{2 c^2 (\mu_T)_{r=r_n}} \quad (36)$$

This result is then substituted into Eq (16) to update μ_T . The new value of μ_T is substituted into Eq (36) to produce a better approximation of $\left(\frac{\partial u}{\partial r}\right)_{r=r_n}$. This process is repeated until changes in successive values of $\left(\frac{\partial u}{\partial r}\right)_{r=r_n}$ are sufficiently small to indicate convergence. This iteration is performed for all interval boundaries excluding the boundary at the wall. The velocity gradients for a laminar mean flow are obtained in a straightforward manner without iteration, since μ is known.

The values of the averaged velocity in each flow interval can be found from the velocity gradients at each interval boundary with the aid of the recursion relationships for the coefficients of the piecewise defined polynomials developed in Chapter II. The derivative of Eq (15) evaluated at the interval boundary provides an expression for the velocity gradients:

$$\left(\frac{\partial u}{\partial r}\right)_{r_n} = \begin{cases} p'(x, r_1, t) = 2\delta_1 c_2 & n = 1 \\ p'(x, r_n, t) = b_n + 2\delta_n c_n + 3\delta_n^2 d_n & n = 2, \dots, M \end{cases} \quad (37)$$

where $\delta_n = r_n - r_{n-1}$. Recall that b_n can be expressed in terms of c_2 through c_M and d_M as shown in Appendix C. Substitution of the recursion relations into Eq (37) for $M = 4$ produces Eq (38). Equation (38) is easily solved for c_2 , c_3 , c_4 and d_4 . The resulting values are used with Eq (9) to produce values of u_n for steady flow. An

expression similar to Eq (38) can be generalized for any number of flow intervals:

$$\begin{bmatrix} \frac{\partial u}{\partial r} \bigg|_1 \\ \frac{\partial u}{\partial r} \bigg|_2 \\ \frac{\partial u}{\partial r} \bigg|_3 \\ \frac{\partial u}{\partial r} \bigg|_4 \end{bmatrix} = \begin{bmatrix} 2\delta_1 & 0 & 0 & 0 \\ (2\delta_1 + \delta_2) & \delta_2 & 0 & 0 \\ (2\delta_1 + \delta_2) & (\delta_2 + \delta_3) & \delta_3 & 0 \\ (2\delta_1 + \delta_2) & (\delta_2 + \delta_3) & (\delta_3 + 2\delta_4) & 3\delta_4^2 \end{bmatrix} \begin{bmatrix} c_2 \\ c_3 \\ c_4 \\ d_4 \end{bmatrix} \quad (38)$$

IV. Numerical Scheme

Two-Step Lax-Wendroff Method

Equations (5) through (7) and (10) through (12), with the appropriate boundary conditions, must be solved simultaneously to obtain the transient response using a suitable numerical method. Tsao chose the two-step, Lax-Wendroff numerical approximation which uses centered differences in the spatial coordinate to solve a linearized form of the damped-wave equations (70:590). Tsao notes that his results for the transient response of a blocked line to a step input compared well with those of Brown (7; 70:592). The Lax-Wendroff scheme works well for the linearized damped-wave equations and provides formal second-order accuracy. However, it does not perform as well as other methods with respect to numerical diffusion when the local speed of sound is not constant.

The linear, damped-wave equations, Eqs (10) and (12), written in matrix form without damping terms are shown below:

$$q_t + A q_x = 0 \quad (39)$$

$$\text{where } q_t = \begin{bmatrix} \text{Ln}(p) \\ u \end{bmatrix}_t, \quad q_x = \begin{bmatrix} \text{Ln}(p) \\ u \end{bmatrix}_x, \quad \text{and } A = \begin{bmatrix} 0 & \gamma \\ \frac{c^2}{\gamma} & 0 \end{bmatrix}.$$

In terms of Eq (39), the Lax-Wendroff algorithm is written (2:102)

$$\frac{q_{j+1/2}^{n+1/2} - (q_{j+1}^n + q_j^n)/2}{\Delta t/2} + A \frac{q_{j+1}^n - q_j^n}{\Delta x} = 0 \quad (\text{Step 1}) \quad (40)$$

$$\frac{q_j^{n+1} - q_j^n}{\Delta t} + A \frac{q_{j+1/2}^{n+1/2} - q_{j-1/2}^{n+1/2}}{\Delta x} = 0 \quad (\text{Step 2}) \quad (41)$$

The accuracy of finite-difference algorithms can be compared by finding the modified equation and determining the amplification factor for each algorithm. The modified equation is the partial differential equation that is actually solved when a finite-difference method is applied to the original partial differential equation. The amplification factor shows the dissipation and dispersion errors resulting from the application of the finite-difference algorithm.

A scalar form of the modified equation more clearly illustrates the behavior of the numerical algorithm. Equation (39) is written as

$$T q_t + T A T^{-1} T q_x = 0 \quad (42)$$

The source of the matrix T will be explained during discussion of alternative finite-difference methods later in this chapter. A has two linearly independent eigenvectors making it similar to the diagonal matrix $[\Lambda_A]$ containing the eigenvalues of A so that $T A T^{-1} = [\Lambda_A]$. Equation (42) produces a system of two uncoupled, scalar equations. The expression

$$\frac{\partial q}{\partial t} + \rho_c \frac{\partial q}{\partial x} = 0 \quad (43)$$

is written from Eq (42) to determine the most restrictive conditions regarding accuracy and stability for algorithms applied to Eq (39). ρ_c

is the spectral radius of A (18:228) and is the value of the modulus of the eigenvalue with the largest modulus. Application of the Lax-Wendroff algorithm to Eq (43) produces

$$q_j^{n+1} = q_j^n - \frac{c}{2} \frac{\Delta t}{\Delta x} (q_{j+1}^n - q_{j-1}^n) + \frac{c^2}{2} \frac{(\Delta t)^2}{(\Delta x)^2} (q_{j+1}^n - 2q_j^n + q_{j-1}^n) \quad (44)$$

The modified equation is obtained from Eq (44) by substituting the Taylor-series expansions for q_j^{n+1} , q_{j+1}^n , and q_{j-1}^n to get

$$q_t + \rho_c q_x = -\frac{\Delta t}{2} q_{tt} - \frac{(\Delta t)^2}{6} q_{ttt} - \frac{(\Delta t)^3}{24} q_{tttt} + (\rho_c)^2 \frac{\Delta t}{2} q_{xx} + \rho_c \frac{(\Delta x)^2}{2} q_{xxx} + (\rho_c)^2 \frac{\Delta t (\Delta x)^2}{24} q_{xxxx} \quad (45)$$

All derivatives with respect to time are eliminated from Eq (45) using Eq (45) itself, to produce the scalar form of the modified equation (2:101):

$$q_t + \rho_c q_x = -\rho_c \frac{(\Delta x)^2}{6} (1 - \nu^2) q_{xxx} - \rho_c \frac{(\Delta x)^3}{8} \nu (1 - \nu^2) q_{xxxx} + \dots \quad (46)$$

where ν is the Courant number (21:212), which is written as $\rho_c \frac{\Delta t}{\Delta x}$. If Δt and Δx are chosen so that $\nu = 1$, the algorithm described by Eqs (41) and (42) provides the exact solution to Eq (40) since the right-hand side of Eq (43) is zero. As a result, the Lax-Wendroff algorithm satisfies the shift condition (2:92). At $\nu = 1$, this scheme is equivalent to solving Eq (43) exactly, using the method of characteristics.

The extent of the error resulting from the application of the Lax-Wendroff, finite-difference method is shown by the amplification factor. For a computational domain of length L in the x -direction, von Neumann stability analysis (27:525) assumes the roundoff error is written as

$$\varepsilon(x,t) = \sum_j e^{ja\Delta t} e^{j(i\beta)} \quad (47)$$

where $\beta = k_j \Delta x$, $k_j = \frac{j\pi}{L}$, and $j = 0, 1, \dots, N$. $j = 1$ denotes the fundamental frequency whose period is $2L$ and M is the number of Δx intervals contained in length L . Equation (47) must satisfy the finite-difference algorithm shown in Eq (44). A single term of Eq (47) is written as $\varepsilon_j = e^{ja\Delta t} e^{j(i\beta)}$ (2:72) and is used to generate the amplification factor G for Eq (44) shown below (2:102):

$$G = 1 - \nu^2(1 - \cos\beta) - i\nu \sin\beta \quad (48)$$

Note that each value of β represents a Fourier mode in von Neumann stability analysis.

Equation (48) can be written as $G = |G| e^{i\phi}$ where $|G|$ is the magnitude of G while ϕ is the phase of G . For Eq (44) to be stable, $|G| < 1$ for all values of β from 0 to 2π . Values of $|G|$ greater than one will allow roundoff error to grow without bound. Figures 3 and 4 show plots of $|G|$ and the relative phase error. The total dissipation from the application of the two-step, Lax-Wendroff method may be found from $(1 - |G|^n)A_0$ where A_0 is the initial amplitude of the wave and n is the

number of time steps. Similarly, if ϕ_0 represents the analytical phase of the left-hand side of Eq (46), the total dispersion error of the Lax-Wendroff method after n time steps is found from $n(\phi_0 - \phi)$. The total dispersion error $\phi_0 - \phi$ is the difference between the phase of the finite-difference solution and the phase of the exact solution of the differential equation. The relative phase-shift error ϕ/ϕ_0 and the amplification factor modulus $|G|$ will be used to characterize dispersion error and the dissipation error respectively, for a single time step.

Plots of $|G|$ and ϕ/ϕ_0 are used to compare the performance of other finite-difference methods to the performance of the Lax-Wendroff method. Figure 3 shows that the Lax-Wendroff method exhibits a lagging phase error for most values of β . A relative phase error greater than one indicates the numerical solution moves faster than, or leads the exact solution. For a relative phase errors less than one, the opposite is true.

The use of finite-difference methods on long transmission lines requires many time steps to generate a solution, allowing dissipation and dispersion errors to accumulate. Additionally, when the local speed of sound varies with signal amplitude, the Courant number cannot be chosen to be 1 everywhere along the line. The value of ν may be 1 at the location of highest pressure but will be less than 1 at other locations in the transmission line. To maintain accuracy, the total dissipation and dispersion errors must be small for a range of Courant numbers less than or equal to 1. Methods that produce the smallest numerical errors when $\nu < 1$ should be chosen as alternatives to the Lax-Wendroff method for the damped-wave equations. Maintenance of

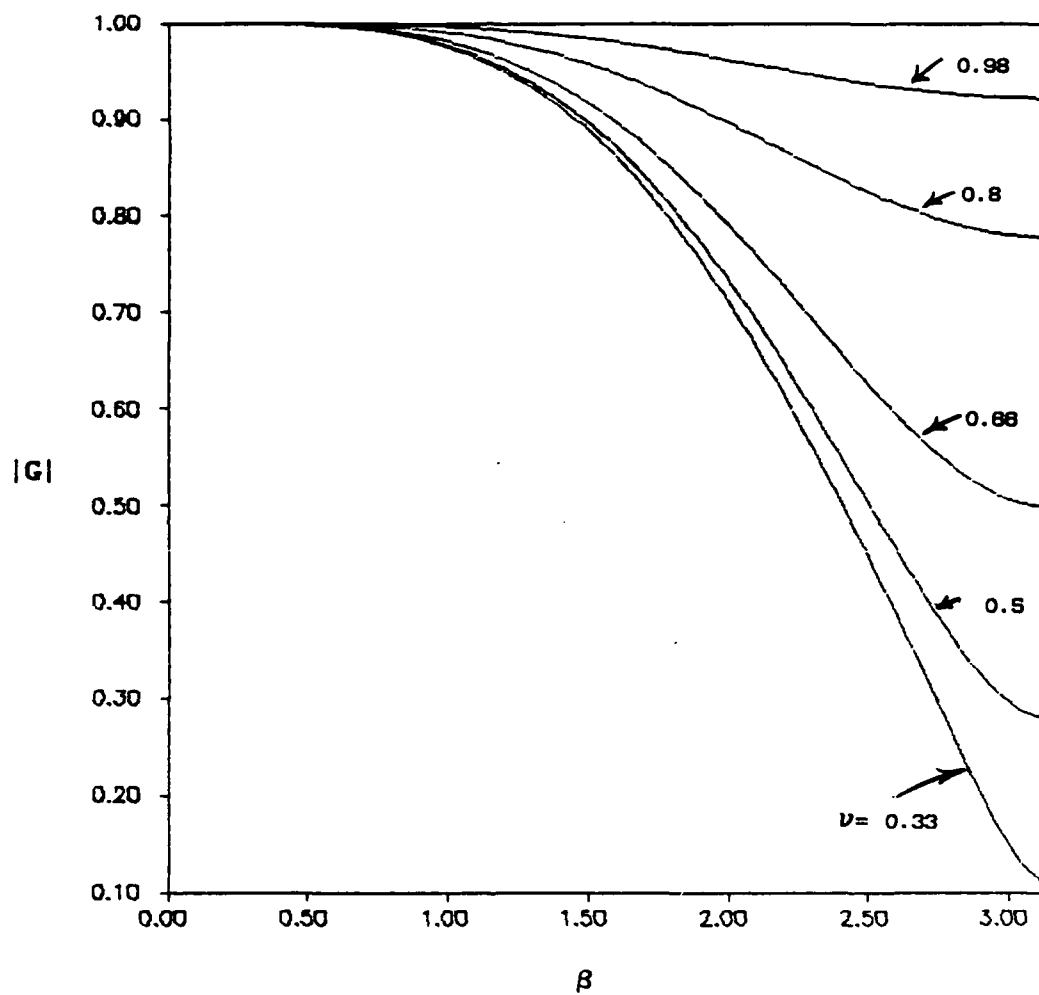


Fig. 3. Magnitude of Amplification Factor for Two-Step, Lax-Wendroff Method

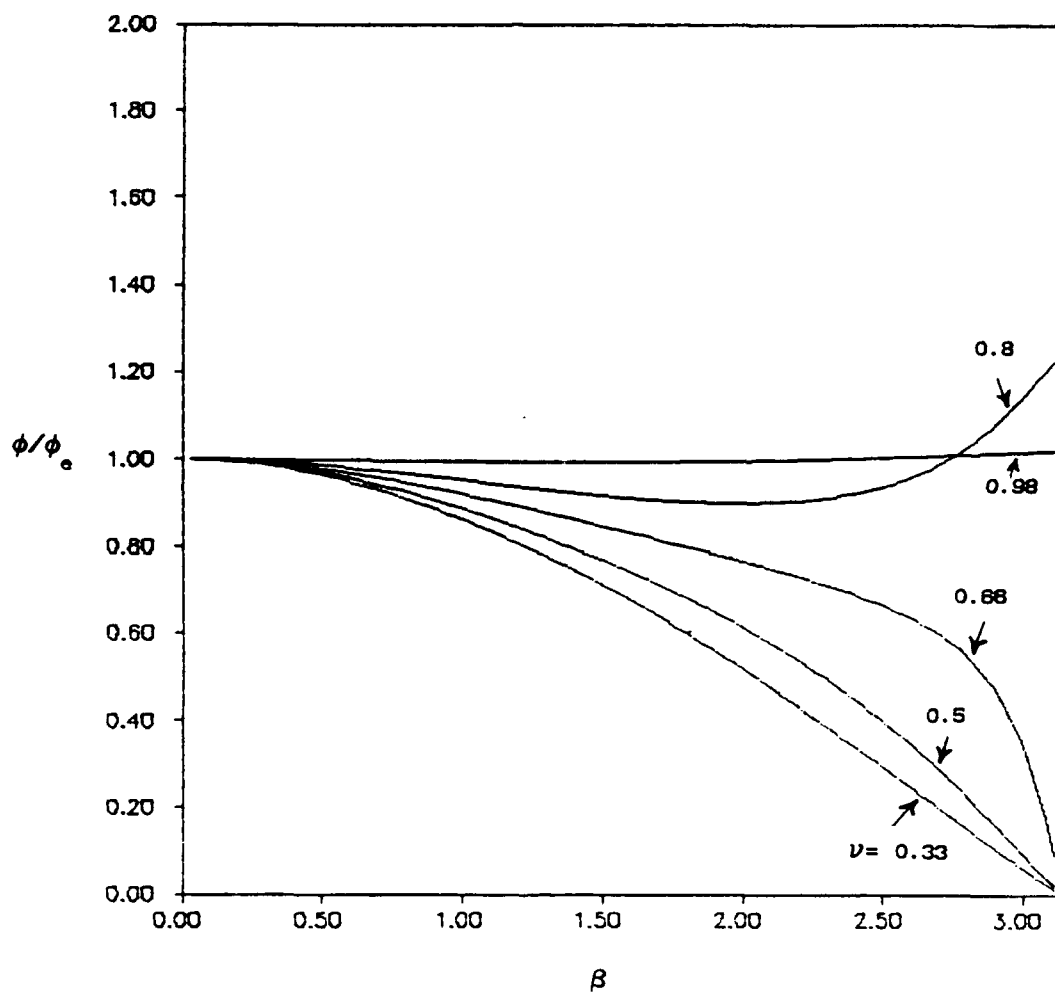


Fig. 4. Relative Phase Error for Two-Step, Lax-Wendroff Method

accuracy in the nonlinear case is what motivates the use of an alternative algorithm to the Lax-Wendroff method.

In a liquid, where the local speed of sound can be assumed constant, the method of characteristics yields an almost exact solution of the governing equations. However, if the wavespeed is strongly dependent on the local pressure or temperature, as it is in a gas, interpolation must be used with the method of characteristics when applied to a fixed grid. Traditional application of the method of characteristics uses a free-running grid (1). The position of the point on a fixed grid must be interpolated from points on the free-running grid whose location is not known until after the calculations are complete. Manning uses such a scheme on a rectangular grid by approximating the characteristic curves locally by straight line segments (41). It is this local linearization of the characteristic curves and subsequent interpolation of boundary points that reduces the accuracy of this method when applied to a fixed rectangular grid. This interpolation reduces the accuracy of the method of characteristics, making alternate numerical methods more attractive.

A number of finite-difference methods for solving the unsteady, Euler equations for compressible flow have been developed (15; 20; 45). The finite-difference method developed by Gabutti (21) was chosen for this study due to its small numerical dissipation and dispersion errors for the flow conditions under consideration. The basis for this selection is discussed below.

The damped-wave equations developed in Chapter II must be transformed to make use of the finite-difference methods developed for

the unsteady Euler equations. Eqs (5) and (6) are written

$$q_t + A q_x = \mathcal{F} \quad (49)$$

where $q = \begin{bmatrix} \ln(p) \\ u_n \end{bmatrix}$, $A = \begin{bmatrix} u_{av} & \gamma \\ \frac{c}{\gamma} & u_n \end{bmatrix}$, and $\mathcal{F} = \begin{bmatrix} H_{av} \\ F_n \end{bmatrix}$.

Equation (49) can be transformed to the required form, as described by Chakravorthy, by a process similar to that used to obtain the compatibility equations for the method of characteristics (15:2-4). Following Chakravorthy, the eigenvalues of the matrix A are found to be $\lambda = u_n \pm c$. A left eigenvector is associated with each eigenvalue λ . For $\lambda = u_n + c$:

$$l_1^T \begin{bmatrix} -c & \gamma \\ \frac{c^2}{\gamma} & -c \end{bmatrix} = 0 \quad \text{producing} \quad l_1 = \alpha \begin{bmatrix} 1 \\ \frac{\gamma}{c} \end{bmatrix} \quad (50)$$

where α is an arbitrary multiplier which arises because the length of the eigenvector is not unique. Similarly, for $\lambda = u_n - c$, the left eigenvector is found:

$$l_2^T \begin{bmatrix} c & \gamma \\ \frac{c^2}{\gamma} & c \end{bmatrix} = 0 \quad \text{producing} \quad l_2 = \beta \begin{bmatrix} -1 \\ \frac{\gamma}{c} \end{bmatrix} \quad (51)$$

where β is also an arbitrary multiplier. L is a matrix whose columns are the two left eigenvectors l_1 and l_2 with the multipliers α and β set equal to one.

$$L = \begin{bmatrix} 1 & -1 \\ \frac{\gamma}{c} & \frac{\gamma}{c} \end{bmatrix} \quad \text{and} \quad T^{-1} = L^T \quad (52)$$

Eq (49) is multiplied by T^{-1} to get:

$$\begin{bmatrix} 1 & \frac{\gamma}{c} \\ -1 & \frac{\gamma}{c} \end{bmatrix} \begin{bmatrix} \text{Ln}(p) \\ u_n \end{bmatrix}_t + \begin{bmatrix} 1 & \frac{\gamma}{c} \\ -1 & \frac{\gamma}{c} \end{bmatrix} \begin{bmatrix} u_n & \gamma \\ \frac{c^2}{\gamma} & u_n \end{bmatrix} \begin{bmatrix} \text{Ln}(p) \\ u_n \end{bmatrix}_x = \begin{bmatrix} 1 & \frac{\gamma}{c} \\ -1 & \frac{\gamma}{c} \end{bmatrix} \begin{bmatrix} H_n \\ F_n \end{bmatrix} \quad (53)$$

Two equations result from Eq (53):

$$\frac{\partial(\text{Ln}[p])}{\partial t} + \frac{\gamma}{c} \frac{\partial u_n}{\partial t} + (u_n + c) \frac{\partial(\text{Ln}[p])}{\partial x} + \frac{\gamma}{c} (u_n + c) \frac{\partial u_n}{\partial x} = H_n + \frac{\gamma}{c} F_n \quad (54)$$

$$-\frac{\partial(\text{Ln}[p])}{\partial t} + \frac{\gamma}{c} \frac{\partial u_n}{\partial t} - (u_n - c) \frac{\partial(\text{Ln}[p])}{\partial x} + \frac{\gamma}{c} (u_n - c) \frac{\partial u_n}{\partial x} = -H_n + \frac{\gamma}{c} F_n \quad (55)$$

These equations are used to incorporate the boundary conditions at each end of the transmission line into the algorithm for the interior points. u_{av} is substituted for u_n in Eqs (54) and (55) when solving for $\text{Ln}(p)$.

An alternate form of the governing equations for the internal points is needed. For each eigenvalue λ_i there is a left eigenvector l_i^T that must satisfy $l_i^T (A - \lambda_i I) = 0$, which is equivalent to $l_i^T A = l_i^T \lambda_i = \lambda_i l_i^T$. Following Chakravorthy, Eq (53) is written as (15:2-4)

$$\mathbb{T}^{-1} \mathbf{q}_t + [\Lambda_A] \mathbb{T}^{-1} \mathbf{q}_x = \mathbb{T}^{-1} \mathcal{F} \quad (56)$$

Where $[\Lambda_A]$ is a diagonal matrix of the eigenvalues of A .

Multiplication by \mathbb{T} produces

$$\mathbf{q}_t + \mathbb{T} [\Lambda_A] \mathbb{T}^{-1} \mathbf{q}_x = \mathcal{F} \quad (57)$$

Equation (49) has been recovered since $[\Lambda_A]$ is similar to A (18:196).

The original matrix A is now written as $\mathbb{T} [\Lambda_A] \mathbb{T}^{-1}$. The matrix $[\Lambda_A]$ is split into its positive and negative parts to get

$[\Lambda_A] = [\Lambda_A]^+ + [\Lambda_A]^-$. A is now written as:

$$A = \mathbb{T} [\Lambda_A]^+ \mathbb{T}^{-1} + \mathbb{T} [\Lambda_A]^- \mathbb{T}^{-1} = A^+ + A^- \quad (58)$$

where

$$\mathbb{T} = \begin{bmatrix} \frac{1}{2} & -\frac{1}{2} \\ \frac{c}{2\gamma} & \frac{c}{2\gamma} \end{bmatrix}; \quad \mathbb{T}^{-1} = \begin{bmatrix} 1 & \frac{\gamma}{c} \\ -1 & \frac{\gamma}{c} \end{bmatrix}; \quad [\Lambda_A]^+ = \begin{bmatrix} u_n + c & 0 \\ 0 & 0 \end{bmatrix} \quad \text{and}$$

$$[\Lambda_A]^- = \begin{bmatrix} 0 & 0 \\ 0 & u_n - c \end{bmatrix}.$$

Equation (49) is becomes

$$\mathbf{q}_t + A^+ \mathbf{q}_x + A^- \mathbf{q}_x = \mathcal{F} \quad (59)$$

The matrices A^+ and A^- in Eq (59) are obtained from Eq (58):

$$A^+ = \begin{bmatrix} \frac{u_n + c}{2} & \frac{\gamma(u_n + c)}{2c} \\ \frac{c}{2\gamma}(u_n + c) & \frac{u_n + c}{2} \end{bmatrix} \quad A^- = \begin{bmatrix} \frac{u_n - c}{2} & -\frac{\gamma(u_n - c)}{2c} \\ \frac{c}{2\gamma}(u_n - c) & \frac{u_n - c}{2} \end{bmatrix}$$

Note that $A^+ + A^- = A$. The A^+ and A^- matrices for the linear damped-wave equations Eqs (10) and (11) are determined as shown above:

$$A^+ = \begin{bmatrix} \frac{c}{2} & \frac{\gamma}{2} \\ \frac{c^2}{2\gamma} & \frac{c}{2} \end{bmatrix} \quad A^- = \begin{bmatrix} -\frac{c}{2} & \frac{\gamma}{2} \\ -\frac{c^2}{2\gamma} & -\frac{c}{2} \end{bmatrix}$$

The linear matrices differ only by the lack of u_n in each matrix element.

Substituting these expressions into Eq (59) and performing the required multiplication produces a set of simultaneous partial differential equations:

$$\frac{\partial(\ln[p])}{\partial t} + \frac{u_{av} + c}{2} \frac{\partial(\ln[p])}{\partial x} + \frac{\gamma}{2c}(u_{av} + c) \frac{\partial u_{av}}{\partial x} + \frac{u_{av} - c}{2} \frac{\partial(\ln[p])}{\partial x} - \frac{\gamma}{2c}(u_{av} - c) \frac{\partial u_{av}}{\partial x} = H_{av} \quad (60)$$

$$\frac{\partial u_n}{\partial t} + \frac{c}{2\gamma}(u_n + c) \frac{\partial(\ln[p])}{\partial x} + \frac{u_n + c}{2} \frac{\partial u_n}{\partial x} - \frac{c}{2\gamma}(u_n - c) \frac{\partial(\ln[p])}{\partial x} + \frac{u_n - c}{2} \frac{\partial u_n}{\partial x} = F_n \quad (61)$$

Appropriate one sided differences must be used to approximate the

spatial derivatives. Derivatives with coefficients containing $u_n + c$ are approximated using backward differencing, since these coefficients result from the A^+ matrix and represent right running waves.

Similarly, derivatives with coefficients containing $u_n - c$ are approximated using forward differencing. This is known as upwind differencing and is always in the opposite direction of propagation.

Three finite-difference methods applicable to Eqs (60) and (61) were considered. The method with the least numerical dispersion and dissipation is sought. A first-order method by Chakravarthy et al., known as the split-coefficient, matrix method (SCM), relies on a two-point differencing scheme (15). The finite-difference representation of Eqs (60) and (61) is written as

$$q_j^{n+1} = q_j^n - \frac{\Delta t}{\Delta x} (A^+ \nabla q_j^n + A^- \Delta q_j^n) \quad (62)$$

where $\nabla q_j^n = q_j^n - q_{j-1}^n$ and $\Delta q_j^n = q_{j+1}^n - q_j^n$. This method is first-order accurate in space and time, requiring relatively few operations to calculate successive points. However, a very fine grid is required to achieve good accuracy.

Second-order-accurate methods require fewer computational nodes to achieve a given accuracy than do first-order methods but more arithmetic operations are required to calculate successive points. A number of second-order methods suitable for application to the damped-wave equations exist. One method proposed by Moretti uses three-point differences in a predictor-corrector arrangement (46). At the predictor level

$$\overline{q_j^{n+1}} = q_j^n - \Delta t (A^+ q_x^- + A^- q_x^+) \quad (63)$$

$$\text{where } q_x^- = \frac{2q_j^n - 3q_{j-1}^n + q_{j-2}^n}{\Delta x} \quad \text{and} \quad q_x^+ = \frac{q_{j+1}^n - q_j^n}{\Delta x}.$$

At the corrector level

$$q_j^{n+1} = \frac{1}{2} (q_j^n + \overline{q_j^{n+1}} + \Delta t q_t^n) \quad (64)$$

where q_t^n denotes $q_t^n = A^+ q_x^- + A^- q_x^+$. The differencing is reversed from that of the predictor level:

$$q_x^- = \frac{q_j^{n+1} - q_{j-1}^{n+1}}{\Delta x} \quad \text{and} \quad q_x^+ = \frac{-2q_j^{n+1} + 3q_{j+1}^{n+1} - q_{j+2}^{n+1}}{\Delta x} \quad (65)$$

This scheme is second-order accurate, however it does not satisfy the shift condition.

A family of second-order-difference schemes that do satisfy the shift condition has been developed (21). The Gabutti schemes use a predictor-corrector approach, as does the Moretti scheme, but the differencing scheme is changed and the predictor is subdivided into two parts:

$$\overline{q_j^{n+1}} = q_j^n - \Delta t (A^+ q_x^- + A^- q_x^+) \quad (66)$$

$$q_t^n = A^+ q_x^- + A^- q_x^+ \quad (67)$$

The spatial differences for the first part of the predictor are

$$q_x^- = \frac{q_j^n - q_{j-1}^n}{\Delta x}, \quad q_x^+ = \frac{q_{j+1}^n - q_j^n}{\Delta x} \quad (68)$$

For the second part of the predictor the spatial differences are

$$q_x^+ = \frac{-2q_j^n + 3q_{j+1}^n - q_{j+2}^n}{\Delta x}; \quad q_x^- = \frac{2q_j^n - 3q_{j-1}^n + q_{j-2}^n}{\Delta x} \quad (69)$$

The corrector is written

$$q_j^{n+1} = q_j^n + \frac{\Delta t}{2} (q_t^n + \overline{q_t^{n+1}}) \quad (70)$$

where $\overline{q_t^{n+1}}$ is defined as

$$\overline{q_t^{n+1}} = A^+ q_x^- + A^- q_x^+ \quad (71)$$

and

$$q_x^- = \frac{\overline{q_j^{n+1}} - \overline{q_{j-1}^{n+1}}}{\Delta x}, \quad q_x^+ = \frac{\overline{q_{j+1}^{n+1}} - \overline{q_j^{n+1}}}{\Delta x} \quad (72)$$

This same scheme was earlier developed by Warming and Beam (2:294).

Equations (66) through (72) are combined to produce

$$q_j^{n+1} = q_j^n + \frac{\Delta t}{2}(q_t^n + \overline{q_t^{n+1}}) + \frac{\Delta t}{2\Delta x} A^- \Delta^2 q_j^n - \frac{\Delta t}{2\Delta x} A^+ \nabla^2 q_j^n \quad (73)$$

Scalar expressions for numerical dispersion, numerical dissipation and the modified equations for the three algorithms described above, obtained as discussed for the Lax-Wendroff method, are shown below for the wave equation with $\nu > 0$:

Upstream Method (SCM) (2:90-93)

$$q_t + \rho_c q_x = \rho_c \frac{\Delta x}{2}(1 - \nu)q_{xx} - \rho_c \frac{(\Delta x)^2}{6}(2\nu^2 - 3\nu + 1)q_{xxx} + \dots \quad (74)$$

$$G = 1 - \nu(1 - \cos\beta) + i\nu \sin\beta \quad (75)$$

Moretti λ Differencing (21:212)

$$q_t + \rho_c q_x = \rho_c \frac{(\Delta x)^2}{6}(2 + \nu^2)q_{xxx} - \rho_c \frac{(\Delta x)^3}{24}(6 + 3\nu - 2\nu^3)q_{xxxx} + \dots \quad (76)$$

$$G = 1 - \nu(1 - \cos\beta)^2 - \nu^2(1 + \cos\beta - 4\cos^2\beta + 2\cos^3\beta) - i\nu \sin\beta[2 - \cos\beta - 2\nu(1 - \cos\beta)^2] \quad (77)$$

Upwind Method (Gabutti, Warming-Beam) (2:103-104; 21:219)

$$q_t + \rho_c q_x = \rho_c \frac{(\Delta x)^2}{6}(1 - \nu)(2 - \nu)q_{xxx} - \rho_c \frac{(\Delta x)^3}{8}(1 - \nu)^2(2 - \nu)q_{xxxx} + \dots \quad (78)$$

$$G = 1 - 2\nu \left[\nu + 2(1-\nu) \sin^2 \frac{\beta}{2} \right] \sin^2 \frac{\beta}{2} - i\nu \sin \beta \left[1 + 2(1-\nu) \sin^2 \frac{\beta}{2} \right] \quad (79)$$

Figures 5 through 10 show the dissipation and relative phase errors for each of the above finite-difference methods. These figures show the error behavior for one time step. Up to 200 time steps are required to obtain the transient response of the systems considered in this study. The result is continued accumulation of dissipation and phase error at each time step. Based on amplification factors developed from the scalar equations shown above, the algorithm that exhibits the least dissipation error and relative phase error was selected for use in this study. An examination of Figures 3 through 10 indicates that the Gabutti method produces the least dissipation and dispersion error. Further, Gabutti states that in the case of subsonic flow, the phase errors produced by the forward and backward differences used in this algorithm tend to balance out (21:214).

Equation (80) is the complete amplification factor for the Gabutti method as applied to Eq (39) (21:220):

$$G = 1 - \frac{\Delta t}{\Delta x} [(A^+ - A^-)(1 - \cos \beta)^2 - i[\Lambda_A] \sin \beta (2 - \cos \beta)] + \left(\frac{\Delta t}{\Delta x} \right)^2 [(A^+)^2 + (A^-)^2] \cos \beta (\cos \beta - 1) + i \left(\frac{\Delta t}{\Delta x} \right)^2 [(A^+)^2 - (A^-)^2] \sin \beta (1 - \cos \beta) \quad (80)$$

Complete amplification factors for the other split coefficient methods discussed above are not shown but the expressions are of similar form and contain A^+ and A^- .

Additionally, Chaudhry and Hussaini compared the performance of

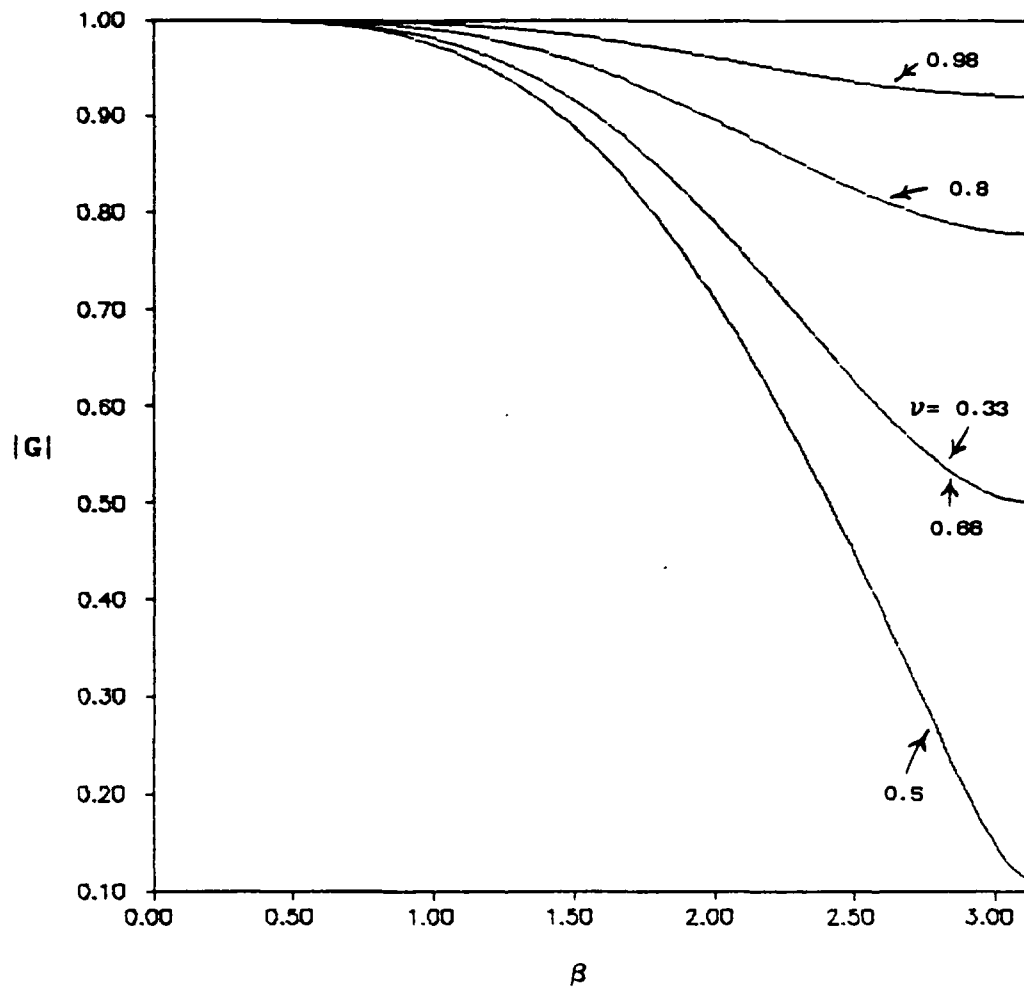


Fig. 5. Magnitude of Amplification Factor for Upstream (SCM) Method

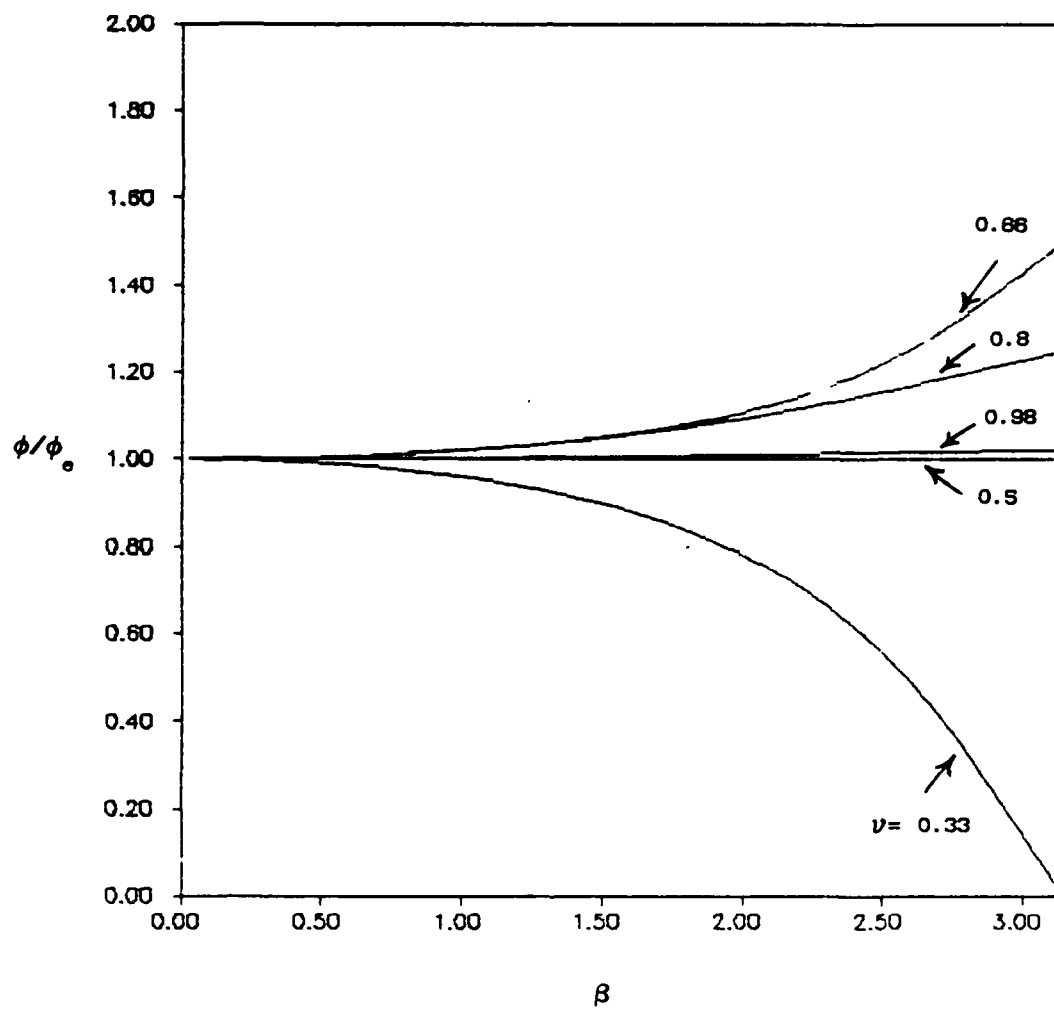


Fig. 6. Relative Phase Error for Upstream (SCM) Method

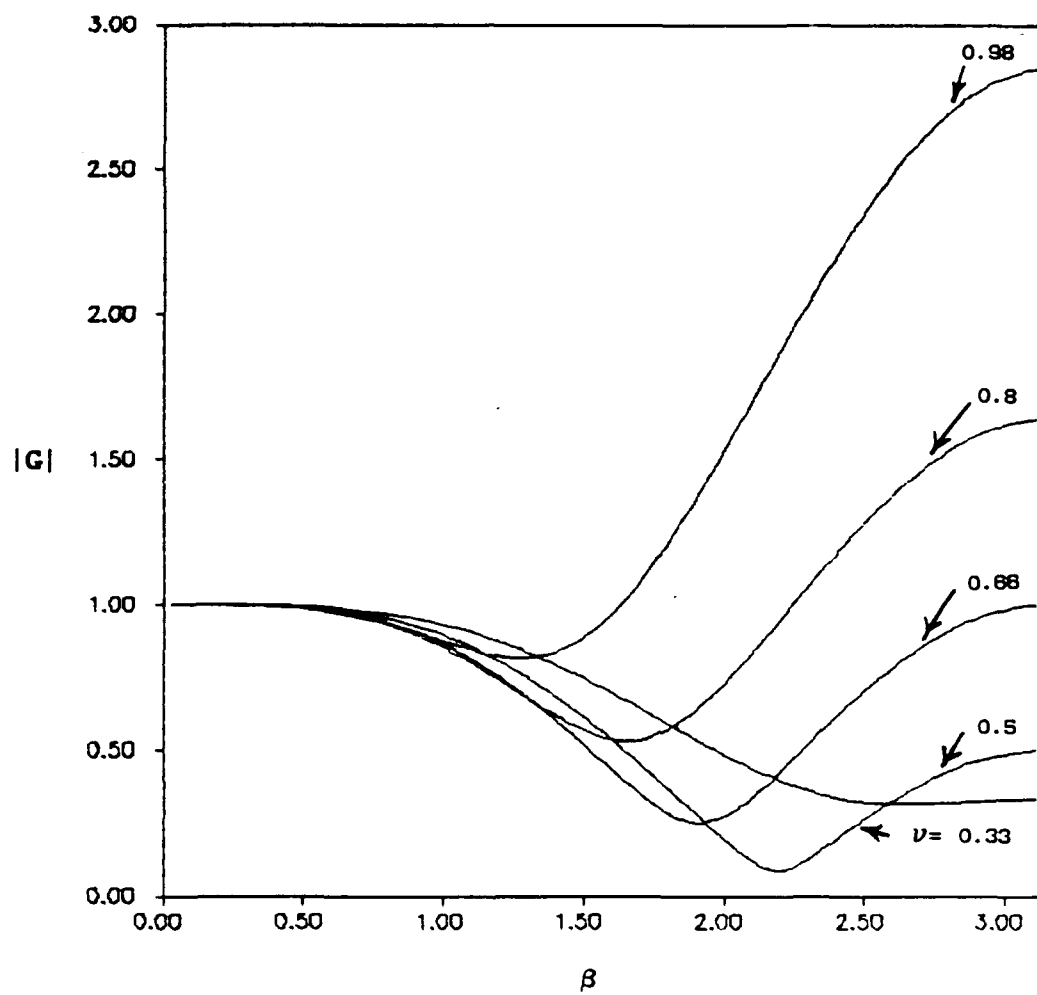


Fig. 7. Magnitude of Amplification Factor for Moretti λ Differencing Method

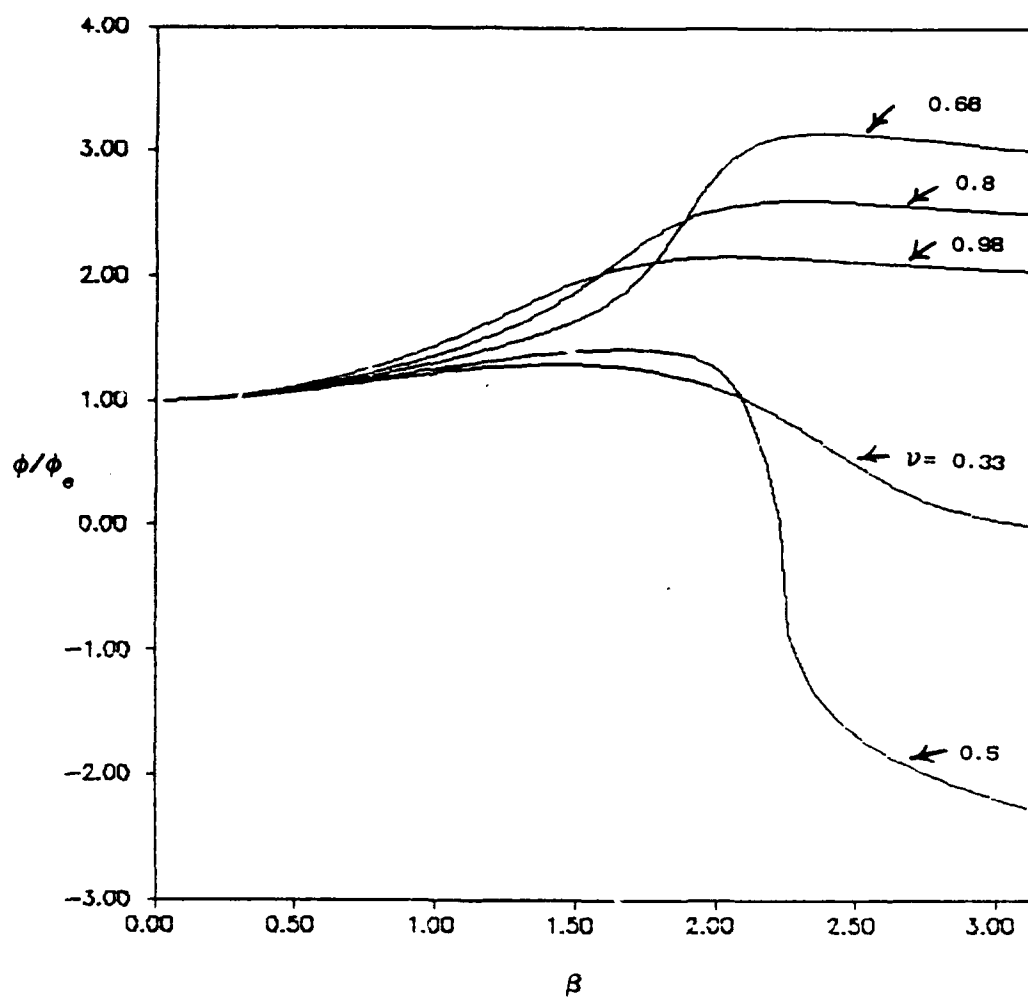


Fig. 8. Relative Phase Error for Moretti λ Differencing Method

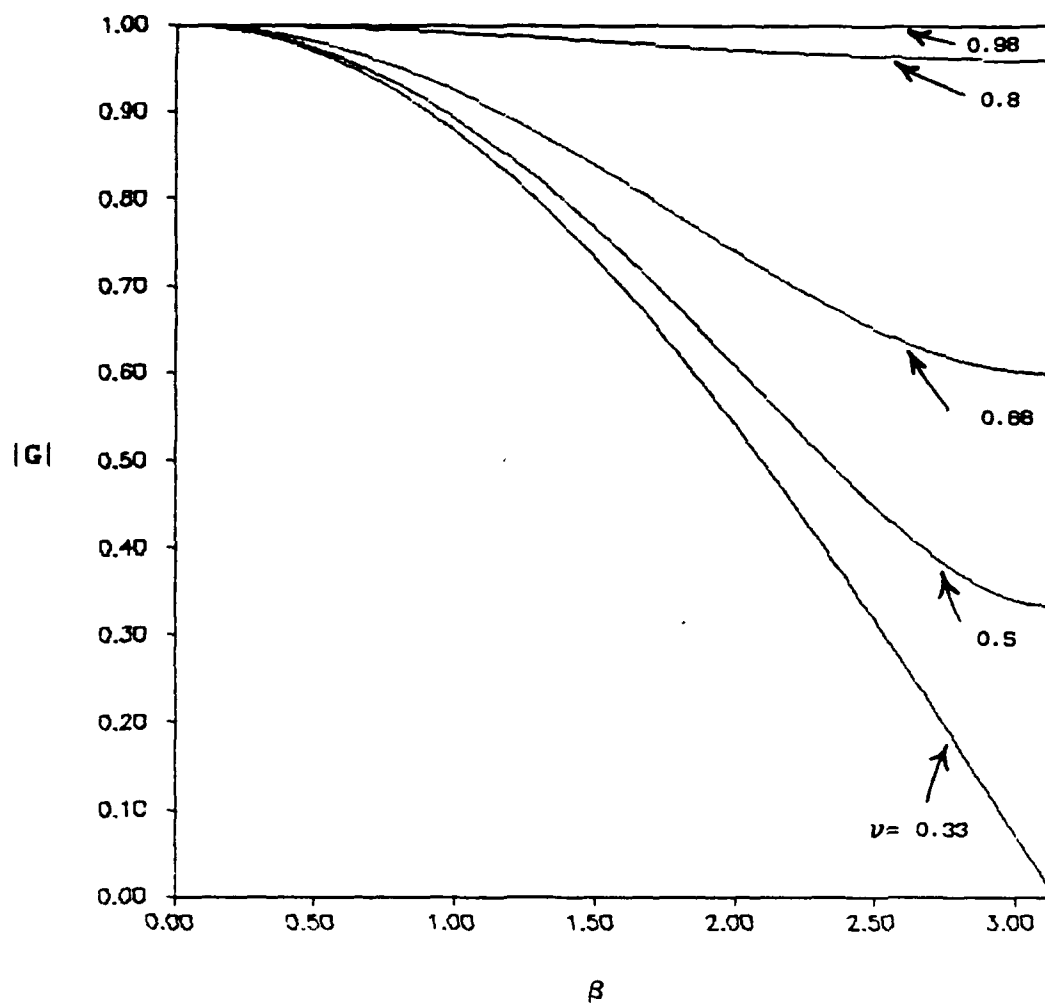


Fig. 9. Magnitude of Amplification Factor for Upwind (Gabutti)
Method

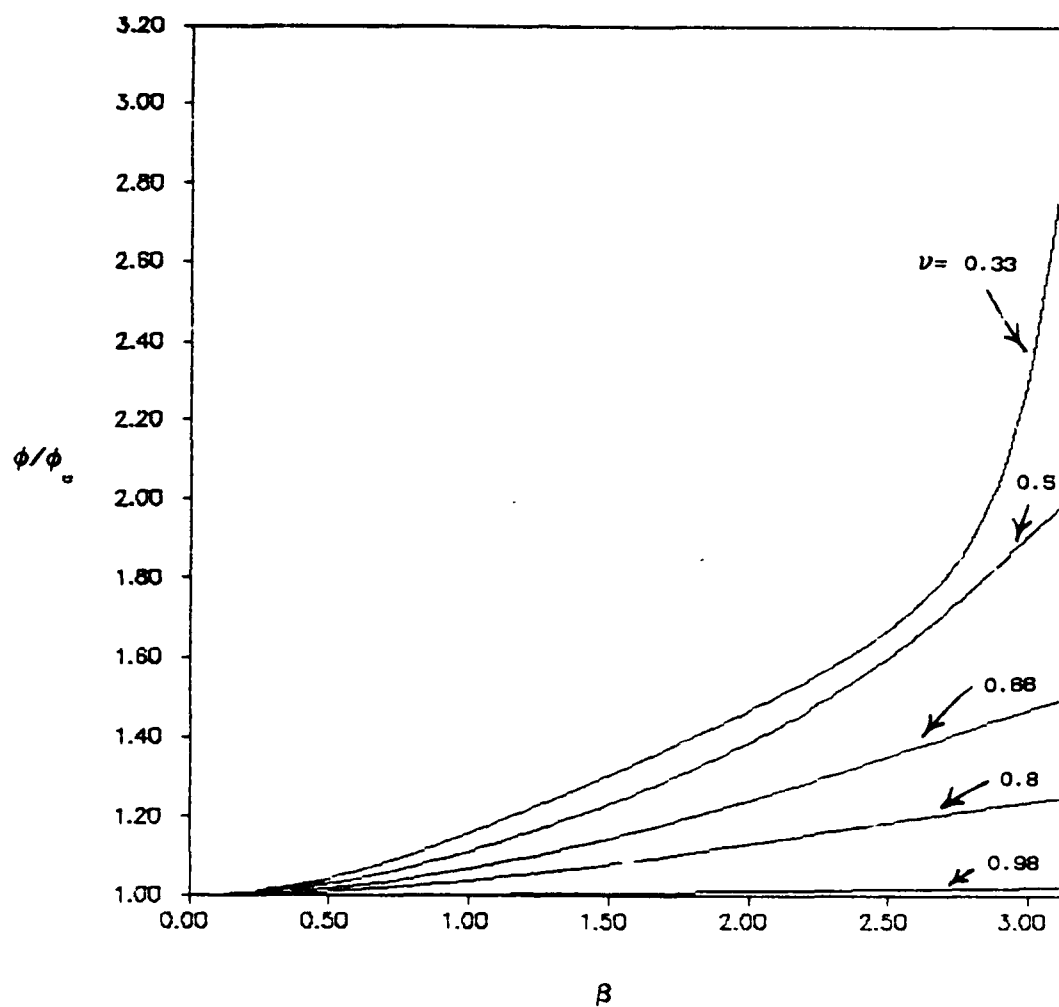


Fig. 10. Relative Phase Error for Upwind (Gabutti) Method

the Moretti λ -scheme, Gabutti scheme, the method of characteristics, and the MacCormack method for a waterhammer wave produced by an instantaneous valve closure in a pipeline (16). The system of equations used to compare the methods is shown below:

$$H_t + \frac{a^2}{gA} Q_x = 0 \quad (81)$$

$$Q_t + gA H_x + RQ|Q| = 0 \quad (82)$$

The MacCormack method is a variation of the two-step, Lax-Wendroff method and exhibits the same dissipation and dispersion behavior as the Lax-Wendroff method (2:103). A comparison of the error between the computed solution and the exact solution was made for the different numerical schemes using Courant numbers less than one. These results are important to this study since the Courant numbers will be less than one at points in the transmission line removed from points of peak pressures when the numerical method is applied to a nonlinear problem. The Moretti method produced unacceptable post shock oscillations. In fact, Gabutti shows that the Moretti method is unstable for $\nu > 2/3$, so this result is not surprising (21:213). The performance of the Gabutti method, the MacCormack method, and the method of characteristics compared well with the exact solution at Courant numbers less than one. This comparison of methods did not address errors resulting from numerical dispersion.

The Chaudhry and Hussaini comparison of numerical methods, in conjunction with the numerical performance of the three methods, discussed earlier, supports the Gabutti method as the best alternative

to the Lax-Wendroff method for a nonlinear system with respect to numerical error. A comparison of computational steps for each of these methods has not been made.

V. Lumped Parameter Representation of Transmission Line

Lumped-Parameter Models of Fluid Transmission Lines

The components of a finite-difference model for fluid transmission lines were developed in the previous chapters. While this model is very useful for understanding transient behavior of single transmission lines, application to fluid systems containing many components and other transmission lines requires computer capability normally not available to the design engineer. Practical fluid system design requires an engineering model that accounts for transmission line transient behavior in the total system response while requiring only modest computer resources.

A transmission line is usually part of a complex system consisting of devices represented in terms of time only. Unlike the distributed-parameter model developed in previous chapters, the lumped-parameter model describes the dynamic behavior of a fluid transmission line in terms of time only. A number of lumped-parameter approximations for the linear transmission-line model have been developed. One particularly useful lumped-parameter model is based on modal superposition (31; 40). This formulation results in a system of equations compatible with the state-space method commonly used in calculating the transient response of control systems.

Modal superposition, which is based on classical mechanics, approximates the total transmission-line response by superposing the transmission-line response for each of its normal modes. A system with

n degrees of freedom will have n natural frequencies. Under free vibration at one of its natural frequencies, a definite relationship exists among the amplitudes of each of the n coordinates corresponding to each of the n frequencies for a mechanical system such as a prismatic beam. This relationship is known as a normal mode of the beam (62:16-17).

Modal superposition describes the dynamic properties of the transmission line in terms of its modes of "vibration". The modes of vibration can only be defined for linear, dynamic, systems but nonlinear effects may be empirically incorporated into modal superposition by adjustment of the model coefficients (47). In the analysis of structural transients, the description of a structure's dynamic properties by a normal-mode model is computationally efficient since it involves relatively few parameters. The dynamic properties of a fluid transmission line may also be defined by specifying its modes of "vibration." When the dynamic properties of a structure or a transmission line have been determined, they can be used to predict transient responses to an arbitrary excitation.

Simplified Equations for Solution by Normal Modes

The same principles used to model the longitudinal vibration of prismatic beams in classical dynamics may be applied to a fluid transmission line. Tsao (70) developed a set of linearized damped-wave equations which provide a connection between the equations developed in Chapter II and modal superposition:

$$\frac{A}{\gamma p_0} \frac{\partial p}{\partial t} + \frac{\partial Q}{\partial x} = \frac{2\pi a(\gamma-1)}{\gamma p_0} k_T \left. \frac{\partial T}{\partial r} \right|_{r=a} \quad (83)$$

$$\frac{\partial Q}{\partial t} + \frac{A}{\rho_0} \frac{\partial p}{\partial x} = \frac{2\pi a}{\rho_0} \mu_T \left. \frac{\partial u}{\partial r} \right|_{r=a} \quad (84)$$

Equation (83) as originally shown by Tsao is incorrect. The right-hand side of Tsao's Eq (19) becomes $\frac{2\pi a(\gamma-1)T_0}{\gamma p_0}$ when $\frac{\nu}{\sigma}$ is rewritten as $\frac{kRT_0}{c_p p_0}$. A check of Tsao's development of the equation shows the factor $\frac{1}{T}$ was omitted from the second term of Tsao's Eq (9). Equations (83) and (84) are in terms of pressure and volumetric flow. The dissipation terms on the right hand side of each equation present a problem to modal superposition since the information necessary to evaluate the velocity and temperature gradients is not available. The left-hand sides of the equations pose no problem.

The perfect gas law $p_0 = \rho_0 RT$ and the expression for the speed of sound $c^2 = \gamma RT$, where R is the gas constant, are used to rearrange Eqs(83) and (84). Neglecting the heat transfer term and assuming Hagen-Poiseuille flow, Eqs (83) and (84) can be written as shown below (40:459; 61.20):

$$\frac{c^2}{A} \frac{\partial Q}{\partial x} + \frac{1}{\rho} \frac{\partial p}{\partial t} = 0 \quad (85)$$

$$\frac{1}{\rho} \frac{\partial p}{\partial x} + \frac{1}{A} \frac{\partial Q}{\partial t} + \frac{F}{A} Q = 0 \quad (86)$$

Following Lebrun, the dissipation resulting from friction is expressed as FQ where F is a loss coefficient calculated as $F = 8u/a^2$ for Hagen-Poiseuille flow (40:459). Although heat transfer is important

for transient, compressible flow, no simple expression for heat transfer in terms of Q alone can be developed for the right-hand side of Eq (83). A disturbance must be applied to each end of the transmission line to introduce pressure or flow signals. For the case of pressure signals, a forcing function Φ for use with Eq (86) is written as

$$\Phi = \frac{1}{L} [p_1 \delta(0) + p_2 \delta(L)] \quad (87)$$

where δ stands for the Dirac delta function.

As shown by Karnopp (31), Eqs (85) through (87) are combined to form a single second order partial differential equation in terms of Q :

$$\frac{\rho}{A} \frac{\partial^2 Q}{\partial t^2} + \frac{\rho F}{A} \frac{\partial Q}{\partial t} - \frac{\rho c^2}{A} \frac{\partial^2 Q}{\partial x^2} = \frac{1}{L} [\dot{p}_1 \delta(0) + \dot{p}_2 \delta(L)] \quad (88)$$

The dots placed above variables denote differentiation with respect to time.

Modal Superposition

Following the development of Lebrun (40), rename Q and p as f and e respectively. The symbol f denotes a flow variable while e denotes an effort variable. These variables are the power variables associated with bond graph modeling (42:96). Bond graphs are a concise, pictorial representation of interactive system dynamics from which governing system state-space equations can be derived directly (42:94). Bond

graphs also allow dependent and independent variables to be determined in an organized manner. Lebrun's development of modal superposition and proper application of the model to complex fluid systems rely on bond graphs. A detailed explanation of bond graph modeling techniques is provided by Karnopp and Rosenberg (32). Lebrun's modal representation of Eq (88) is obtained by expressing f as the product of mode shapes, $G_1(x)$, times modal general coordinates, $\xi_1(t)$ (31:439):

$$f(x,t) = \sum_{i=0}^{\infty} G_i(x) \xi_i(t) \quad (89)$$

ξ_1 is an independent coordinate analogous to the general coordinate used to analyze the motion of a mechanical system by modal superposition. Substitution of Eq (89) into Eq (88) produces

$$\frac{\rho}{A\xi_1} \frac{\partial^2 \xi_1}{\partial t^2} + \frac{\rho F}{A\xi_1} \frac{\partial \xi_1}{\partial t} - \frac{\rho c^2}{AG_1} \frac{\partial^2 G_1}{\partial x^2} = 0 \quad (90)$$

The forcing function on the right-hand side has been temporarily set to zero, since the normal modes are determined under free vibration (32:82). From Eq (85), $\left. \frac{\partial f}{\partial x} \right|_{x=0} = 0$, and $\left. \frac{\partial f}{\partial x} \right|_{x=L} = 0$, in the absence of the forcing function. These are the boundary conditions for Eq (90). From Eq(90), the separation of variables technique, detailed in Appendix E, produces a system of equations with the dependence upon the spatial variable, x , removed:

$$\frac{\rho L}{2A} \frac{\partial^2 \xi_1}{\partial t^2} + \frac{\rho L F}{2A} \frac{\partial \xi_1}{\partial t} + \frac{\rho c^2 i^2 \pi^2}{2AL} \xi_1 = \dot{e}_1 + \dot{e}_2 (-1)^i \quad (91)$$

The variables e_1 and e_2 denote pressure inputs at $x = 0$ and $x = L$, respectively. Integration over time produces the following:

$$\frac{\rho L}{A} \frac{\partial \xi_0}{\partial t} + \frac{\rho L F}{A} \xi_0 = e_1 + e_2 \quad (92)$$

$$\frac{\rho L}{2A} \frac{\partial \xi_1}{\partial t} + \frac{\rho L F}{2A} \xi_1 + \frac{\rho c^2 l^2 \pi^2}{2AL} \int_0^t \xi_1 dt = e_1 + e_2 (-1)^1 \quad (93)$$

Karnopp points out that Eq (92) represents the line as a single, lumped, inertia while Eq (93) represents a collection of modal oscillators (31:439). The following electrical analogies are drawn for this system of equations (32:40):

$$e_1 = \phi_R \xi_1 \quad (94)$$

$$e_1 = \phi_C^{-1} \int_0^t \xi_1 dt \quad (95)$$

$$e_1 = \frac{d}{dt} [\phi_I \xi_1] \quad (96)$$

where ϕ_R , ϕ_C , and ϕ_I symbolize resistance, capacitance, and inertance elements respectively. Equations (94) through (96) allow the inertia, capacitance, and resistance parameters in Eqs (92) and (93) to be identified by inspection. These parameters are listed in Table 3 where R , C , and I denote values of ϕ_R , ϕ_C and ϕ_I , respectively. The stiffness K is defined as $1/C$.

The significant frequency components of the input signals are likely to be contained inside some bandwidth. Let 0 to ω_0 be the frequency range containing the significant frequency components of the

Table 3

Inertia, Capacitance, and Resistance Parameters Pressure Inputs

	I	C	R
i=0	$\frac{\rho L}{A}$	∞	$\frac{\rho L F}{A}$
i=1, 2,	$\frac{\rho L}{2A}$	$\frac{2AL}{\pi^2 \rho c^2 i^2}$	$\frac{\rho L F}{2A}$

pressure signal imposed at the ends of the transmission line. There are an infinite number of modes as shown in Table 3, however, all modes above ω_0 may be treated as stiffness controlled (32:84). This approximation allows all frequency modes above ω_0 to be represented by a residual compliance. The effects of all modes above the frequency of the highest mode retained are summed up using this residual compliance. An expression for residual compliance is derived in Appendix E:

$$C_{eq} = \begin{bmatrix} C_{11} & C_{12} \\ C_{21} & C_{22} \end{bmatrix} = \frac{2AL}{\rho c^2 \pi^2} \begin{bmatrix} \sum_{j=1}^{\infty} \frac{1}{(n+j)^2} & \sum_{j=1}^{\infty} \frac{(-1)^{n+j}}{(n+j)^2} \\ \sum_{j=1}^{\infty} \frac{(-1)^{n+j}}{(n+j)^2} & \sum_{j=1}^{\infty} \frac{1}{(n+j)^2} \end{bmatrix} \quad (97)$$

Equations (95) and (96) may be written in general form by defining a new set of generalized coordinates (32:84; 40:461):

$$q_i = \int^t \xi_i dt \quad (98)$$

$$p_i = \int^t e_i dt \quad (99)$$

In terms of these general coordinates, Eqs (93) and (94) are written as

$$M \frac{d^2}{dt^2} q + R \frac{d}{dt} q + K q = H^T e_e \quad (100)$$

Symbols used in Eq (100) are defined in Table 4. A matrix form of Eq (96) is written as

$$M \frac{d}{dt} \dot{\xi} = M \frac{d^2}{dt^2} q = e \quad (101)$$

where $\dot{\xi}$ is a vector with components $\dot{\xi}_i$. Integrating once over time produces

$$M \frac{d}{dt} q = \int^t e \, dt = p \quad (102)$$

Equations (101) and (102) allow Eq (100) to be written in a state-space format:

$$\dot{p} = H^T e_e - K q - R M^{-1} p \quad (103)$$

$$\dot{q} = M^{-1} p \quad (104)$$

where \dot{p} and \dot{q} denote differentiation of p and q , respectively, with respect to time. At each end of the transmission line there is an applied pressure and a resultant flow. An output expression for the flows caused by the application of the pressure signals is needed.

The bond graph in Figure 11 represents Eqs (103) and (104) with a pressure input and a flow output at each end (40:460). The variables

Table 4

Definition of terms in modal state equations (39:461)

$$\mathbf{q} = \begin{bmatrix} q_0 & q_1 & \cdots & q_n \end{bmatrix}^T \quad \text{generalized displacement vector}$$

$$\mathbf{p} = \begin{bmatrix} p_0 & p_1 & \cdots & p_n \end{bmatrix}^T \quad \text{generalized momentum vector}$$

$$\mathbf{e} = \begin{bmatrix} e_{s1} & e_{s2} \end{bmatrix} \quad \text{input effort vector}$$

$$\mathbf{f} = \begin{bmatrix} f_{s1} & f_{s1} \end{bmatrix} \quad \text{output flow vector}$$

$$\mathbf{M} = \begin{bmatrix} I_0 & & 0 \\ & \cdot & \\ 0 & & I_n \end{bmatrix} \quad \text{inertance matrix}$$

$$\mathbf{K} = \begin{bmatrix} 0 & & 0 \\ & \cdot & \\ 0 & & K_n \end{bmatrix} \quad \text{stiffness matrix}$$

where $K_1 = \frac{\rho c^2 l^2 \pi^2}{2AL}$

$$\mathbf{R} = \begin{bmatrix} R_0 & & 0 \\ & \cdot & \\ 0 & & R_n \end{bmatrix} \quad \text{resistance matrix}$$

$$\mathbf{H} = \begin{bmatrix} 1 & 1 & 1 & \cdots & 1 \\ & & & \cdot & \\ 1 & -1 & 1 & & (-1) \end{bmatrix} \quad \text{coefficients of input vector}$$

chosen as input variables are clearly shown on the diagram and determine the output expression. The subscript e denotes inputs while the subscript s denotes outputs. The output relations for f_{s1} and f_{s2} are obtained directly from Figure 11 by performing the summations indicated by the 0-node at each end of

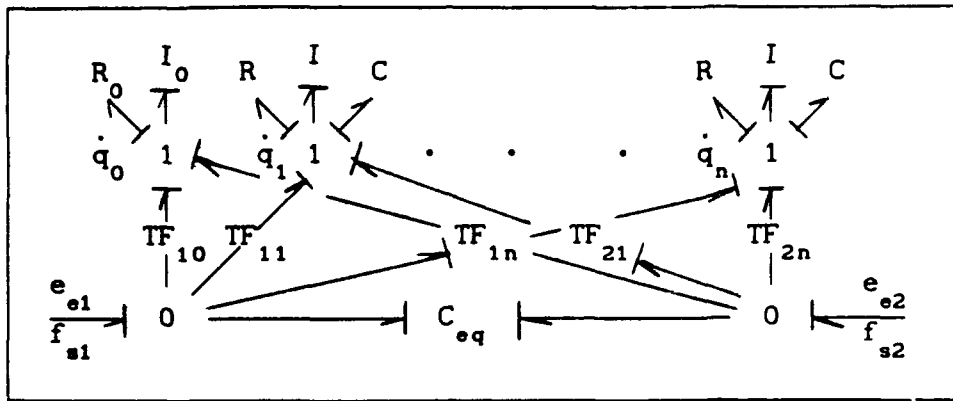


Fig. 11. Bond Graph for Eqs (106) and (107) with Pressure Inputs at Each End

the transmission line. The result is then integrated with respect to time. $\int^t f_{s1} dt$ and $\int^t f_{s2} dt$ are treated as displacements

$$\begin{bmatrix} \int^t f_{s1} dt \\ \int^t f_{s2} dt \end{bmatrix} = \begin{bmatrix} \int^t \sum_{i=0}^{\infty} \xi_i(t) dt \\ \int^t \sum_{i=0}^{\infty} (-1)^i \xi_i(t) dt \end{bmatrix} + C_{eq} \int^t \begin{bmatrix} \dot{e}_{e1} \\ \dot{e}_{e2} \end{bmatrix} dt$$

Displacement Sum of Displacements Displacement Due to
 at Ends of Line from Individual Modes Application of Force

(105)

Solving Eq (105) for f_s produces the output expression for the transmission line with a pressure applied to both ends

$$\int^t f_s dt = H q + C_{eq} e_e \quad (106)$$

The H matrix in Eq (106) results from the factorization of the first term on the right-hand side of Eq (105)

$$\begin{bmatrix} \int_0^t \sum_{i=0}^{\infty} \xi_i(t) dt \\ \int_0^t \sum_{i=0}^{\infty} (-1)^i \xi_i(t) dt \end{bmatrix} = \begin{bmatrix} 1 & 1 & \cdots & 1 \\ 1 & -1 & \cdots & (-1)^i \end{bmatrix} \int_0^t \begin{bmatrix} \xi_1(t) \\ \vdots \\ \xi_i(t) \end{bmatrix} dt \quad (107)$$

An alternate output expression is required for a transmission line having a pressure input at one end and a flow input at the other. For this case, the vectors e and f now contain the elements e_{e1} , e_{s2} and f_{s1} , f_{e1} , respectively. Each vector has one input and one output variable. The blocked line is an example of this case. The flow input at the blocked end is constant at zero while a pressure signal is applied at the open end. Figure 12 shows the bond graph for this case.

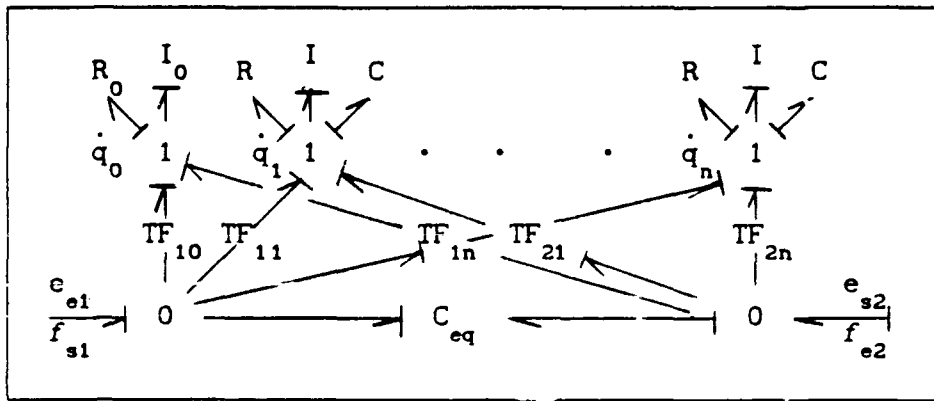


Fig. 12. Bond Graph for Mixed Pressure and Flow Inputs

Following Lebrun, Eq (106) is first solved for f_{s1} to produce:

$$f_{s1} = \left[c_{11} - \frac{c_{12} c_{21}}{c_{22}} \right] \dot{e} + \left[L_1 H - \frac{c_{21}}{c_{22}} L_2 H \right] \dot{q} + \frac{c_{21}}{c_{22}} f_{e2} \quad (108)$$

where $L_1 H$ and $L_2 H$ denote the upper row and lower row of matrix H , respectively. Equation (106) is then solved for e_{s2} with Eq (108) substituted for f_{s1} in the result:

$$e_{s2} = \frac{1}{c_{22}} \left[\int^t f_{s2} dt - L_2 H q \right] - \frac{c_{12}}{c_{22}} e_{s1} \quad (109)$$

Equations (103) and (104) with Eqs (108) and (109) as output relations form the system of simultaneous equations governing the dynamics of the blocked line shown in Figure 12.

The expressions for I , C , and R shown in Table 3 are of the same form as those contained in the average friction model for a circular line with no heat transfer (36:78):

$$I_a = \frac{\rho}{A} \quad (110)$$

$$C_a = \frac{A}{\rho c^2} \quad (111)$$

$$R = \frac{8\pi\mu}{A^2} \quad (112)$$

Equations (91) and (93) are rewritten in terms of Eqs (110) through (112) and the generalized coordinates defined in Eqs (98) and (99):

$$L I_a \frac{\partial^2 q_0}{\partial t^2} + L R \frac{\partial q_0}{\partial t} = e_1 + e_2 \quad (113)$$

$$\frac{L}{2} I_a \frac{\partial^2 q_1}{\partial t^2} + \frac{L}{2} R \frac{\partial q_1}{\partial t} + \frac{1^2 \pi^2}{2 L} \frac{1}{C_a} q_1 = e_1 + e_2 (-1)^1 \quad (114)$$

Equations (113) and (114) describe the linear behavior of a fluid transmission line assuming the parameters I_a (inertance), R (resistance), and C_a (conductance) are known. Similar equations may be obtained for an electrical transmission line.

Transmission line theory requires four distributed parameters to characterize a line (37). Figure 13 shows an infinitesimal section of length Δx of a uniform transmission line.

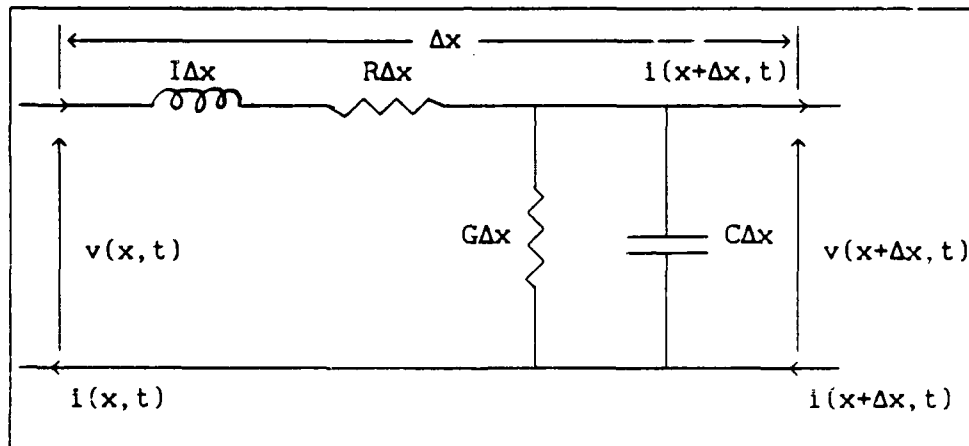


Fig. 13. Equivalent Circuit of an Infinitesimal Portion of Uniform Transmission Line in Time Domain

Electric circuit theory produces two partial differential equations from Figure 13:

$$\frac{\partial v(x, t)}{\partial x} = -R i(x, t) - I \frac{\partial i(x, t)}{\partial t} \quad (115)$$

$$\frac{\partial i(x,t)}{\partial x} = -G v(x,t) - C \frac{\partial v(x,t)}{\partial t} \quad (116)$$

where v denotes voltage and i denotes current. These two expressions are combined to form one equation in the same manner that Eq (88) was obtained from Eqs (85) and (86):

$$I \frac{\partial^2 i(x,t)}{\partial t^2} + \left(\frac{I G}{C} + R \right) \frac{\partial i(x,t)}{\partial t} - \frac{1}{C} \frac{\partial^2 i(x,t)}{\partial x^2} + \frac{R G}{C} i(x,t) = 0 \quad (117)$$

Equation (117) is similar in form to Eq (88) with the forcing function set to 0. In Eq (117), i replaces Q , I replaces $\frac{\rho}{A}$, $\frac{I G}{C} + R$ replaces $\frac{\rho F}{A}$, and $\frac{1}{C}$ replaces $\frac{\rho c^2}{A}$. The modal representation of Eq (117) with the forcing function set to zero is obtained by the same method used to obtain Eqs (92) and (93):

$$L I \frac{\partial^2 q_0}{\partial t^2} + L R \frac{\partial q_0}{\partial t} = 0 \quad (118)$$

$$\frac{L}{2} I \frac{\partial^2 q_k}{\partial t^2} + \frac{L}{2} R \frac{\partial q_k}{\partial t} + \frac{L}{2} \left(\frac{k^2 \pi^2}{L^2} \frac{1}{C} + \frac{R G}{C} \right) q_k = 0 \quad (119)$$

where $q_k = \int^t \xi_k dt$, $i(x,t) = \sum_{k=0}^{\infty} G_k(x) \xi_k(t)$, and $G_k(x)$ is the mode shape. Comparison of these equations with Eqs (113) and (114) suggests a way to include the parameter G into the modal representation of the fluid transmission line provided there is some means to calculate G . Note that Eqs (118) and (119) reduce to Eqs (113) and (114) for $G = 0$.

An approximation of the modal frequencies for the transmission line is obtained using the expressions for I and C shown in Table 3 with Eqs (103), (104), (108), and (109):

$$\left| \omega^2 \mathbf{I} - \mathbf{M}^{-1} \left(\mathbf{L}_2 \mathbf{H}^T \frac{1}{\mathbf{C}_{22}} \mathbf{L}_2 \mathbf{H} + \mathbf{C}^{-1} \right) \right| = 0 \quad (120)$$

Detailed development of this expression is shown in Appendix E. Solution of Eq (120) produces an approximation of the line's modal frequencies for whatever number of modes considered. Note that the effect of damping has been neglected and G has been assumed to equal zero. More accurate expressions for I and C produce better approximations of the modal frequencies as well as improve solution accuracy for the transient response of the transmission line to an applied signal.

The expressions for I, R, and C, shown in Table 3, do not vary with frequency. It is well known that values of these parameters as well as values for the conductance, G, are strong functions of frequency. Frequency dependent values for these parameters can be obtained from the frequency-domain techniques developed to calculate accurate values for I, R, C and G.

Since I, R, C, and G are functions of frequency, values must be calculated at the correct frequencies for the system under consideration. One method to obtain the correct modal frequencies is to use Eq (120) in conjunction with frequency dependent expressions for I, R, C, and G. This method requires iteration and repeated determination of the eigenvalues from Eq (120) and ignores the effects

of viscous damping and heat transfer. A more efficient method calculates the modal frequencies from the transmission line transfer matrix (36:68):

$$\frac{P_2}{P_1} = \frac{(Z_L/Z_c)}{\sinh \Gamma L + (Z_L/Z_c) \cosh \Gamma L} \quad (121)$$

where Z_L is the load impedance, Z_c is the characteristic impedance, and Γ is the propagation operator. The ratio P_2/P_1 is calculated over a range of frequencies containing the significant frequency components of the input signal. The values of ω where both $\frac{d P_2/P_1}{d\omega} = 0$ and $\frac{d^2 P_2/P_1}{d\omega^2} < 0$ are the modal frequencies.

Values of Z_L , Z_c , and Γ in Eq (121) are obtained as shown in Appendix A. Expressions requiring evaluation of complex Bessel functions have been developed for calculating I, R, C, and G (47:7), however, a simple, but accurate, approximation of these expressions exists. These approximate expressions, modified for use with Eqs (118) and (119), are shown below (37):

$$R(\omega) = \frac{8\pi\mu}{A^2} [DR] \quad (122)$$

$$I(\omega) = \frac{\rho}{A} + \frac{8\pi\mu}{A^2} [DL] \quad (123)$$

$$C(\omega) = \frac{A}{\gamma P} + \frac{(\gamma - 1) P [DC]}{\gamma P \{ [DC]^2 + [DG]^2 \}} \quad (124)$$

$$G(\omega) = \frac{(\gamma - 1) A [DG]}{\gamma P \left\{ [DC]^2 + [DG]^2 \right\}} \quad (125)$$

where

$$DR = \frac{3}{8} + \frac{1}{4} h_v + \frac{3}{8} \frac{1}{h_v} \quad (126)$$

$$DI = \frac{1}{4} h_v - \frac{15}{64} \frac{1}{h_v} \quad (127)$$

$$DC = \frac{1}{4} + \frac{1}{2} h_T + \frac{1}{4} \frac{1}{h_T} \quad (128)$$

$$DG = \frac{1}{2} h_T - \frac{1}{4} \frac{1}{h_T} \quad (129)$$

Expressions for h_v and h_T are shown in Appendix A.

Equations (122) through (129) are used to calculate values for I, R, C, and G at the various values of ω as Eq (121) is evaluated over the frequency range under consideration. The modal frequencies, determined in this manner, are then used in Eqs (122) through (129) to calculate values of I, R, C, and G for use as modal parameters. The values of these four parameters determine the transient response of the transmission line to an applied input signal when substituted into Eqs (118) and (119). A complementary set of equations of the same form as Eqs (103), (104), and (106) may also be obtained by eliminating the variable Q instead of p in Eqs (85) and (86). The procedure is exactly the same as previously shown. These complementary equations are summarized in Appendix E.

VI. Numerical Results

Summary of Figures

A summary of the performance of the finite-difference model developed in Chapters II through IV is shown in Figures 14 through 70. The capabilities and limitations of this model are demonstrated for the four basic transmission line configurations listed in Table 5.

Table 5
TRANSMISSION LINE CONFIGURATIONS ANALYZED
WITH FINITE-DIFFERENCE MODEL

LINE CONFIGURATION	ID (in)	LENGTH (ft)	TERMINATION
1	0.305	40	open
2	0.170	5	blocked
3	0.170	5	volume
4	0.170	5	open

The model is designed to predict the transient response of fluid transmission lines for input signals of arbitrary shape. However, only three input signals, a trapezoidal pulse, a sinusoidal pulse, and a terminated ramp, were used to study model performance. Input signal characteristics are shown in Table 6. The pulses provide sudden acceleration followed by sudden deceleration of the fluid with the trapezoidal pulse posing the most difficulty for the algorithm. The terminated ramp input was used in lieu of a step function since the

Table 6

Input Signal and Line Characteristics for Figures 14-52

Fluid Properties		Line Characteristics	
$\mu = 0.044 \frac{\text{lb}}{\text{ft hr}}$		$L = 40 \text{ ft}$	
$\rho_0 = 0.0747 \frac{\text{lb}}{\text{ft}^3}$		$D = 0.305 \text{ in}$	
$T_0 = 530^\circ \text{ R}$		$M = 4$	
		$r_1 = 0.12 \text{ in}$	
		$r_2 = 0.14 \text{ in}$	
		$r_3 = 0.15 \text{ in}$	
		$r_4 = 0.1525 \text{ in}$	
$c_0 = 1128.4 \frac{\text{ft}}{\text{sec}}$		Gridpoints	see text
SIGNAL CHARACTERISTICS			
SIGNAL	RISE TIME	DURATION	DECAY TIME
Trapezoidal Pulse	0.0002 sec	0.005 sec	0.0002 sec
Sinusoidal Pulse	—	0.005 sec ($\lambda = 5.64 \text{ ft}$)	—
Step	0.0002 sec	—	—

finite-difference algorithm does not cope well with discontinuities. These three signals provide a good assessment of the capabilities of the algorithm. Additionally, some published data for the step response of fluid transmission lines is available. Comparisons with published data are made where possible.

A linearized version of the finite-difference algorithm was also run for comparison with the nonlinear algorithm. Comparison of linear and nonlinear results from the same basic algorithm highlights the capability of the model to identify nonlinear effects resulting from an input signal of finite amplitude.

In addition to the finite-difference model results, Figures 71 through 86 demonstrate the performance of the modal superposition method developed in Chapter V. Comparisons between modal superposition results and results from the finite-difference algorithms are also shown. Figures shown in this chapter are summarized in Table 7. The term steady friction is used to denote friction losses calculated using a constant Darcy-Weisbach friction. Unsteady friction denotes viscous losses calculated directly from the transient velocity profile as opposed to a constant friction factor. In addition to unsteady friction, there is unsteady heat transfer which is calculated from the transient temperature profile. This nomenclature will be used to simplify discussion throughout this chapter.

Semi-infinite Line Simulation

Linear and nonlinear versions of the numerical algorithm were run using 1 psi amplitude input signals applied at $x = 0$ in the computational domain simulating a semi-infinite, 0.305 in ID, fluid transmission line. This is the first configuration listed in Table 5. The actual length of the computational domain simulated for this transmission line is 40 ft. The traveling wave produced by the input pressure pulse never reaches the opposite end of the computational domain during the time period of interest. This prevents any portion of the traveling wave from being reflected, producing results approximating the transient response of a semi-infinite transmission line. The effects of numerical dispersion and dissipation produced by the algorithm as well as the effects of the viscous damping and heat

Table 7

SUMMARY OF FIGURES

Figure	Line	Algorithm	Input Signal	Damping	Comments
14	0	N	TP	None	Profile, 40, 120, and 200 Grid
15	0	N	TP	None	Time History, 40, 120, 200 Grid
16	0	L	TP	None	Profile, 40, 120, and 200 Grid
17	0	L	TP	None	Time History, 40, 120, 200 Grid
18	0	N/L	TP	None	Time History, Flg 6.2, Flg 6.3
19	0	N	SP	None	Profile, 40, 120, and 200 Grid
20	0	N	SP	None	Time History, 40, 120, 200 Grid
21	0	L	SP	None	Profile, 40, 120, and 200 Grid
22	0	L	SP	None	Time History, 40, 120, 200 Grid
23	0	N	TP	None	Profile/Time History, Filtering
24	0	N	TP	SF	Profile/Time History
25	0	L	TP	SF	Profile/Time History
26	0	N	TP	UF	Profile/Time History
27	0	L	TP	UF	Profile/Time History
28	0	N/L	TP	UF	Profile/Time History
29	0	N	TP	SF/UF	Profile/Time History
30	0	L	TP	SF/UF	Profile/Time History
31	0	N	TP	FH	Profile/Time History
32	0	L	TP	FH	Profile/Time History
33	0	N/L	TP	FH	Profile/Time History
34	0	N	TP	UF/FH	Profile/Time History
35	0	L	TP	UF/FH	Profile/Time History
36	0	N	TP	SF/FH	Profile/Time History
37	0	N	TR	UF	Profile/Time History
38	0	L	TR	UF	Profile/Time History
39	0	N	TR	FH	Profile/Time History
40	0	L	TR	FH	Profile/Time History
41	0	N/L	TR	UF&FH	Profile
42	0	N/L	TR	UF&FH	Time History
43	0	N&L	TR	UF/FH	Profile
44	0	N&L	TR	UF/FH	Time History
45	0	N	SP	FH	Profile, 1, 5, 10 psi amplitude

Table 7 (continued)

SUMMARY OF FIGURES

Figure	Ramp Line	Algorithm	Input Signal	Damping	Comments
46	O	L	SP	FH	Profile, 1, 5, 10 psi amplitude
47	O	N/L	SP	FH	Profile, 1, 5, 10 psi amplitude
48	O	N/L	SP	FH	Time History, 1, 5, 10 psi
49	O	N/L	SP	FH	Convergence of N and L Results
50	O	L	TP	FH	Laminar/Turbulent Damping
51	O	L	TP	FH	Different Interval Boundaries
52	O	L	TR	FH	Velocity Profile Snapshots
53	-	-	--	--	Line Configurations
54	B	L	TR	FH	Laminar/Turbulent Friction, Data
55	B	L	TR	FH	Time History, 0.25, 1.0, 2.0 psi
56	B	N/L	TR	FH	Time History
57	V	L	TR	FH	Time History, 0.25, 1.0, 2.0 V_L
58	V	L	TR	FH	Time History, $V_c = 0.5 V_L$, Inlet
59	V	L	TR	FH	Time History, $V_c = 0.5 V_L$, Exit
60	V	L	TR	FH	Time History, $V_c = 1.0 V_L$, Inlet
61	V	L	TR	FH	Time History, $V_c = 1.0 V_L$, Exit
62	O	N/L	TR	FH	Time History, 0.25 psi
63	O	L	TR	FH	Time History, 1.0 psi, Inlet
64	O	L	TR	FH	Time History, 1.0 psi, Exit
65	O	L	TR	FH	Time History, 2.0 psi, Inlet
66	O	L	TR	FH	Time History, 1.0 psi, Exit
67	B/O	L	TR	FH	Time History, 1.0 psi, Inlet
68	B/O	L	TR	FH	Time History, 2.0 psi, Inlet
69	-	-	--	--	Polynomial Velocity Profiles
70	SC	L	--	UF	Oil-Filled Line, Sudden Closure
71	B	L	TR	--	Steady LRC/Finite-Difference
72	B	L	TR	--	Unsteady LRC/Finite-Difference
73	B	L	TR	--	Unsteady LRCG/Finite-Difference
74	B	L	TR	--	Unsteady LRCG/Unsteady LRC
75	B	L	TR	--	Unsteady LRCG, 6 Modes
76	B	L	TR	--	Unsteady LRCG, 10 Modes
77	B	L	TR	--	Unsteady LRCG, 15 Modes

Table 7 (continued)

SUMMARY OF FIGURES

Figure	Line	Algorithm	Input Signal	Damping	Comments
78	B	L	TR	--	Unsteady LRCG, 20 Modes
79	V	L	TR	--	LRCG/Finite-Difference, Inlet 15 Modes, $V_c = V_L$, Pressure
80	V	L	TR	--	LRCG/Finite-Difference, Inlet 15 Modes, $V_c = V_L$, Velocity
81	V	L	TR	--	LRCG/Finite-Difference, Exit 15 Modes, $V_c = V_L$, Velocity
82	B	L	TR	--	LRCG, Branched Line
83	O	L	TR	--	LRCG/Finite Difference, Inlet, 15 Modes, Velocity, 1.0 psi
84	O	L	TR	--	LRCG/Finite Difference, Exit, 15 Modes, Velocity, 1.0 psi
85	O	L	TR	--	LRCG/Finite Difference, inlet, 15 Modes, Velocity, 0.25 psi
86	O	L	TR	--	LRCG/Finite Difference, Exit, 15 Modes, Velocity, 0.25 psi

B = Blocked Line

O = Open Line

V = Volume Terminated
Line

TP = Trapezoidal

SP = Sinusoidal

TR = Terminated
Ramp

SF = Steady Friction

UF = Unsteady Friction

FH = Combined Unsteady
Friction and Heat
Transfer

transfer functions can be more easily observed with no reflections present.

Figure 14 shows the profiles of a trapezoidal pressure pulse at three separate times as it travels from left to right along a line with no damping. The nonlinear version of the numerical algorithm for Eqs (54), (55), (60), and (61) is used with the viscous damping and heat transfer terms neglected. As discussed in Chapter II, the damped-wave equations are coupled together through the damping and heat transfer functions. Setting these functions to zero, as in Figure 14, is

equivalent to specifying a uniform velocity over the cross section, making the system of equations equivalent to a one-dimensional system. In the nonlinear algorithm, coefficients containing axial velocity, u , and sonic velocity, c , vary locally, with c being a function of the local temperature in this model. In contrast, the linear version of the algorithm neglects the axial velocity in these coefficient terms and uses a constant value of c based on the line conditions present before signal application. The three curves shown in each part of Figure 14 represent a plot of pressure versus axial distance at three separate times. These are three snapshots of the same pressure pulse as it travels down the transmission line. This figure highlights effects caused by numerical errors introduced by the algorithm and shows the importance of choosing a sufficiently small value for the spatial discretization.

Figure 14a was produced using a computational domain containing 40 grid points over a distance of 40 ft (1 grid point per ft). This severe rounding results from the use of an insufficient number of points to accurately convey the information contained in the input signal to the algorithm. The input signal that the algorithm "sees" lacks most of the detail of the original input signal. The high frequency components necessary to resolve the corners and steep slopes of the pulse cannot be carried by the coarse mesh.

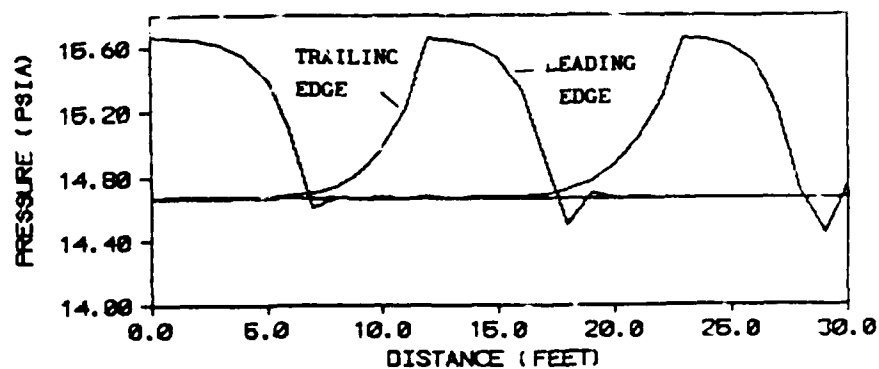
In addition to the distortion caused by a lack of waveform detail for the input signal, numerical distortion appears in the form of oscillations at the leading edge of the waveform. These oscillations result from the numerical dispersion error introduced by the algorithm. The oscillations are not very severe in Figure 14a since Δx is quite

large for the coarse grid. The value of the error term containing the fourth derivative in the modified equation Eq (80) becomes significant, providing numerical dissipation. This tends to damp out the oscillations produced by the third derivative error term.

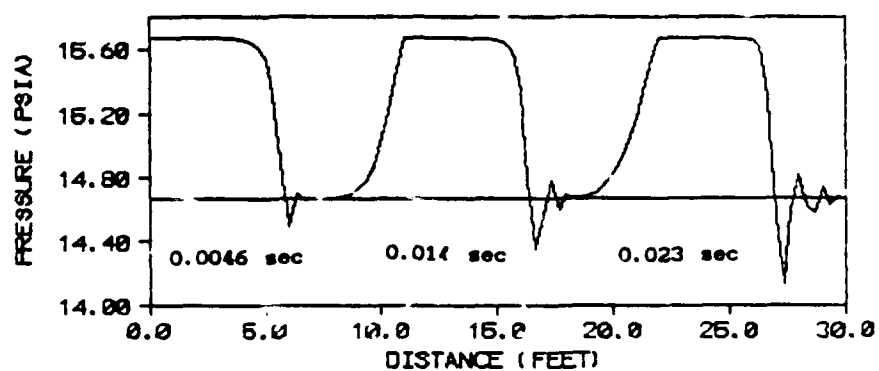
Figures 14b and c use 120 and 200 grid points, respectively, providing significantly improved resolution of the waveform. The oscillations produced by the numerical dispersion become more severe due to a decrease in the damping provided by the fourth derivative error term of the modified equation. The oscillations in Figure 14c are very severe, and actually extend well below the horizontal axis of the chart. The graphics program used to produce the chart ignores points with pressure values less than the lower limit of the vertical axis, exaggerating the distortion to the leading edge of the waveform.

Notice that the slope of the leading edge of the waveform steepens while the slope of the trailing edge flattens as it progresses down the line. This is a nonlinear effect caused by locally varying values of c and u in the coefficient terms of the damped wave equations. Results from the linear, finite-difference algorithm show no steepening of the waveform, as will be seen in Figures 16 and 17.

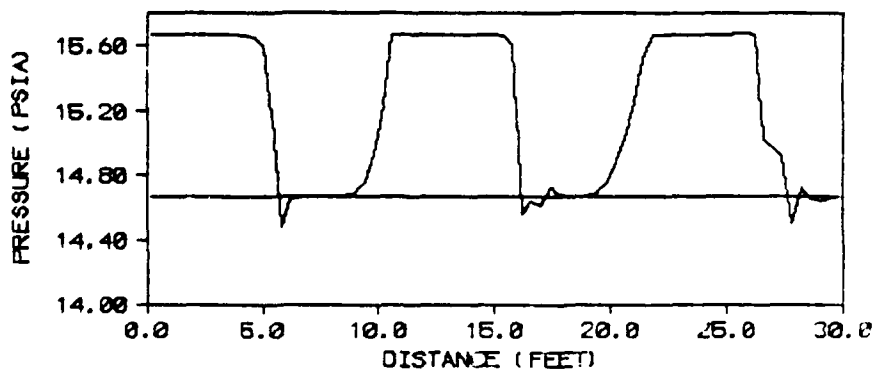
Figure 15 shows the signal pressure as a function of dimensionless time at the 0, 10, and 20 ft tube axial locations. This is the same transmission line shown in Figure 14 but the waveform information is shown at discrete locations as a function of time instead of discrete times as a function of location. The same waveform shape change and oscillations observed in Figure 14 appear here. Note that the curves in Figure 15a appear much cruder than their counterparts in Figure 14a. In Figure 14a, the pressure is mapped at each grid point contained in



a. 40 Grid Points



b. 120 Grid Points

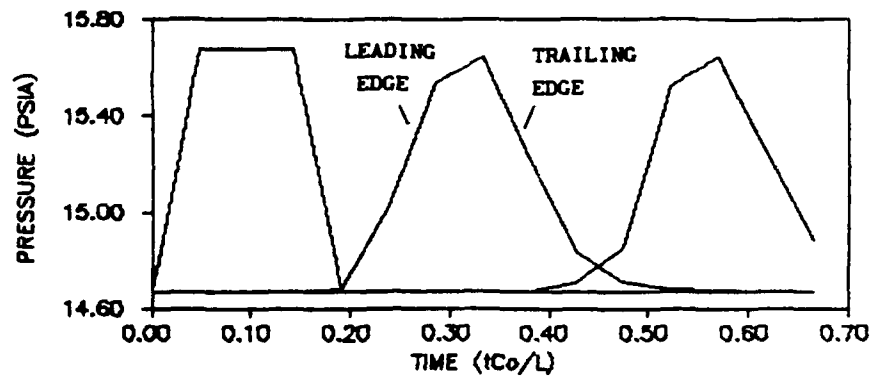


c. 200 Grid Points

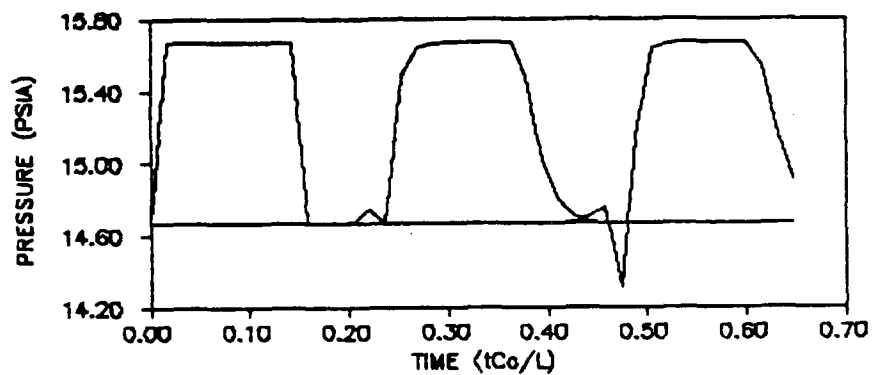
Fig. 14. Single Trapezoidal Pulse Traveling to Right, Nonlinear Results, No Damping, Times and Relative Positions of Leading and Trailing Edges Are The Same for All Signal Profiles.

the 30 ft span shown on the horizontal axis. In Figure 15a, the pressure is calculated at each value of time, with $\Delta t = \frac{\Delta x}{c}$. For long lines with relatively few grid points, Δt may be quite large compared to the rise and decay times of the waveform. With more grid points, the resolution increases dramatically as shown in Figures 15b and 15c. These results clearly show that the choice of computational grid resolution must consider the waveform of the input signal. Slowly changing signals require fewer grid points than signals with steep slopes and spikes to achieve good resolution. Note that there is no significant change in the amplitude of the wave in Figures 14b, 14c, 15b, and 15c. Some numerical dissipation will be present using the nonlinear form of the algorithm since the local Courant number ν is not always exactly 1.0, however, it causes no noticeable damping effect on the waveform over the time period of interest. When $\nu = 1$, the error terms in the modified equation Eq (78) for the numerical algorithm are zero. No oscillations at the leading edge of the wave are present when the linear version of the algorithm is used. The value of ν is 1.0 at all points and all times for the linear algorithm. For a fixed, uniform grid, the value of ν cannot always be 1.0 with the nonlinear algorithm. As a result, numerical errors appearing as oscillations in the solution are produced.

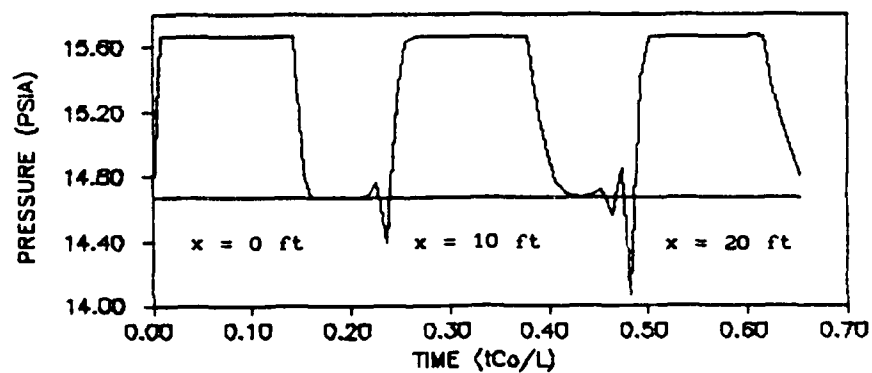
Results from application of the numerical algorithm to Eqs (10) through (12), the linear, damped-wave equations, are shown in Figures 16 and 17. The same semi-infinite line used in Figures 14 and 15 is used here. The effect of the number of grid points on the resolution can again be seen, however the waveform undergoes no shape change as it travels down the tube. Also, for the reasons discussed above, the



a. 40 Grid Points

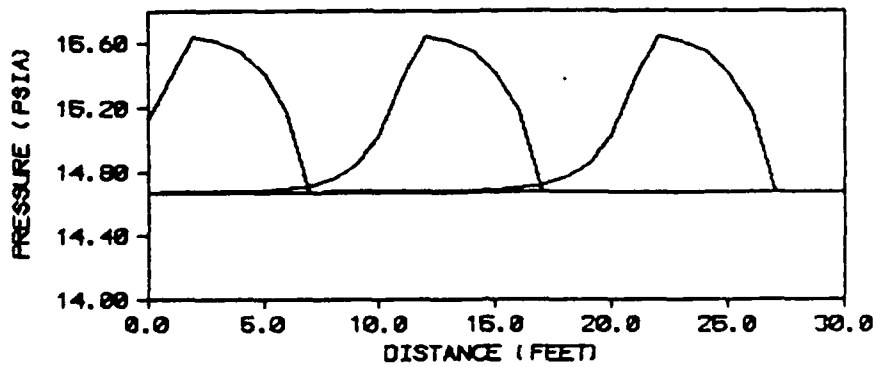


b. 120 Grid Points

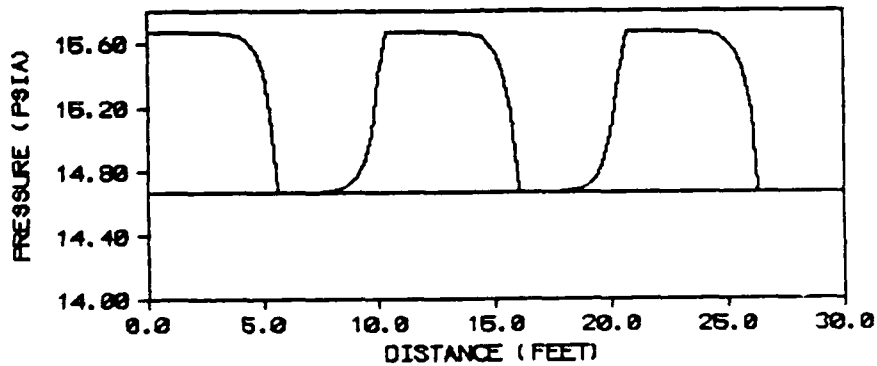


c. 200 Grid Points

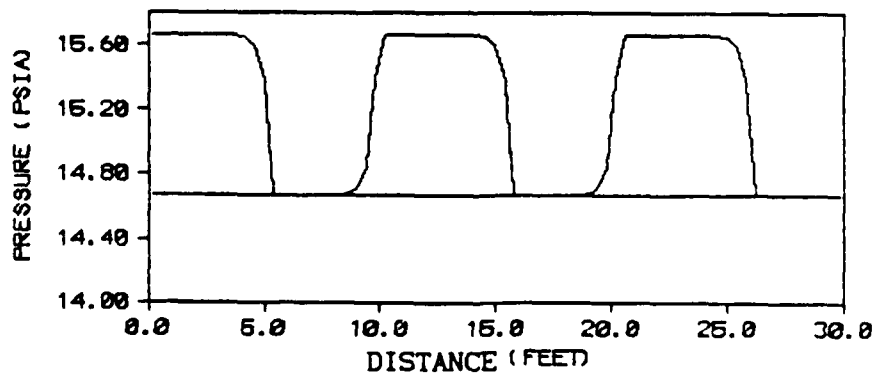
Fig. 15. Time History of Single Trapezoidal Pulse at 0, 10, 20 ft, Nonlinear Results, No Damping, Relative Position of Leading and Trailing Edges Are The Same for All Signal Time Histories.



a. 40 Grid Points

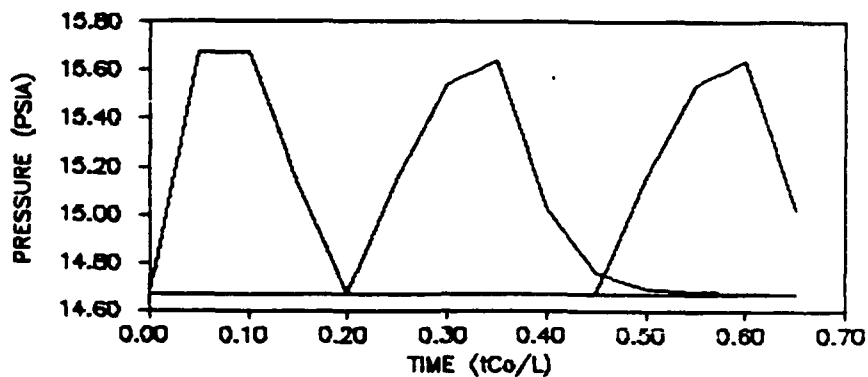


b. 120 Grid Points

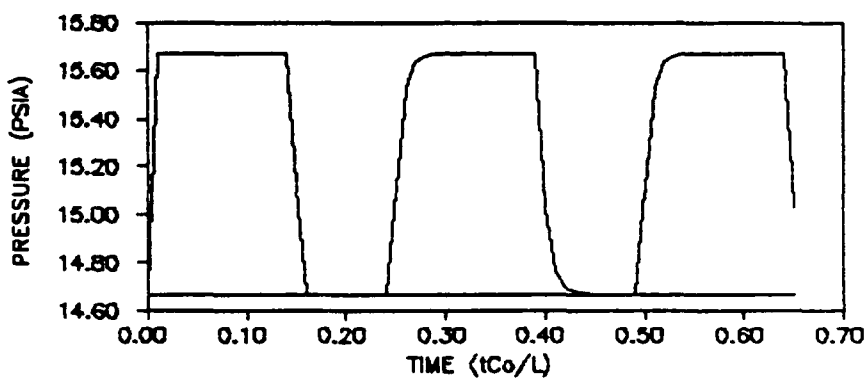


c. 200 Grid Points

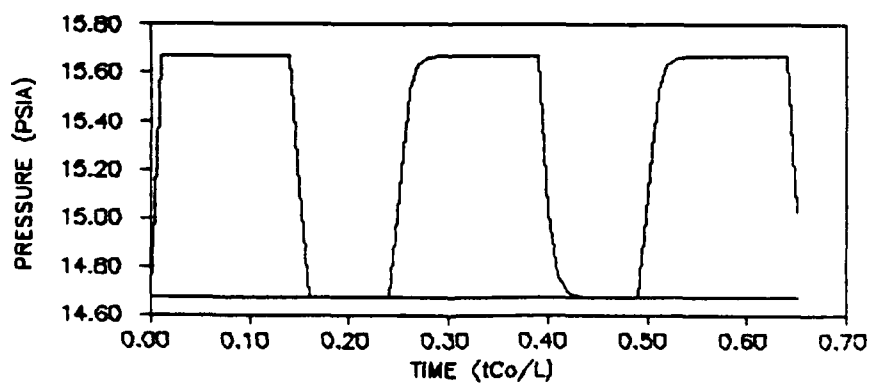
Fig. 16. Single Trapezoidal Pulse Traveling to Right, Linear Results, No Damping



a. 40 Grid Points

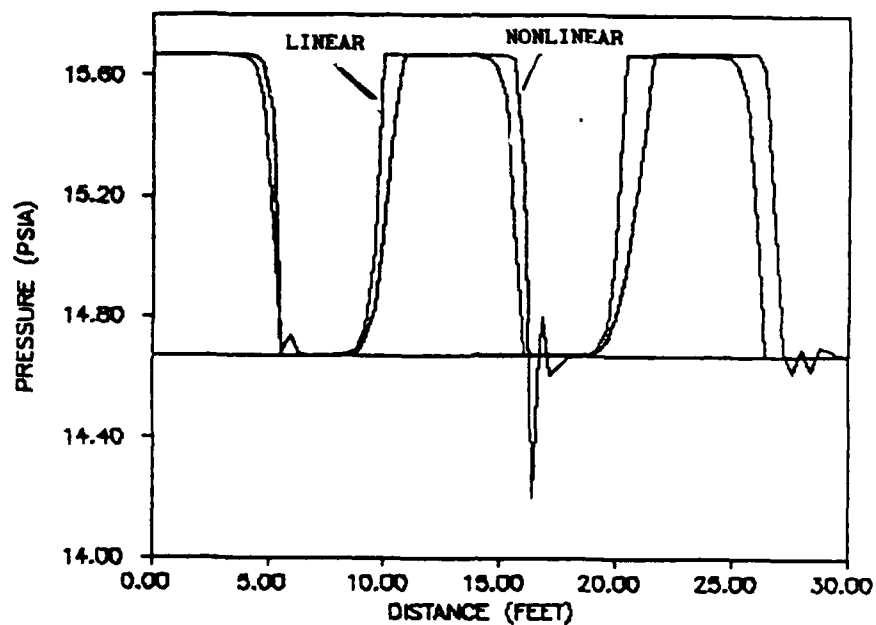


b. 120 Grid Points

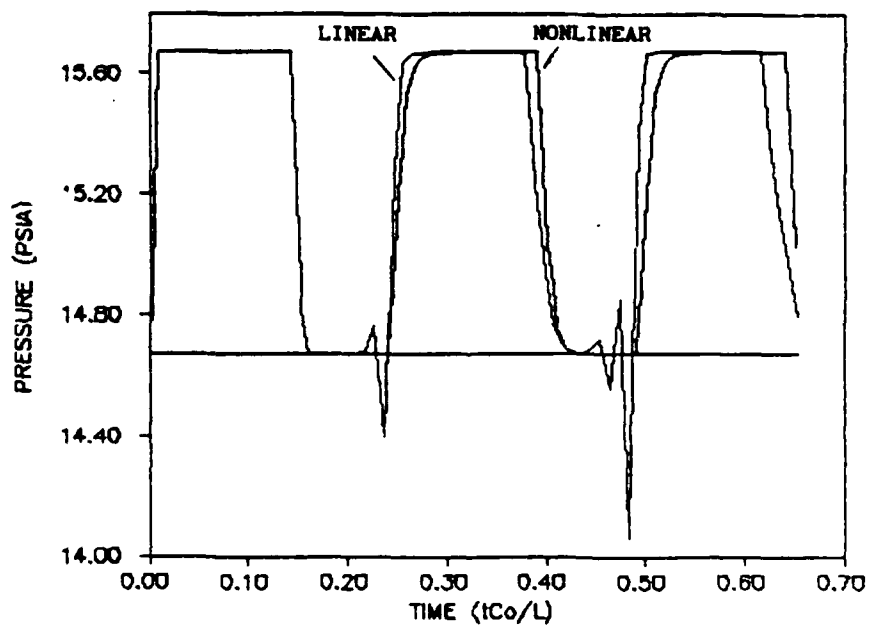


c. 200 Grid Points

Fig. 17. Time History of Single Trapezoidal Pulse at 0, 10, 20 ft,
Linear Results, No Damping



a. Profile at Three Successive Times



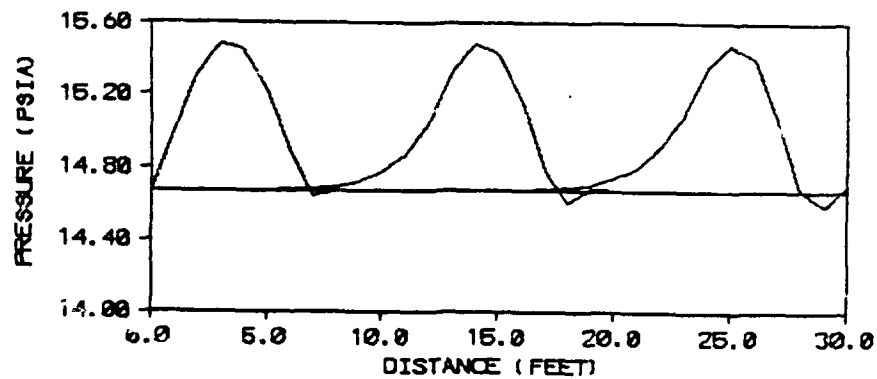
b. Time History at 0, 10, and 20 ft

Fig. 18. Comparison of Linear (Fig. 16) and Nonlinear (Fig. 15) Results for Trapezoidal Pulse, No Damping, 200 Grid Points

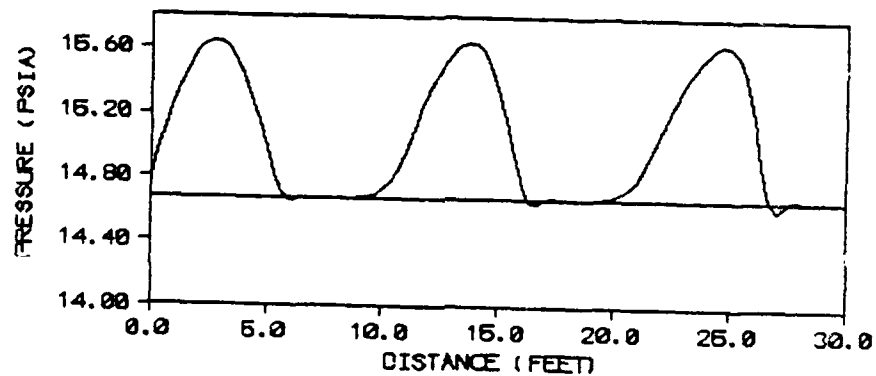
oscillations are absent at the leading edge of the waveform. The loss of high-frequency information with a coarse grid is still evident. Figure 18 directly compares the linear and nonlinear results from the previous figures. Although the input signal amplitude of 1 psi is less than seven percent of the initial 14.67 psia undisturbed condition there is noticeable difference between the linear and the nonlinear results. As the input signal amplitude decreases, the linear and nonlinear results will converge. Conversely, higher input signal amplitudes will cause the nonlinear results to deviate significantly from linear results. This will be shown in Figures 47 through 49.

A 1 psi sinusoidal pulse is used in Figures 19 through 22. The input pulse is the positive half of a sinusoid. The pulse begins at an amplitude of 0 and peaks at 1 psi. With a shallower slope than the trapezoidal pulse, the distortion present at the leading edge of the waveform for the nonlinear case shown in Figures 19 and 20 is not nearly as severe. However, the shape change of the waveform as it travels down the tube is obvious with the oscillations appearing at the leading edge as the wave form steepens. This waveform evolution is consistent with experimental results obtained by Sandoz (59). The roughly sinusoidal pulses used by Sandoz exhibit the same steepening of the leading edge of the waveform shown by the numerical algorithm developed in this study. Figures 21 and 22 show the linear results for this case.

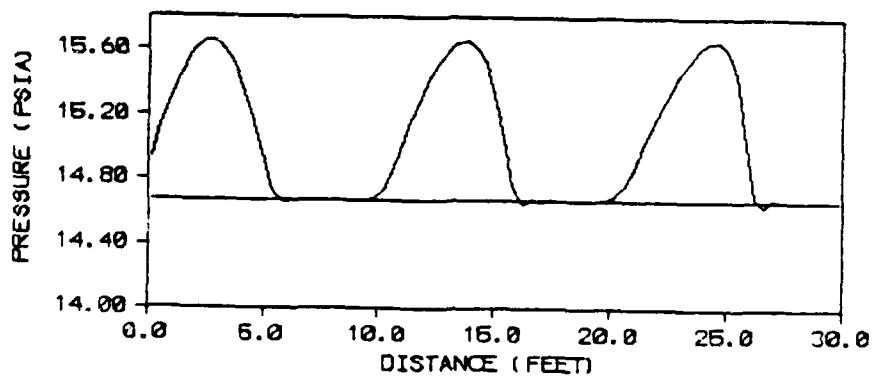
The oscillations at the leading edge of the waveform may be filtered out by a simple algorithm used to post-process the results of the primary finite-difference algorithm. An example of a simple smoothing algorithm described by Vliegenhart is shown below (72):



a. 40 Grid Points

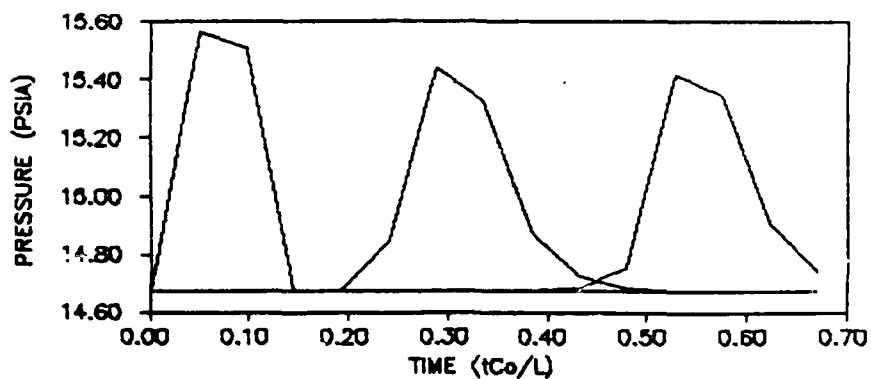


b. 120 Grid Points

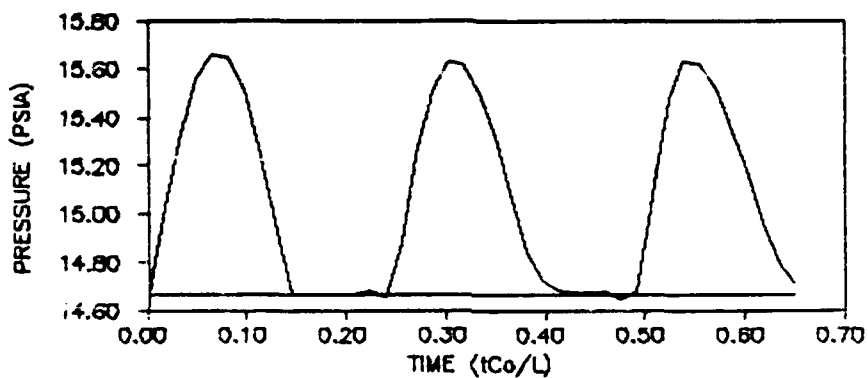


c. 200 Grid Points

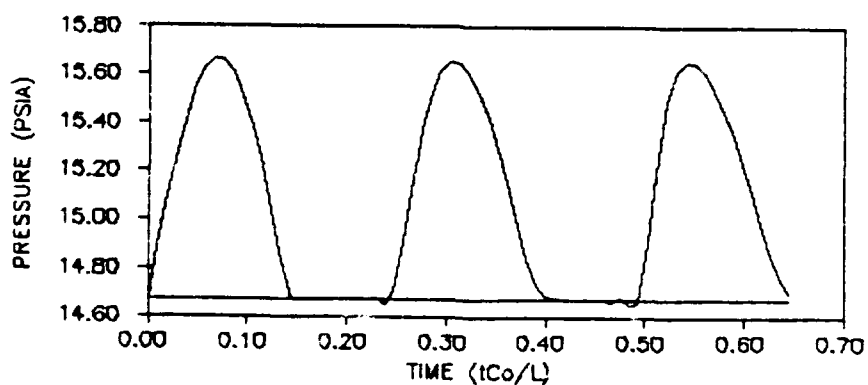
Fig. 19. Single Positive Half-Sinusoidal Pulse Traveling to Right,
Nonlinear Results, No Damping



a. 40 Grid Points

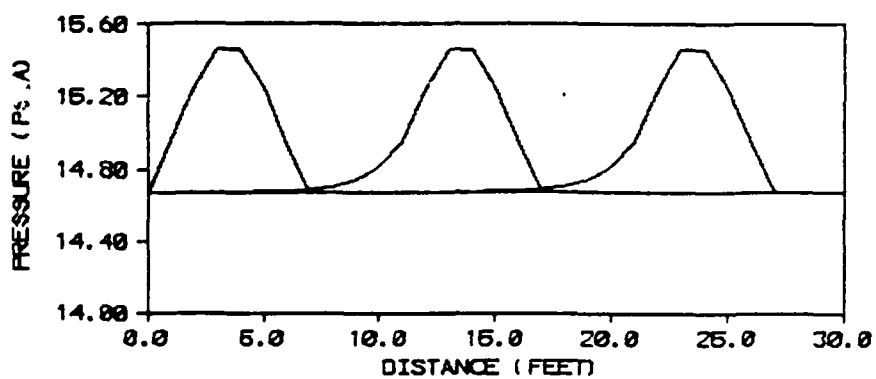


b. 120 Grid Points

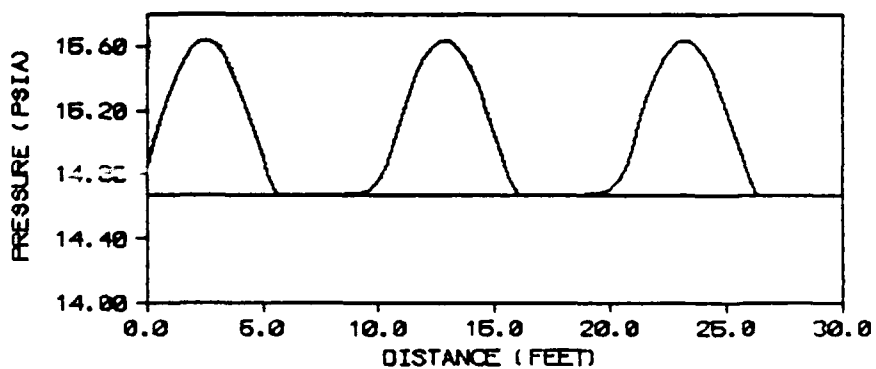


c. 200 Grid Points

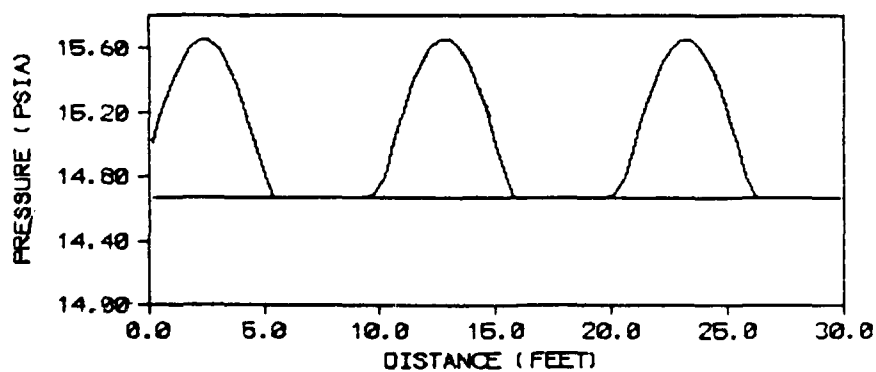
Fig. 20. Time History of Single Positive Half-Sinusoidal Pulse at 0, 10, 20 ft, Nonlinear Results, No Damping



a. 40 Grid Points

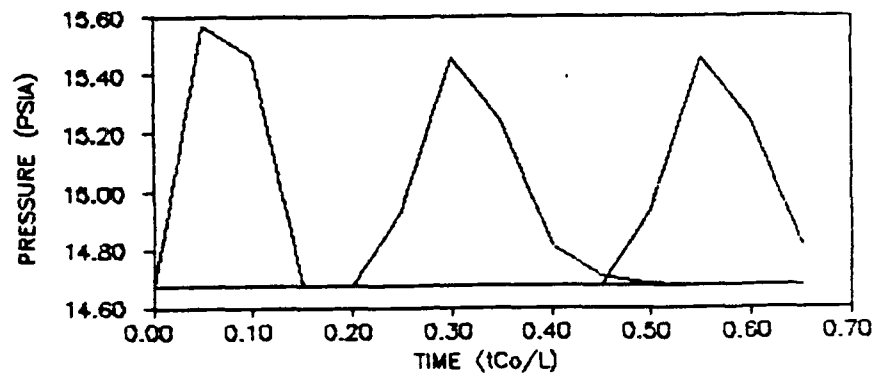


b. 120 Grid Points

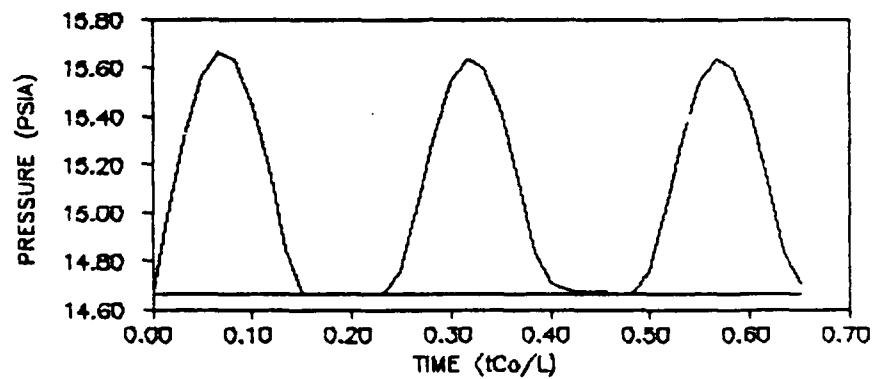


c. 200 Grid Points

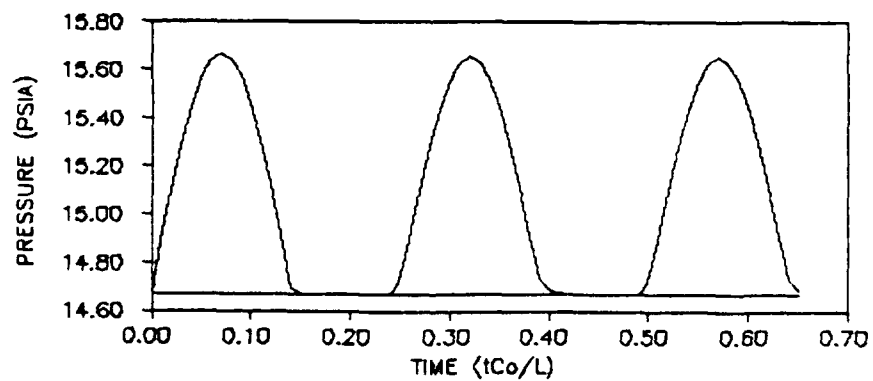
Fig. 21. Single Positive Half-Sinusoidal Pulse Traveling to Right,
Linear Results, No Damping



a. 40 Grid Points



b. 120 Grid Points



c. 200 Grid Points

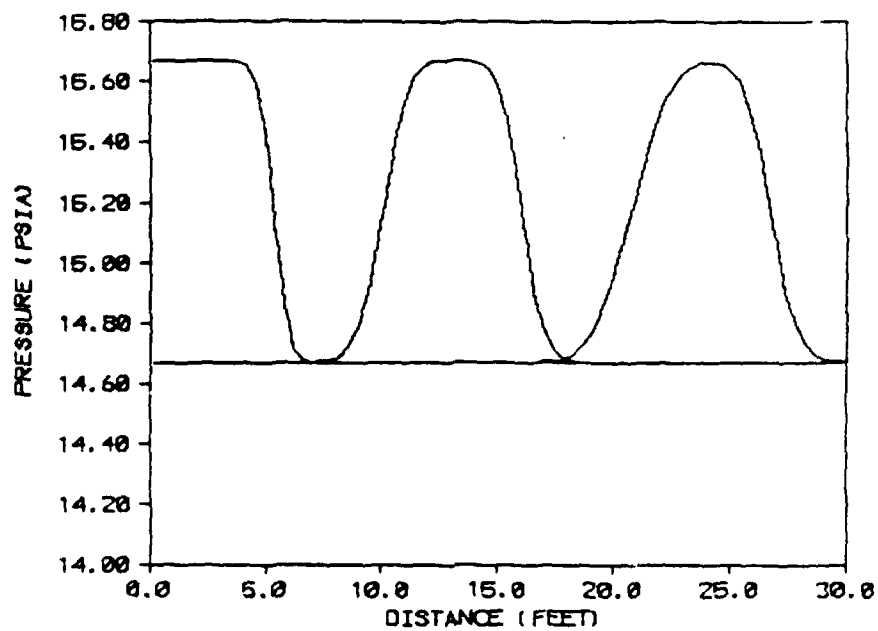
Fig. 22. Time History of Single Sinusoidal Pulse at 0, 10, 20 ft.,
Linear Results, No Damping

$$q_1' = \frac{1}{4} (q_{1+1} + 2q_1 + q_{1-1}) \quad (130)$$

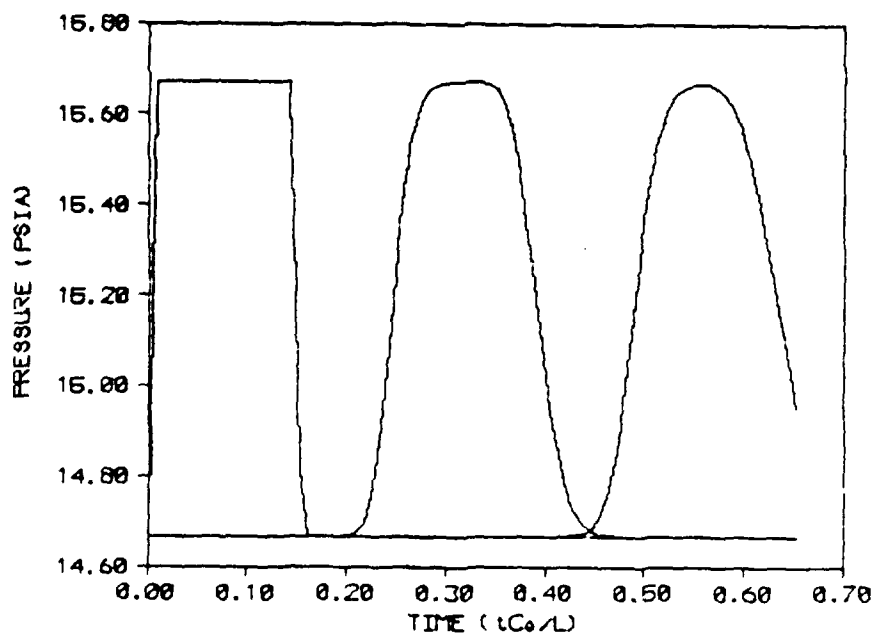
q_1 is replaced by q_1' at each timestep. If the post-processing algorithm is not chosen carefully, attenuation of the higher frequency components present in the solution may occur, eliminating rapidly fluctuating portions of the solution. Equation (130) maintains formal second order accuracy, but, as can be seen from Figure 23, introduces a significant numerical error which appears as rounding of the sharp corners of the original trapezoidal waveform. The loss of important waveform features appears far more serious than any error resulting from the oscillations. Other more sophisticated, higher-order, filtering algorithms are available: however, they require a significant increase in computer resources to implement. They must be applied at every grid point although not necessarily at each time step (16:13; 38:168):

$$q_1' = q_1 + \nu \frac{\Delta t}{\Delta x} \Delta \left[\Delta q_{1+1} \left| \Delta q_{1+1} \right| \right] \quad (131)$$

Equation (131) is third-order accurate and does reduce numerically induced oscillations without significantly attenuating important information (38:168). However, when performed at each grid point and every few time steps, it significantly increases the number of arithmetic operations required to obtain the solution. As can be seen, use of filtering algorithms may introduce error into the solution as well as increase the computational workload for the computer. The



a. Profiles at 0.0046, 0.014, and 0.023 sec



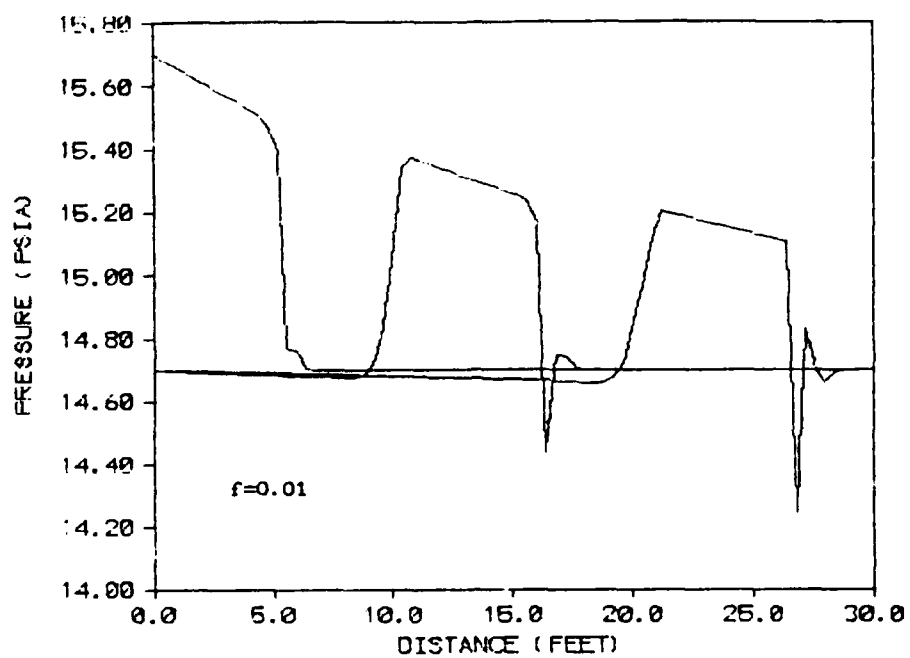
b. Time History at 0, 10, and 20 ft

Fig. 23. Single Trapezoidal Pulse, Nonlinear Results, No Damping, Filtering Algorithm Applied, 200 Grid Points

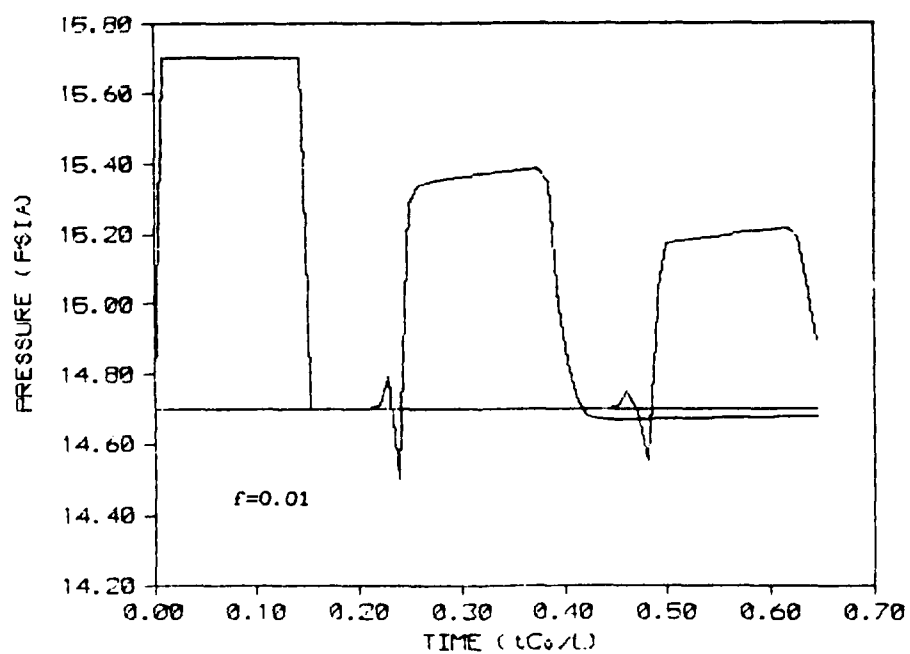
finite-difference model developed in the present study is part of a design tool meant for use on modest computers easily accessible to designers of fluid systems. With this goal in mind, computer resources required by this model are being kept as small as possible. Use of this model on modern supercomputers would, of course, allow better filtering algorithms and other difference operators to be used. No higher-order filtering algorithms are used or recommended for this particular finite-difference model in order to limit computer processing requirements.

Viscous damping using the Darcy-Weisbach friction factor has been added to the nonlinear algorithm for Figures 24 and 25. The algorithm is still equivalent to a one-dimensional algorithm, as in the previous figures, since the damping is calculated as a function of average velocity. It is important to note that the steady-state friction results shown in Figures 24 and 25 were obtained using a constant friction factor f based on the predicted peak value of transient average velocity in the transmission line with no damping present. This method was used for the present study, since calculating f as a function of the transient average velocity produced no discernible attenuation in the numerical result. This was also the approach used by Sandoz (59). The attenuation produced by steady-state friction will be compared to the attenuation produced by unsteady friction in Figures 29 and 30.

The next several figures employ the damping expression shown in Eq (16), modified for transient flow. With the addition of the unsteady friction term, velocity profiles may be obtained, producing a solution containing a two-dimensional velocity field. Recall that the cross

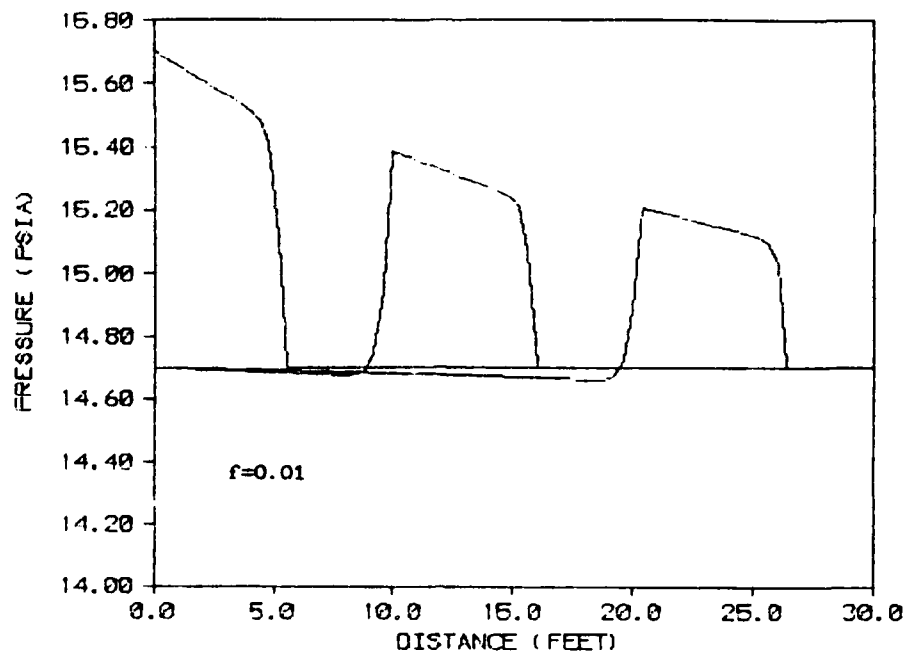


a. Profiles at 0.0046, 0.014, and 0.023 sec

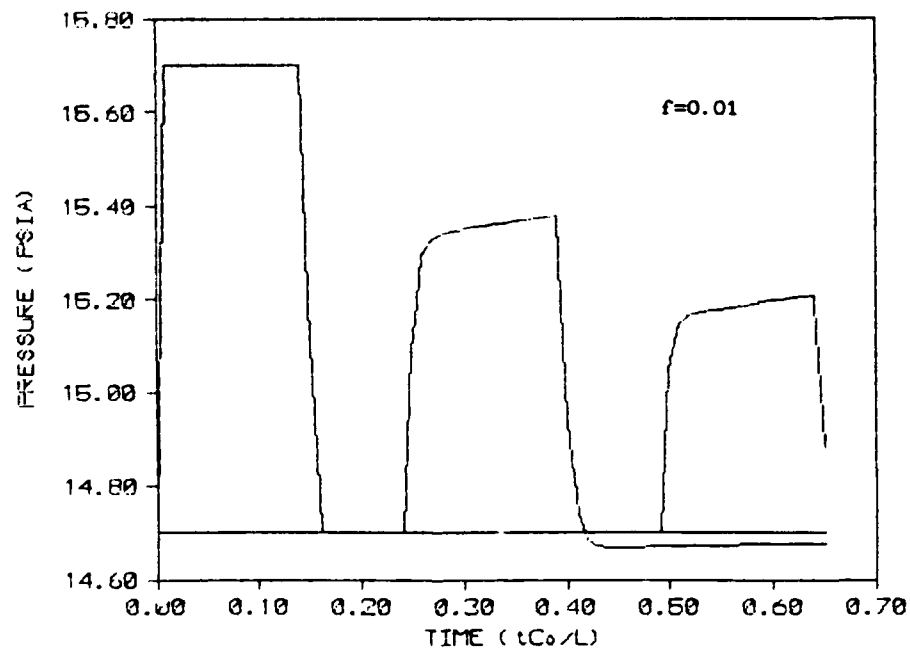


b. Time History at 0, 10, and 20 ft.

Fig. 24. Single Trapezoidal Pulse, Nonlinear Results, Steady Friction, 200 Grid Points



a. Profiles at 0.0046, 0.014, and 0.023 sec



b. Time History at 0, 10, and 20 ft.

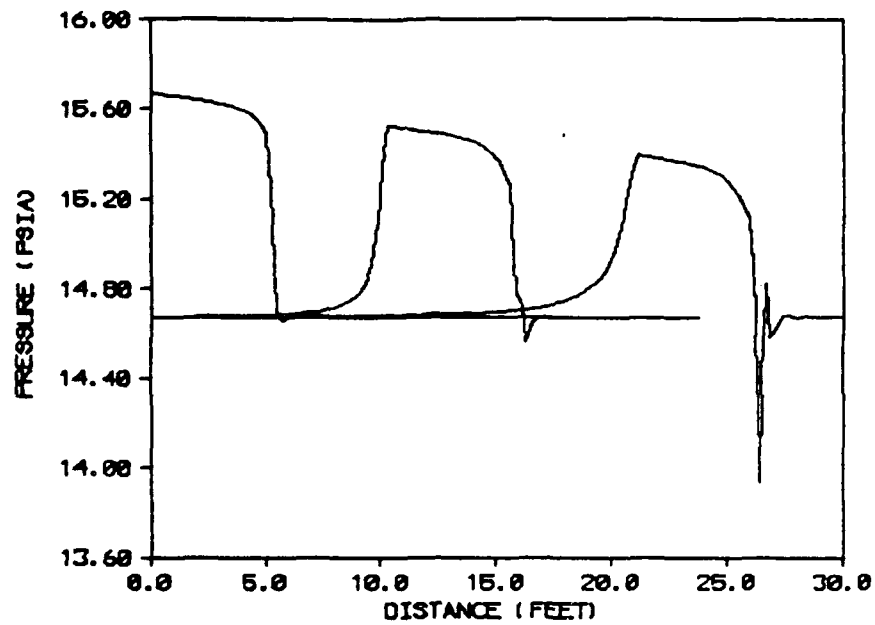
Fig. 25. Single Trapezoidal Pulse, Linear Results, Steady Friction

section of the transmission line is broken into four intervals where an average velocity is calculated for each interval. The intervals are narrow near the wall to provide a higher resolution where the velocity changes are the most extreme. The intervals widen toward the center of the transmission line.

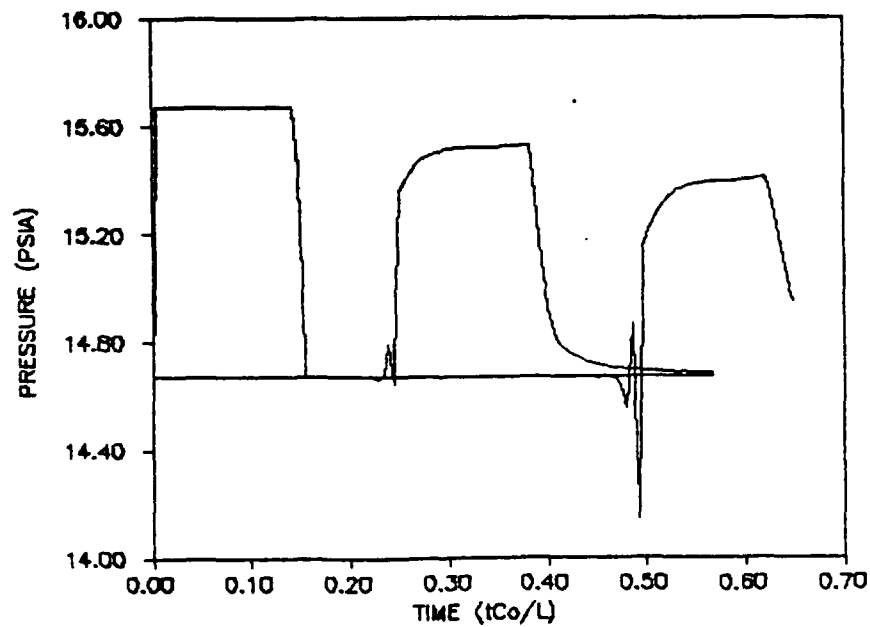
The velocity profile is recovered from these average velocities and used to calculate the velocity gradients for use with Eq (16). Figures 26 and 27 show results from the nonlinear and linear algorithms with unsteady frictional damping for a 1 psi trapezoidal pulse input signal. In both the linear and the nonlinear cases there is a significant rounding of the leading edge of the pulse. Figures 26 and 27 show that the unsteady, frictional damping produces a significantly different waveform than steady-state frictional damping. This is supported by the results of Wood and Funk (74). Also, for the nonlinear case, the effect of unsteady damping on the waveform appears to overwhelm numerical distortion present at points away from the leading edge based on comparisons with Figures 14 and 15 where no damping is present. The effect of the oscillations on most of the waveform does not appear to be significant in the presence of the unsteady damping at this input signal level and the propagation distances considered.

Results from both linear and nonlinear algorithms with unsteady friction are directly compared in Figure 28. Differences in waveform result from shape evolution produced by the nonlinear algorithm. Aside from the presence of the numerical oscillations in the nonlinear results, the waveforms are very similar in shape and magnitude.

A comparison of steady versus unsteady frictional damping is shown

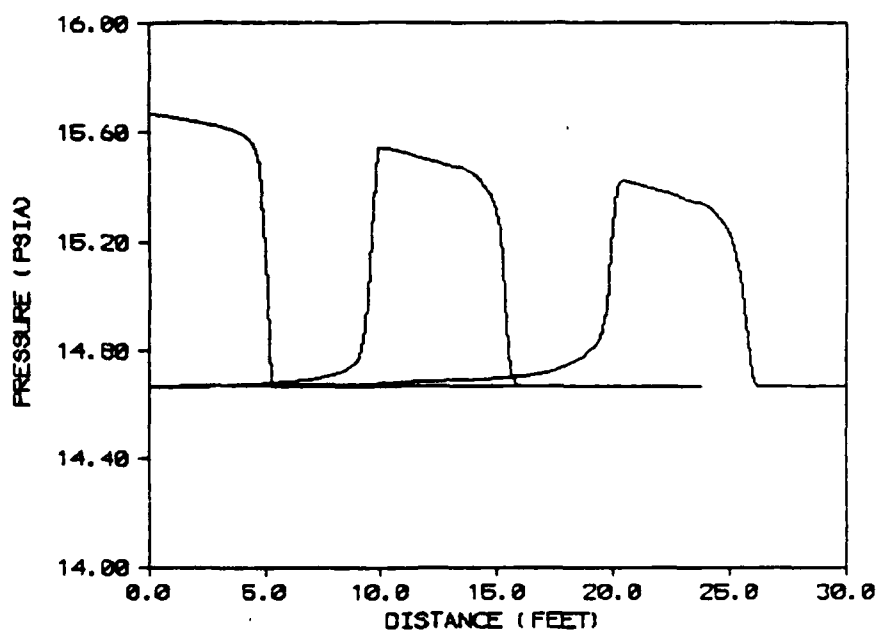


a. Profiles at 0.0046, 0.014, and 0.023 sec

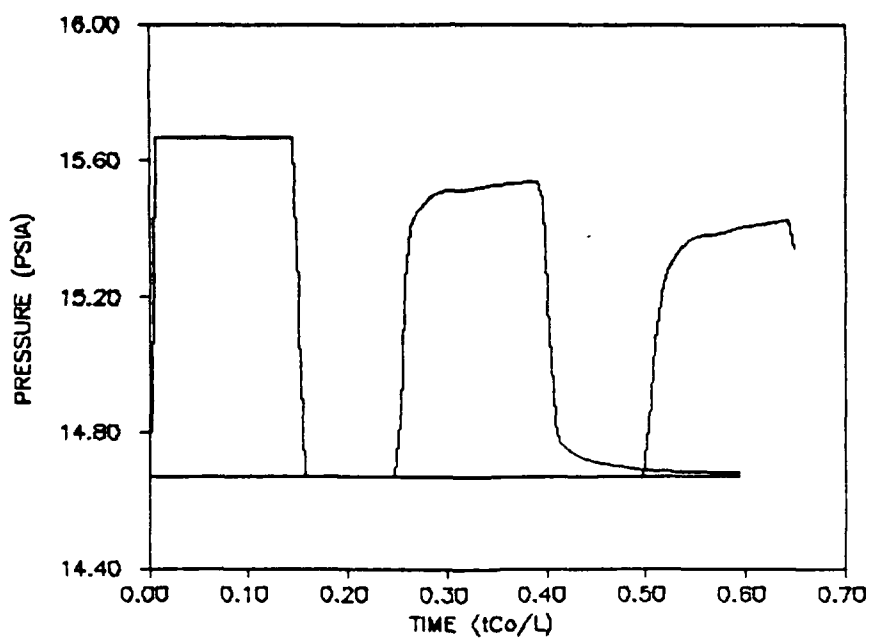


b. Time History at 0, 10, and 20 ft

Fig. 26. Single Trapezoidal Pulse, Nonlinear Results, Unsteady Friction

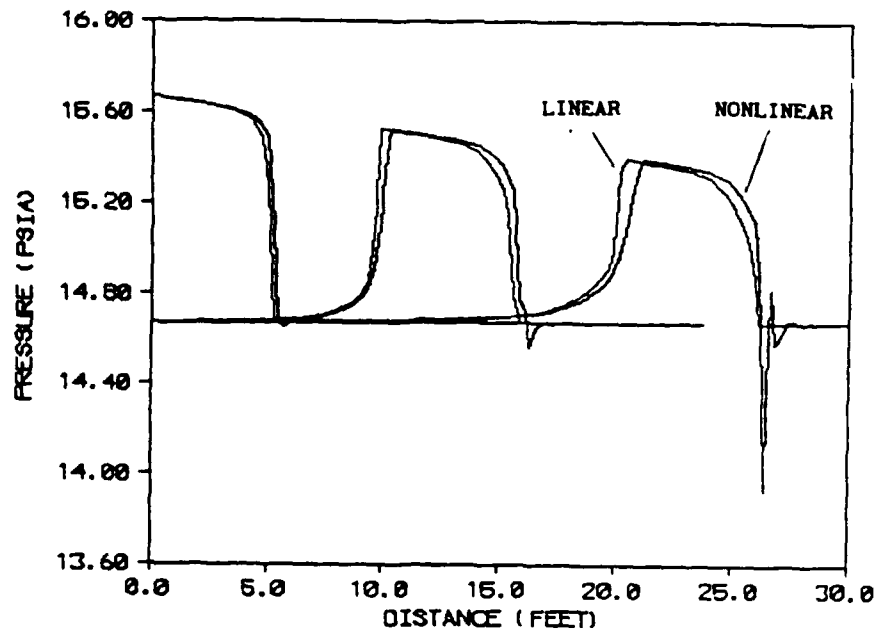


a. Profiles at 0.0046, 0.014, and 0.023 sec

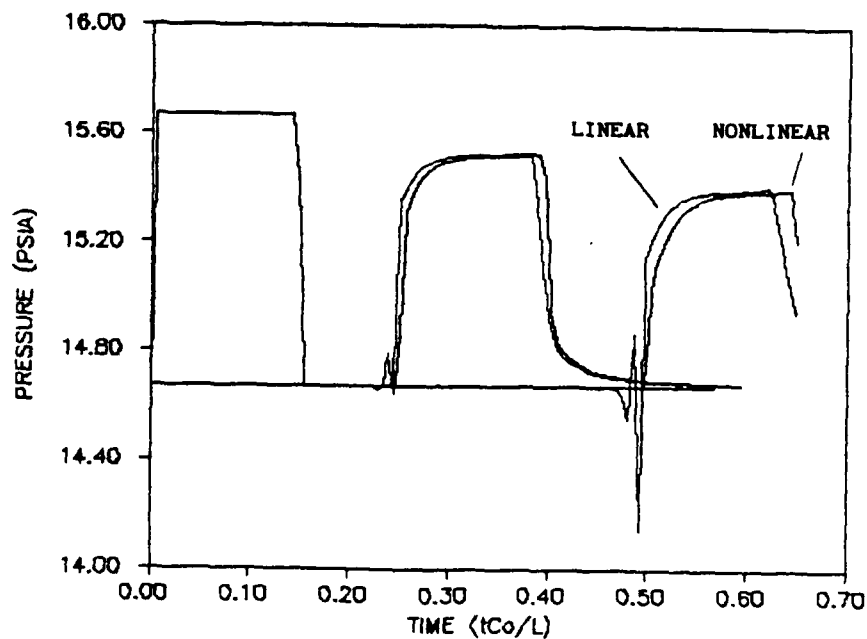


b. Time History at 0, 10, and 20 ft

Fig. 27. Single Trapezoidal Pulse, Linear Results, Unsteady Friction



a. Profiles at 0.0046, 0.014, and 0.023 sec

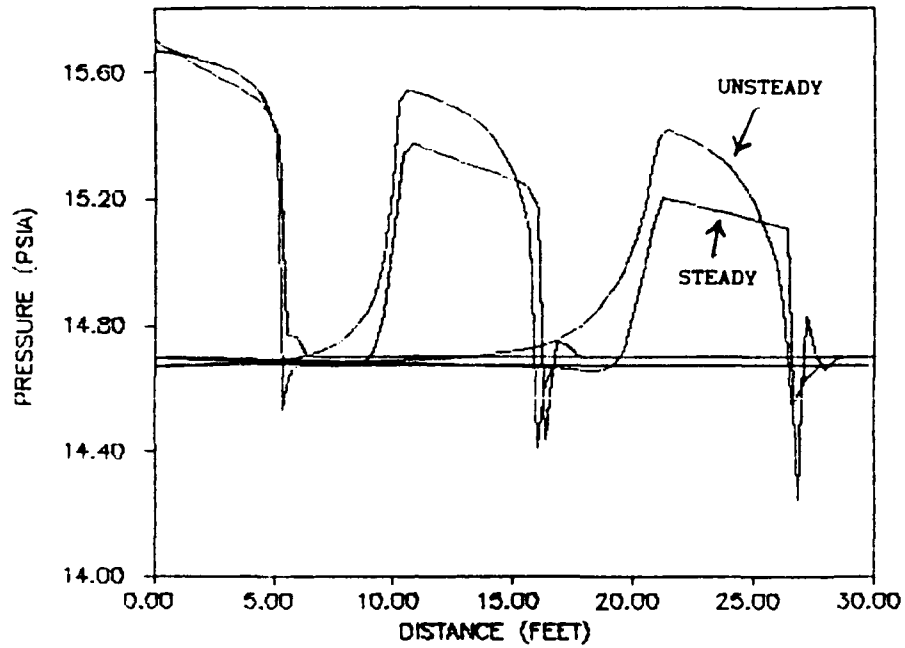


b. Time History at 0, 10, and 20 ft

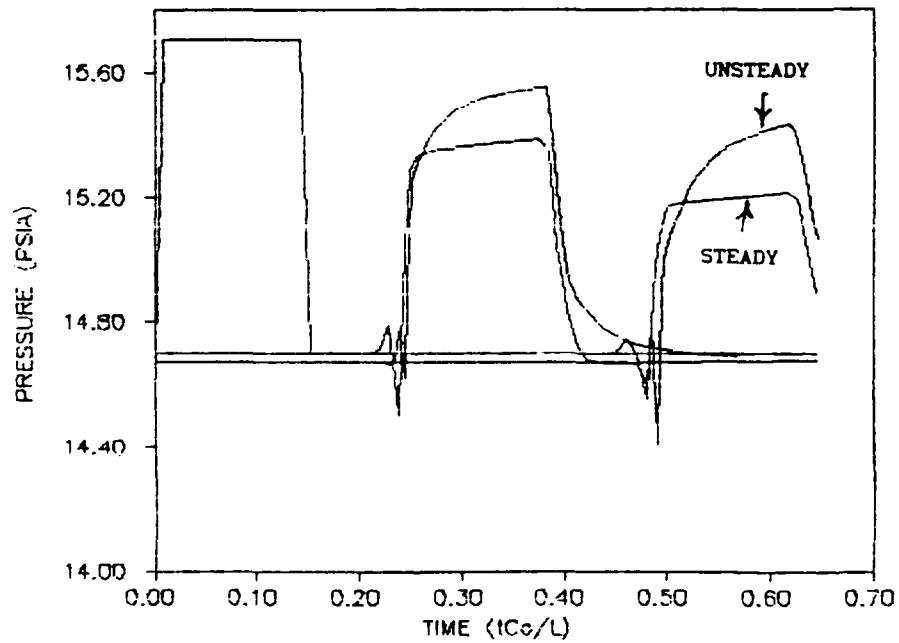
Fig. 28. Single Trapezoidal Pulse, Comparison of Linear (Fig. 27) and Nonlinear (Fig. 26) Results

for the nonlinear case in Figure 29 and the linear case in Figure 30. Here, both steady and unsteady damping functions were calculated for the same 0.305 in ID transmission line. The attenuation of the waveform produced using steady friction depends on the choice of the friction factor. It is possible to select a value for the friction factor that will produce a desired level of attenuation. However, this must be done on a trial and error basis as shown by Sandoz (59). The unsteady friction models used in this study are not empirical in nature and do not require a trial and error process to determine accurate values of damping as. The friction factor is empirical in nature and only valid for flows that are steady or very near steady with fully developed velocity profiles. It loses its validity in the transient flows induced by the passage of a pressure wave.

Figures 31 and 32 show the waveforms resulting from the nonlinear and linear algorithms, respectively, using combined unsteady friction and heat transfer. The turbulent component of the total thermal conductivity k_T is calculated using Reynolds analogy to obtain a value for k_{Turb} from μ_{Turb} . The laminar component of k_T is the physical property k of the fluid under consideration. Figures 31 and 32 are combined in Figure 33, again showing a noticeable difference between the linear and nonlinear results. Here, the signal attenuation for the linear results is greater than that for the nonlinear results. In contrast, Figure 28, which compares linear and nonlinear results for unsteady friction alone, shows almost no difference in magnitude between the linear and the nonlinear results. The presence of convective terms in the nonlinear energy equation is thought by the author to be responsible for this behavior. The only difference

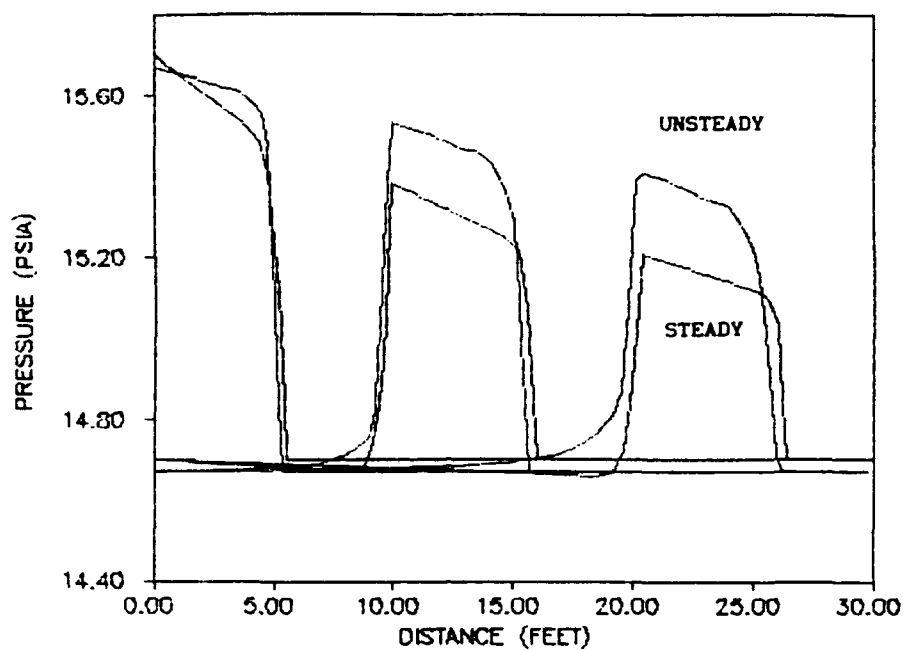


a. Profiles at 0.0046, 0.014, and 0.023 sec

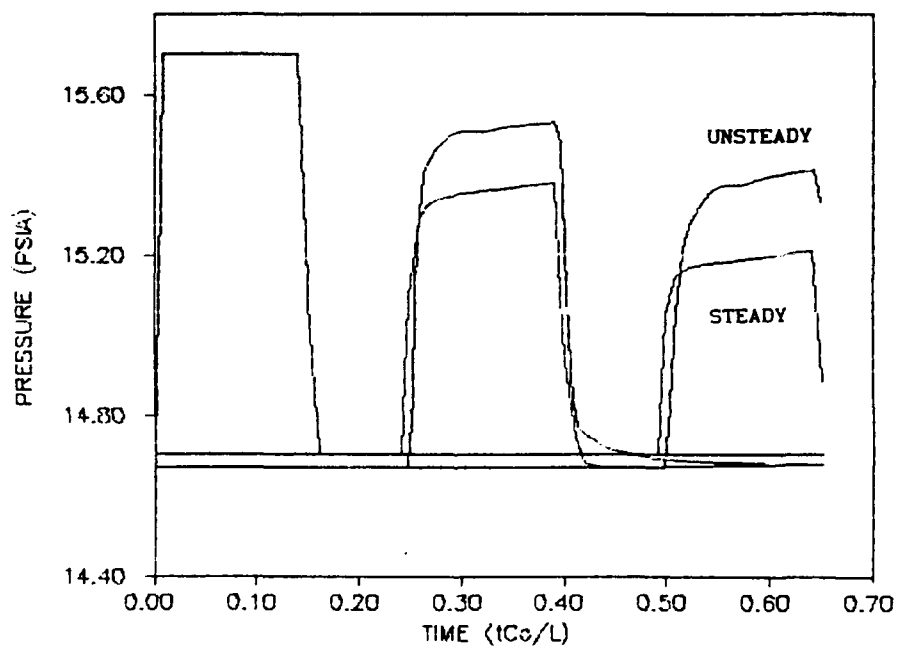


b. Time History at 0, 10, and 20 ft.

Fig. 29. Single Trapezoidal Pulse, Comparison of Steady (Fig. 24) and Unsteady (Fig. 26) Friction, Nonlinear

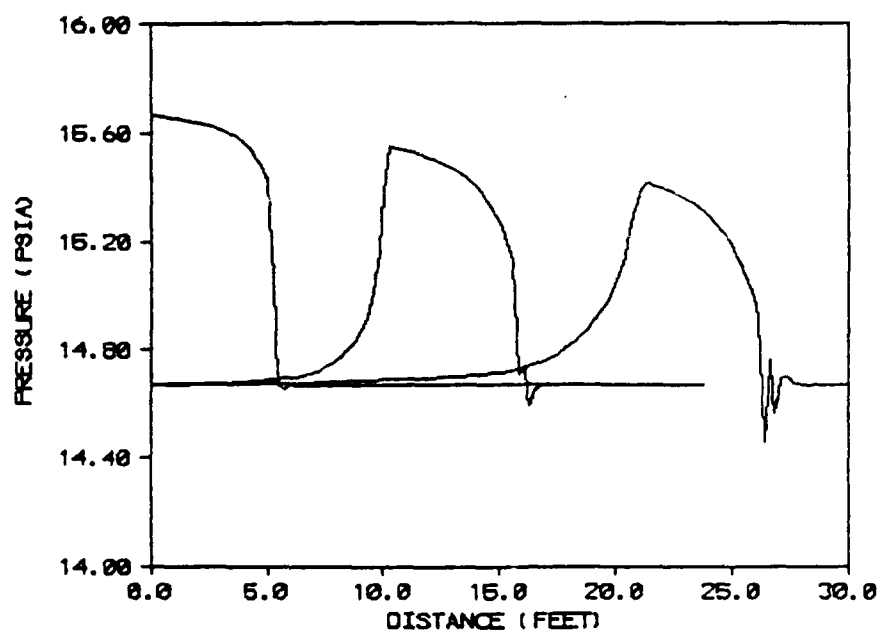


a. Profiles at 0.0046, 0.014, and 0.023 sec

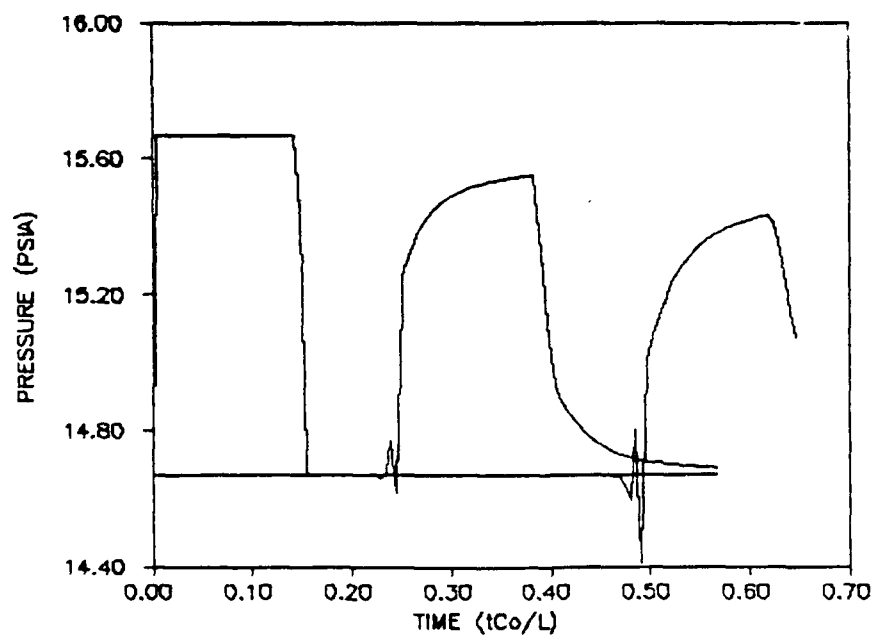


b. Time History at 0, 10, and 20 ft.

Fig. 30. Single Trapezoidal Pulse, Comparison of Steady (Fig. 25) and Unsteady (Fig. 27) Friction, Linear

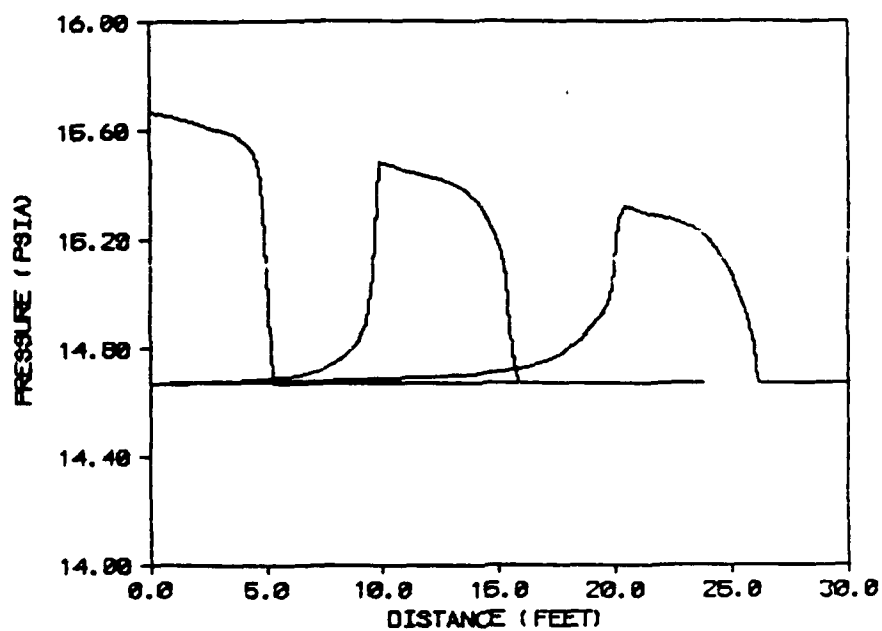


a. Profiles at 0.0046, 0.014, and 0.023 sec

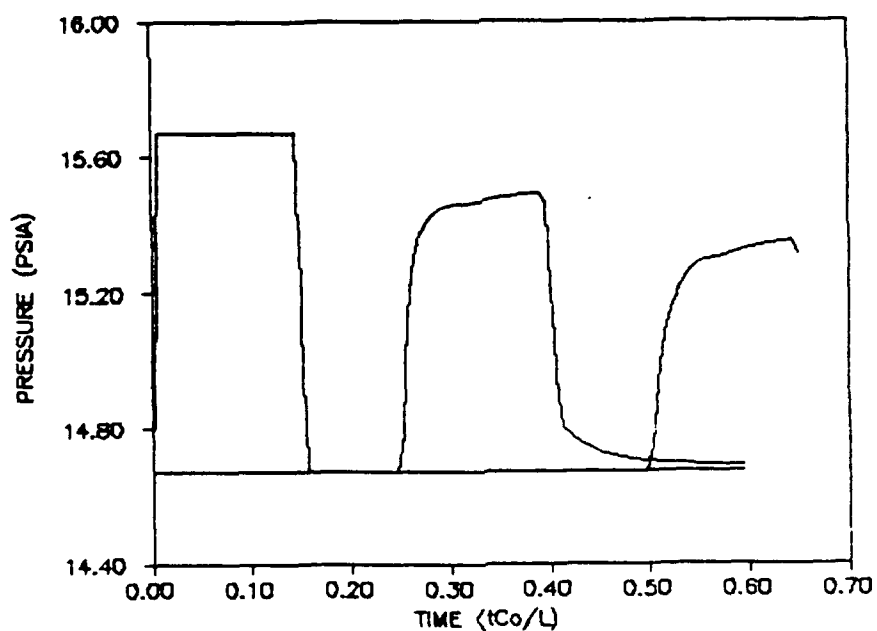


b. Time History at 0, 10, and 20 ft

Fig. 31. Single Trapezoidal Pulse, Nonlinear Results, Combined Unsteady Friction and Heat Transfer

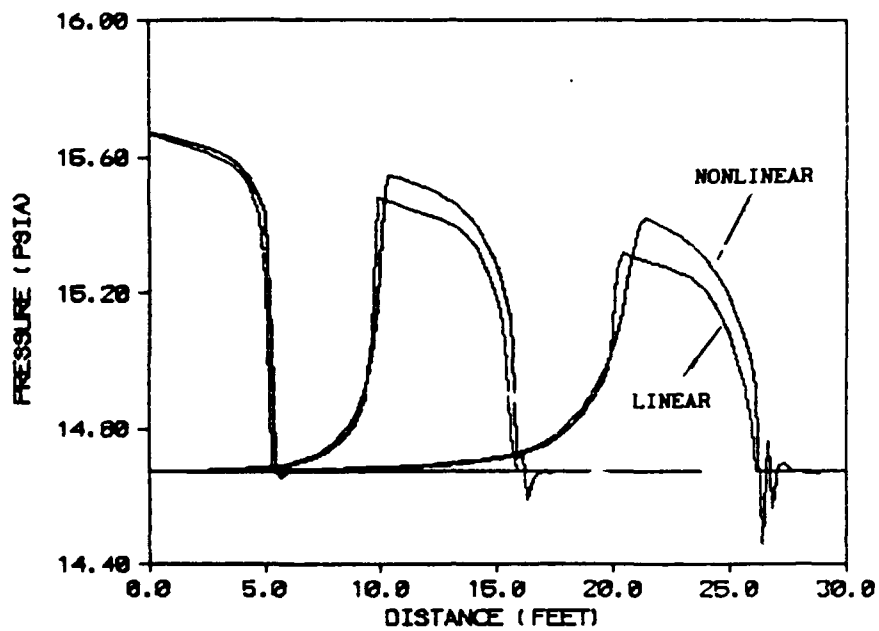


a. Profiles at 0.0046, 0.014, and 0.023 sec

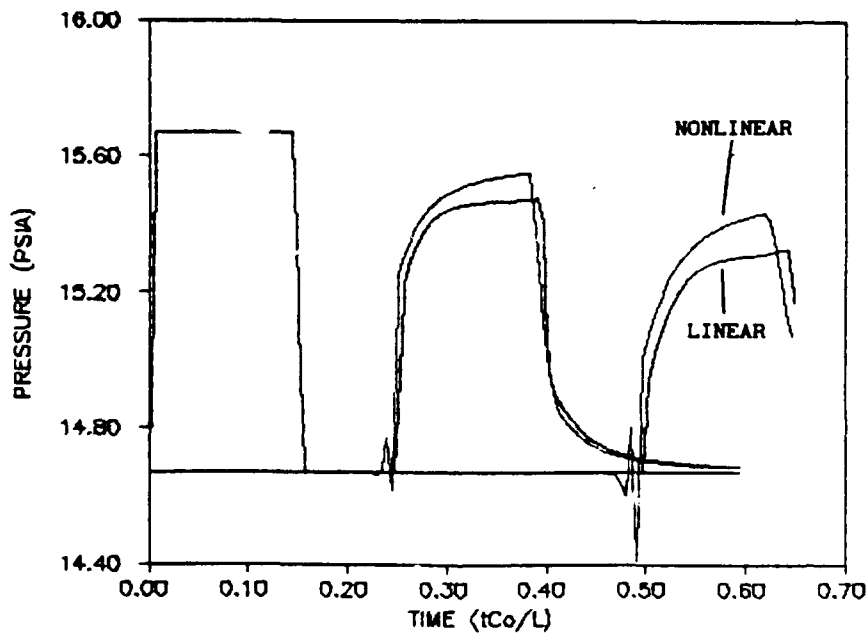


b. Time History at 0, 10, and 20 ft

Fig. 32. Single Trapezoidal Pulse, Linear Results, Combined Unsteady Friction and Heat Transfer



a. Profiles at 0.0046, 0.014, and 0.023 sec



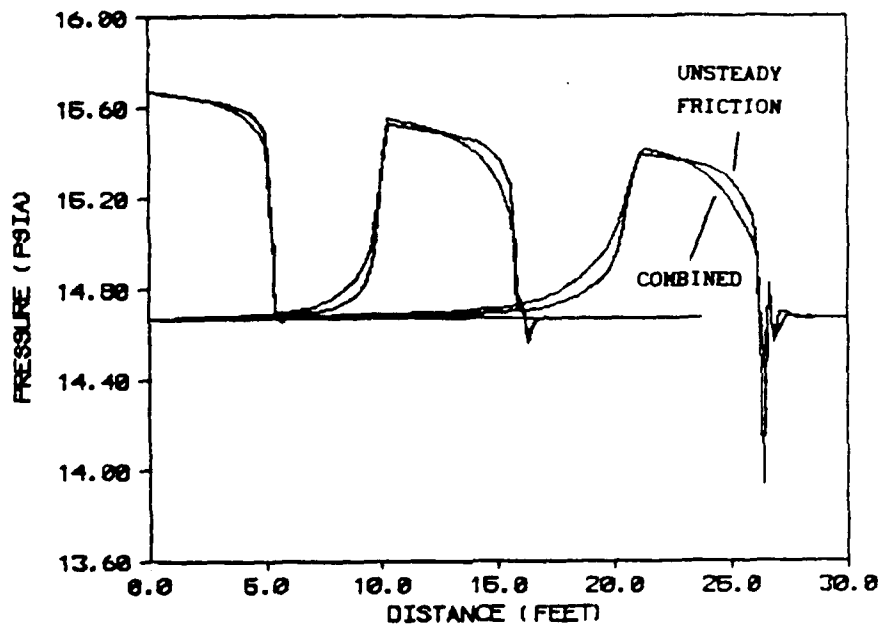
b. Time History at 0, 10, and 20 ft

Fig. 33. Single Trapezoidal Pulse, Comparison of Linear (Fig. 32) and Nonlinear (Fig. 31) Results, Combined Unsteady Friction and Heat Transfer

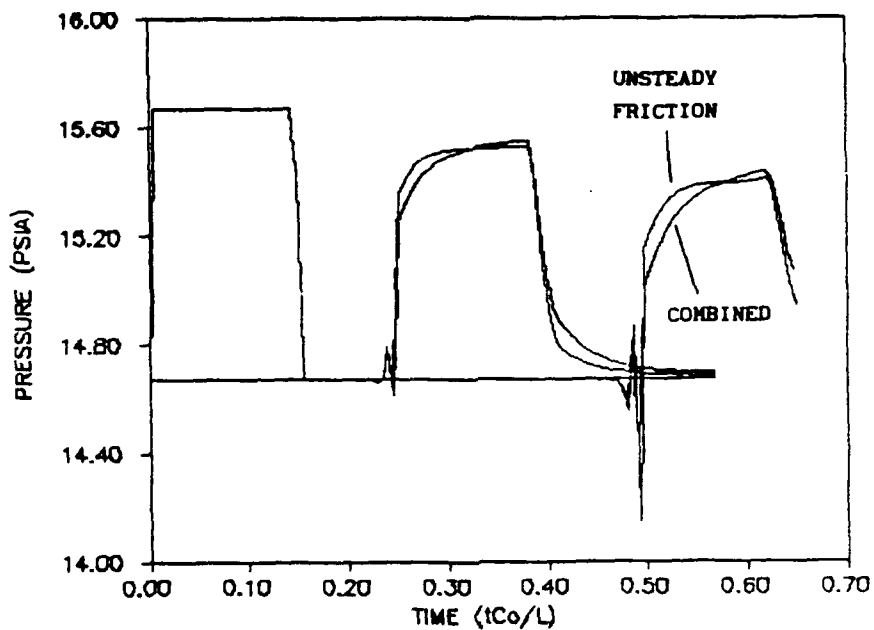
between the linear and nonlinear versions of the damped-wave equations in split coefficient form are the factors $u_n + c$ and $u_n - c$ appearing in Eqs (54) and (55). In the linear equations, u_n is zero and c is constant. For the signal amplitudes under consideration in this study, the magnitude of $u_n + c$ and $u_n - c$ in Eqs (54) and (55) varies only a few percent from the constant value c used in the linear equations. However, this small becomes significant for signals of longer duration as will be seen when the terminated ramp signal is considered. The linear and nonlinear energy equations used to calculate the temperature field differ with the presence of the terms $u_n \frac{\partial T}{\partial x}$ and $\frac{c^2}{\gamma c_p} r u_n \frac{\partial(\ln p)}{\partial x}$ in the nonlinear energy equation Eq (7). The contribution of these terms appears significant as shown by Figure 33.

A direct comparison of nonlinear results, with and without unsteady heat transfer, for the trapezoidal pulse is shown in Figure 34. The waveform obtained using combined unsteady friction and heat transfer exhibits more rounding at the leading edge and a slightly higher peak at the trailing edge than the waveform with unsteady friction alone. The peak amplitudes, however, are virtually the same.

Figure 35 is the linear analog of Figure 34 and shows a definite difference between the magnitudes of the waveforms. In each chart, the curve of lesser magnitude results from combined unsteady friction and heat transfer while the remaining curve is produced using unsteady friction only. The difference between waveforms seen in Figure 34 (more rounding at the leading edge and a slightly higher peak at the trailing edge) is absent for the linear case in Figure 35. This comparison indicates the importance of the convective term in the

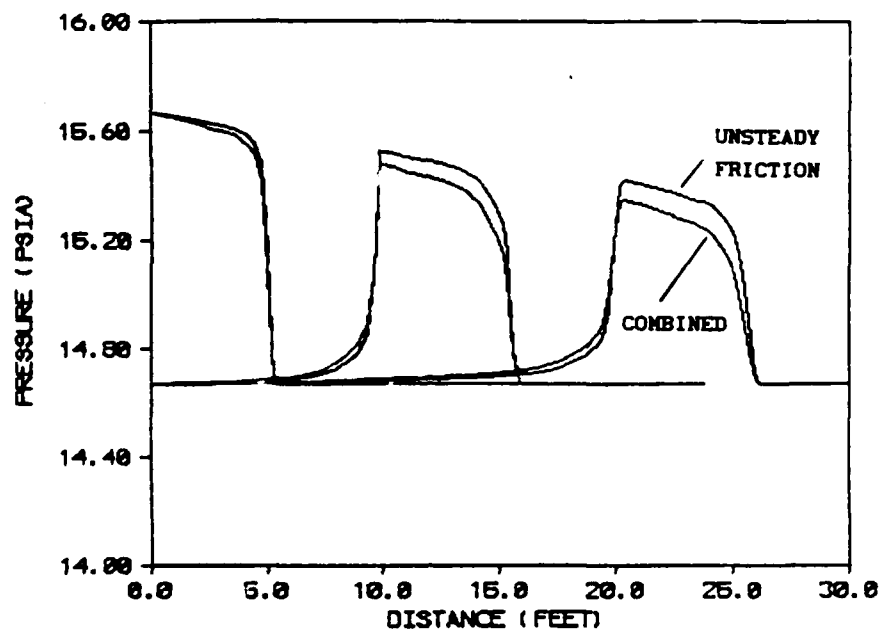


a. Profiles at 0.0046, 0.014, and 0.023 sec

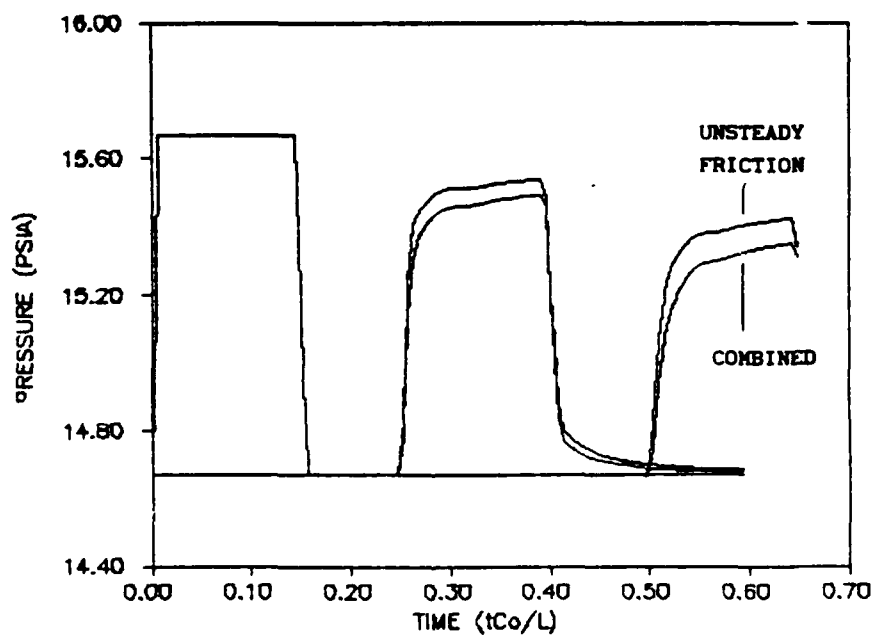


b. Time History at 0, 10, and 20 ft

Fig. 34. Single Trapezoidal Pulse, Comparison of Unsteady Friction (Fig. 26) and Combined Unsteady Friction and Heat Transfer (Fig. 31).
Nonlinear Results



a. Profiles at 0.0046, 0.014, and 0.023 sec



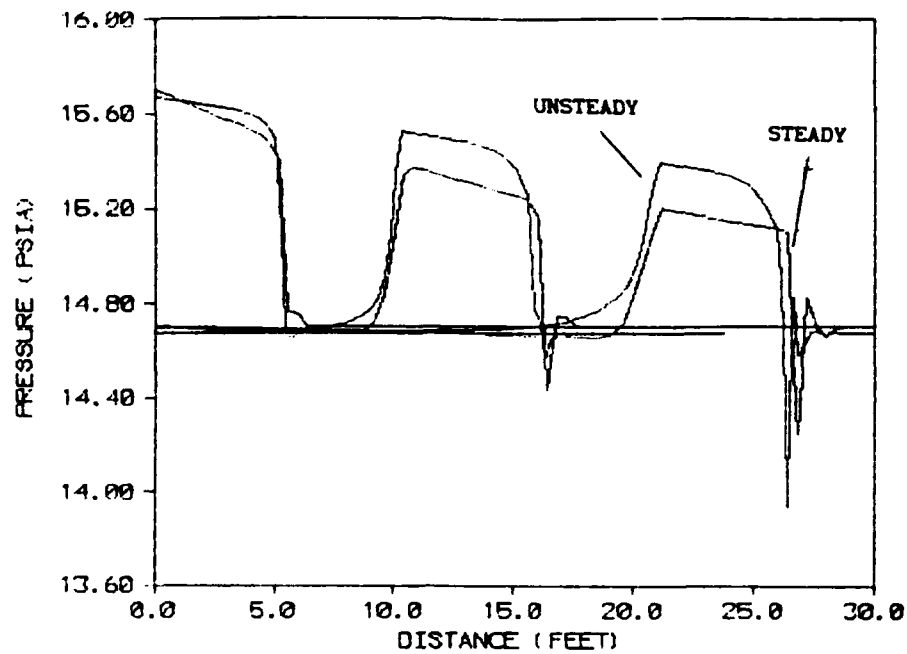
b. Time History at 0, 10, and 20 ft

Fig. 35. Single Trapezoidal Pulse, Comparison of Unsteady Friction (Fig. 27) and Combined Unsteady Friction and Heat Transfer (Fig. 32), Linear Results

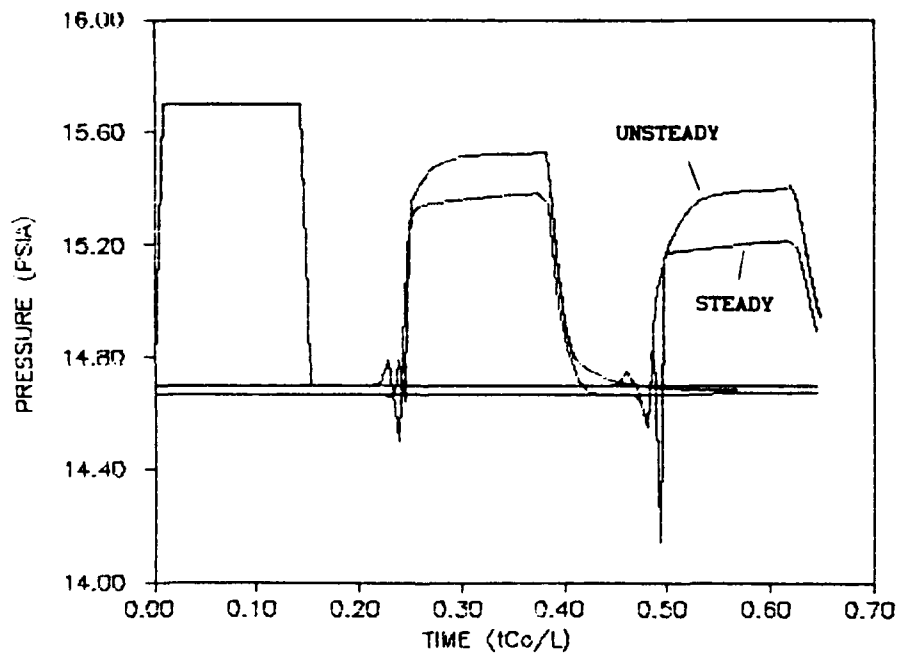
energy equation with regard to waveshape and attenuation. A significant transport of thermal energy by convection is apparent. As a point of reference, nonlinear steady friction and unsteady combined friction and heat transfer results for a 1 psi trapezoidal pulse are compared in Figure 36.

Pulses have been examined so far, but the step, or more properly in this case, the terminated ramp, also provides information on the behavior of these algorithms. Unlike the pulse, the terminated ramp has no trailing edge to produce a sudden deceleration of the fluid. The effects of the unsteady turbulent friction model is much easier to observe.

Nonlinear results for unsteady frictional damping, alone, and combined friction and heat transfer are shown in Figures 37 and 39 respectively. Linear results are shown in Figures 38 and 40. The snapshots at successive times shown in these four charts are useful in indicating the rate of damping as the wavefront travels along the transmission line. A nonlinear effect on the signal amplitude not seen in pulses shows up with the terminated ramp input signal for the case of unsteady friction alone. Recall that for the pulse in Figure 28 there was no significant difference between the amplitude of the linear and nonlinear results for the trapezoidal pulse as it traveled along the transmission line. Only the shape of the waveform changed. With the terminated ramp, there is a very noticeable difference between the linear and nonlinear results as can be seen in Figure 41a which compares results from Figures 37a and 38a. The curve with the greater magnitude in each pair is the nonlinear result. This difference between waveforms would indicate that this effect increases in

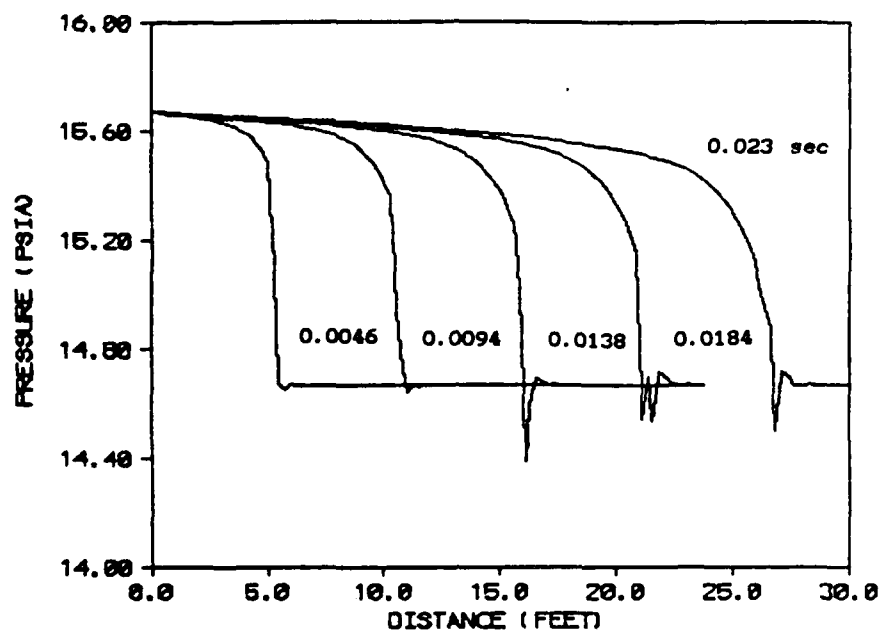


a. Profiles at 0.0046, 0.014, and 0.023 sec

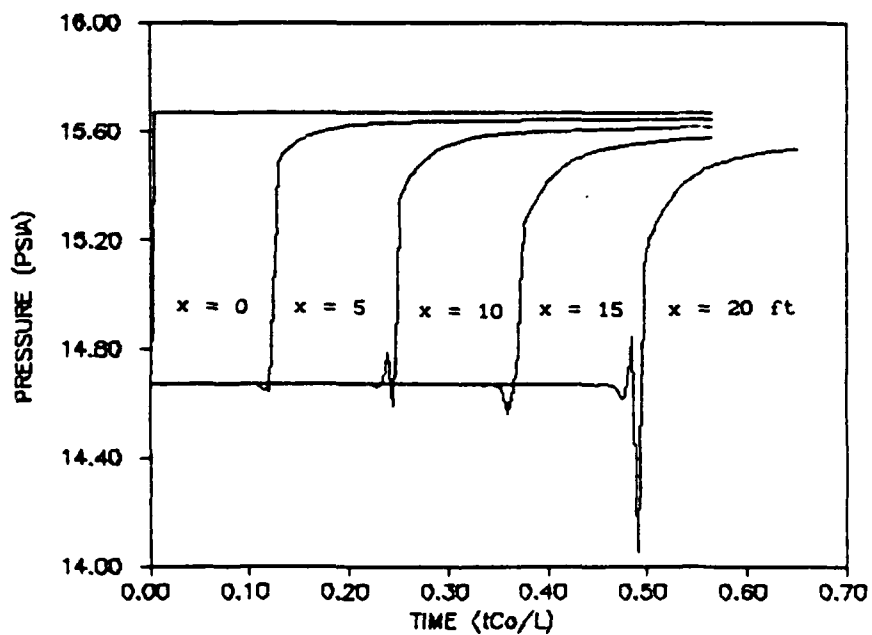


b. Time History at 0, 10, and 20 ft.

Fig. 36. Single Trapezoidal Pulse, Comparison of Steady Friction (Fig. 24) and Combined Unsteady Friction and Heat Transfer (Fig. 31), Nonlinear Results

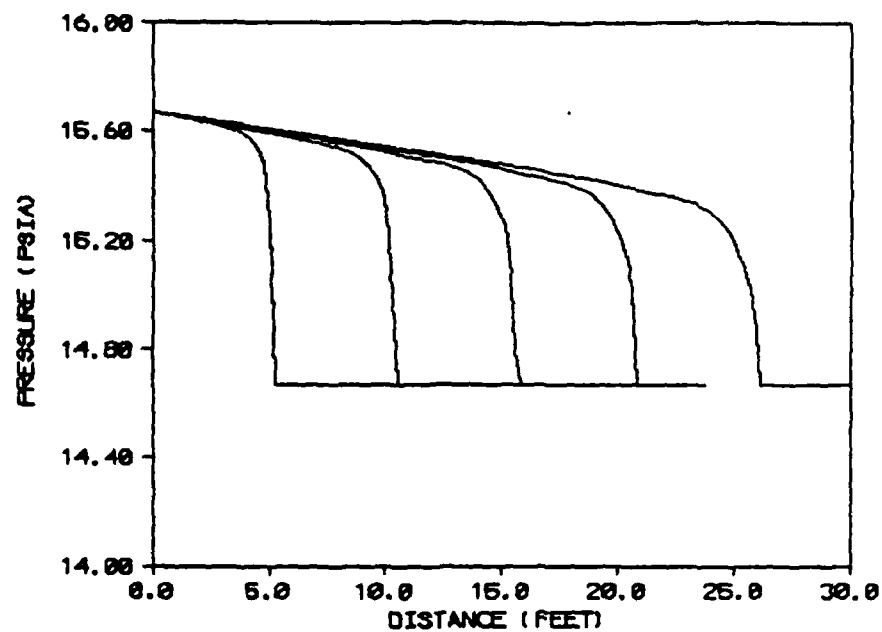


a. Profiles at 0.0046, 0.0094, 0.0138, 0.0184, and 0.023 sec

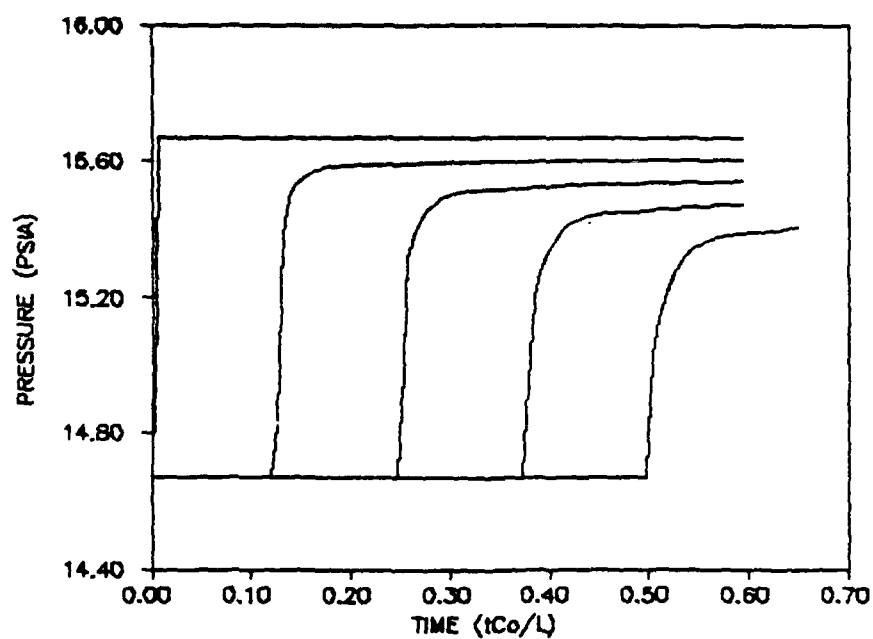


b. Time History at 0, 5, 10, 15 and 20 ft

Fig. 37. Terminated Ramp, Nonlinear Results, Unsteady Friction

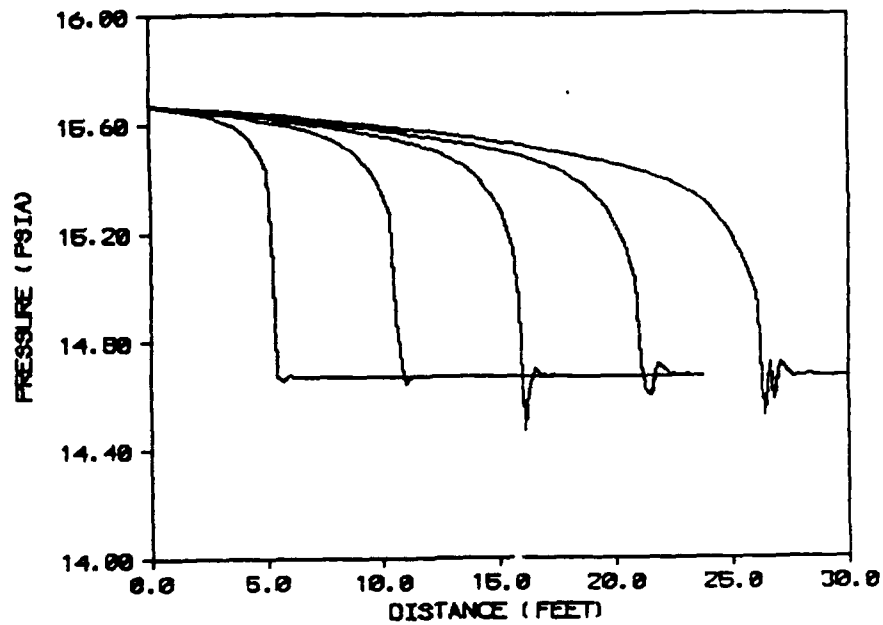


a. Profiles at 0.0046, 0.0094, 0.0138, 0.0184, and 0.023 sec

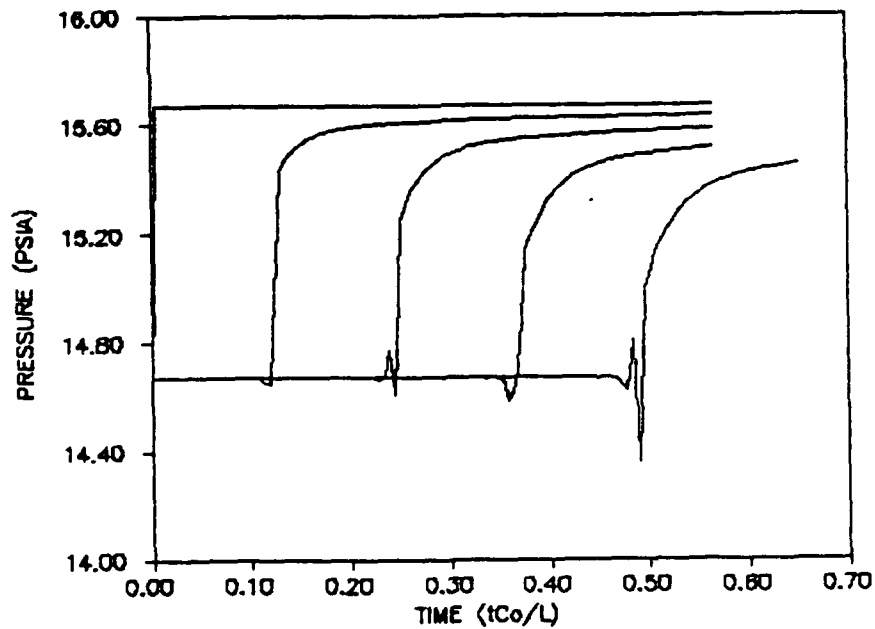


b. Time History at 0, 5, 10, 15 and 20 ft

Fig. 38. Terminated Ramp, Linear Results, Unsteady Friction

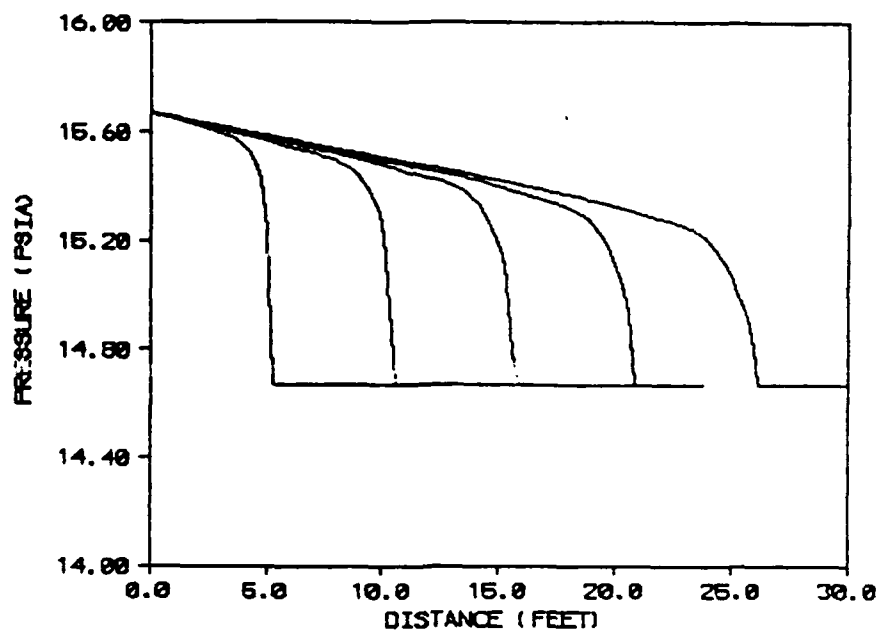


a. Profiles at 0.0046, 0.0094, 0.0138, 0.0184, and 0.023 sec

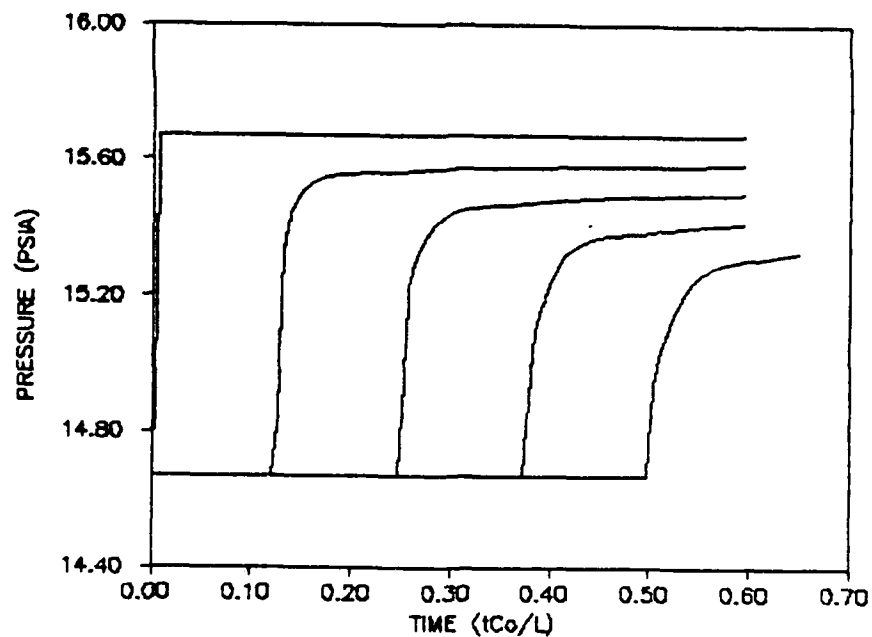


b. Time History at 0, 5, 10, 15 and 20 ft

Fig. 39. Terminated Ramp, Nonlinear Results, Combined Unsteady Friction and Heat Transfer



a. Profiles at 0.0046, 0.0094, 0.0138, 0.0184, and 0.023 sec



b. Time History at 0, 5, 10, 15 and 20 ft

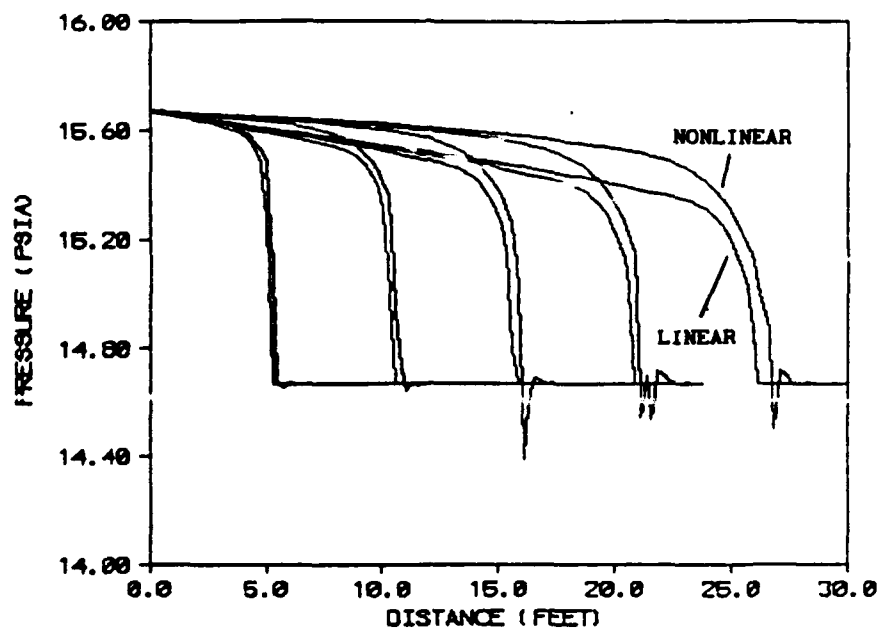
Fig. 40. Terminated Ramp, Linear Results, Combined Unsteady Friction and Heat Transfer

magnitude as pulse duration increases. This difference between linear and nonlinear results was not seen in the trapezoidal pulse due to its short duration. In a pulse, the flow is cut off as the trailing edge of the pulse passes, preventing the nonlinear convective terms from contributing significantly to the amplitude. This would suggest that the longer the pulse duration, the greater the effect of the nonlinear convection terms in the damped wave equations.

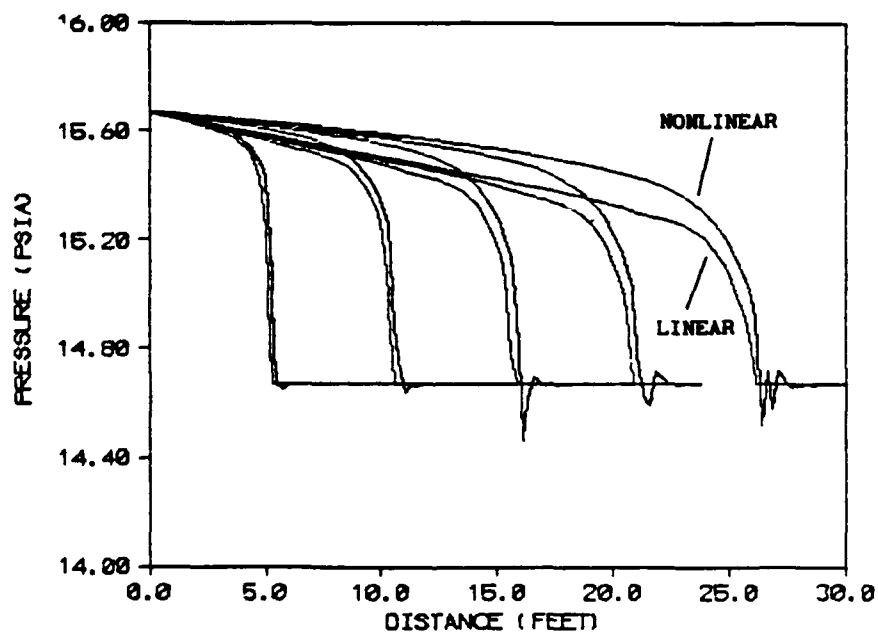
Linear and nonlinear results with combined friction and heat transfer are compared in Figure 41b. The curve with the greater amplitude of each pair is the nonlinear result. This same relationship between linear and nonlinear results was observed in Figure 33 for the trapezoidal pulse. The difference between the linear and nonlinear results is due to the presence of the nonlinear terms in the energy equation, as it was for the trapezoidal pulse. Figures 42a and 42b are the time histories for Figures 41a and 41b respectively.

Figures 43 and 44, again, show the presence of the heat transfer damping term produces a noticeable difference from results with frictional damping alone. Linear results are compared in part a of each figure while nonlinear results are compared in part b. In each pair of curves, the one with the greater amplitude represents unsteady friction alone. The remaining curve results from combined friction and heat transfer.

One trend absent from results for the terminated ramp input signal is the distortion of the step waveform shown experimentally in previous studies of long transmission lines (5:7; 28:280; 30:500-501). Braden and Kantola noted an amplitude dependent effect that distorted the leading edge of the step at points downstream of the point of signal

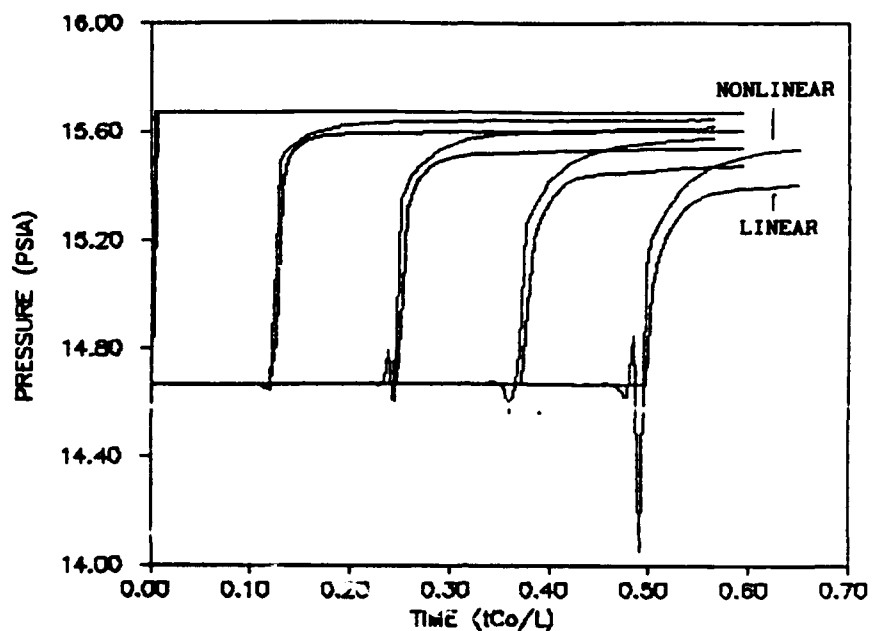


a. Unsteady Friction (Figs 6.24a, 6.25a)

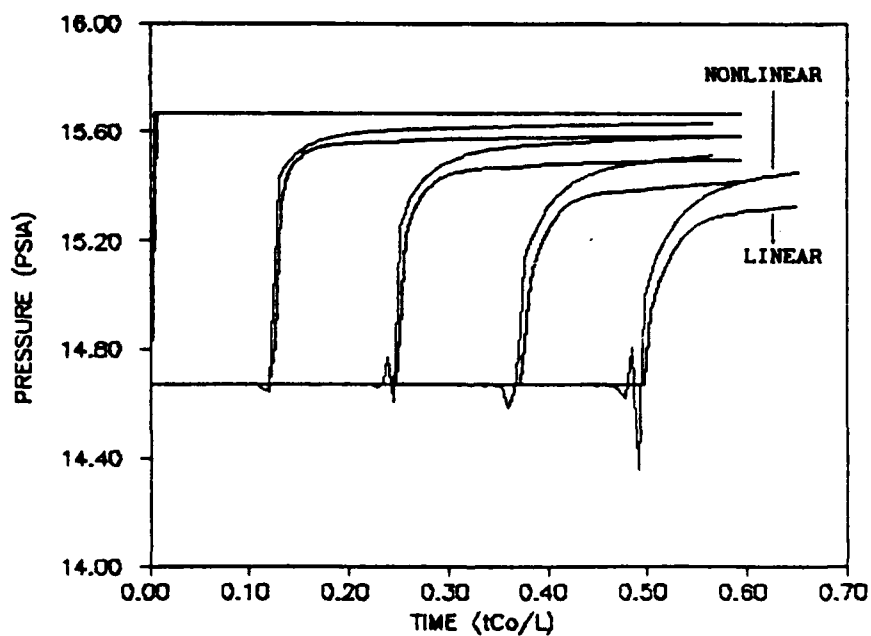


b. Combined Unsteady Friction and Heat Transfer (Figs 6.26a, 6.27a)

Fig. 41. Terminated Ramp, Comparison of Linear and Nonlinear Results

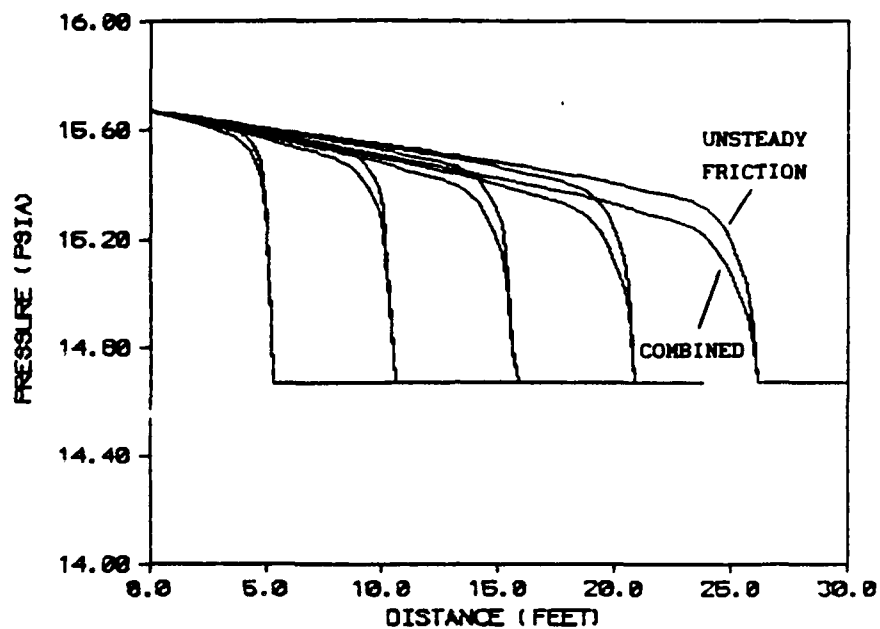


a. Unsteady Friction (Figs 6.24b, 6.25b)

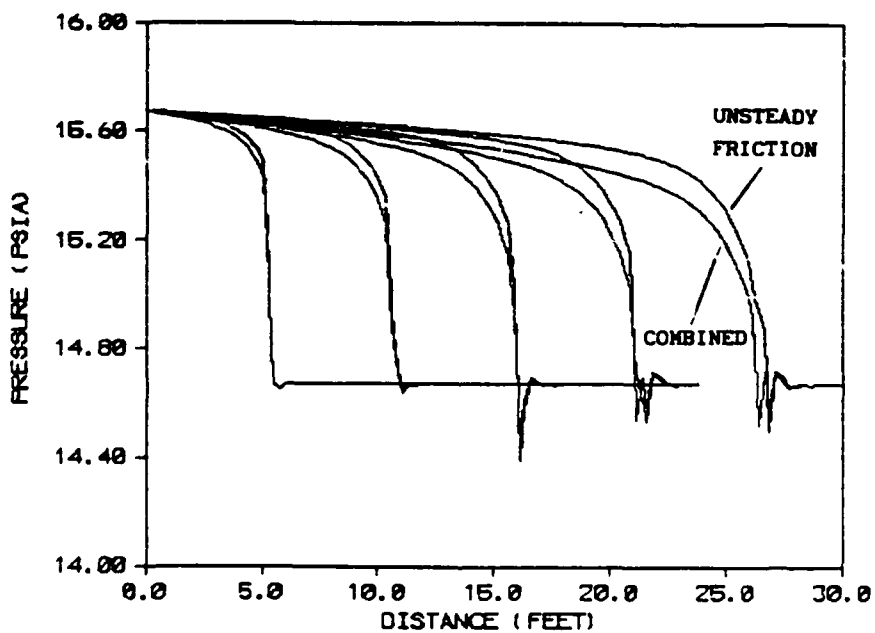


b. Combined Unsteady Friction and Heat Transfer (Figs 6.26b, 6.27b)

Fig. 42. Terminated Ramp, Comparison of Linear and Nonlinear Results, Time History

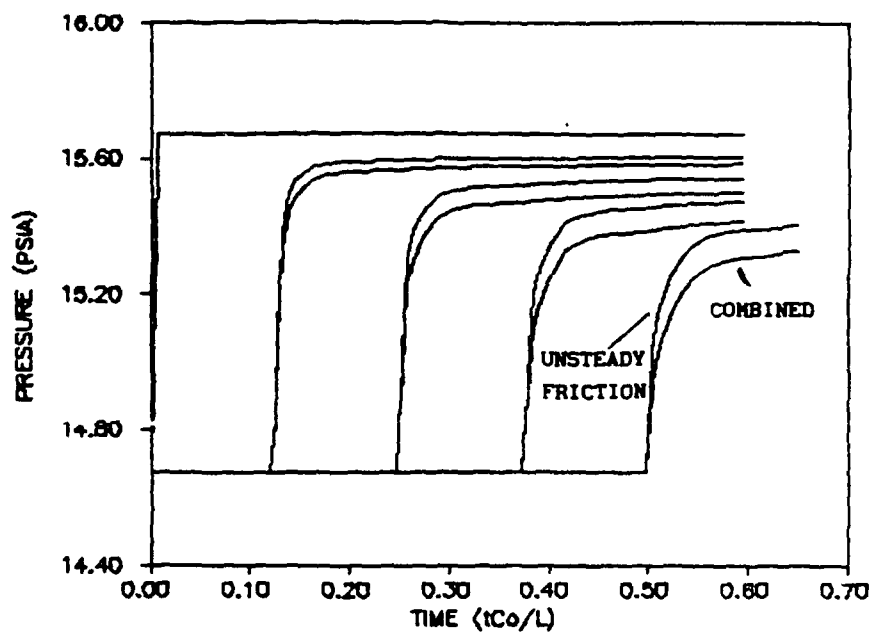


a. Linear Results (Figs 6.24a, 6.26a)

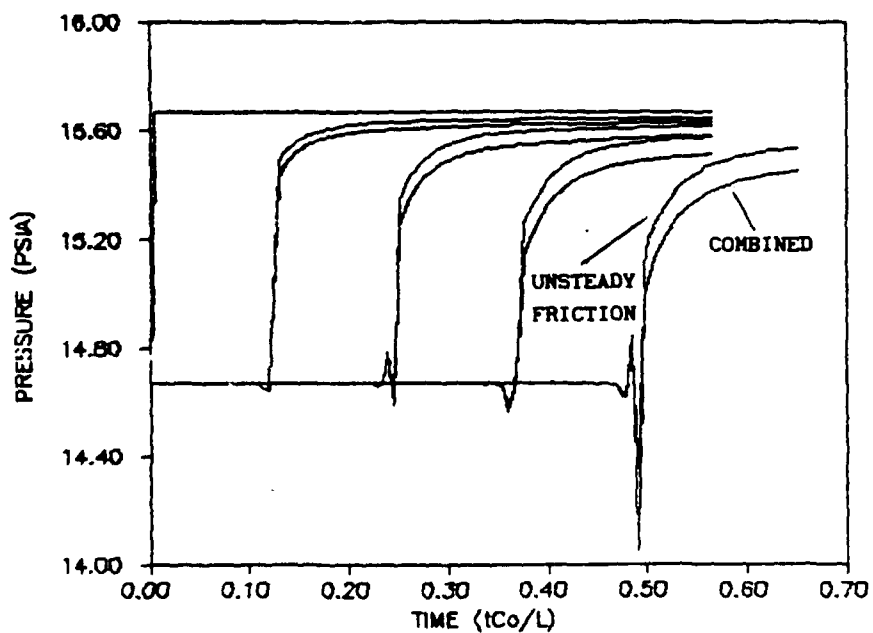


b. Nonlinear Results (Figs 6.25a, 6.27a)

Fig. 43. Terminated Ramp, Comparison of Unsteady Friction and Combined Unsteady Friction and Heat Transfer



a. Linear Results (Figs 6.24b, 6.26b)

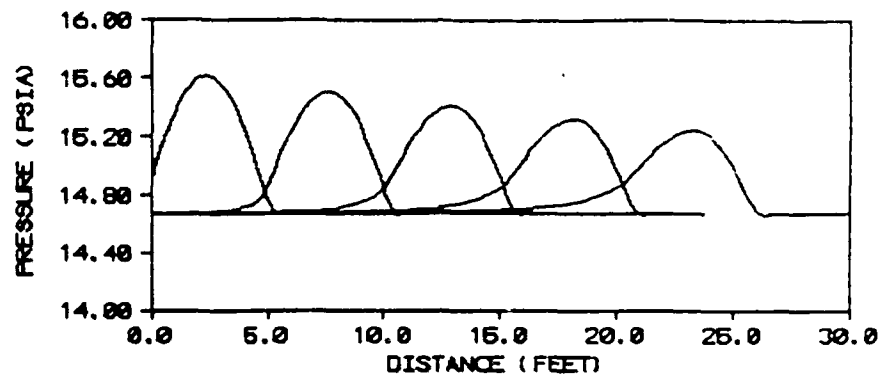


b. Nonlinear Results (Figs 6.25b, 6.27b)

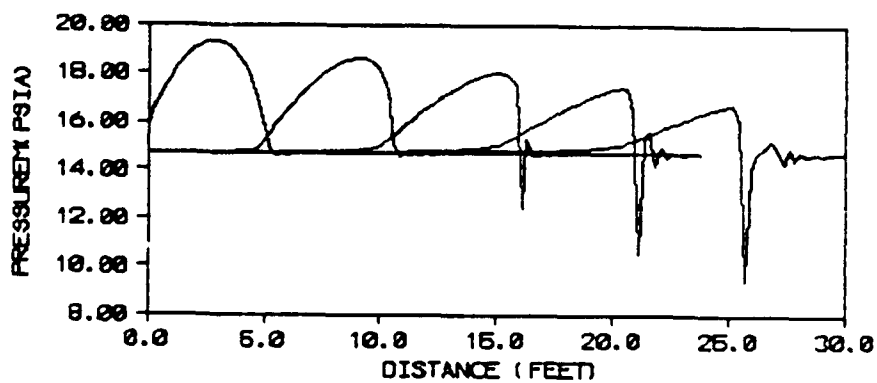
Fig. 44. Terminated Ramp, Comparison of Unsteady Friction and Combined Unsteady Friction and Heat Transfer, Time History

application. Kantola described this effect as an initial rapid rise followed by a nearly constant amplitude, persisting for some time, followed by a slower rise. He attributed the inability of his model to predict this behavior to the lack of nonlinear terms capable of accounting for convected mass, momentum, and heat transfer in his basic equations. Karam and Leonard noted similar behavior at an upstream location in a 50 ft line (30). In both cases, the tubing was coiled. The basic equations used in this study retain the nonlinear convective terms but still fail to predict this experimentally observed behavior. One possible explanation is that nonlinear convection alone is not responsible for this effect. Additional unsteady frictional effects caused by the distortion of the transient velocity profile in the coiled tube may play an important role in producing this amplitude dependent damping effect. No data for comparison on straight long lines has been found in the course of this study. Although a straight line was used by Sandoz, her work was restricted to short pulses and no result similar to that described above was reported.

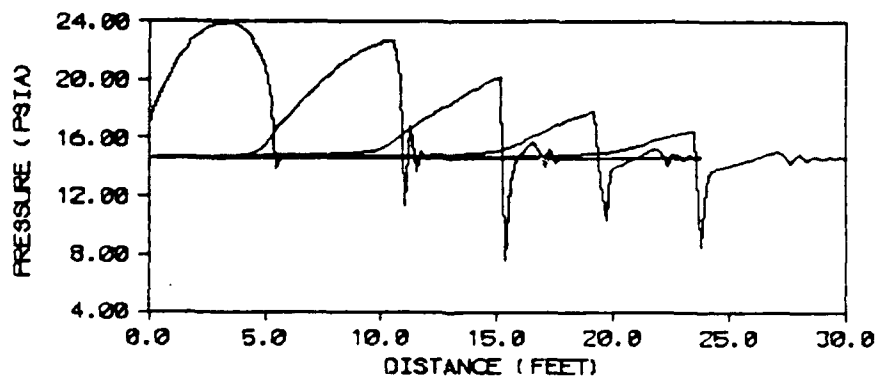
The effect of increased signal amplitude on the algorithm is demonstrated in Figures 45 through 46 using a sine pulse as an input signal. Figures 45 and 46 show nonlinear and linear results respectively for combined unsteady friction and heat transfer. More rapid distortion and ultimate formation of a discontinuity are evident in the nonlinear case for the higher pressures. Over the 30 ft distance considered in the graph, the higher amplitude input signal formed a discontinuity much earlier than the smaller amplitude inputs. Once a discontinuity forms using this algorithm, the accuracy is suspect since this algorithm produces severe oscillations which



a. 1 PSI Amplitude

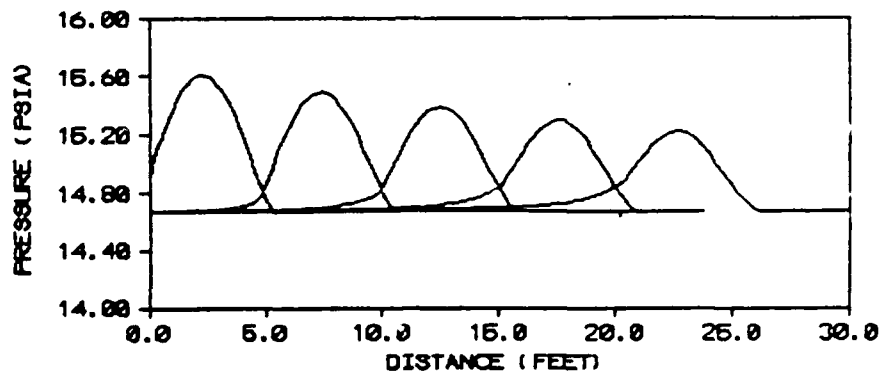


b. 5 PSI Amplitude

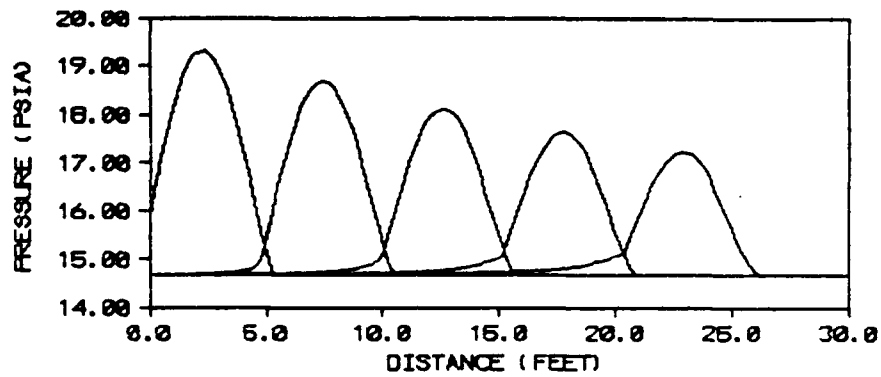


c. 10 PSI Amplitude

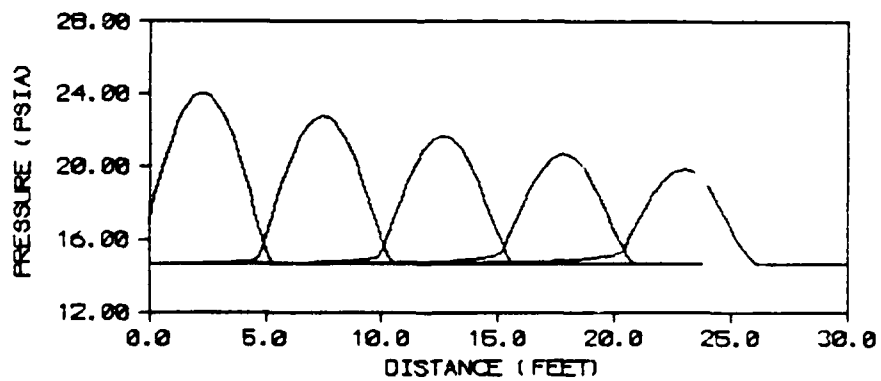
Fig. 45. Single Positive Half-Sinusoidal Pulse Traveling to Right,
Nonlinear Results



a. 1 PSI Amplitude



b. 5 PSI Amplitude



c. 10 PSI Amplitude

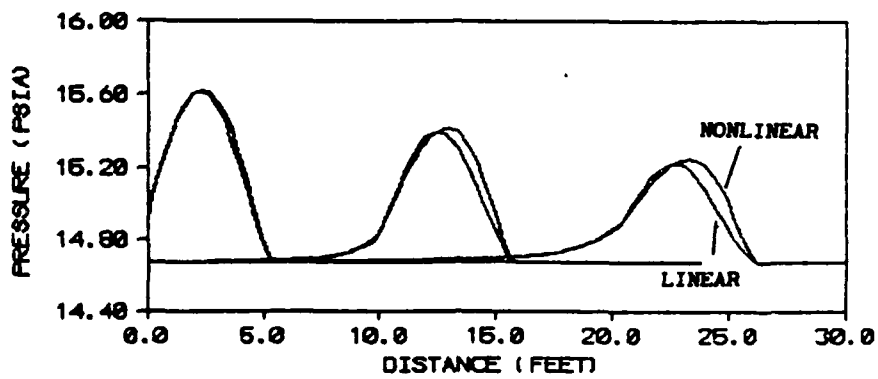
Fig. 46. Single Sinusoidal Pulse Traveling to Right, Linear Results

overwhelm the rest of the solution. Also, the nonlinear algorithm is invalid in the presence of discontinuities since the damped-wave equations are in nonconservative form and may permit the existence of small mass sources or sinks (2:52). Special treatment of discontinuities is required. When the linear algorithm is used the higher input signal pressures cause no oscillations and only result in signals of higher amplitudes.

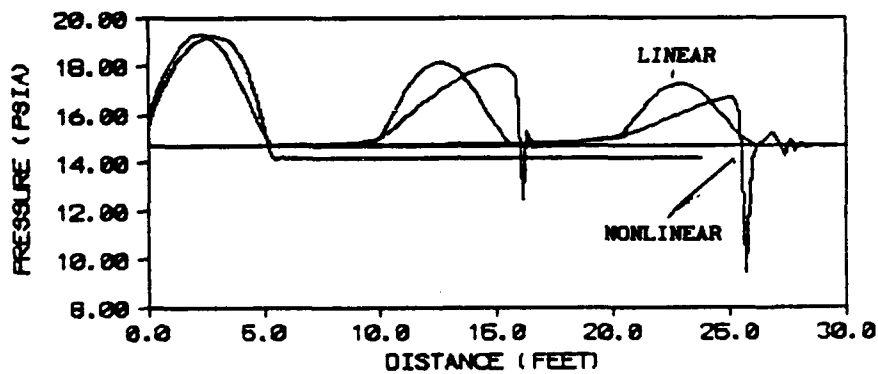
Linear and nonlinear results are compared on the same coordinate axes in Figures 47 and 48 for sinusoidal pulses of 1 psi, 5 psi and 10 psi. The importance of nonlinear effects on propagating signals is clearly demonstrated for large pressure amplitudes.

An input signal amplitude of 0.25 psi produces the results shown in Figure 49. The behavior of the nonlinear algorithm results closely follow those produced by the linear algorithm. Even for this small signal (1.7 percent of the initial pressure) a change in waveform can still be observed as the signal travels down the transmission line. The shape distortion is a cumulative process and small effects accumulated over a large distance become significant.

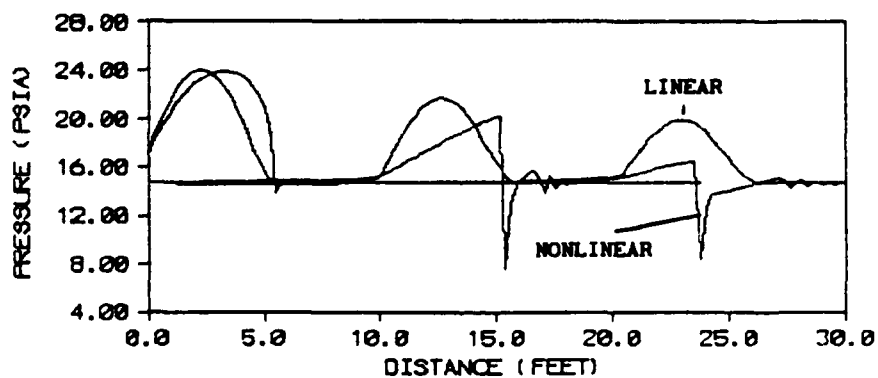
As stated before, the damping functions include a model for turbulent friction which engages when the Reynolds number, based on the average axial velocity at each axial node location, exceeds 2300. No data indicating criteria for the onset of turbulence in transient flow was found. The value of 2300 was chosen from steady flow theory for lack of a better value. Figure 50 compares laminar and turbulent results for the same transmission line configuration. Linear results were used for this comparison so that nonlinear effects like shape evolution and oscillations would not mask the difference between the



a. 1 PSI Amplitude

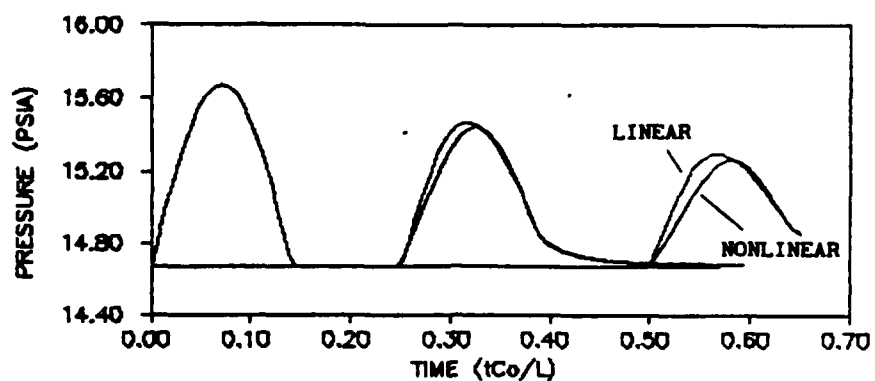


b. 5 PSI Amplitude

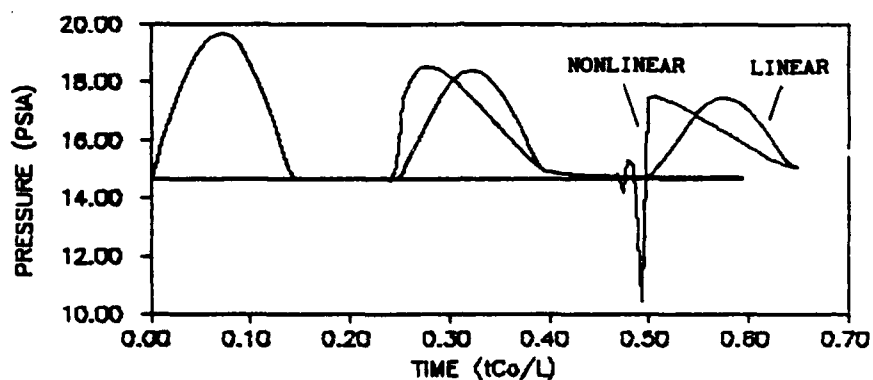


c. 10 PSI Amplitude

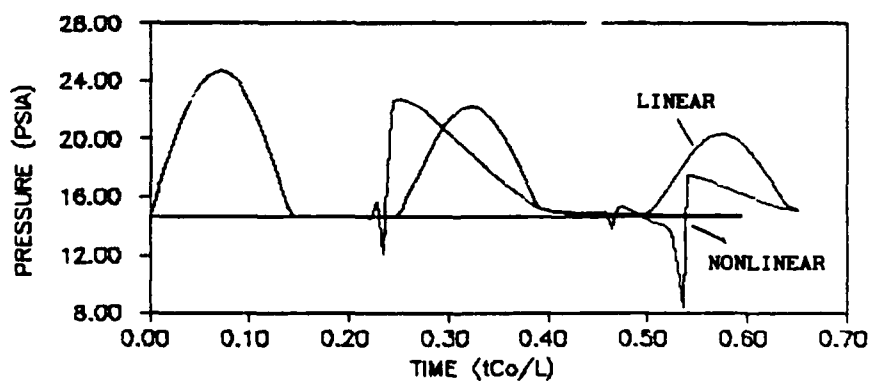
Fig. 47. Single Positive Half-Sinusoidal Pulse Traveling to Right, Comparison of Linear (Fig. 45) and Nonlinear (Fig. 46) Results, Combined Unsteady Friction and Heat Transfer



a. 1 PSI Amplitude

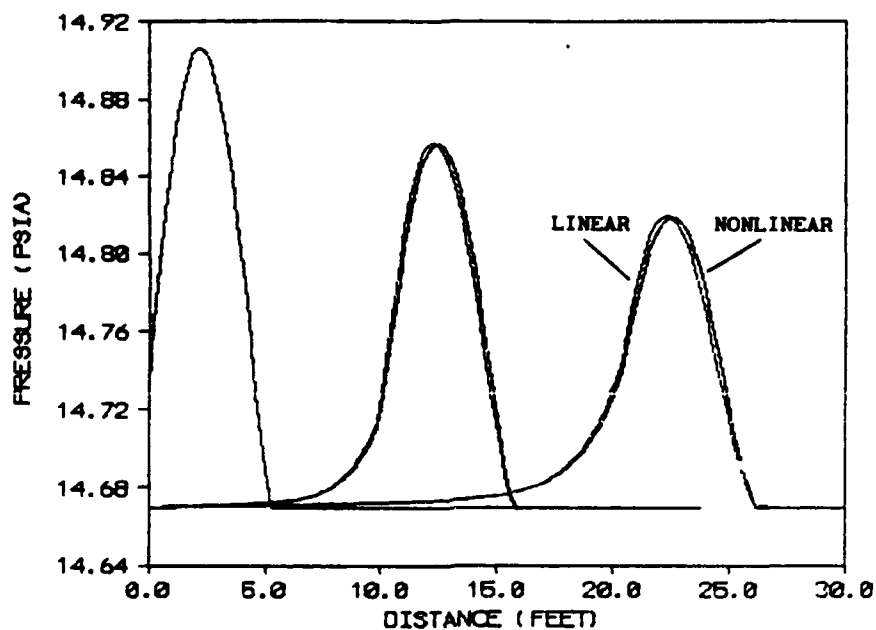


b. 5 PSI Amplitude

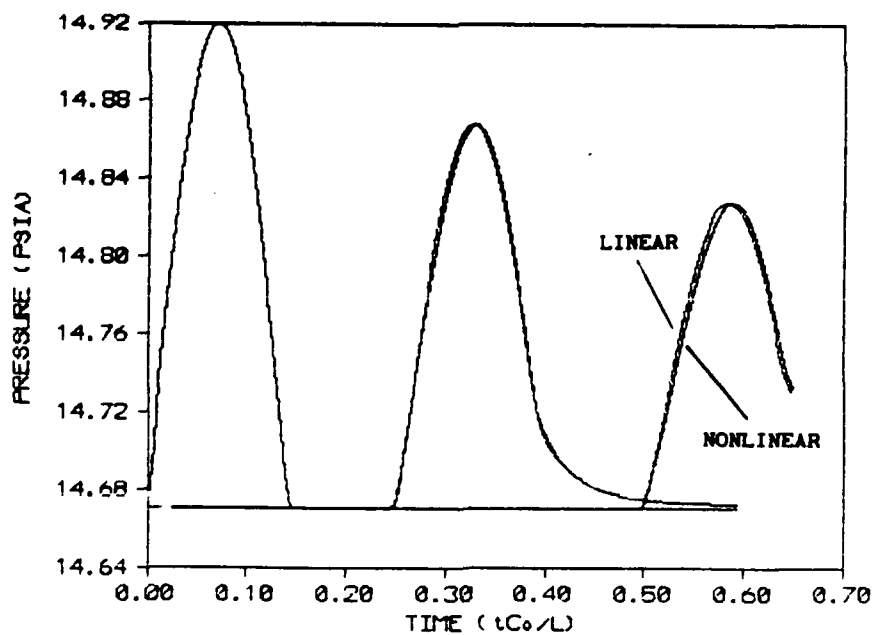


c. 10 PSI Amplitude

Fig. 48. Single Sinusoidal Pulse, Comparison of Linear and Nonlinear Results, Combined Unsteady Friction and Heat Transfer, Time History



a. Profiles at 0.0046, 0.014, and 0.023 sec



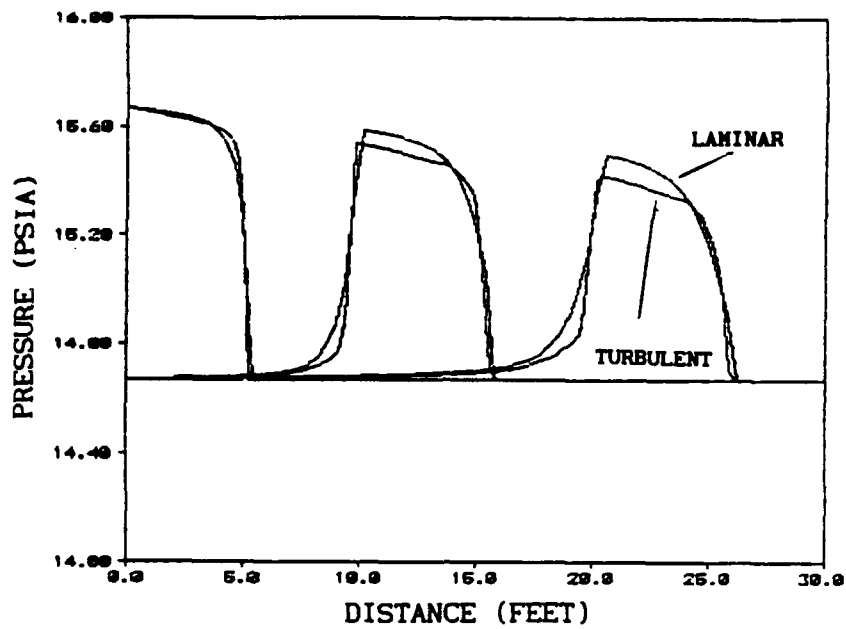
b. Time History at 0, 10, and 20 ft.

Fig. 49. Single Positive Half-Sinusoidal Pulse, Convergence of Linear and Nonlinear Results for Sufficiently Small Amplitude

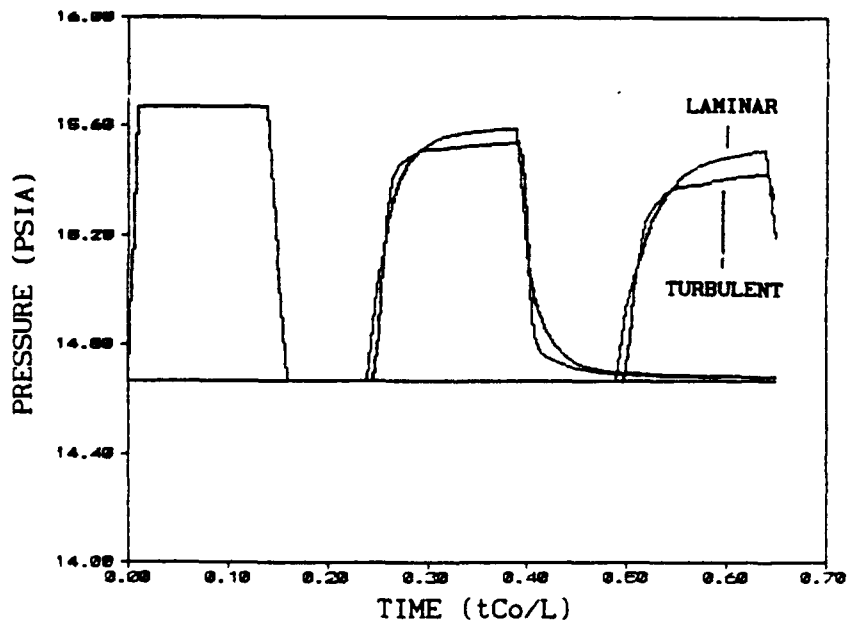
caused severe instability in the results. This problem was easily laminar and turbulent friction models. The waveform with the greater amplitude is obtained using laminar friction only. The waveform produced using turbulent friction damping has a steeper slope at the leading edge, is square at the top, and decays somewhat faster than the laminar result.

So far, with the exception of Figures 24 and 25, the location of the boundaries of the flow intervals dividing the cross section of the transmission line have remained fixed. For the 0.305 in ID line, these boundaries are located at 0.12, 0.14, 0.15, and 0.1525 in measured from the centerline. Figure 51 compares the results from the boundary locations shown above to results from boundaries located at 0.07625, 0.122, 0.1375, and 0.1525 in. There is only a slight difference in the waveform. The results do, however, show that location of the flow interval boundaries does affect the results to a small degree. The location of the inner boundary of the outermost flow interval has the most effect on the results. Results appear to be insensitive to the locations of the other boundaries if the thickness of the outer interval is less than ten percent of the transmission-line radius.

Large fluctuations in the value of the damping function at the wall were produced when too narrow an outside interval ($r_{M-1} < r < r_M$) was used. These fluctuations often fixed by decreasing the time step, and consequently the spatial discretization, with an associated increase in computer cpu time, or by increasing the width of the outside interval. To ensure good resolution at the wall, the inner boundary of the outer interval was kept within what was estimated to be the viscous sublayer for the expected flow conditions. This type of

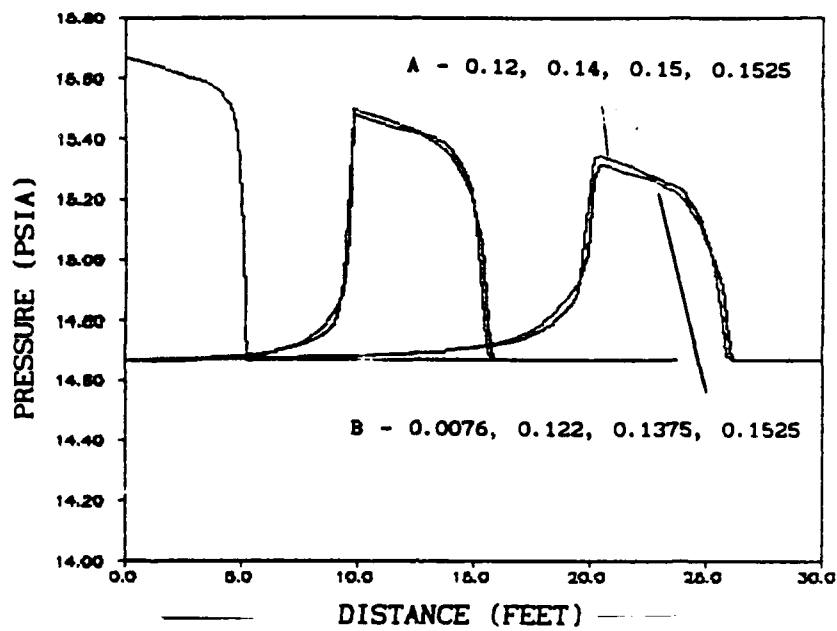


a. Profiles at 0.0046, 0.014, and 0.023 sec

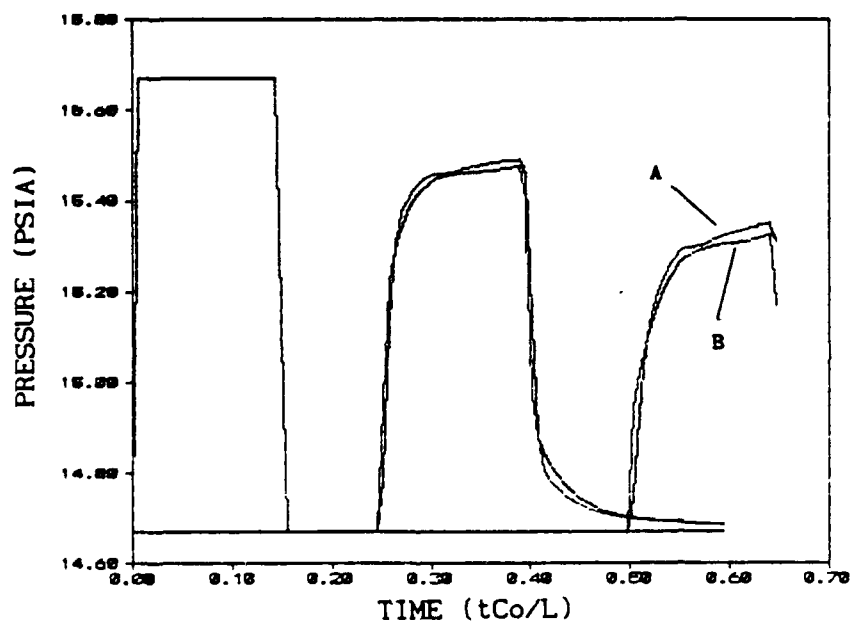


b. Time History at 0, 10, and 20 ft.

Fig. 50. Single Trapezoidal Pulse, Comparison of Laminar (Fig. 27) and Turbulent Unsteady Friction



a. Profiles at 0.0046, 0.014, and 0.023 sec

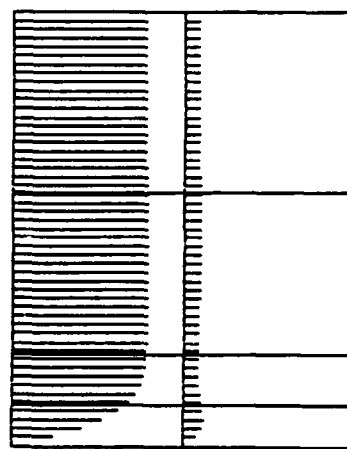
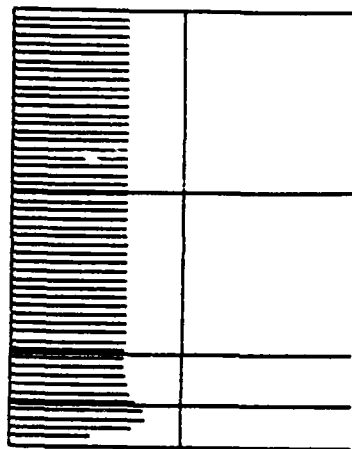


b. Time History at 0, 10, and 20 ft.

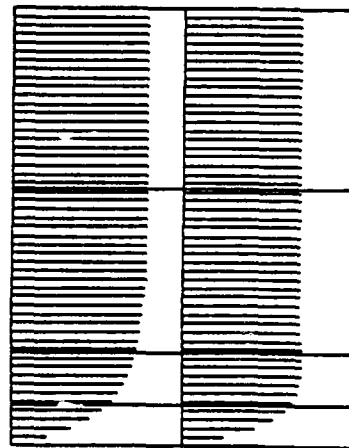
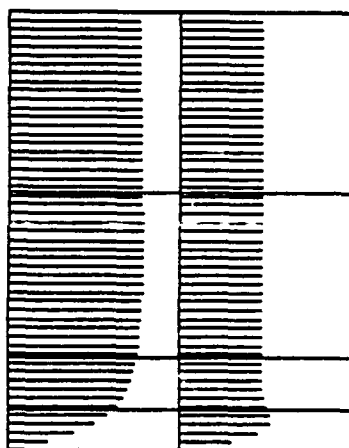
Fig. 51. Trapezoidal Pulse, Comparison of Two Different Sets of Flow Interval Boundary Locations

from the wall. It is the effect of this unsteady velocity profile that instability has also been noted using the method of characteristics with steady damping on narrow lines (16:9). More detail on the effects of interval boundary location and the optimum number of intervals was not pursued in this study. As few intervals as possible were used in keeping with the goal to minimize the computer resources required to model the transmission line.

Use of the piecewise defined polynomial allows information about the instantaneous velocity profiles to be obtained for each node location at each time step. This velocity profile information is the basis for calculation of the unsteady friction and heat transfer damping functions at the boundary of each flow interval. Figures 52a through 52d show the transient velocity profiles in a line at the point of signal application and at a point 5 ft downstream. Each individual figure is a snapshot of the velocity profile caused by a 1 psi terminated ramp input signal as it progresses down the transmission line. Note the bulge in the profile near the wall as the flow is initially accelerated by the arrival of the pressure wave at the 5 ft location. Similar behavior of the velocity profile near the wall was observed experimentally by Shih for pressure inputs produced by means of burst discs (63). Significant damping occurs near the wall as a result of this bulge in the velocity profile while little happens away from the wall. The use of the friction factor, which is based on steady, fully developed flow, is inaccurate. A short time after the initial arrival of the pressure wave, the velocity profile begins to take on a more familiar shape as the fluid continues to be accelerated and the steady velocity profile continues to develop.



a. Flow Accelerated at Station 1, b. Wavefront Arrives at Station 2
No Signal at Station 2



c. Flow Accelerating at Station 2 d. Steady Velocity Profile
Developing at Station 2

Fig. 52. Instantaneous Velocity Profiles Produced by Passage of
Terminated Ramp Input Signal

Lines of Finite Length

All cases discussed so far involve approximations of semi-infinite transmission lines. This configuration kept the effects of numerical dispersion and the damping functions on the input waveform from being masked by reflections from the transmission line ends. Finite lines represent more realistic configurations often found in complex pneumatic and hydraulic systems. An important goal of the present study is to arrive at a practical way to analyze real systems containing one or more transmission lines.

A 5 ft, 0.170 in ID air-filled finite transmission line was simulated. Three types of terminations were examined: the blocked line, the volume-terminated line, and the open line. These are shown in Figure 53.

Figure 54 shows the response to a step input for the blocked line configuration. Results with turbulent and laminar friction are compared to data obtained by Karam and Leonard (30:501). The curve with the most severe attenuation was produced using turbulent friction. The turbulent and laminar results bracket the data with the curve shape following the shape of the data quite well. Figure 55 compares nonlinear results generated by terminated ramp inputs of 0.25, 1.0, and 2.00 psi for the 5 ft, 0.170 in ID blocked line. The magnitude of peaks of the transient waveforms differ according to the input pressure amplitude with the largest input pressure producing the largest peak. The relation among the amplitudes of the peaks is retained as the signal attenuates. The slope of leading edge of each waveform steepens in relation to the input pressure amplitude, with the steepest slope

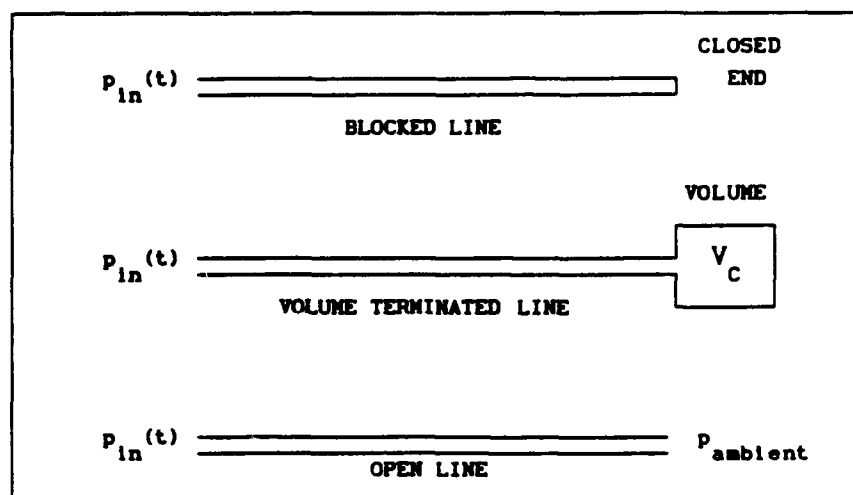


Fig. 53. Finite-Length, Transmission-Line Configurations

produced by the largest input pressure. Figure 56 compares the linear and nonlinear, finite-difference results for a 2. psi input pressure terminated ramp. Although the two curves are in close agreement, a definite difference in slopes can be seen. A 5 ft line is relatively short. For longer lines, the difference between linear and nonlinear results would differ by considerably more due to the longer travel time over which the nonlinear effects could accumulate.

The volume-terminated line is examined next. Figure 57 compares the pressure response to a step input for the volume-terminated line with V_c equal to $0.25V_L$, V_L , and $2.0V_L$ where V_c is the volume of the terminating chamber and V_L is the volume of the 5 ft line. Compression in the volume is assumed to occur isothermally. The volume is described by the following equation (19:3):

$$\frac{\partial p}{\partial t} = \frac{\pi a^2 n p u_{av}}{V_c} \quad (131)$$

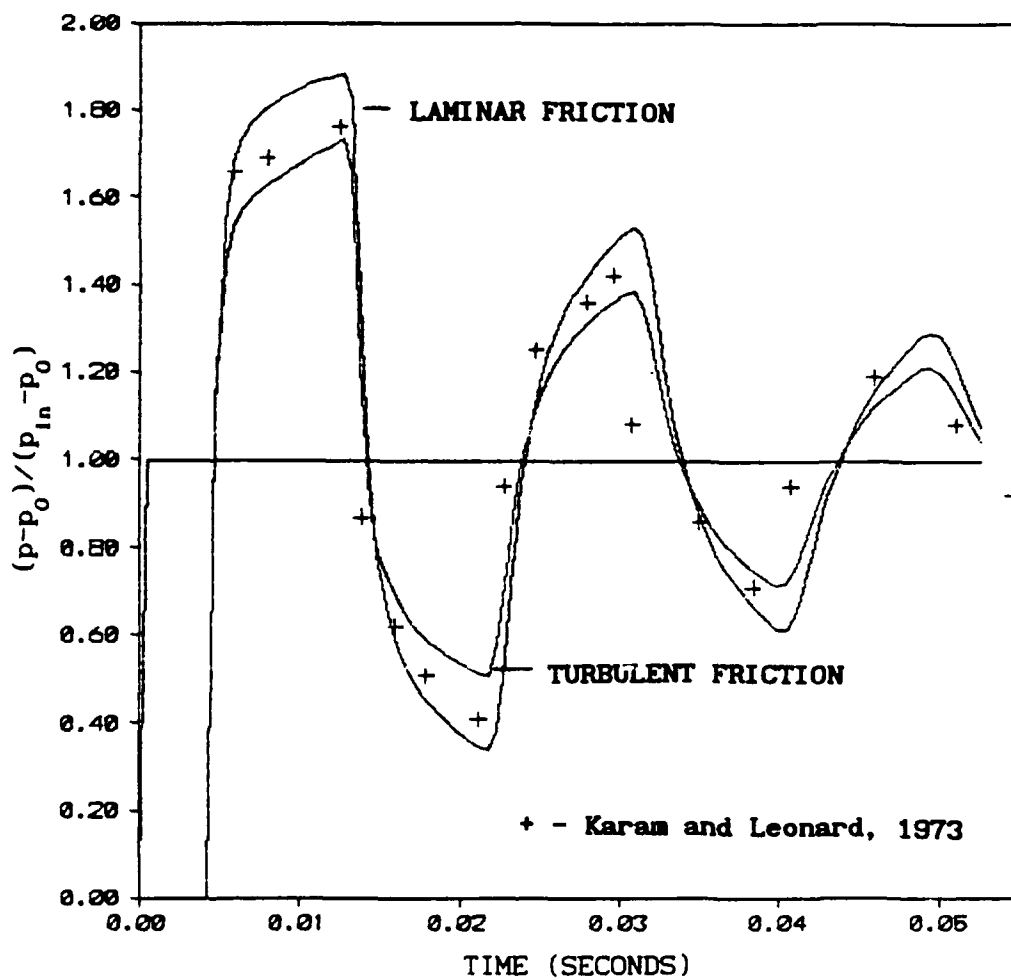


Fig. 54. Transient Response for Blocked 5 ft, 0.170 in ID Line, Linear Results, Terminated Ramp Input

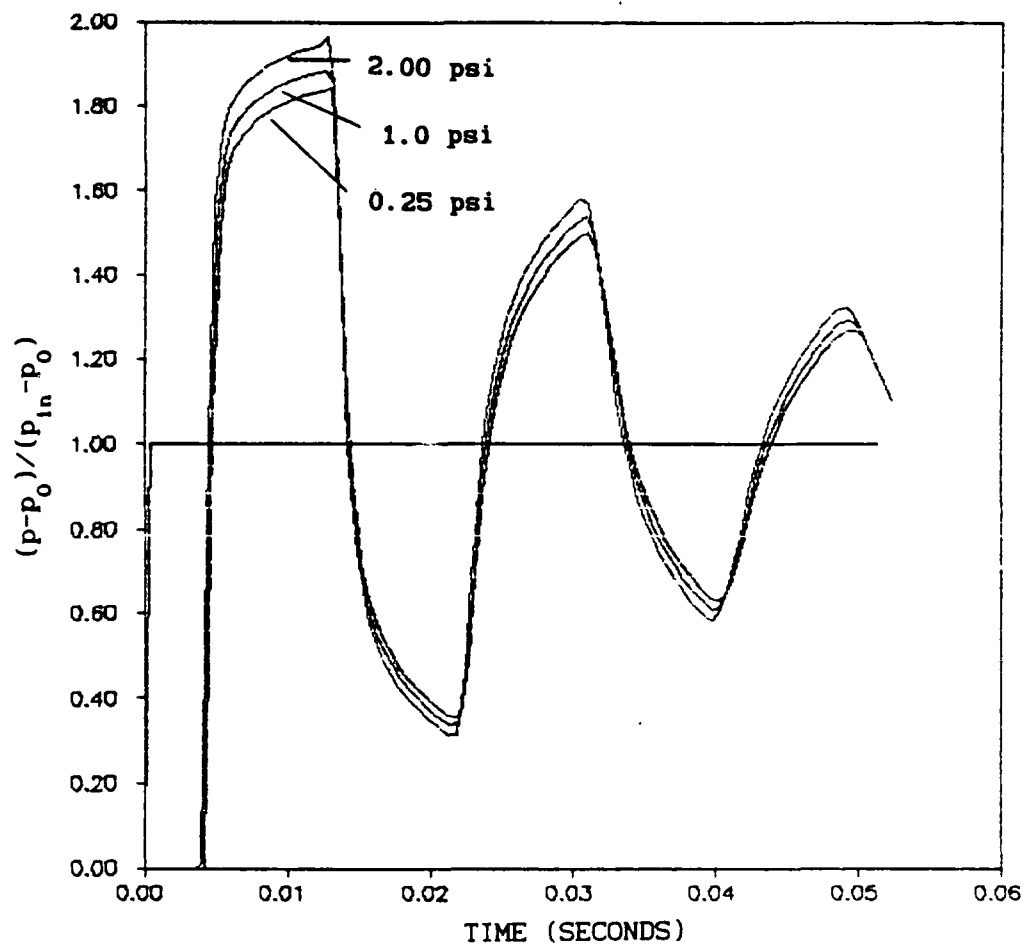


Fig. 55. Transient Response for Blocked 5 ft. 0.170 in ID Line,
Linear Results, Terminated Ramp Input

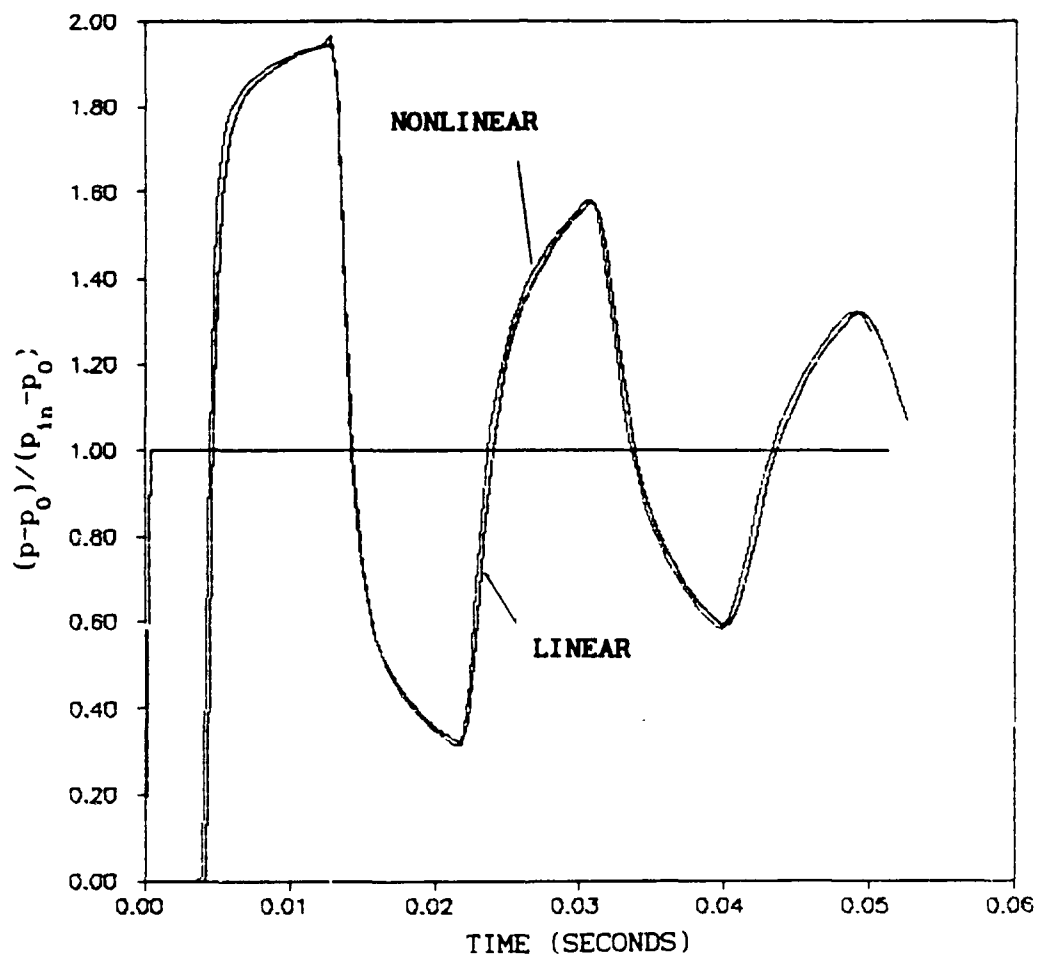


Fig. 56. Comparison of Linear and Nonlinear Response to 2.0 psi Terminated Ramp in 5 ft, 0.170 in ID Blocked Line

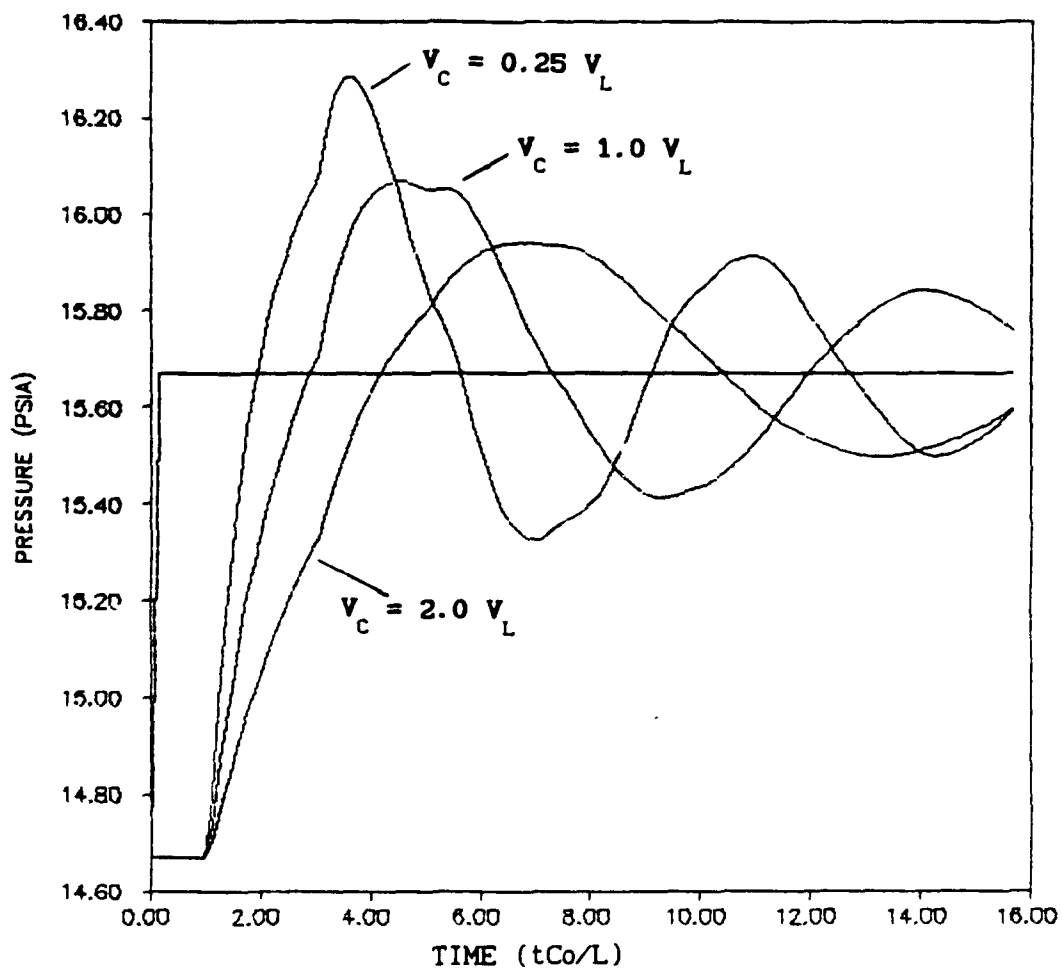


Fig. 57. 1.0 psi Terminated Ramp Input in 5 ft, 0.170 in ID Volume
Terminated Line

where $n = 1$ ($n = 1.4$ for adiabatic behavior). The volume of the termination has a very significant effect on the overall response of the system. The behavior of the average line inlet and exit velocities is shown in Figures 58, 59, 60 and 61. Rapid velocity fluctuations with sharp reversals can be seen.

The final line termination examined is the open-end line where the end of the transmission line is maintained at ambient pressure. This configuration proved the most demanding of all with regards to numerical stability of the algorithm. A comparison of linear and nonlinear results is shown in Figure 62 for a 0.25 psi terminated ramp input. The results are identical up to the point where the nonlinear results diverge and continue to increase while the linear results approach a steady-state value. Note the presence of periodic velocity spikes appearing at regular intervals in the linear results. These spikes are more pronounced at an input pressure of 1.0 psi as shown in the linear results of Figure 63 and 64. These spikes are thought to be the main cause of the instability of the nonlinear numerical algorithm when used with the open line configuration.

Input pressures greater than 0.25 psi caused the nonlinear algorithm to fail completely unless the time step, and consequently, the computational mesh size in the axial direction were significantly reduced in size. No attempt was made to see if these spikes ultimately damp out or remain in the solution indefinitely. A constant pressure is used for the boundary condition at the open end of the line. It is still unknown whether these velocity spikes are an artifact of the numerical algorithm due to an inaccurate description of the boundary condition or represent a phenomenon that could be experimentally

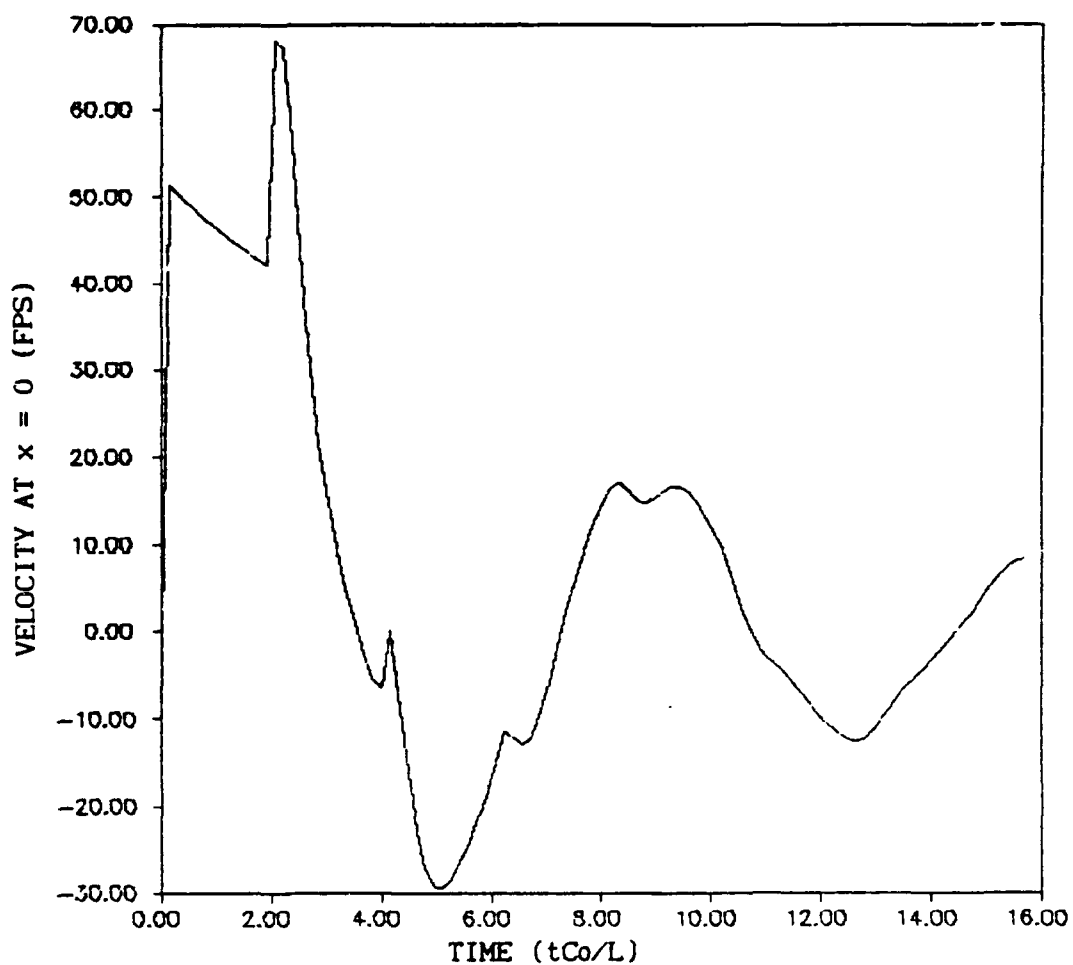


Fig. 58. Transient Velocity Response, 1.0 psi Terminated Ramp Input
in 5 ft, 0.170 in ID Volume Terminated Line, $V_c = 0.5 V_L$

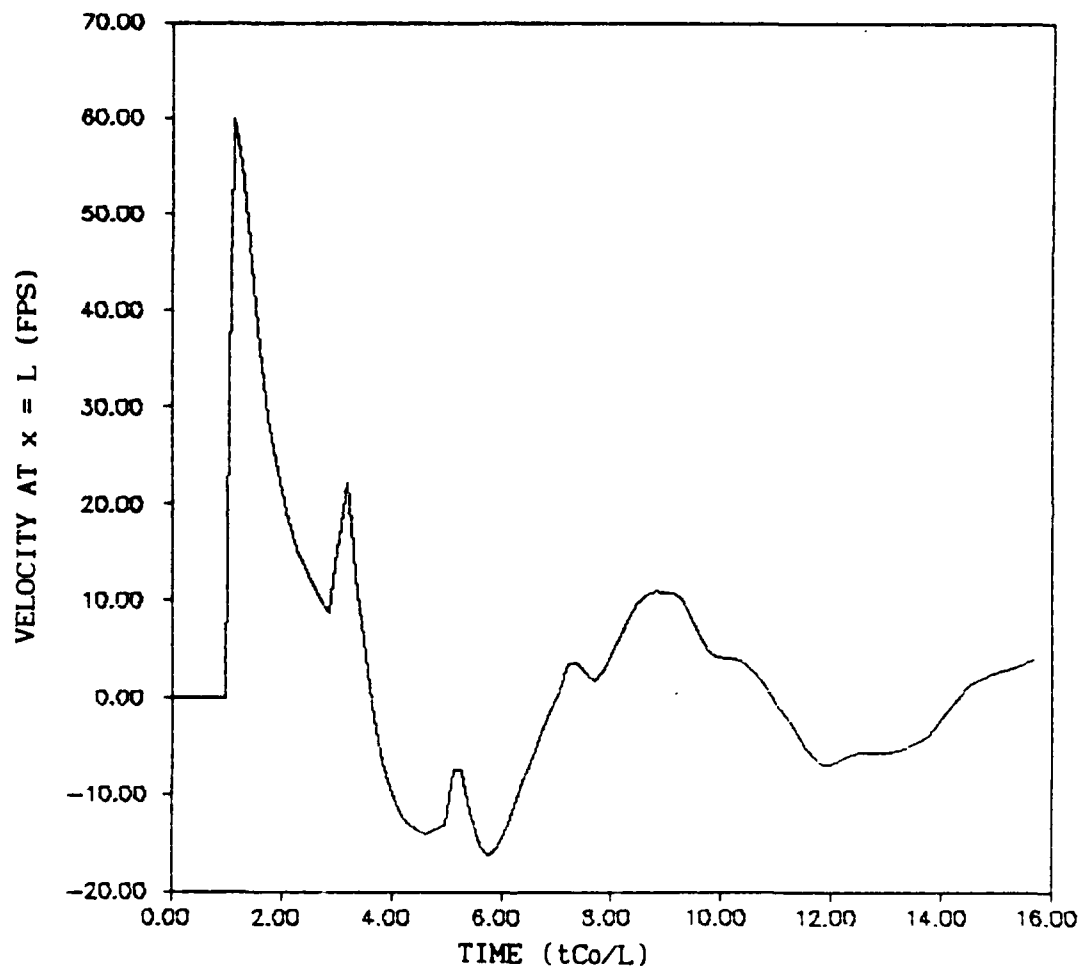


Fig. 59. Transient Velocity Response, 1.0 psi Terminated Ramp Input
in 5 ft, 0.170 in ID Volume Terminated Line, $V_C = 0.5 V_L$

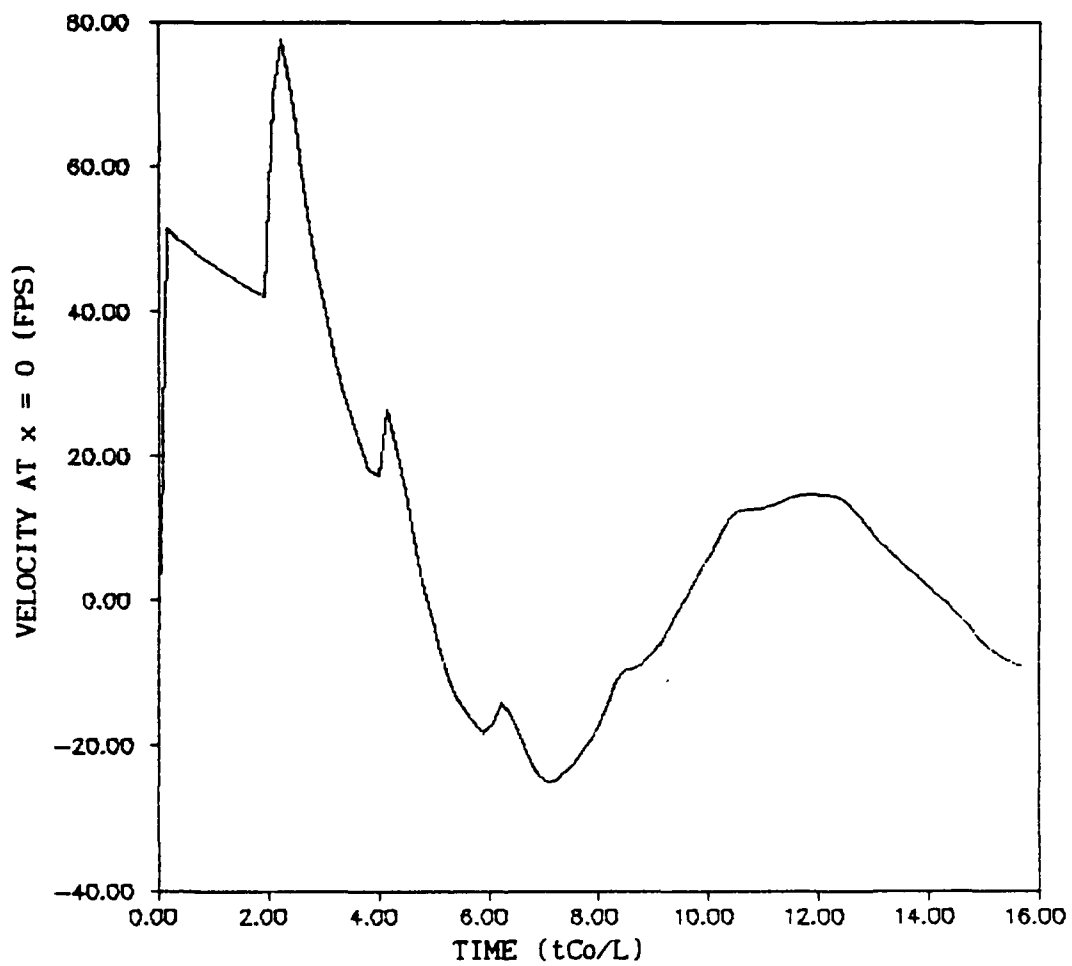


Fig. 60. Transient Velocity Response, 1.0 psi Terminated Ramp Input
in 5 ft, 0.170 in ID Volume Terminated Line, $V_c = 1.0 V_L$

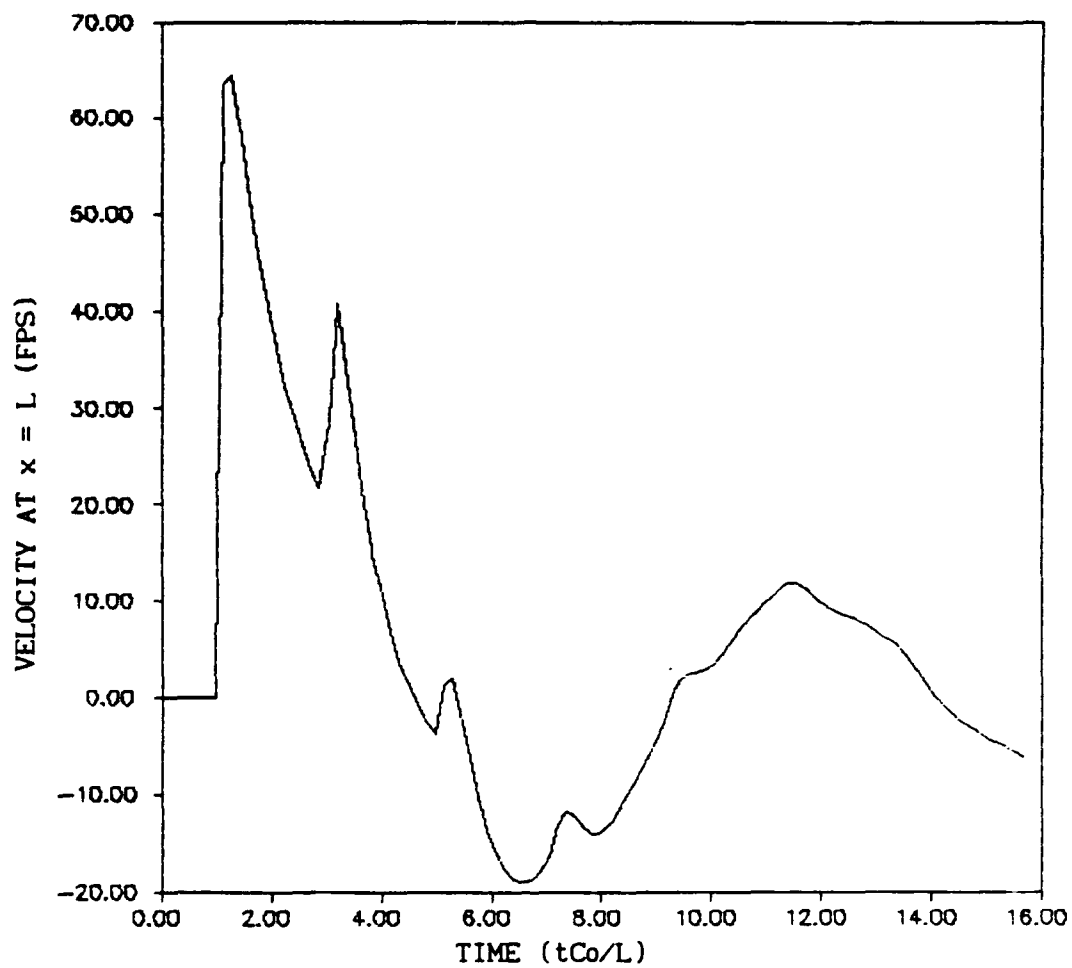


Fig. 61. Transient Velocity Response, 1.0 psi Terminated Ramp Input
in 5 ft, 0.170 in ID Volume Terminated Line, $V_C = 1.0 V_L$

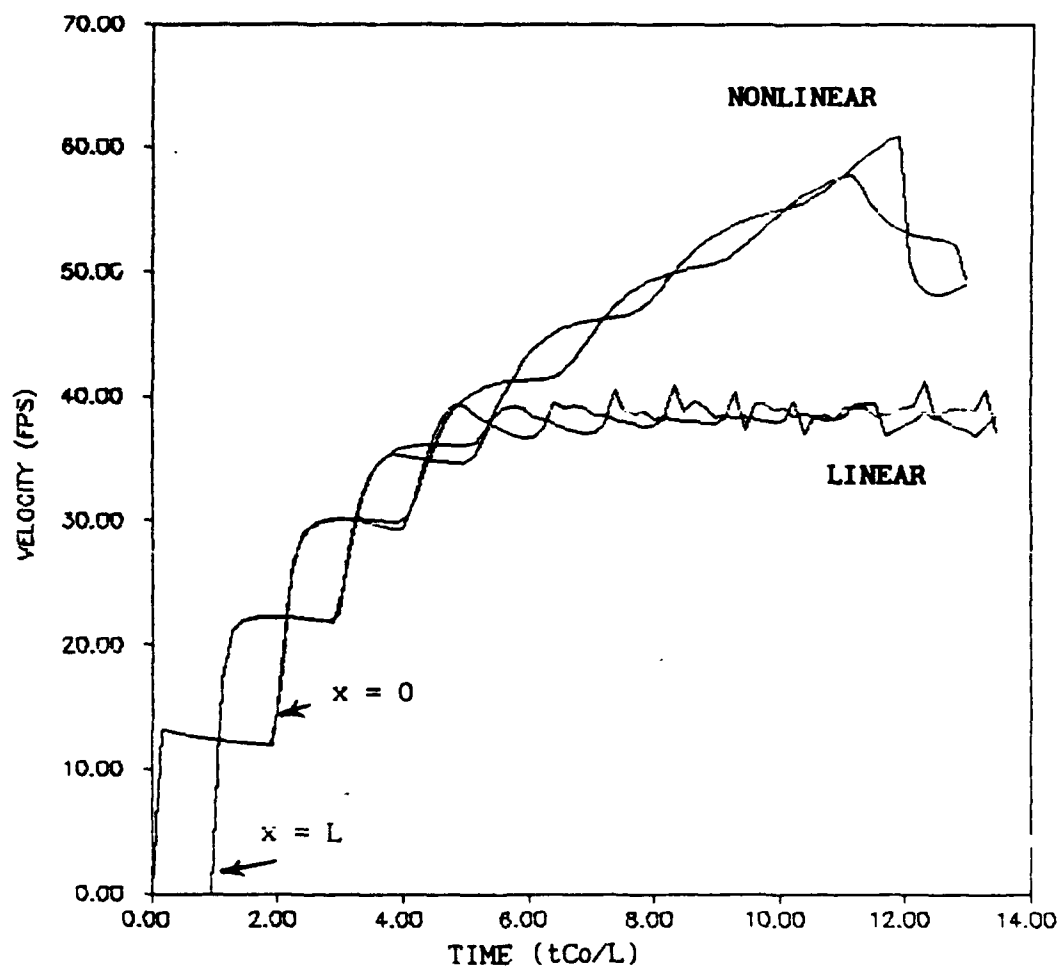


Fig. 62. Comparison of Linear and Nonlinear Results for 0.25 psi Terminated Ramp Input to 5 ft, 0.170 in ID Open Line

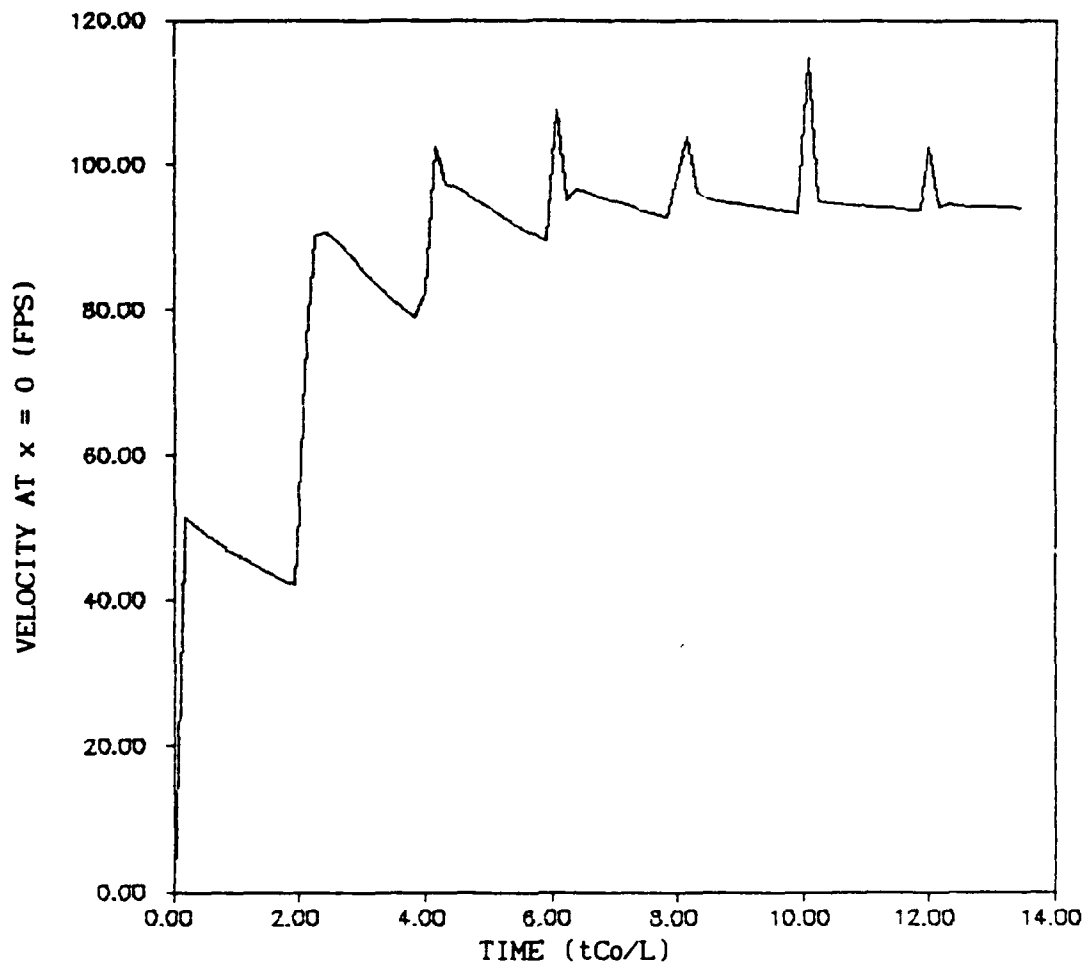


Fig. 63. Transient Velocity Response, 1.0 psi Terminated Ramp Input
in 5 ft, 0.170 in ID Open Line, Linear Results

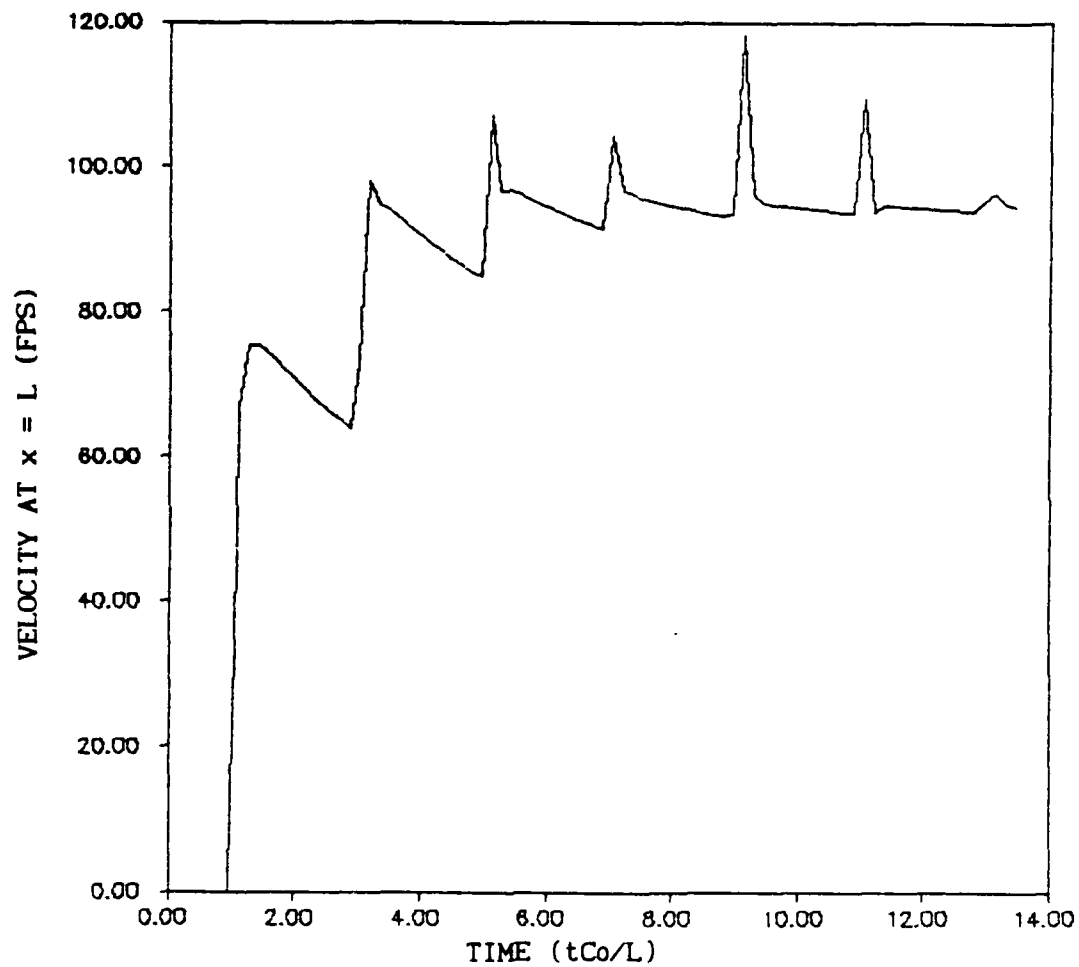


Fig. 64. Transient Velocity Response, 1.0 psi Terminated Ramp Input
in 5 ft, 0.170 in ID Open Line, Linear Results,

observed. No experimental or theoretical transient velocity data for open-end lines was found.

The linear algorithm was used to examine the transient response for input pressures above 0.25 psi since the nonlinear algorithm became unstable. When the amplitude of the input pressure step was increased to 2 psi, the velocity spikes became almost nonexistent as shown in Figures 65 and 66. Since this spike phenomena is present in the linear results as well as the nonlinear results, it cannot be solely attributed to the nonlinear algorithm.

It is informative to look at a comparison of the inlet velocity of the closed-end and open-end line configuration. Figure 67 compares the velocity time history resulting from a 1.0 psi input pressure using the linear algorithm. Notice that up until $t = 2.0$, the velocity traces of both configurations are exactly the same. The same is true in Figure 68 for the 2 psi input pressure. In each figure, the velocity spikes and steep rises occur approximately 2.0 dimensionless time units apart which is the time it takes the wave to travel twice the length of the 5 ft line. The spikes are obviously produced and maintained by the downstream open-end boundary condition. It should also be noted that the response of the transmission line is exactly the same until sufficient time passes for the effects of the downstream boundary condition to propagate to the inlet.

All cases examined so far have been for a line with no steady mean flow. One advantage of using a numerical approach to model a transmission line is the ease of incorporating an established mean flow as a set of initial conditions. However, it is important that the method used to obtain the initial flow field is consistent with the

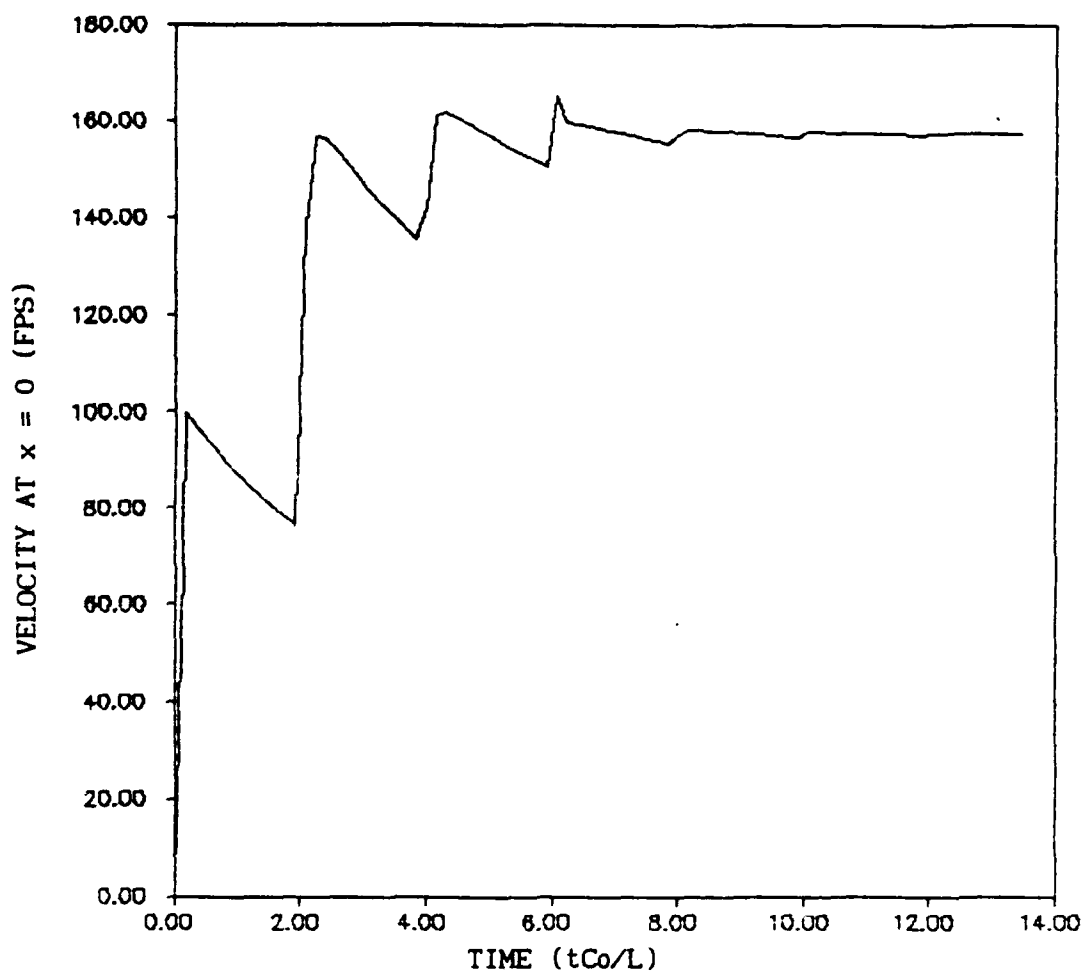


Fig. 65. Transient Velocity Response, 2.0 psi Terminated Ramp Input
in 5 ft, 0.170 in ID Open Line, Linear Results

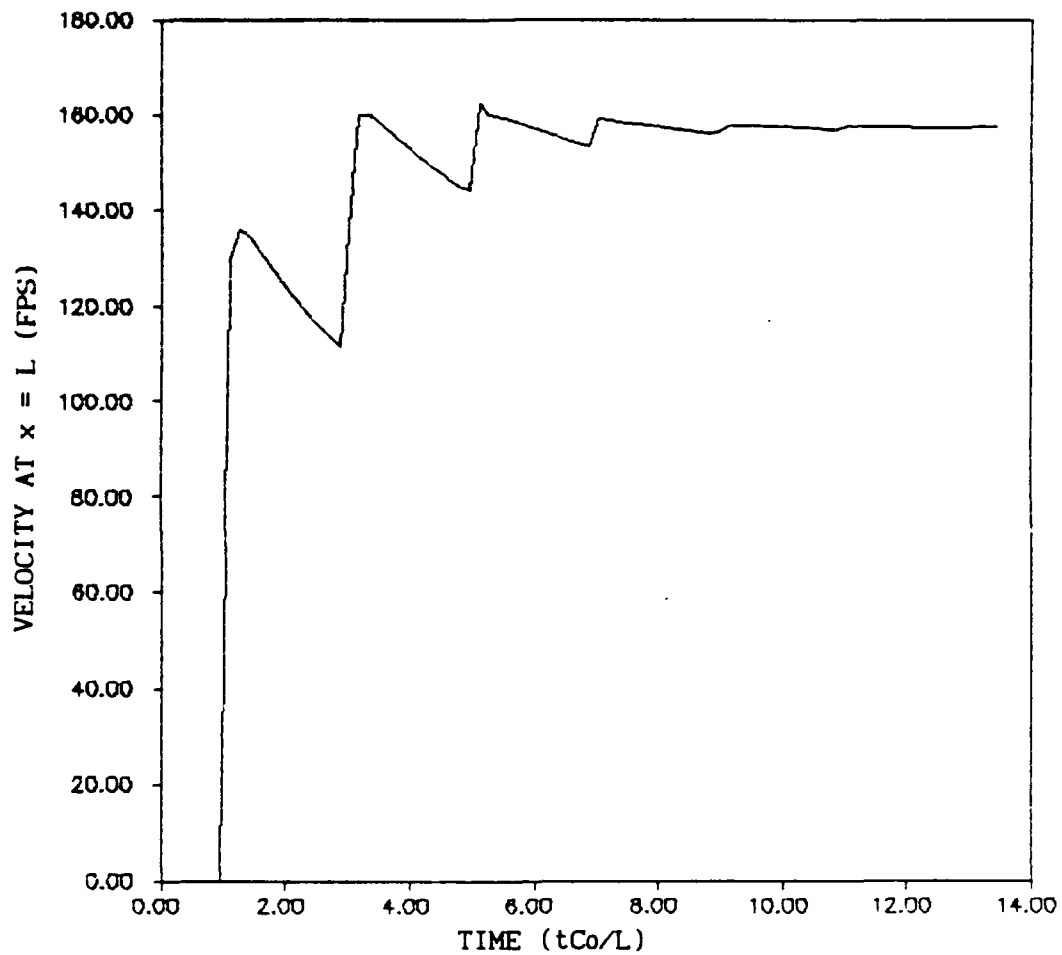


Fig. 66. Transient Velocity Response, 2.0 psi Terminated Ramp Input
in 5 ft, 0.170 in ID Open Line, Linear Results

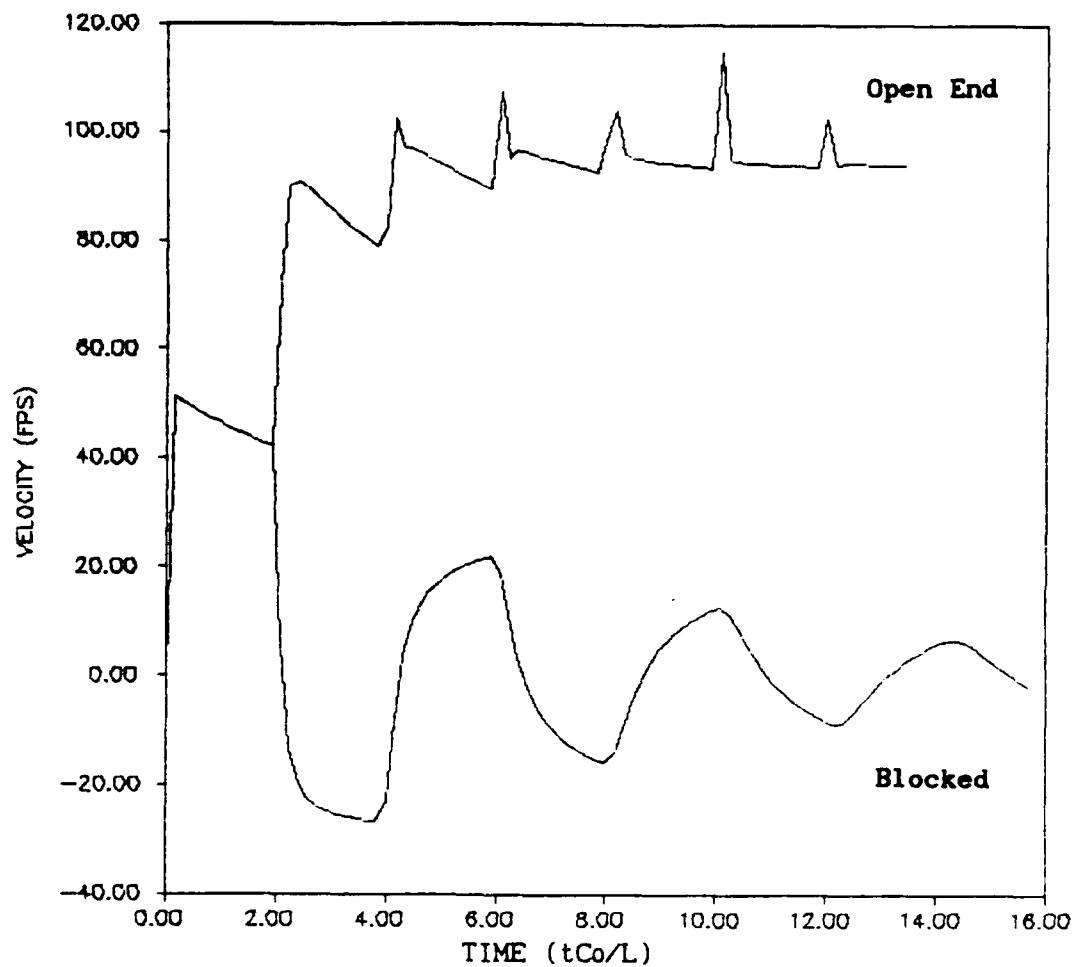


Fig. 67. Comparison of Inlet Velocity Response for Blocked and Open 5 ft, 0.170 in ID Lines, 1.0 psi Terminated Ramp, Linear Results

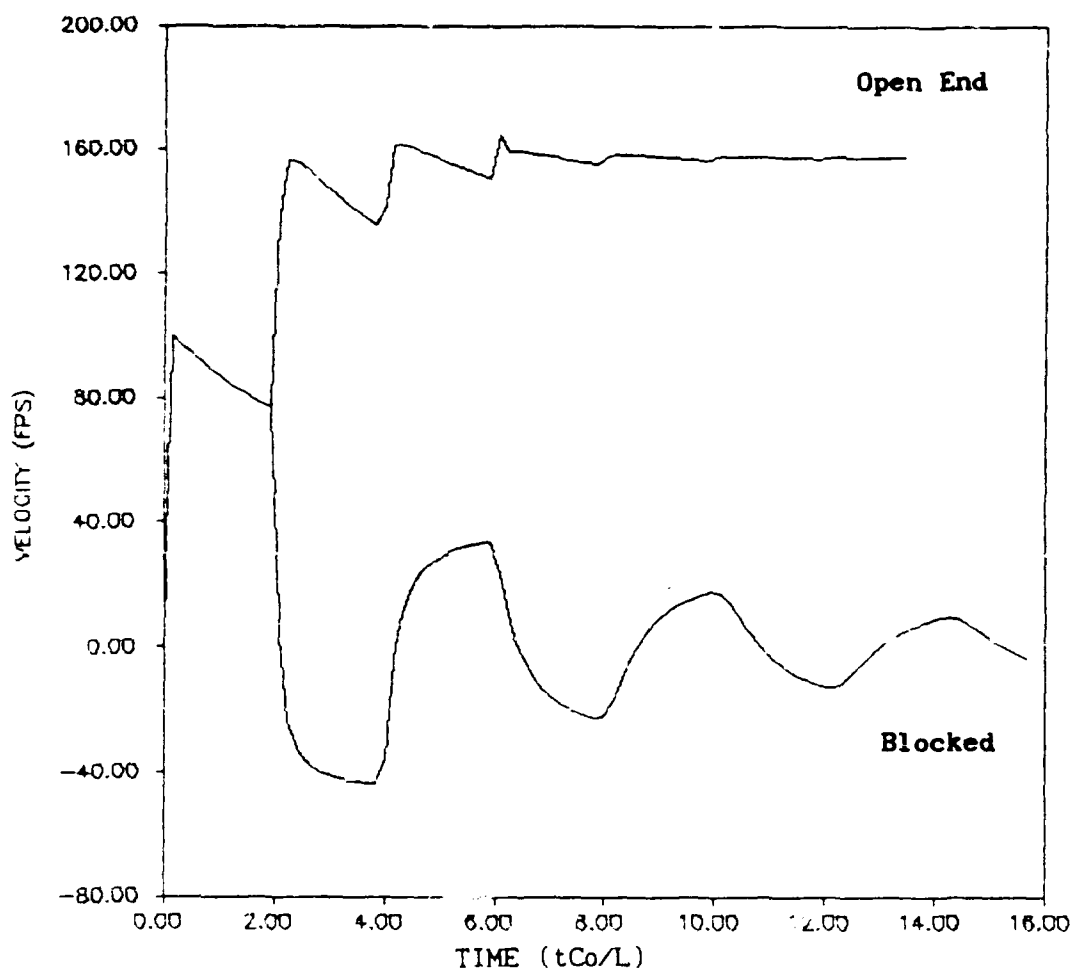
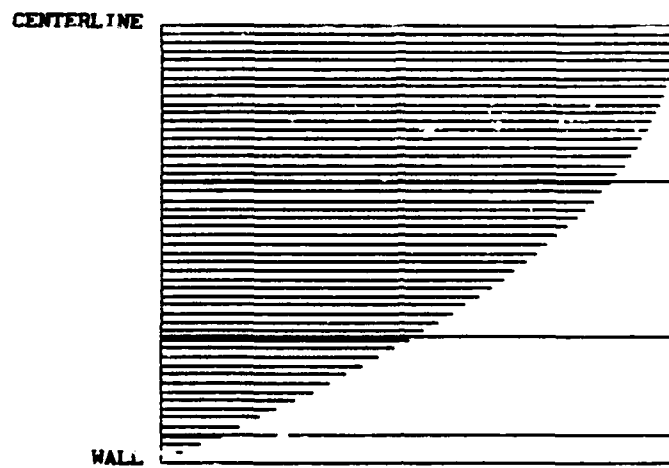


Fig. 68. Comparison of Inlet Velocity Response for Blocked and Open 5 ft, 0.170 in ID Lines, 2.0 psi Terminated Ramp, Linear

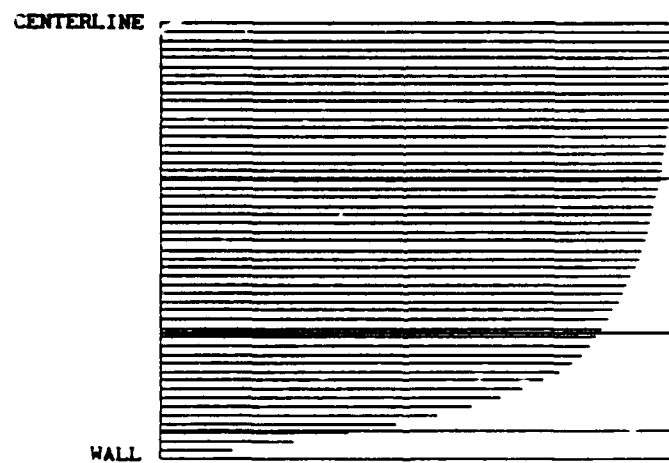
algorithm being used. The initial flow field is considered consistent with the numerical algorithm in this study if, when introduced into the algorithm with no signal present, continued iteration of the algorithm produces no significant change in the pressure, velocity, or temperature fields. The method of calculating this initial flow field was developed in Chapter III and relies on Eq (38). The initial flow field is obtained with the same friction model used in the algorithm itself. This distinction is made because empirical formulas were first used to calculate the initial flow field with very poor results.

Figure 69 shows the velocity profiles obtained for the initial flow fields with the method developed in Chapter III. Figure 69a resulted from a pressure differential of 0.20 psi while Figure 69b was produced with a 0.25 psi differential. Note that the steady-state profile for each flow regime has the correct shape. Figure 69a exhibits the parabolic shape characteristic of the steady laminar flow velocity profile. The flattened profile with a steep gradient near the wall, typical of turbulent flow, is shown in Figure 69b. These qualitative profiles are produced by specifying a constant pressure differential between the upstream and downstream ends of the transmission line. Only the piecewise continuous polynomials are used to calculate the profile. The empirical and analytic expressions commonly used to generate the steady velocity profiles were not used to obtain these profiles.

Tables 8 through 17 are presented to demonstrate the performance of the method used to generate the steady-state profiles described in Chapter III. For simplicity, only six axial grid points



a. Laminar Friction



b. Turbulent Friction

Fig. 69. Velocity Profile for Steady Flow from Piecewise Defined
Polynomials

and four flow intervals were used to produce these tables, however, this method can be used to generate a steady flow field for any number of grid points and flow intervals.

Tables 8 through 13 show the steady flow results for air in a straight, 1.0 ft long, 0.062 in ID tube. In Table 8, the dimensionless pressures at each grid point are shown with two columns of dimensionless average velocities. The tables are in terms of the dimensionless quantities described in Chapter II since this procedure was designed to provide an initial pressure and velocity field to the numerical algorithm in dimensionless terms. The pressures in psia and velocities in fps may be recovered from the tables by multiplying the dimensionless pressures by 20.538 and dimensionless velocities by 1128.6, respectively.

TABLE 8
One-Dimensional Pressures and Velocities
for Laminar Flow
($\Delta p = 0.20$ psi, $r_n = 0.011, 0.022, 0.029, 0.031$ in)

i	p	u_{av}	
		ANALYTIC	POLYNOMIAL
0	0.72402376	0.05523999	0.05524000
1	0.72208675	0.05538818	0.05538818
2	0.72014448	0.05553756	0.05553756
3	0.7181	0.05568816	0.05568817
4	0.7161	0.05584000	0.05584001
5	0.71428571	0.05599309	0.05599310

The velocities in the column labeled "analytic" were calculated using the one-dimensional compressible flow equations described in Chapter

IV. The values in the column labeled "polynomial" were calculated using the piecewise continuous polynomial method described in Chapter III. Values in the column labeled "i" denote axial location along the line with the upstream end at $i = 0$ and the downstream end at $i = 5$.

Wall shear stress values are required to begin solving for the unknown polynomial coefficients. Once these coefficients are found, the velocity profile as well as average velocities and velocity gradients can then be reconstructed. Close agreement between the analytic and polynomial results for average velocities is seen in Table 8. Comparisons of the steady laminar velocity profile and velocity gradient at each gridpoint also show close agreement. Tables 9 and 10 demonstrate the accuracy of the piecewise polynomial approximation for laminar flow at gridpoint $i = 1$.

Initial values of the averaged velocity function in each flow interval are required to begin the numerical solution of the damped wave equations. The averaged velocity function produces the average velocity of the flow in each flow interval. An example of dimensionless values of these functions for the steady flow case are shown in Table 11. Moving from left to right in each row or, physically, from the center flow interval to the wall, the decrease in the averaged velocity of each flow interval can be seen.

Varying the locations of the flow interval boundaries has no noticeable effect on the agreement between the analytic and polynomial results for laminar flow. A different choice of flow

TABLE 9

Comparison of Analytic and Polynomial Velocities
for Laminar Flow

($\Delta p = 0.20$ psi, $r_n = 0.011, 0.022, 0.029, 0.031$ in)

RADIAL LOCATION	VELOCITY	
	ANALYTIC	POLYNOMIAL
0.0000000000E+00	1.1077636000E-01	1.1077636000E-01
1.0000000000E-01	1.0966859640E-01	1.0966859640E-01
2.0000000000E-01	1.0634530560E-01	1.0634530560E-01
3.0000000000E-01	1.0080648760E-01	1.0080648760E-01
4.0000000000E-01	9.3052140429E-02	9.3052142400E-02
5.0000000000E-01	8.3082268158E-02	8.3082270000E-02
6.0000000000E-01	7.0896868687E-02	7.0896870400E-02
7.0000000000E-01	5.6495942016E-02	5.6495943600E-02
8.0000000000E-01	3.9879491717E-02	3.9879489600E-02
9.0000000000E-01	2.1047510775E-02	2.1047508400E-02
1.0000000000E+00	4.3918815251E-09	6.0450307501E-13

TABLE 10

Comparison of Velocity Gradient
for Laminar Flow

($\Delta p = 0.20$ psi, $r_n = 0.011, 0.022, 0.029, 0.031$ in)

RADIAL LOCATION	SLOPE OF RADIAL VELOCITY PROFILE	
	ANALYTIC	POLYNOMIAL
0.0000000000E+00	0.0000000000E+00	0.0000000000E+00
1.0000000000E-01	-2.2155272000E-02	-2.2155272000E-02
2.0000000000E-01	-4.4310544000E-02	-4.4310544000E-02
3.0000000000E-01	-6.6465816000E-02	-6.6465816000E-02
4.0000000000E-01	-8.8621086709E-02	-8.8621088000E-02
5.0000000000E-01	-1.1077635871E-01	-1.1077636000E-01
6.0000000000E-01	-1.3293163071E-01	-1.3293163200E-01
7.0000000000E-01	-1.5508690271E-01	-1.5508690400E-01
8.0000000000E-01	-1.7724217342E-01	-1.7724217600E-01
9.0000000000E-01	-1.9939744542E-01	-1.9939744800E-01
1.0000000000E+00	-2.2155271387E-01	-2.2155272000E-01

TABLE 11

Dimensionless Values of Averaged Velocity Functions
for Laminar Flow

($\Delta p = 0.20$ psi, $r_n = 0.011, 0.022, 0.029, 0.031$ in)

FLOW INTERVAL				
1	1	2	3	4
0	0.10352470	0.07570351	0.03431663	0.00689781
1	0.10380240	0.07590659	0.03440868	0.00691632
2	0.10408236	0.07611131	0.03450148	0.00693497
3	0.10436461	0.07631771	0.03459504	0.00695378
4	0.10464917	0.07652579	0.03468937	0.00697274
5	0.10493608	0.07673560	0.03478447	0.00699185

interval boundary locations is shown in Tables 12 and 13.

TABLE 12

Comparison of Radial Velocity Profile
for Laminar Flow

($\Delta p = 0.20$ psi, $r_n = 0.020, 0.024, 0.028, 0.031$ in)

RADIAL LOCATION	VELOCITY	
	ANALYTICAL	POLYNOMIAL
0.0000000000E+00	1.1077636000E-01	1.1077636000E-01
1.0000000000E-01	1.0966859640E-01	1.0966859640E-01
2.0000000000E-01	1.0634530560E-01	1.0634530560E-01
3.0000000000E-01	1.0080648760E-01	1.0080648760E-01
4.0000000000E-01	9.3052142400E-02	9.3052142400E-02
5.0000000000E-01	8.3082270000E-02	8.3082270000E-02
6.0000000000E-01	7.0896870400E-02	7.0896870400E-02
7.0000000000E-01	5.6495940758E-02	5.6495943600E-02
8.0000000000E-01	3.9879492587E-02	3.9879489600E-02
9.0000000000E-01	2.1047512032E-02	2.1047508400E-02
1.0000000000E+00	2.3003039473E-09	6.0450307501E-13

TABLE 13

Comparison of Radial Velocity Profile
for Laminar Flow

($\Delta p = 0.20$ psi, $r_n = 0.020, 0.024, 0.028, 0.031$ in)

RADIAL LOCATION	SLOPE OF RADIAL VELOCITY PROFILE	
	ANALYTIC	POLYNOMIAL
0.000000000E+00	0.000000000E+00	0.000000000E+00
1.000000000E-01	-2.215527200E-02	-2.215527200E-02
2.000000000E-01	-4.431054400E-02	-4.431054400E-02
3.000000000E-01	-6.646581600E-02	-6.646581600E-02
4.000000000E-01	-8.862108800E-02	-8.862108800E-02
5.000000000E-01	-1.107763600E-01	-1.107763600E-01
6.000000000E-01	-1.329316320E-01	-1.329316320E-01
7.000000000E-01	-1.550868952E-01	-1.550869040E-01
8.000000000E-01	-1.772421695E-01	-1.772421760E-01
9.000000000E-01	-1.993974415E-01	-1.993974480E-01
1.000000000E+00	-2.215527158E-01	-2.215527200E-01

Several other sets of flow interval locations as well as additional numbers of flow intervals were run with the same close agreement between analytical and polynomial results as shown above.

The steady flow results shown above result from a pressure differential of 0.20 psi across the ends of the tube. At this pressure differential, the Reynolds number based on diameter indicates laminar flow. When the pressure differential is raised to 0.25, turbulent flow is predicted. Calculation of the velocity profile is no longer as straightforward as it is with laminar flow. Agreement of the analytical and polynomial average velocities is not nearly as good as it is in laminar flow. Analytical and polynomial average velocities are shown in Tables 14 through 16. As the pressure differential is increased, the agreement becomes better. It is also possible to improve the agreement at any pressure differential by adjusting the

TABLE 14
One-Dimensional Pressures and Velocities
for Turbulent Flow

($\Delta p = 0.25$ psi, $r_n = 0.011, 0.022, 0.029, 0.031$ in)

i	p	AVERAGE VELOCITY	
		ANALYTIC	POLYNOMIAL
0	0.72645827	0.06876869	0.03337146
1	0.72404035	0.06899834	0.03349131
2	0.72161422	0.06923032	0.03360368
3	0.71917980	0.06946467	0.03371719
4	0.71673699	0.06970142	0.03383187
5	0.71428571	0.06994062	0.03395680

TABLE 15
One-Dimensional Pressures and Velocities
for Turbulent Flow

($\Delta p = 0.50$ psi, $r_n = 0.011, 0.022, 0.029, 0.031$ in)

i	p	AVERAGE VELOCITY	
		ANALYTIC	POLYNOMIAL
0	0.73863083	0.07282066	0.05648626
1	0.73382741	0.07329732	0.05689787
2	0.72899186	0.07378352	0.05727394
3	0.72412351	0.07427957	0.05765761
4	0.71922170	0.07478582	0.05804913
5	0.71428571	0.07530262	0.05849654

TABLE 16
One-Dimensional Pressures and Velocities
for Turbulent Flow

($\Delta p = 1.0$ psi, $r_n = 0.011, 0.022, 0.029, 0.031$ in)

i	p	AVERAGE VELOCITY	
		ANALYTIC	POLYNOMIAL
0	0.76297595	0.10707231	0.09229894
1	0.75349819	0.10841910	0.09365498
2	0.74389560	0.10981863	0.09484924
3	0.73416304	0.11127446	0.09609093
4	0.72429504	0.11279050	0.09738332
5	0.71428571	0.11437104	0.09898636

locations of the flow interval boundaries. One possible reason for disagreement between polynomial and analytic results for turbulent flow is the nature of the turbulent friction model and not the method of determining the steady velocities. The algebraic turbulence model is qualitatively good since it produces the correct profile shapes. However, a different turbulent friction model may be required to produce results consistent with the average velocities produced by the one-dimensional empirical equations for steady-flow. No work to accomplish this has been yet been done.

Table 17 is analogous to Table 11 except the flow is turbulent. Comparison of the these two tables shows the turbulent profile contained in Table 17 is, as would be expected, much flatter near the center of the line than the laminar profile shown in Table 11.

TABLE 17

Values of Averaged Velocity Functions
for Turbulent Flow

($\Delta p = 0.25$ psi, $r_n = 0.011, 0.022, 0.029, 0.031$ in)

FLOW INTERVAL				
1	1	2	3	4
0	0.04493990	0.04132258	0.02980270	0.00827153
1	0.04510187	0.04147166	0.02990921	0.00830020
2	0.04525317	0.04161079	0.03000957	0.00832807
3	0.04540602	0.04175133	0.03011096	0.00835623
4	0.04556043	0.04189331	0.03021338	0.00838468
5	0.04572928	0.04204873	0.03032440	0.00841455

The figures and tables discussed above were all for compressible flow; however, the routine used is easily modified for incompressible flow. An initial flow field was generated for a 1.0 in ID rigid line filled with oil in order to gauge the performance of the numerical algorithm combined with the steady flow initialization process. Parameters used for this system are shown in Table 18. Figure 70 shows the transient response of the system for sudden closure of a valve at the downstream end of the rigid line with the oil initially flowing at 0.42 fps. The initial velocity field was obtained using the piecewise defined polynomials described in Chapter III. At this velocity, the Reynolds number is much less than 2300 indicating the initial flow is laminar. The oil is treated as an incompressible fluid with a constant sonic velocity. The fluid velocity is less than 1.0×10^{-6} percent of the sonic velocity. As a result, both the linear and nonlinear numerical algorithm produce the same result since the magnitude of the

Table 18
Oil Filled Line

Fluid Properties	Line Characteristics
$\mu = 0.04508 \frac{\text{lb}_m}{\text{ft sec}}$	$L = 118.375 \text{ ft}$
$\rho = 57.43 \frac{\text{lb}_m}{\text{ft}^3}$	$D = 1.0 \text{ in}$
$T = 530^{\circ} \text{ R}$	$M = 4$
$c = 4232.3 \frac{\text{ft}}{\text{sec}}$	$r_1 = 0.18 \text{ in}$
	$r_2 = 0.25 \text{ in}$
	$r_3 = 0.34 \text{ in}$
	$r_4 = 0.50 \text{ in}$
$u_{av_0} = 0.42 \frac{\text{ft}}{\text{sec}}$	Gridpoints 100

error terms in the modified equation Eq (4.39) is small. Data points from a paper by Zielke (82:114) are shown in the figure for comparison. The data points agree well with the results produced with either algorithm. Results from the linear algorithm are shown in Figure 70. It is important to note that the finite-difference model was not "tuned" to fit the data. The damped-wave equations and numerical algorithm resulted from straightforward manipulation of the basic fluid dynamic equations and polynomial approximations. The use of the piecewise continuous polynomials in conjunction with the damped-wave equations appears to accurately represent this system.

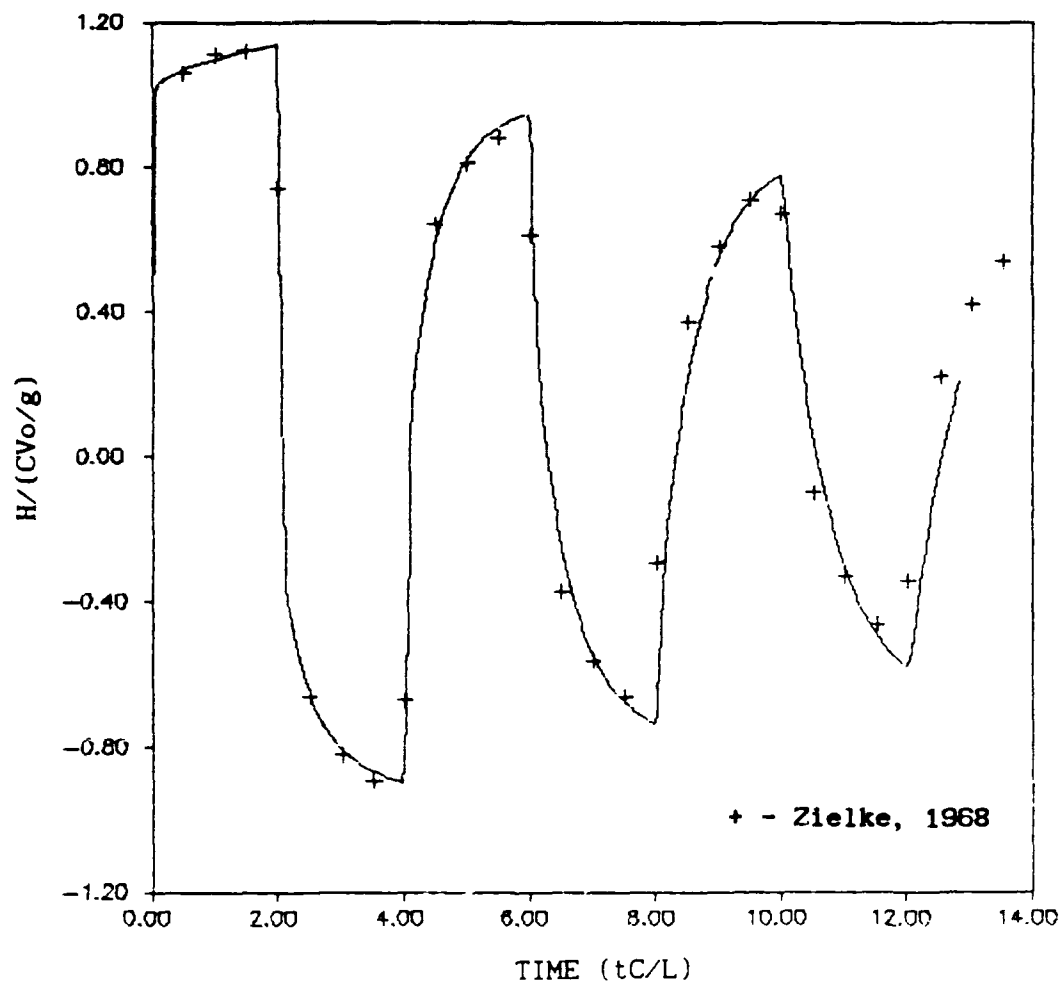


Fig. 70. Response of Oil-Filled Line with 0.42 fps Flow Velocity to Sudden Closure of Upstream Valve

Results Using Modal Superposition

The results presented for finite length lines were obtained from the finite-difference solution of the damped wave equations developed in Chapter II. The comparison of these results with data is good but modest computer resources were required. Additionally, the numerical algorithm used to solve the damped-wave equations is not compatible with the time domain methods commonly used to analyze and design control systems. A second type of transmission-line model which provides a reasonably accurate approximation to the solutions of the linearized damped-wave equations was developed in Chapter V.

The transient responses shown in Figure 54 and in Figures 58 through 68 exhibit periodic characteristics related to the physical characteristics of the fluid transmission line. The spikes in Figure 65 and 66 are separated by approximately 2.0 dimensionless time units throughout the response. The peaks of Figure 54 are separated by approximately 4.0 dimensionless time units as the curve decays. This periodic behavior suggests natural frequencies and time constants characteristic of the line. A model based on the modal superposition method should provide a good basis for the approximation of the finite-difference solutions.

The transient response for the blocked, 5 ft, 0.170 in ID transmission line filled with air is shown in Figure 71. Steady-state values for the L, R, and C modal parameters, as developed by Lebrun (40:459), were used here. The modal superposition results exhibit the periodic behavior shown by the linear finite-difference results for the same transmission line configuration used in Figure 54. However, the

period of the modal superposition results is noticeably different from the period of the finite-difference results. The waveform and the damping also differ significantly between the two models.

When unsteady values of L , R , and C are calculated and used with the modal superposition method described in Chapter V, the result greatly improves as shown in Figure 72. The diamonds represent modal superposition results while the solid line represents the finite-difference solution with laminar friction and no heat transfer. The conductance G was set to zero in Figure 72, however, when values for G are calculated as described in Chapter V, the response shown in Figure 73 results. The modal superposition result, shown by the triangles, closely follows the finite-difference result although the peaks are flatter and of somewhat smaller amplitude than in the finite-difference results. The majority of the information contained in the waveform produced by the finite-difference solution is contained in the waveform produced by the modal superposition. It is important to note that, like the development of the finite-difference model, modal superposition and all parameters used are based on straightforward mathematical manipulation of the equations of fluid dynamics. No parameters have been adjusted to fit the modal results to the finite-difference results. The modal superposition requires significantly less computer resources than does the solution of the finite-difference model. The two modal superposition solutions are compared in Figure 74. The importance of the parameter G to the modal solution can clearly be seen.

The number of modes retained using modal superposition directly affects the quality of the solution. The minimum number of modes

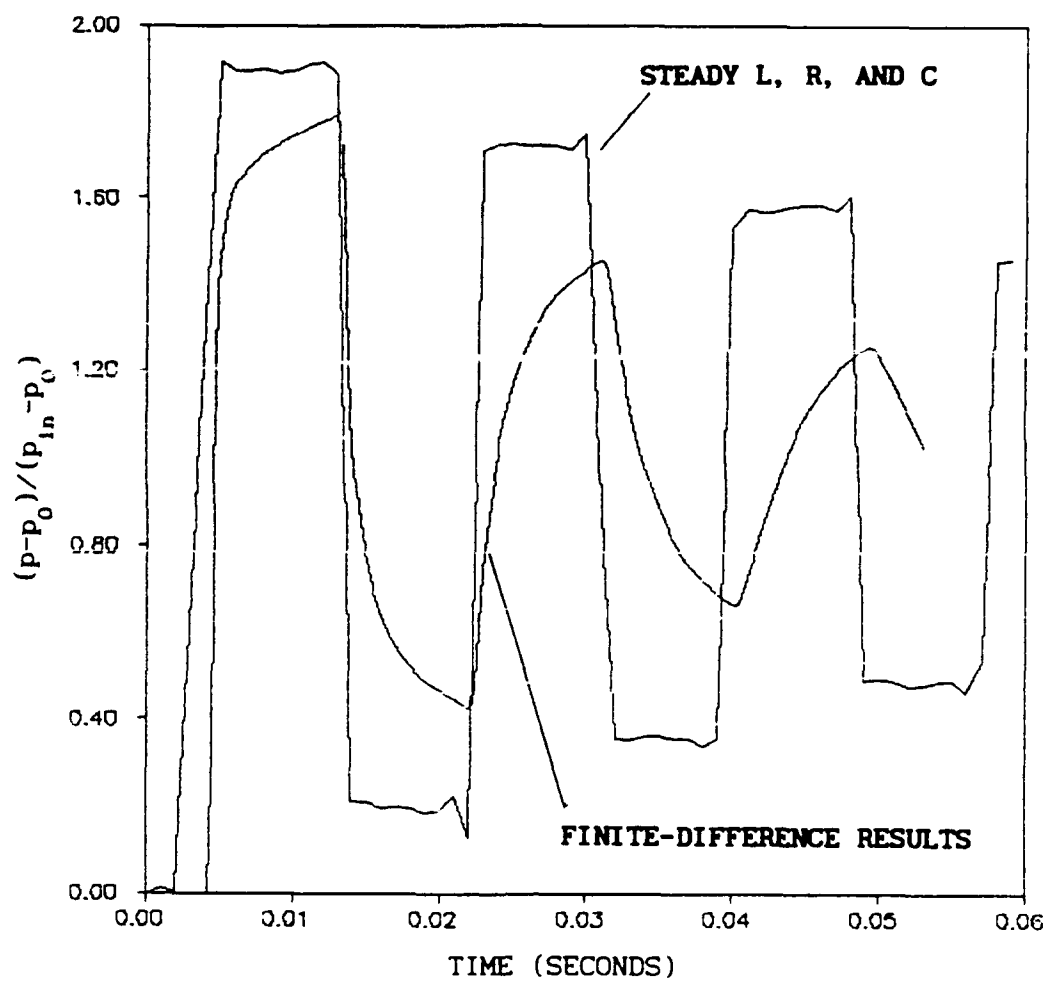


Fig. 71. 1.0 psi Terminated Ramp Input in 5 ft, 0.170 in ID Blocked Line, Modal Superposition Results

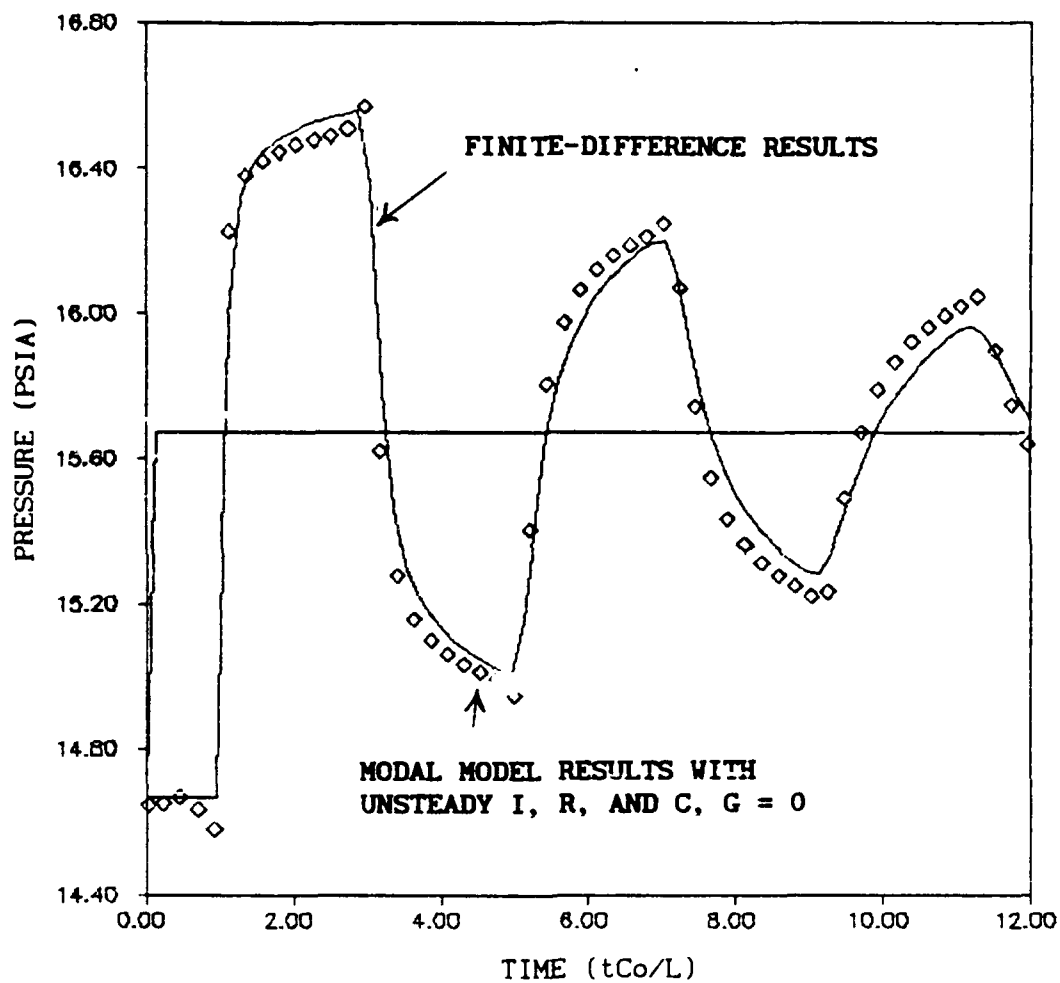


Fig. 72. 1.0 psi Terminated Ramp Input in 5 ft, 0.170 in ID Blocked Line, Modal Superposition Results

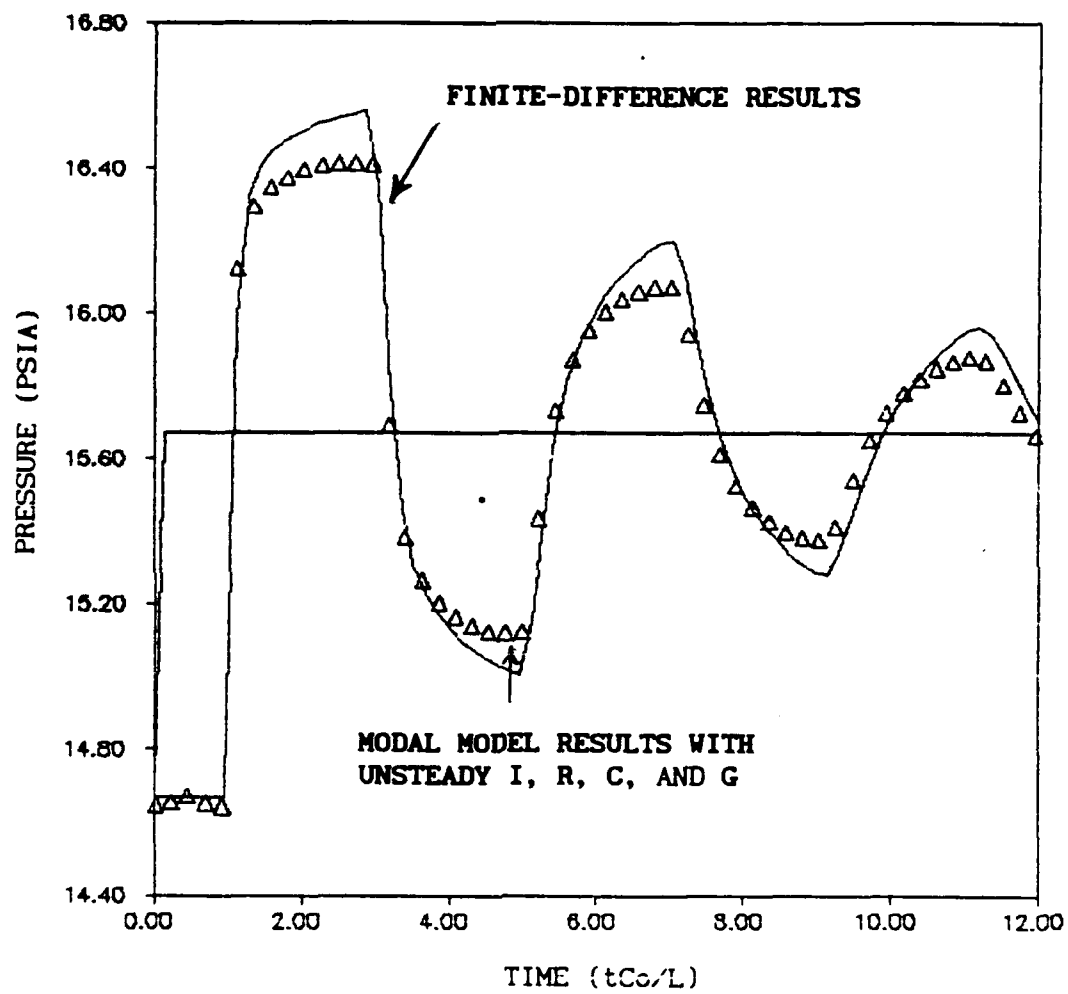


Fig. 73. 1.0 psi Terminated Ramp Input in 5 ft, 0.170 in ID Blocked Line, Modal Superposition Results

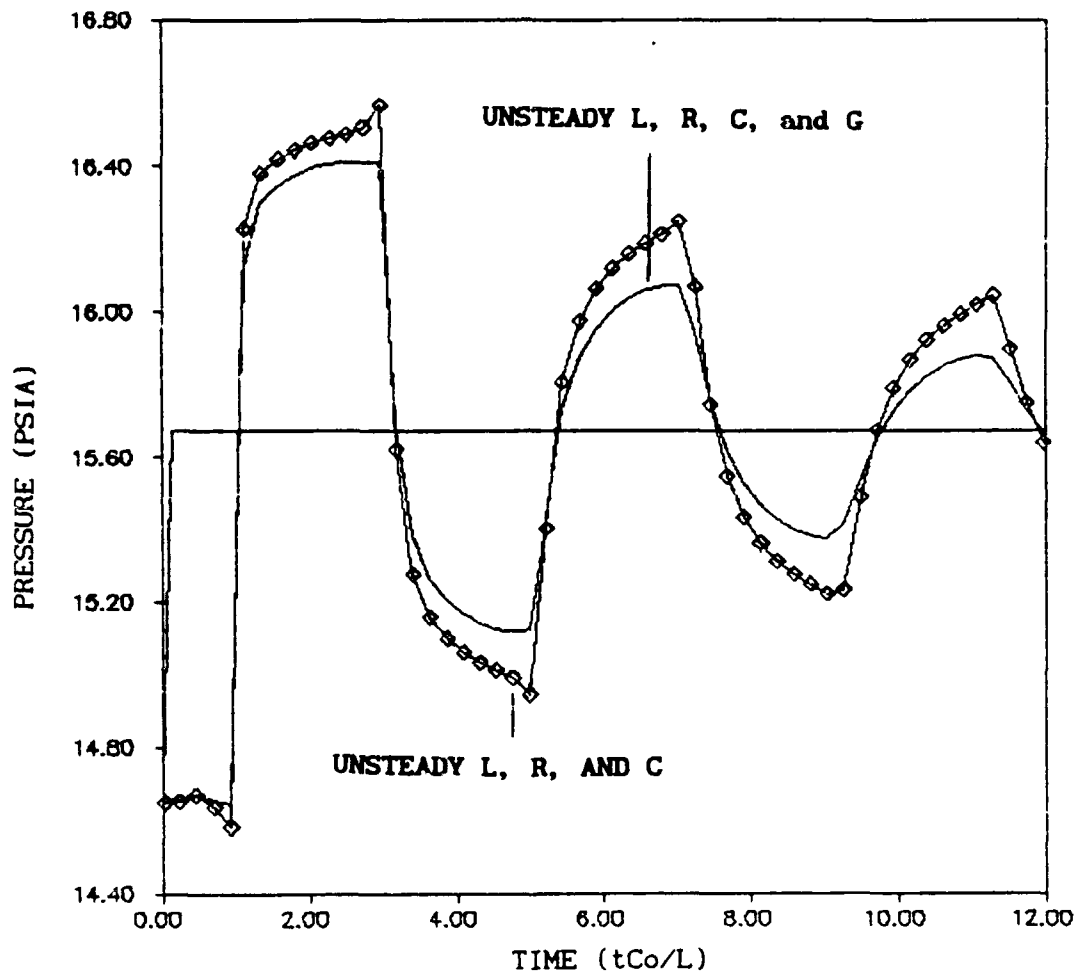


Fig. 74. 1.0 psi Terminated Ramp Input in 5 ft, 0.170 in ID Blocked Line, Comparison of Modal Superposition Results

required for a desired solution accuracy should be retained to minimize computer resource requirements. The results shown in Figure 75 were obtained with only 6 modes. The low quality of the solution is evident in the fluctuations preceding the first peak of the response. As time progresses, the highest frequency modes are attenuated and become increasingly less important in the solution. Figures 76, 77, and 78 involve 10, 15, and 20 modes respectively. The quality of the solution increases noticeably with the additional modes. In this case, retaining more than 20 modes produced a negligible increase in quality. The modal superposition result in Figure 78 compares very well with data obtained by Karam and Leonard (30:501) for the same system.

For the case of the 5 ft blocked line examined above, the modal superposition results compare very well with the finite-difference results. Modal superposition must also produce good results for other terminations if it is to be as flexible as the finite-difference model. Figure 79 shows the modal superposition result for a volume terminated line. The modal superposition result tracks the finite difference result quite closely. The modal superposition result contains the inflection at the first peak exhibited by the finite-difference solution. Although the pressure response curve is fairly smooth, the velocity responses at the inlet of the line, shown in Figure 80, and at the entrance into the volume, shown in Figure 81, contain several peaks and valleys. Every inflection and peak contained in the finite-difference solution is tracked by modal superposition in both figures.

Figure 82 compares the response of a branched system also studied by Karam and Leonard (30:501). The system consists of a 5 ft, 0.170 in

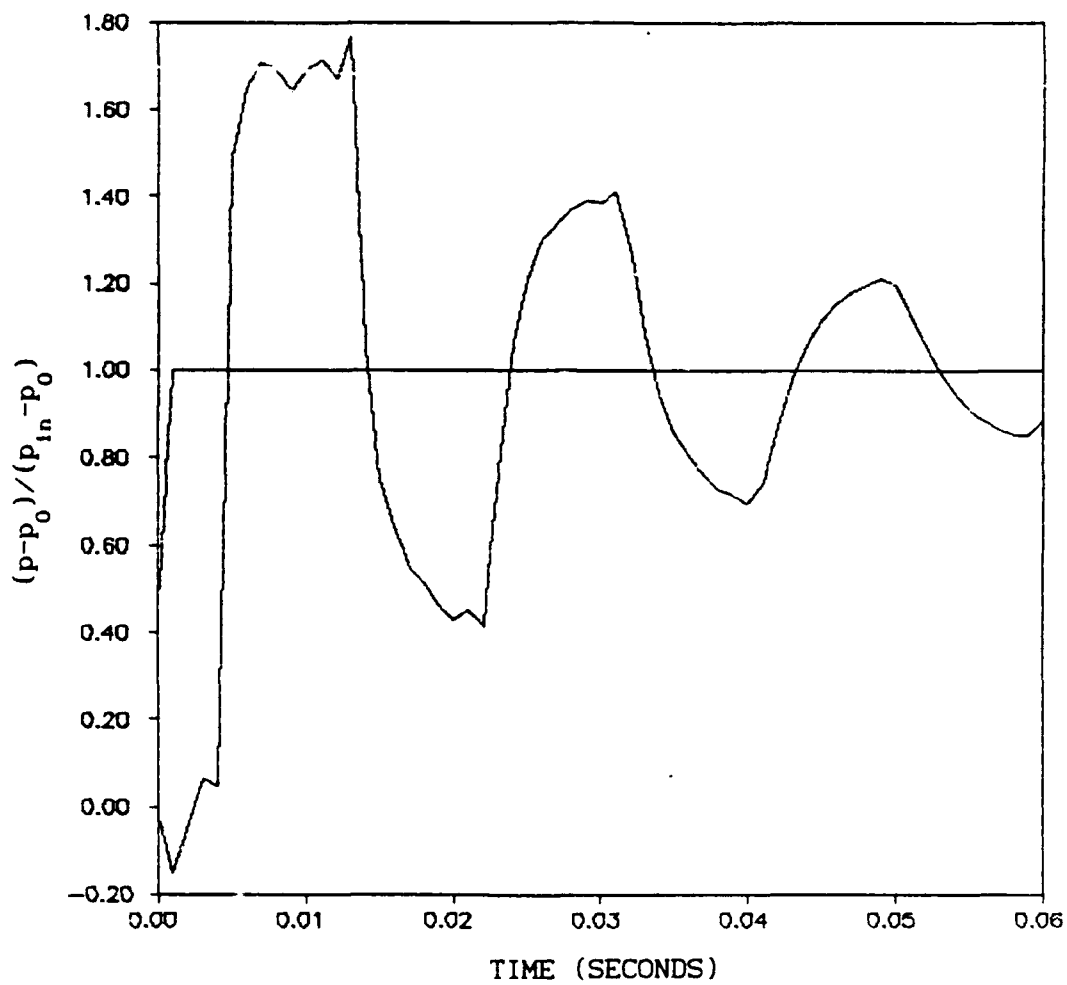


Fig. 75. 1.0 psi Terminated Ramp Input in 5 ft, 0.170 in ID Blocked Line, Modal Superposition Results for 6 Modes

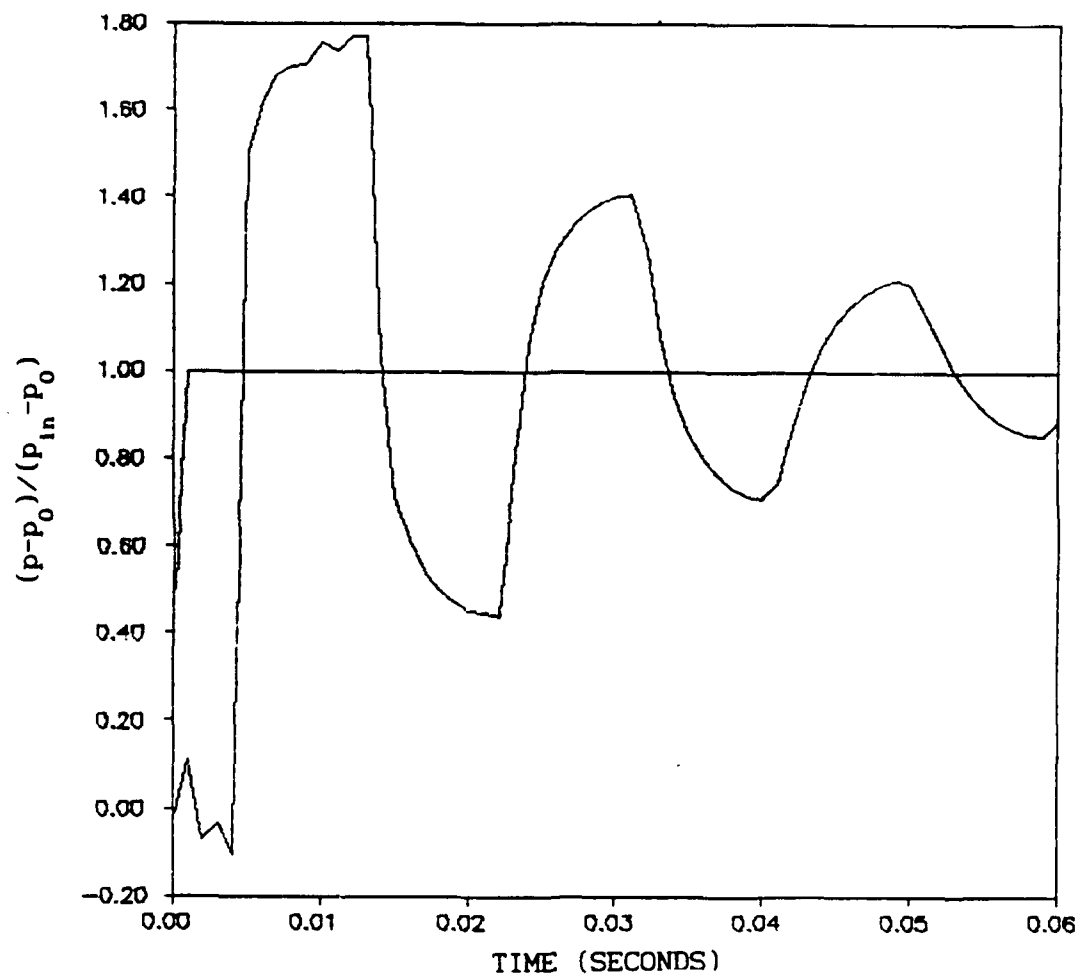


Fig. 76. 1.0 psi Terminated Ramp Input in 5 ft, 0.170 in ID Blocked Line, Modal Superposition Results for 10 Modes

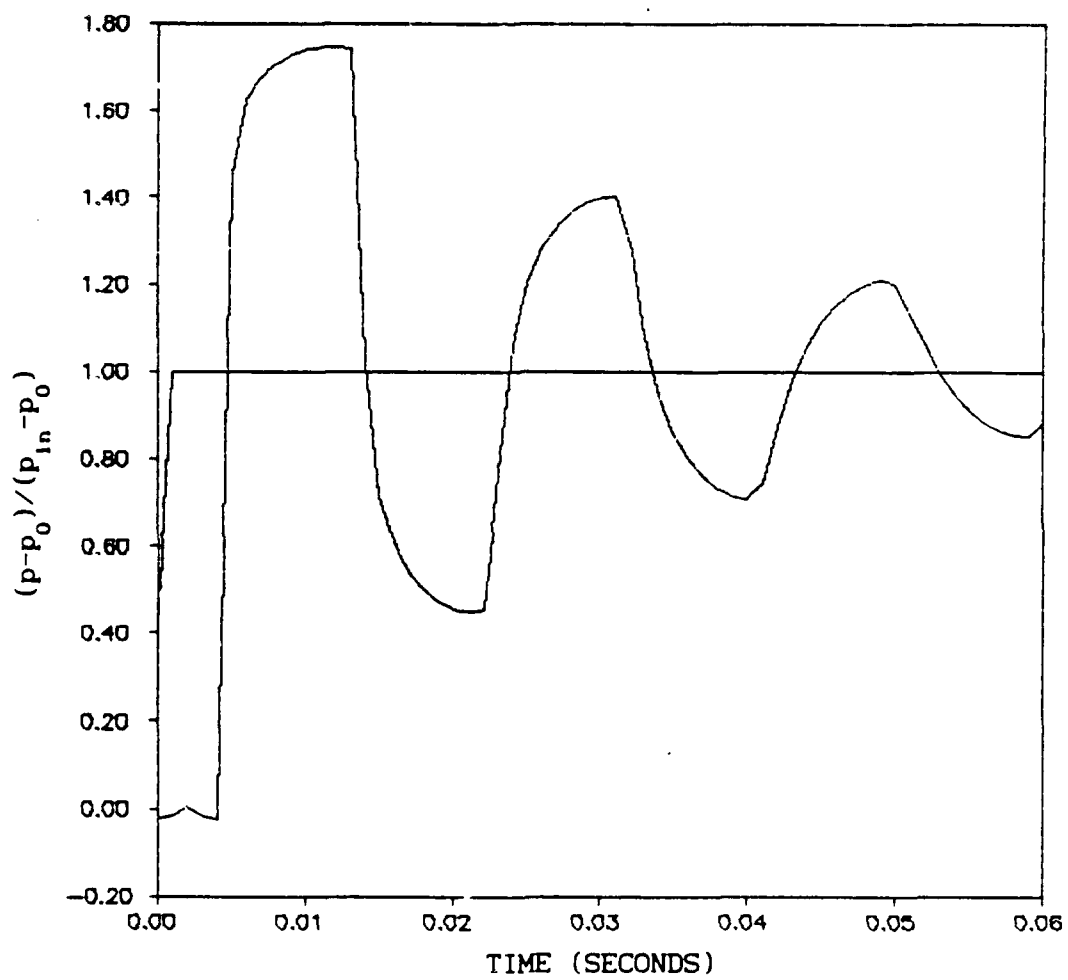


Fig. 77. 1.0 psi Terminated Ramp Input in 5 ft, 0.170 in ID
Blocked Line, Modal Superposition Results for 15 Modes

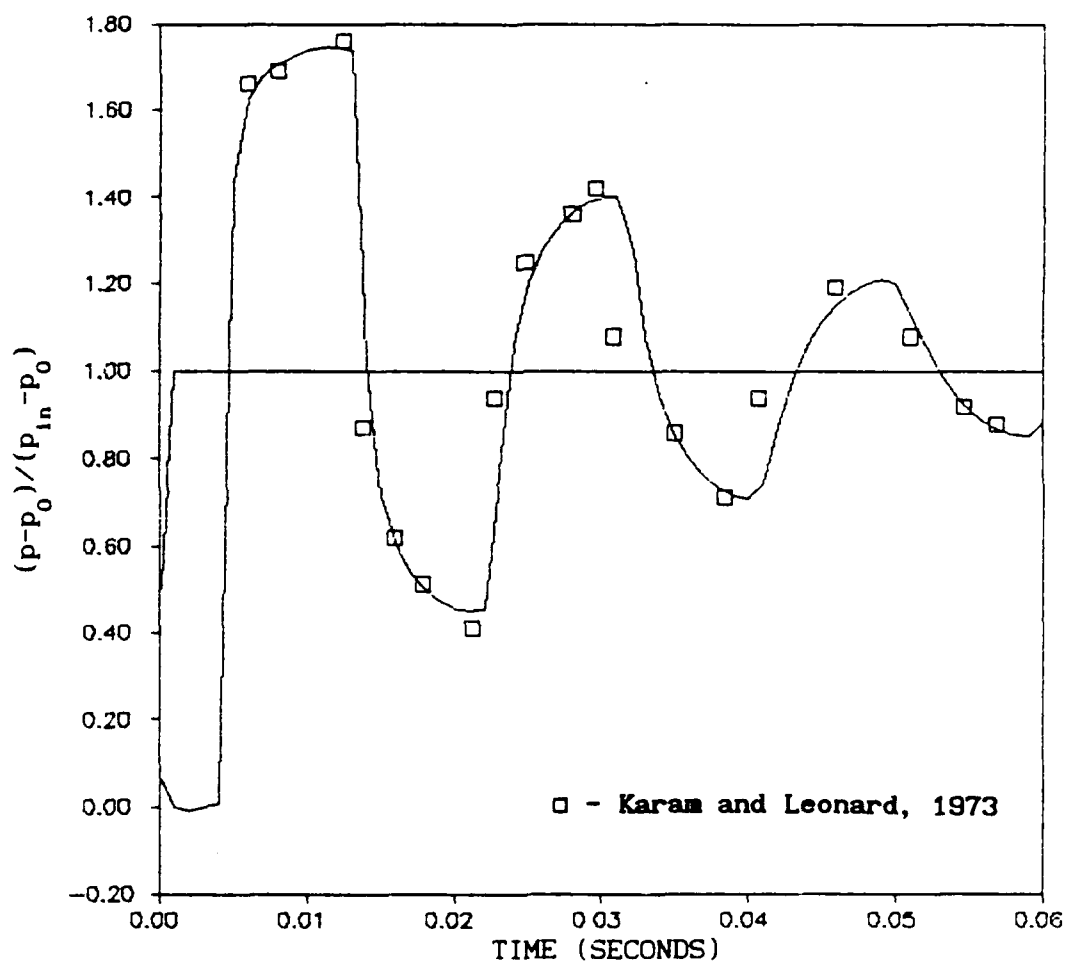


Fig. 78. 1.0 psi Terminated Ramp Input in 5 ft, 0.170 in ID Blocked Line, Modal Superposition Results for 20 Modes

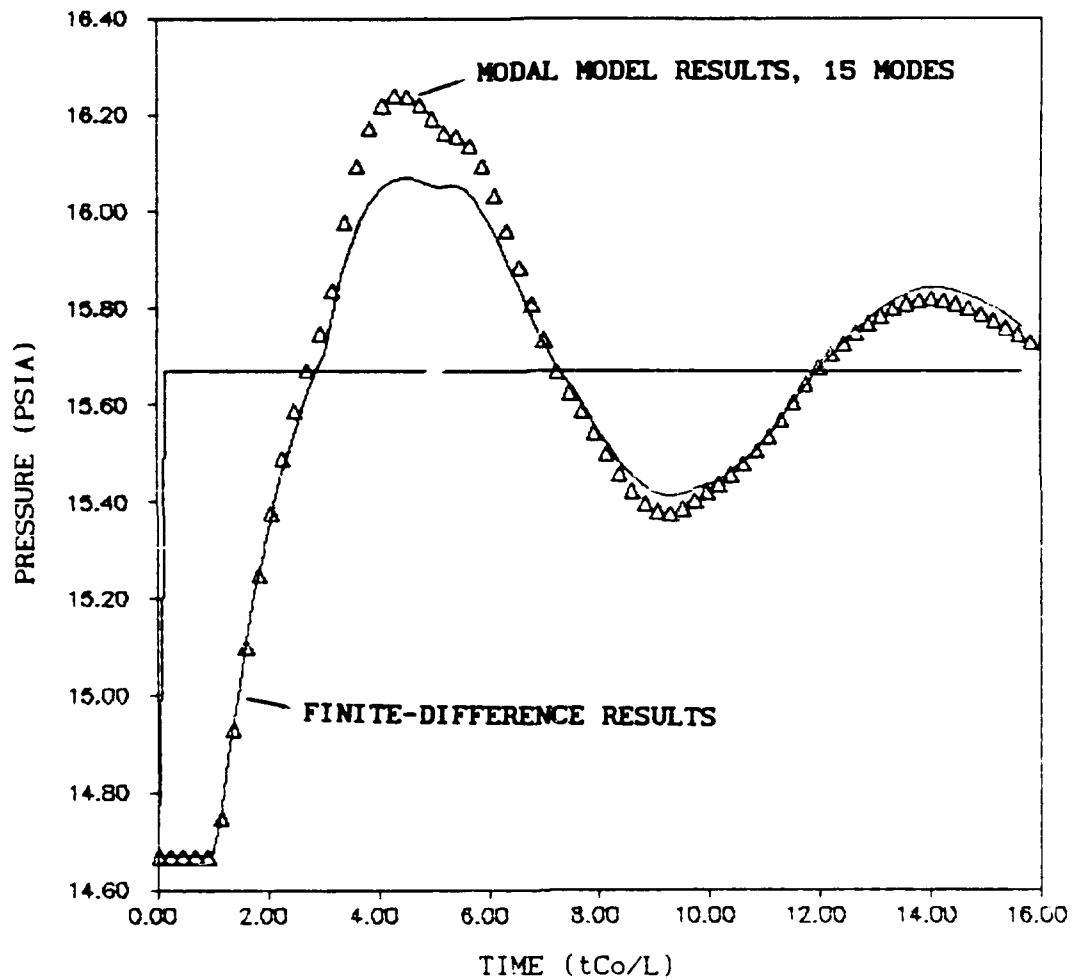


Fig. 79. Transient Response at Exit to Volume, 1.0 psi Terminated Ramp Input in 5 ft, 0.170 in ID Volume Terminated Line, $V_c = V_L$

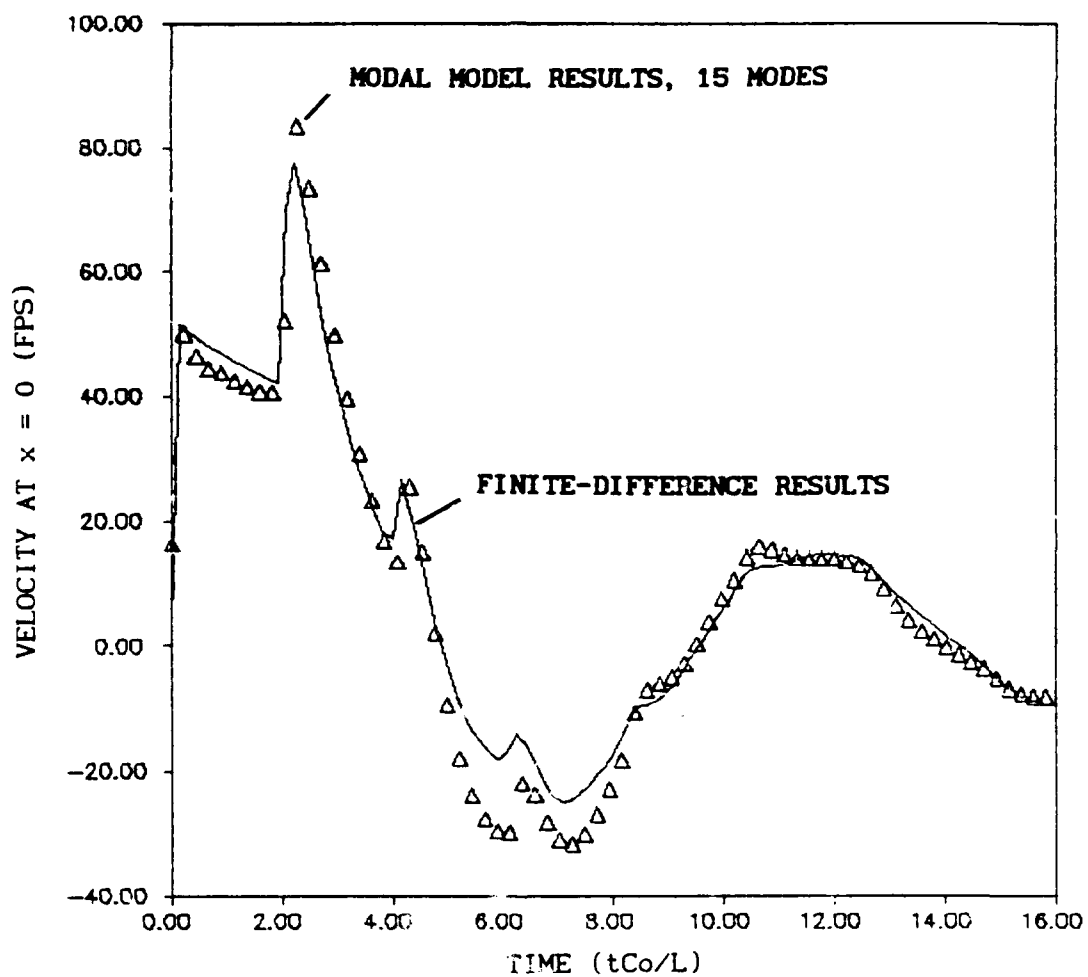


Fig. 80. Transient Velocity Response at Line Inlet, 1.0 psi
Terminated Ramp Input in 5 ft, 0.170 in ID Volume Terminated Line,

$$V_C = V_L$$

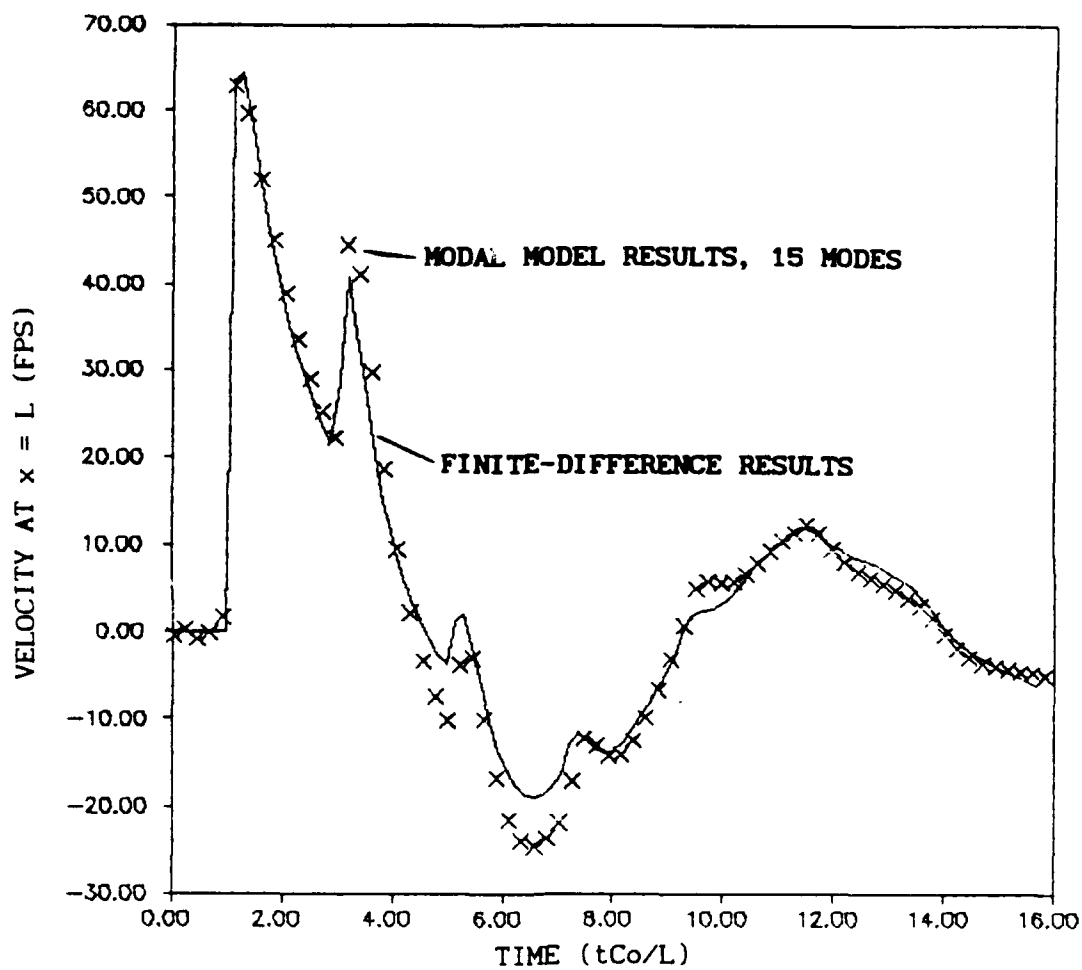


Fig. 81. Transient Velocity Response at Line Exit to Volume, 1.0 psi
Terminated Ramp Input in 5 ft, 0.170 in ID Volume Terminated Line.

$$V_C = V_L$$

ID and a 5 ft 0.25 in ID line, both blocked, branching from another 5 ft, 0.170 in ID line. The response at the blocked end of the 0.25 in I.D. line is shown in the figure with data points from the paper by Karam and Leonard. The modal superposition results were calculated using a separate modal superposition model and a separate matrix of the parameters I, R, G, and C, for each of the three lines. Comparison with the data points is good. Model instability was experienced when the inputs and outputs from each line model were directly coupled. Instability occurs because the trunk line model excites each branch model at its modal frequencies since all three lines are of the same length. This instability was eliminated by coupling the models through a volume equal to one-half of the internal volume of the 5 ft, 0.170 in ID line. Each of the three lines has approximately the same modal frequencies. Several values of coupling volume were tried with virtually identical results. Coupling volumes smaller than one half of the trunk line volume produced instability.

The results for a single 5 ft open line with a 1.0 psi and a 0.25 psi step input are shown in Figures 83 through 86. As in the finite-difference results, the solution "ratchets" up to approach a steady state. Figures 83 and 84 show the 1.0 psi step input. The modal superposition model follows the finite-difference model very closely at first but diverges significantly at later times. The comparison between the modal superposition result and the finite-difference result is much better in Figures 85 and 86 where a 0.25 psi terminated ramp input signal is applied. The large discrepancy in Figures 84 and 85 results from the use of the turbulent friction model in the finite-difference model. The values of I, R, G,

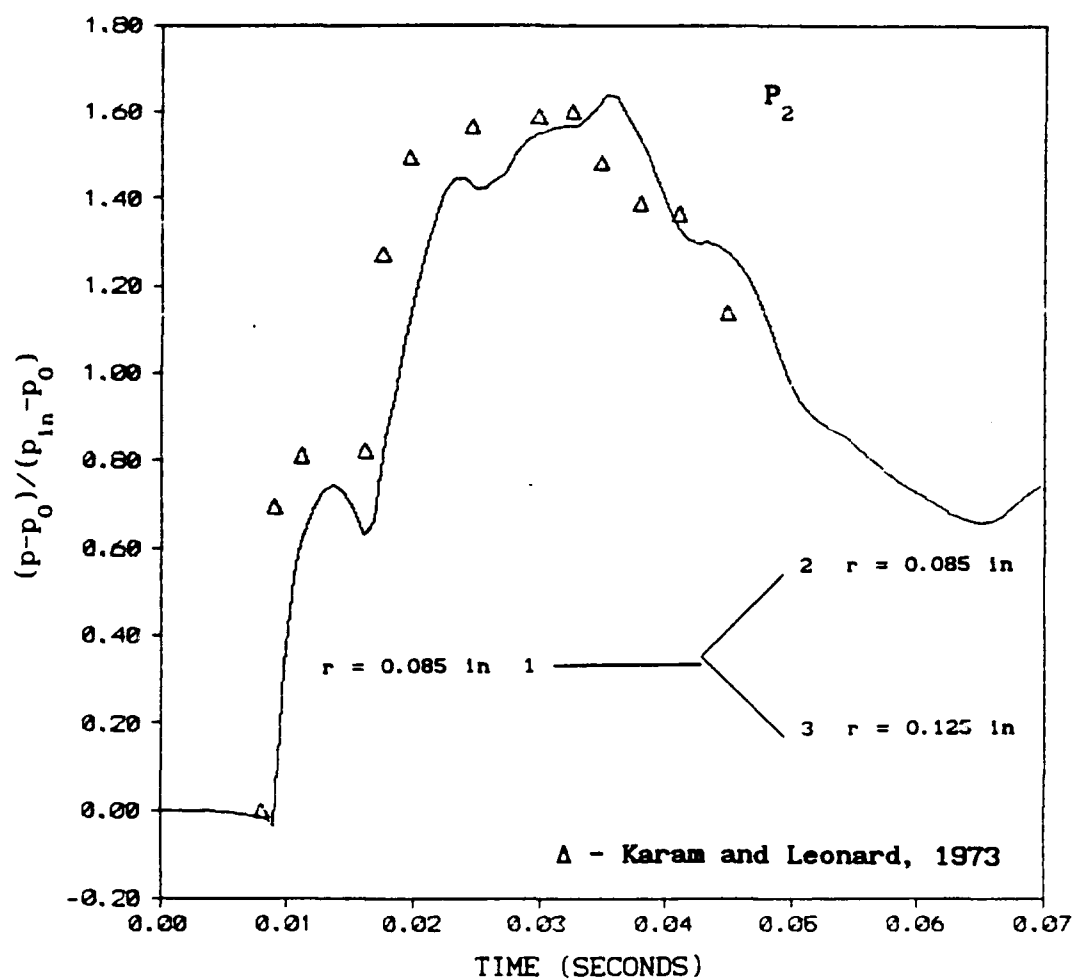


Fig. 82. Transient Response in One Leg of Branched Line, 1.0 psi
Terminated Ramp Input in 5 ft, 0.170 in ID, Blocked Branches, Line 2

and C used in the modal superposition model were calculated using laminar friction only. No method of determining values for these parameters for unsteady turbulent friction has yet been developed for this application. As stated earlier, methods have been developed to incorporate turbulent friction resulting from an established mean turbulent flow into these parameters when determining frequency response. Modal superposition, however, requires a method to account for the unsteady effects of transition to turbulence in an initially undisturbed flow for a signal of arbitrary shape. This poses a difficult problem.

The results from modal superposition demonstrate a capability to accurately predict the linear transient response for laminar flow. Much more work is required to give the modal superposition model the ability to track the nonlinear finite-difference results, as well as account for effects due to unsteady turbulent flow. Modal superposition, although only strictly valid for linear systems, has been modified to model nonlinear transient responses in support cable systems (47). Methods used in these cable models may be applicable to transmission lines.

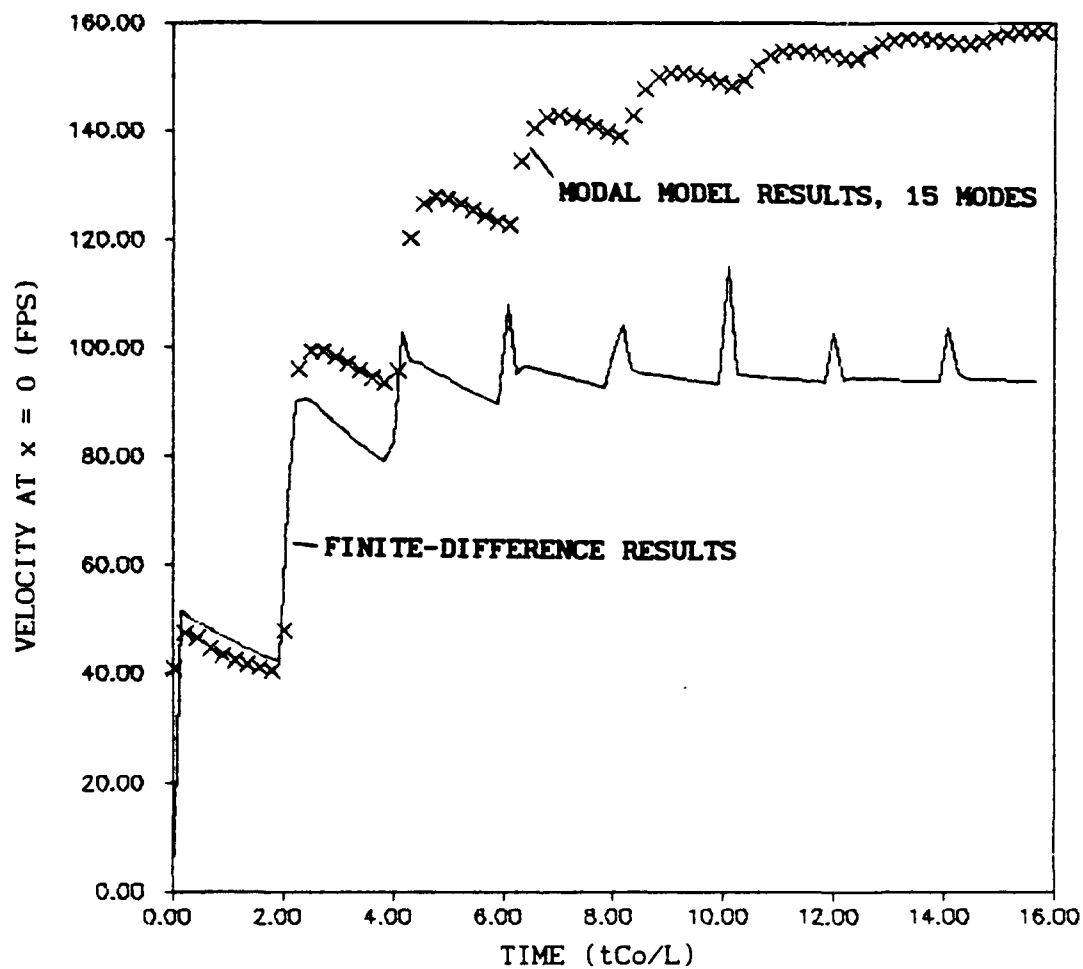


Fig. 83. Transient Velocity Response at Line Inlet, 1.0 psi
Terminated Ramp Input in 5 ft, 0.170 in ID Open Line

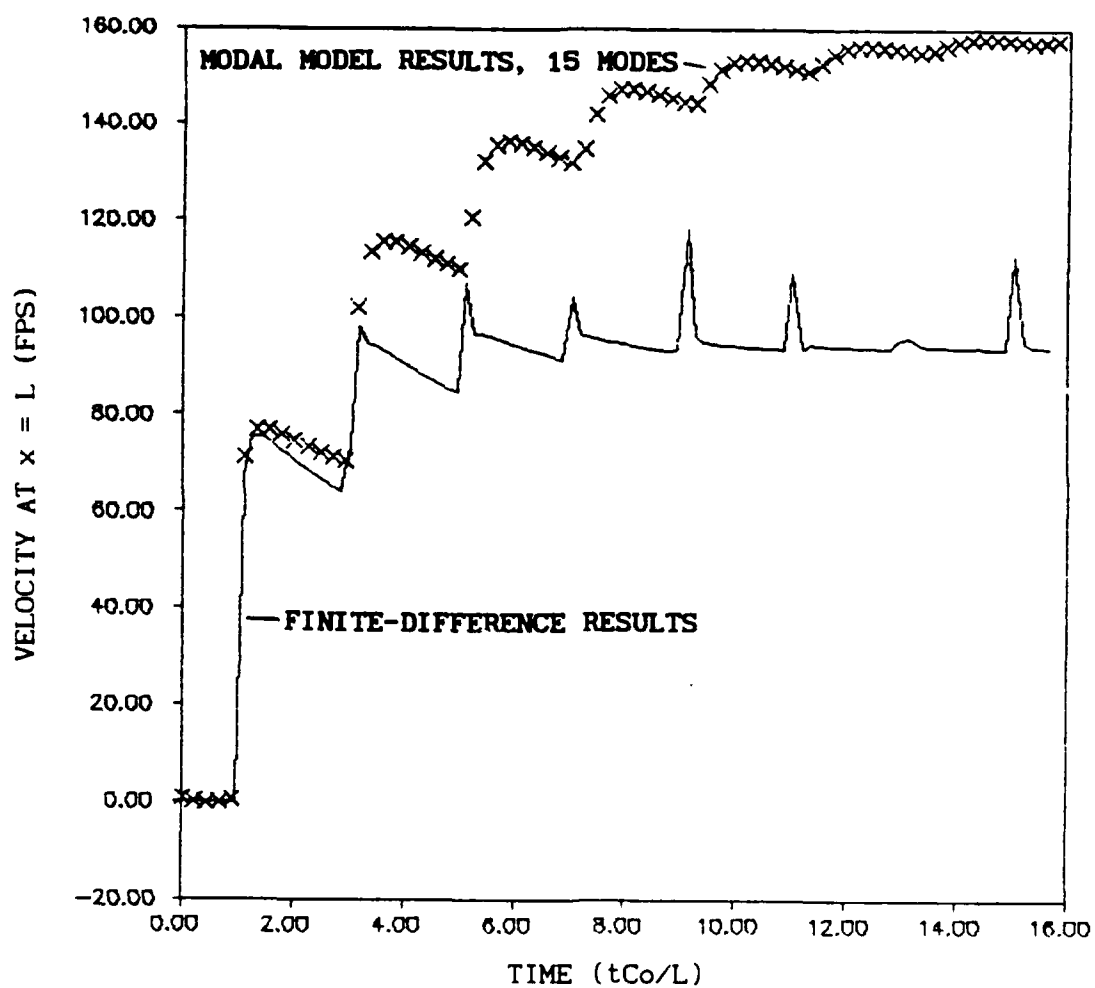


Fig. 84. Transient Velocity Response at Line Exit, 1.0 psi
Terminated Ramp Input in 5 ft, 0.170 in ID Open Line

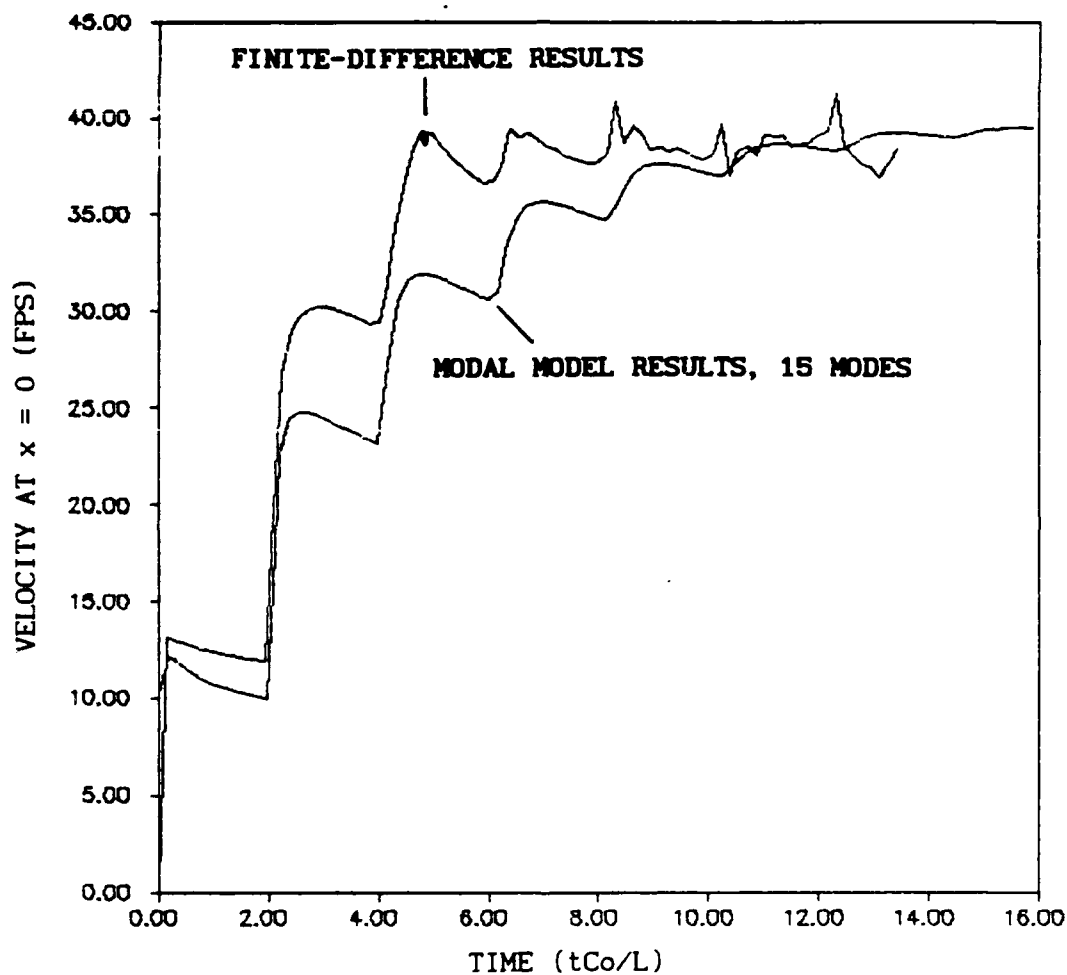


Fig. 85. Transient Velocity Response at Line Inlet, 0.25 psi
Terminated Ramp Input in 5 ft, 0.170 in ID Open Line

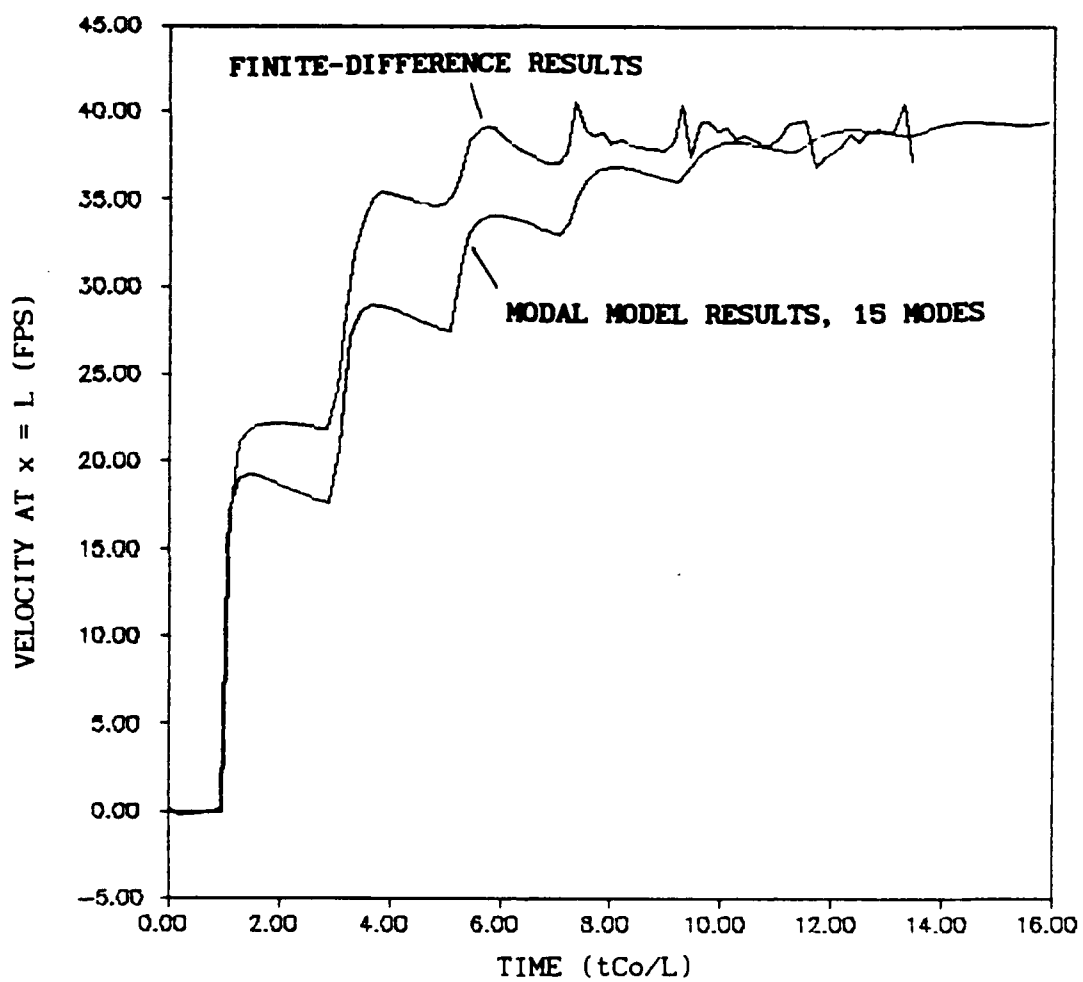


Fig. 86. Transient Velocity Response at Line Exit, 0.25 psi
Terminated Ramp Input in 5 ft, 0.170 in ID Open Line

VII. Conclusions and Suggestions for Further Research

Conclusions

A finite-difference model and a modal superposition model capable of predicting the waveforms of flow and pressure transients from input signals of arbitrary shape and finite amplitude were presented in this study. The finite-difference model improved on the approach of Tsao (67) by using the numerical algorithm developed by Gabutti (21) to more correctly represent the physics of the problem. A method to algebraically generate a steady-state velocity field was also developed to provide initial conditions for cases where a steady, mean flow is present. A simple, turbulent-friction model, modified for transient flow, was included.

The modal superposition model, based on the work of Lebrun (39), was shown to closely track the important features of the linear, finite-difference results when modified to use parameters based on well-known, frequency-domain, transmission-line theory.

The finite-difference model provides the most general method by which to predict the behavior of transient flow in a fluid transmission line. The finite-difference model incorporates unsteady friction and heat transfer, both laminar and turbulent, as well as the effects of an established mean throughflow. This approach is similar to that presented by Tsao (69), in that it uses piecewise defined polynomials to reduce the number of grid points needed in the radial direction. The transient velocity profile at each axial station on the

computational grid can be predicted with relatively modest computer resources.

Two improvements to Tsao's approach have been made in this study. An algorithm developed by Gabutti (21) to represent correctly the physics of a nonlinear problem was applied to a set of nonlinear, damped-wave equations. For the linear case alone, many numerical schemes, such as the Lax-Wendroff algorithm, will correctly represent the physics of the problem when used to solve the damped wave-equations. When nonlinear effects are to be considered, more attention to the physics of the problem is required to select the proper algorithm. Many grid points are required to model the progress of a signal traveling through a transmission line. Failure to account correctly for the physics of the problem produces errors at each grid point which are propagated along with the signal and are cumulative. Use of the Gabutti algorithm reduces this source of error as well as providing a logical and physically consistent means to handle boundary conditions present at the ends of the transmission line.

The second improvement is the use of the piecewise defined polynomials to generate a steady-state velocity field to model a transmission line with a steady, laminar or turbulent, mean flow. A relationship between the well-developed, one-dimensional, steady-flow equations and piecewise defined polynomials was developed for steady-flow velocity profiles recognizing that no net momentum transfer occurs across the flow interval boundaries during steady flow. The initial flow field for a transmission line with a steady, mean flow is now obtained without carrying the solution of the damped-wave equations out to steady state.

The finite-difference model allows the use of separate models to predict the effects of unsteady friction and heat transfer. Studies by Manning and Sandoz used an experimentally determined friction factor to match a one-dimensional model to experimental results. No separate provision was made for heat transfer, the effect of which was assumed to be lumped into the friction factor. The finite-difference model in this study was shown to produce results consistent with published experimental results for finite-length lines without the need for trial and error determination of damping coefficients. The finite-difference model developed in this study is superior to the Sandoz and Manning (60) model in this respect.

The finite-difference model is limited by the amplitude of the input signal. The model was developed from the nonconservative form of the Navier-Stokes equations. As a result, this model fails in the presence of discontinuities, just like the method of characteristics. The performance of this model depends on amplitude of the input signal, the input waveform, transmission-line diameter, and the length of line over which signal must travel. This model was demonstrated in a 0.305 in ID semi-infinite line. For the positive half-sinusoidal signal of 10 psi amplitude, a discontinuity formed in the solution at a distance of 10 ft. Discontinuities form at greater distances for signals of smaller amplitudes. Sufficiently small signals will never produce solutions with discontinuities since the frictional and heat transfer damping terms contained in the model attenuate the signal below amplitudes required to form discontinuities. Signals with steep slopes, such as steps or square pulses, will produce discontinuities much faster than half-sinusoidal signals. Also, lines of smaller

diameter produce greater frictional damping, delaying formation of discontinuities in the solution by attenuating signals more rapidly than larger lines.

Results from the finite-difference model demonstrate that the threshold for nonlinear behavior is much lower than 1.0 psi. This is in agreement with Sandoz and Manning who say that 1.0 psi is well within range of nonlinearity (58). Significant nonlinear behavior was shown at input signal amplitudes of 0.25 psi. No signals with amplitudes below 0.25 psi were tried. However, linear and nonlinear results converge as the amplitude of the input signal decreases.

The unsteady turbulence model used in the finite-difference method provides a qualitative idea of the effects of unsteady turbulent friction, but is very rudimentary. Much more data is needed to improve the turbulent friction model. Improvements are needed to produce consistent results for steady flows with any location of flow interval boundaries. Poor performance in predicting steady-flow velocity profiles does not invalidate the results for transient, turbulent flow. Most of the damping in transient flow occurs near the wall, away from the outer layer where the eddy viscosity model may not be valid. Also, much more data is needed on the transition of unsteady laminar flow to unsteady turbulent flow. No clues as to what significant parameters to base transition on were found in the literature during this study. Some previous studies have experimentally observed that damping significantly increases, with signal amplitude in long, coiled lines (27:280; 29:500-501). Braden (5) developed a model that exhibited this increase in damping with signal amplitude. However, Braden specifically designed his model to produce this effect. No results

matching those of the previous studies were observed. No mechanism was included in the finite-difference model to mimic these results because the source of this amplitude dependent damping observed in the previous studies is not well understood. The nonlinear damping effect observed may result from the effects of the coiled lines or an effect of transition to turbulence in the transient flow, from an initially undisturbed state. As can be seen, development of unsteady transition parameters for use with this model promises to be a difficult problem. However, in spite of its weaknesses, this finite-difference model is a suitable tool for designing experiments to better characterize fast transient flow.

The second model developed in this study was the modal superposition model. This model produced results consistent with results from the finite-difference model. Modal superposition as developed in this study, however, is limited to linear systems with no established mean flow. This model was included in this study as a means to approximate the results of the finite-difference model discussed above. The modal superposition model is convenient to use in the design of fluid networks and requires much less computational power than the finite-difference model. Modifications to modal superposition models allowing the approximation of nonlinear behavior have been successful in structural mechanics. Similar modifications to the model developed in this study may be possible.

The strategy is to use the modal superposition model and finite-difference model as a pair. The finite-difference model, itself too cumbersome for fluid system design, is used to characterize individual transmission lines and signals being considered for use in a

fluid system. The modal superposition model is then adjusted to model finite-difference results for individual transmission lines and, in turn, is used to model entire fluid systems.

Modal superposition, as shown in the previous section of this study, closely tracked the important features of the linear finite-difference results for finite lines. The model and all parameters used were obtained by straightforward manipulation of the governing fluid dynamic equations with no trial and error involved. Model parameters based on the well known linear transmission line theory were used to obtain transient responses directly without the need to invert from the frequency domain to the time domain. Proper modification of the I, R, C, and G parameters used in this model would allow modal superposition to simulate some of the nonlinear effects observed in the finite-difference results. This dual model approach may provide a useful design tool when nonlinear effects must be considered in fluid system design.

Suggestions for Further Research

The results for the finite-difference model presented in Chapter VI show that the frictional and heat transfer damping functions are critical to accurate prediction of the transient response of a fluid transmission line to an applied signal. In the case of laminar friction and heat transfer, evaluation of these damping functions is straightforward, however, transient turbulent friction and heat transfer are poorly understood. With the exception of shock tube studies, no information regarding the transition to turbulence of an

initially undisturbed fluid was found during the course of this study. Experimental work examining this type of transition for single pulse and step input signals must be done before an accurate representation of this effect can be incorporated into a finite-difference model. Data is needed to understand how to properly model unsteady turbulent friction. A more sophisticated model such as the model of Nee and Kovaszny may be required (46). This model consists of a single partial-differential equation in which eddy viscosity is treated as a conserved property. Other, more recent models may also be suitable.

This experimental work may not have been done due to the extreme difficulty in generating pulses of sufficient amplitude and the desired shape. Some experimental work was originally intended as part of this study but the difficulties that arose in creating the required input signals prevented the production of any useful results. Figure 87 shows a diagram of the experimental setup that was tried.

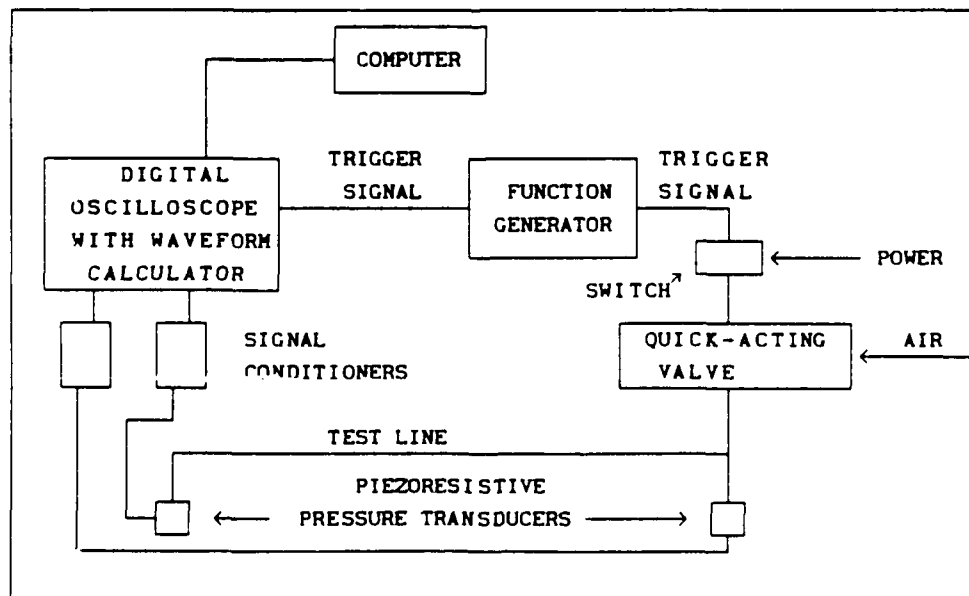


Fig. 87. Transmission Line Transient Measurement Instrumentation

The signal generator consisted of two quick acting electrically operated solenoid valves. Signals produced by this means proved to be of insufficient amplitude and poor shape. A number of generators for sinusoidal signals are available for small-amplitude signals. The development of generators capable of reliably generating well-shaped, high-amplitude pulses is a requirement for continued work in transient turbulent friction in transmission lines.

Much additional work is necessary to incorporate the turbulent friction and heat transfer effects as well as the nonlinear effects produced by the finite-amplitude signals into the modal model introduced in this study. As described in Chapter V, the modal parameters for this model are calculated from approximations of frequency-domain expressions for laminar flow. Modifications to these frequency-domain expressions for I , R , C , and G are needed to account for the effects of turbulence. Some modifications to these expressions are available for turbulence resulting from the presence of an established mean turbulent flow but nothing presently exists to include the effect of transient turbulence. To the best of this author's knowledge, this study is the first direct use of the frequency domain expressions as parameters in a model of this type. The results of this model are good enough to justify further development of this approach.

Incorporation of the nonlinear waveform evolution indicated by the finite-difference model into the modal superposition model also remains. In addition, a means to allow this model to interact with a mean flow is necessary. As it exists now, modal superposition is limited to small amplitude signals traveling in an undisturbed fluid. Two techniques which might be applied to the modal model presented in

this study have been published by Moriss (45) and Thompson and Kohr (66).

Moriss (45) applied the modal superposition method to the calculation of the nonlinear dynamic response of structures. The dynamic equations discussed by Moriss are similar in form to those of the modal model of this study. The nonlinear effects are introduced by modifying the stiffness matrix with functions that change with the deformed position of each structural member (45 :66). Use of this technique for the transmission line modal model would require functions to modify expressions for I, R, C, and G, presently calculated at the beginning of the solution. Frequency-dependent expressions for these parameters, valid for finite-amplitude signals in fluid transmission lines, have been presented, however, their incorporation into modal superposition is not straightforward. Functions which change with pressure might be one alternative. Another potential technique uses sensitivity analysis to develop sensitivity functions which are then minimized with respect to the desired system performance curve (66). This technique was developed for use in compensating nonlinear control systems. This approach offers a means to tune the modal superposition model to mimic results from the finite-difference model.

The modifications discussed above do not address interaction with a mean flow. Methods used to model acoustic streaming and propagation of periodic signals of finite amplitude may be of use here. Much work has been done in the area of nonlinear acoustic waveguides for sinusoidal signals. A number of papers in this area were encountered in the search for information relating to the propagation of finite-amplitude signals. Further examination of literature in the

area of nonlinear acoustics should provide a basis for modification of modal superposition to interact with mean flow and, possibly, a means to modify the stiffness matrix of the modal model to account for nonlinear behavior.

The task of further development of this model will not be simple and much more work is necessary before this model does everything discussed above.

APPENDIX A

Transient Solutions Using The Brown-Nichols Model

An analogy drawn between linear electrical and fluid transmission lines of uniform diameter is useful in obtaining the transient response of a fluid transmission line. The linear dynamic characteristics of a fluid transmission line may be described by four distributed parameters (17:20). These parameters are I (inductance, also known as inertance), R (resistance), G (shunt conductance), and C (shunt capacity or capacitance). These four parameters are combined to produce, $Z = R + jI$ (impedance) and $Y = G + jC$ (admittance). Z and Y are also combined to produce Γ (propagation operator) and Z_c (characteristic impedance). The propagation operator and characteristic impedance result from the solution of the differential equations that arise when R , I , G , and C are assumed to be distributed along the length of a uniform fluid transmission line as shown in Figure A.1. The transmission matrix is obtained from Figure A.1 in terms of the Laplace variable s (36:67):

$$\begin{bmatrix} P_1 \\ Q_1 \end{bmatrix} = \begin{bmatrix} \cosh \Gamma(s)x & Z_c \sinh \Gamma(s)x \\ \frac{1}{Z_c} \sinh \Gamma(s)x & \cosh \Gamma(s)x \end{bmatrix} \begin{bmatrix} P_2 \\ Q_2 \end{bmatrix} \quad (A.1)$$

where the subscripts 1 and 2 denote values at 0 and x , respectively, and P and Q are pressure and flow, respectively. $\Gamma(s)$ and Z_c determine the response of the transmission line.

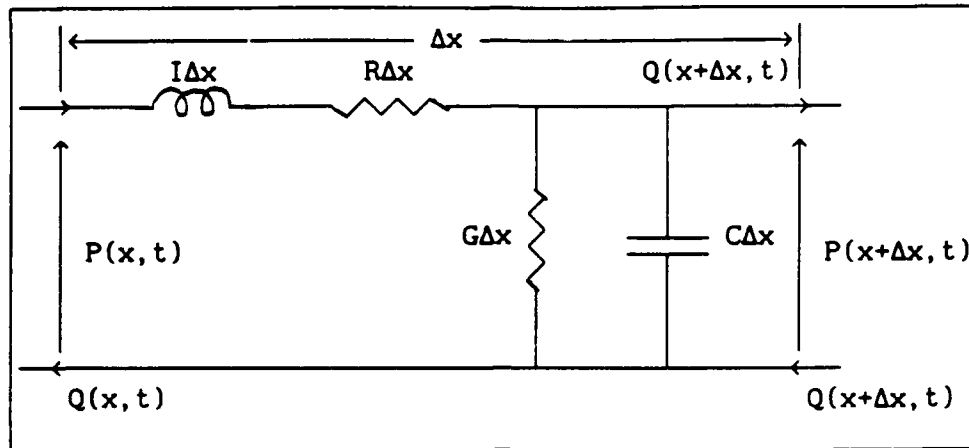


Fig. A.1. Equivalent Circuit of an Infinitesimal Portion of Uniform Transmission Line in Time Domain

The momentum, continuity, energy, and state equations, simplified for a fluid transmission line of uniform diameter, are written (22:4)

$$\rho_0 \left[\frac{\partial u}{\partial t} + \frac{\partial p}{\partial x} \right] = \mu_0 \left[\frac{\partial^2 u}{\partial r^2} + \frac{1}{r} \frac{\partial u}{\partial r} \right] \quad (\text{A.2})$$

$$\frac{\partial \rho}{\partial t} + \rho_0 \left[\frac{\partial u}{\partial x} + \frac{\partial v}{\partial r} + \frac{v}{r} \right] = 0 \quad (\text{A.3})$$

$$\frac{\partial T}{\partial t} + T_0 (\gamma - 1) \frac{\partial p}{\partial t} = \alpha_0 \left[\frac{\partial^2 T}{\partial r^2} + \frac{1}{r} \frac{\partial T}{\partial r} \right] \quad (\text{A.4})$$

$$\frac{d\rho}{\rho_0} = \frac{dp}{K_B} \quad (\text{for liquids}) \quad (\text{A.5a})$$

$$\frac{d\rho}{\rho_0} + \frac{dT}{T_0} = \frac{dp}{P_0} \quad (\text{for gases}) \quad (\text{A.5b})$$

These equations are solved in the Laplace domain in conjunction with the expressions

$$Z(s) F(s) = - \frac{\partial P(s)}{\partial s} \quad (\text{A.6a})$$

$$Y(s) P(s) = - \frac{\partial F(s)}{\partial s} \quad (\text{A.6b})$$

$$F(s) = 2\pi\rho_0 \int_0^a rV(s)dr \quad (\text{A.6c})$$

to produce expressions for $Z(s)$ and $Y(s)$ (7:549):

$$Z(s) = \frac{I_a s}{1 + \frac{2J_1(ja\sqrt{s}/v_0)}{ja\sqrt{s}/v_0 J_0(ja\sqrt{s}/v_0)}} \quad (\text{A.7})$$

$$Y(s) = C_a s \left[1 + \frac{2(\gamma-1)J_1(ja\sqrt{Prs}/v_0)}{ja\sqrt{Prs}/v_0 J_0(ja\sqrt{Prs}/v_0)} \right] \quad (\text{A.8})$$

where $I_a = \frac{\rho}{A}$ and $C_a = \frac{A}{\rho a^2}$. Equations (A.7) and (A.8) can be written in the frequency domain to produce (49:7)

$$Z(\omega) = j\omega I_a \left\{ 1 - \frac{2J_1 \left[j^{3/2} \sqrt{8\omega/\omega_v} \right]}{j^{3/2} \sqrt{8\omega/\omega_v} J_0 \left[j^{3/2} \sqrt{8\omega/\omega_v} \right]} \right\} \quad (\text{A.9})$$

$$Y(\omega) = j\omega C_a \left\{ 1 + \frac{2(\gamma-1)J_1 \left[j^{3/2} \sqrt{8Pr\omega/\omega_v} \right]}{j^{3/2} \sqrt{8Pr\omega/\omega_v} J_0 \left[j^{3/2} \sqrt{8Pr\omega/\omega_v} \right]} \right\} \quad (\text{A.10})$$

The parameter pairs:

$$\omega_v = \frac{8\pi v}{A}; \quad \omega_T = \frac{8\pi v}{A} \quad (\text{A.11a})$$

$$\delta_v = \sqrt{2v/\omega}; \quad \delta_T = \sqrt{2v_T/\omega} \quad (\text{A.11b})$$

$$h_v = \frac{D/2}{\delta_v}; \quad h_T = \frac{D/2}{\delta_T} \quad (\text{A.11c})$$

may be used to simplify Eqs (A.9) and (A.10) (49:6-7):

$$Z(\omega) = j\omega I_a \left\{ 1 - \frac{2J_1 \left[j^{3/2} \sqrt{2} h_v \right]}{j^{3/2} \sqrt{2} h_v J_0 \left[j^{3/2} \sqrt{2} h_v \right]} \right\} \quad (\text{A.12})$$

$$Y(\omega) = j\omega C_a \left\{ 1 + \frac{2(\gamma-1)J_1 \left[j^{3/2} \sqrt{2} h_T \right]}{j^{3/2} \sqrt{2} h_T J_0 \left[j^{3/2} \sqrt{2} h_T \right]} \right\} \quad (\text{A.13})$$

For a semi-infinite line, Brown inverts the expression $\frac{P_2(s)}{P_1(s)} = e^{-\Gamma(s)}$

to obtain the transient response for a semi-infinite line (7:551). For a terminated transmission line of length L, a transfer function relating P_2 to P_1 is obtained using Eq (A.1):

$$\frac{P_2}{P_1} = \frac{1}{\frac{Z_c}{Z_L} \sinh \Gamma L + \cosh \Gamma L} = G(s) \quad (\text{A.14})$$

This transfer function forms the basis of the frequency response

conversion and the fast Fourier transform methods for obtaining the transient response of a terminated transmission line.

The frequency response conversion method uses Eq (A.14) with s replaced by $j\omega$. The input signal, $P_1(t)$ is represented by a Fourier series, $P_1(\omega_k t)$. $G(j\omega)$ is written in polar form as $G(\omega_k) = M_k \angle \phi_k$ for each discrete frequency ω_k resulting from the Fourier series. The expression for the transient response is written (33:4)

$$P_2(t) = \sum_{k=0}^{\infty} M_k P_1(\omega_k t + \phi_k) \quad (A.15)$$

A related method is the fast Fourier transform method. The discrete Fourier transform of the input signal is computed by

$$P_1\left(j \frac{2\pi n}{N\Delta t}\right) = \Delta t \sum_{k=0}^{N-1} P_1(k\Delta t) e^{-j2\pi nk/N} \quad (A.16)$$

For $\omega_k = \frac{2\pi n}{N\Delta t}$, the Fourier transform of the output is described by

$$P_2(j\omega_k) = G(j\omega_k) P_1(j\omega_k) \quad (A.17)$$

The output waveform $P_2(t)$ is obtained from the inverse transform of the complex conjugate of Eq (A.17) (71:214):

$$P_2(k\Delta t) = \Delta f \sum_{n=0}^{N-1} P_2^*(j2\pi n\Delta f) e^{-j2\pi nk/N} \quad (A.18)$$

A third method for obtaining the transient solution relies on a modal approximation of the terms of Eq (A.1) leading to a state space representation (24; 25). The state variables are chosen to be $(P_2)_n$ and $(Z_c Q_1)_n$ where $n = 1, 2, \dots, N$ and:

$$P_2 = (P_2)_1 + (P_2)_1 + \dots \quad (\text{A.19a})$$

$$Z_c Q_1 = (Z_c Q_1)_1 + (Z_c Q_1)_2 + \dots \quad (\text{A.19b})$$

The dynamics of the transmission line are described by the expression

$$\dot{\mathbf{x}} = \mathbf{A} \mathbf{x} + \mathbf{B} \mathbf{u} \quad (\text{A.20})$$

where the components of matrices \mathbf{A} and \mathbf{B} are, themselves, matrices:

$$\mathbf{A} = \begin{bmatrix} \mathbf{A}_1 & & \\ & \mathbf{A}_2 & \\ & & \ddots \\ & & & \mathbf{A}_m \end{bmatrix} \quad \text{where} \quad \mathbf{A}_1 = \begin{bmatrix} A_{11} & A_{12} \\ A_{21} & A_{22} \end{bmatrix} \quad (\text{A.21a})$$

$$\mathbf{B} = \begin{bmatrix} \mathbf{B}_1 \\ \mathbf{B}_2 \\ \vdots \\ \mathbf{B}_m \end{bmatrix} \quad \text{where} \quad \mathbf{B}_1 = \begin{bmatrix} B_{11} & B_{12} \\ B_{21} & B_{22} \end{bmatrix} \quad (\text{A.21b})$$

$$\mathbf{x} = \begin{bmatrix} (P_2)_1 \\ (Z_c Q_1)_1 \\ \vdots \\ (P_2)_m \\ (Z_c Q_1)_m \end{bmatrix} \quad (\text{A.21c})$$

Calculation of the scalar values contained in the A and B matrices is algebraically complex (25).

An approach based on the method of characteristics and Eq (A.7) was also developed (9:219):

$$\pm \frac{1}{aI} \frac{dp}{dt} + \frac{dV}{dt} + \left(\frac{Z_0}{I} \pm a\alpha \right) V = -\mathcal{L}^{-1} \left[\frac{Z_1(s)}{Is} sV \right] \quad (\text{A.22})$$

This approach is a generalization of the one presented by Zielke (82).

APPENDIX B

Derivation of Damped-Wave Equations

The continuity, momentum, energy, and state equations in terms of cylindrical coordinates with mass averaged dependent variables are written as follows (58:11-12):

Continuity

$$\frac{\partial(r\bar{\rho})}{\partial t} + \frac{\partial(r\bar{\rho}\tilde{u})}{\partial x} + \frac{\partial(r\bar{\rho}\tilde{v})}{\partial r} = 0 \quad (\text{B.1})$$

x-momentum

$$\frac{\partial(r\bar{\rho}\tilde{u})}{\partial t} + \frac{\partial}{\partial x} \left[r(\bar{\rho}\tilde{u}\tilde{u} + \bar{p} - \bar{\tau}_{xx} + \overline{\rho u u}) \right] + \frac{\partial}{\partial r} \left[r(\bar{\rho}\tilde{v}\tilde{u} - \bar{\tau}_{xr} + \overline{\rho u v}) \right] = 0 \quad (\text{B.2})$$

r-momentum

$$\begin{aligned} \frac{\partial}{\partial t}(r\bar{\rho}\tilde{v}) + \frac{\partial}{\partial x} \left[r(\bar{\rho}\tilde{u}\tilde{v} - \bar{\tau}_{rx} + \overline{\rho u v}) \right] + \\ \frac{\partial}{\partial r} \left[r(\bar{\rho}\tilde{v}\tilde{v} + \bar{p} - \bar{\tau}_{rr} + \overline{\rho v v}) \right] + \bar{\tau}_{\theta\theta} - \bar{p} - \overline{\rho w w} = 0 \end{aligned} \quad (\text{B.3})$$

Total Energy

$$\begin{aligned}
 \frac{\partial}{\partial t}(r\tilde{e}) + \frac{\partial}{\partial x} \left[\tilde{u}(\tilde{e} + \bar{p}) + \bar{q}_x + \overline{\rho u h} - \tilde{u}(\bar{\tau}_{xx} - \overline{\rho u u}) - \right. \\
 \left. \tilde{v}(\bar{\tau}_{rx} - \overline{\rho v u}) - \overline{u \left(\bar{\tau}_{xx} - \frac{\rho u u}{2} \right)} - \overline{v \left(\bar{\tau}_{rx} - \frac{\rho v u}{2} \right)} - \right. \\
 \left. \overline{w \left(\bar{\tau}_{\theta x} - \frac{\rho w u}{2} \right)} \right] + \frac{\partial}{\partial r} \left[\tilde{v}(\tilde{e} + \bar{p}) + \bar{q}_r + \overline{\rho v h} - \right. \\
 \left. \tilde{u}(\bar{\tau}_{xr} - \overline{\rho u v}) - \tilde{v}(\bar{\tau}_{rr} - \overline{\rho v v}) - \overline{u \left(\bar{\tau}_{xr} - \frac{\rho u v}{2} \right)} - \right. \\
 \left. \overline{v \left(\bar{\tau}_{rr} - \frac{\rho v v}{2} \right)} - \overline{w \left(\bar{\tau}_{\theta r} - \frac{\rho w v}{2} \right)} \right] = 0 \quad (B.4)
 \end{aligned}$$

Equation of State

$$\frac{dp}{p} = \frac{d\rho}{\rho} + \frac{dT}{T} \quad (B.5)$$

The viscous layer formed by transient flow in a long fluid line is thin with respect to the line length provided that $\frac{a}{L} \ll 1$. If the largest viscous term is assumed to be of approximately the same magnitude as the inertia terms, Eqs (B.1) through (B.5) can be greatly simplified by applying the boundary layer assumptions (2:208). These boundary layer assumptions allow the second derivatives in the direction of the flow to be neglected compared to corresponding derivatives transverse to the flow. In other words, the heat transfer and momentum transfer in the radial direction are significantly greater

than in the axial direction for a long, cylindrical line. The boundary layer assumptions also allow the momentum equation for flow in the radial direction to be neglected.

This simplification process is done methodically with an order of magnitude analysis by assuming gradients perpendicular to the surface are of $O(1)$ and gradients parallel to surface are $O(\delta)$ (14:66). Also, for $1 \ll \text{Mach number}$; $\bar{\tau}_{xr} \gg \bar{\tau}_{xx}$ and $\overline{\rho uv} \gg \overline{\rho uu}$ (14:74). Although pulses travel at the local speed of sound, the local fluid velocities induced by the passage of these signals are much less than Mach 1. As a result, only the x-momentum equation for the axial velocity component u is required. The variable u is a function of t , x , and r where r is measured from the centerline.

Despite the assumption of parallel flow, the turbulence remains three dimensional with fluctuating velocity components u' , v' , and w' in the x , r , and θ directions, respectively. Based on the above assumptions, the x-momentum equation Eq (B.1) may be written as follows:

$$\frac{\partial}{\partial t}(r\bar{\rho}u) + \frac{\partial}{\partial x}[r(\bar{\rho}u\tilde{u} + \bar{p})] + \frac{\partial}{\partial r}[r(\bar{\rho}v\tilde{u} - \bar{\tau}_{xr} + \overline{\rho uv})] = 0 \quad (\text{B.6})$$

These same assumptions allow the total thermal energy equation, Eq (B.4), to be written as

$$\begin{aligned} \frac{\partial(r\tilde{e})}{\partial t} + \frac{\partial}{\partial x} r[\tilde{u}(\tilde{e} + \bar{p}) - \tilde{v}(\bar{\tau}_{rx} - \overline{\rho v u})] + \\ \frac{\partial}{\partial r} r[\tilde{v}(\tilde{e} + \bar{p}) + \tilde{q}_r + \overline{\rho v h} - \tilde{u}(\bar{\tau}_{xr} - \overline{\rho uv})] = 0 \end{aligned} \quad (\text{B.7})$$

Terms such as $\overline{\tilde{u}(\tau_{xr} - \frac{\rho_{uv}}{2})}$ in Eq (B.4) are usually neglected since they are much smaller than thermal dissipation terms like $\tilde{u}(\bar{\tau}_{xr} - \overline{\rho_{uv}})$ (57:5).

Under the boundary layer approximation, $\tilde{u} = \bar{u}$ but $\tilde{v} \neq \bar{v}$ (14:75). Even though parallel flow was assumed, \tilde{v} is not zero. The definition of the mass weighted variable allows \tilde{v} to be written as

$$\tilde{v} = \frac{\overline{\rho v}}{\bar{\rho}} = \frac{(\bar{\rho} \bar{v} + \overline{\rho v'})}{\bar{\rho}} \quad (B.8)$$

With \bar{v} equal to zero from the boundary layer assumptions, Eq (B.8)

reduces to $\tilde{v} = \frac{\overline{\rho v'}}{\bar{\rho}}$. In a thin shear layer, $\overline{\rho v'}$ is of $O(\delta)$ as compared to \bar{u} which is of $O(1)$ (14:75). This allows the terms $\tilde{v}(\bar{\tau}_{rx} - \overline{\rho v u})$ and $\tilde{v}(\tilde{e} + \bar{p})$ to be neglected in relation to the terms $\tilde{u}(\tilde{e} + \bar{p})$ and $\bar{q}_r + \overline{\rho v h} - \tilde{u}(\bar{\tau}_{xr} - \overline{\rho u v})$ in the energy equation. The terms retained in the energy equation are all of order $O(1)$. In the momentum equation, the term $\bar{\rho} \tilde{v} \tilde{u} - \bar{\tau}_{xr} + \overline{\rho u v}$ reduces to $-\bar{\tau}_{xr} + \overline{\rho u v}$. It is now possible to write Eqs (B.6) and (B.7) solely in terms of time averaged variables. The momentum equation may be written as

$$\frac{\partial}{\partial t}(r \bar{\rho} \bar{u}) + \frac{\partial}{\partial x}[r(\bar{\rho} \bar{u} \bar{u} + \bar{p})] + \frac{\partial}{\partial r}[r(\overline{\rho u v} - \bar{\tau}_{xr})] = 0 \quad (B.9)$$

Note that the term $\overline{\rho u v}$ in Eq (B.6) has been changed to $\overline{\rho u v}$ in Eq (B.9) (14:73).

Since $\tilde{e} = \bar{e}$ under the boundary layer approximations,

$\bar{e} = \bar{\rho}\bar{h} - \bar{p} + \bar{\rho} \frac{\bar{u}^2}{2}$ (14:75). Expansion of \bar{e} in Eq (B.7) gives the following version of the energy equation:

$$\frac{\partial}{\partial t} \left[\bar{\rho}\bar{h} - \bar{p} + \frac{\bar{\rho}\bar{u}^2}{2} \right] + \frac{\partial}{\partial x} \left[\bar{u} \left(\bar{\rho}\bar{h} + \frac{\bar{\rho}\bar{u}^2}{2} \right) \right] +$$

$$\frac{\partial}{\partial r} \left[\bar{q}_r + \bar{\rho}\bar{v}\bar{h}' - \bar{u} (\bar{\tau}_{xr} - \bar{\rho}\bar{u}\bar{v}') \right] = 0 \quad (B.10)$$

The energy equation can be put into a more convenient form by subtracting the mean kinetic energy equation from the total energy equation where the mean kinetic energy equation is written as follows:

$$\frac{\partial}{\partial t} \left(r \frac{\bar{\rho}\bar{u}}{2} \right) + \frac{\partial}{\partial x} \left(r \bar{u} \frac{\bar{\rho}\bar{u}}{2} \right) + r \bar{u} \frac{\partial \bar{p}}{\partial x} - \frac{\partial}{\partial r} \left[\bar{u} (\bar{\tau}_{xr} - \bar{\rho}\bar{u}\bar{v}') \right] + r (\bar{\tau}_{rx} - \bar{\rho}\bar{u}\bar{v}') \frac{\partial \bar{u}}{\partial r} = 0$$

(B.11)

The resulting energy equation is written below:

$$\frac{\partial}{\partial t} (r \bar{\rho}\bar{h}) - \frac{\partial (r \bar{p})}{\partial t} + \frac{\partial}{\partial x} (r \bar{u} \bar{\rho}\bar{h}) + \frac{\partial}{\partial r} \left[\bar{q}_r + \bar{\rho}\bar{v}\bar{h}' \right] + r \bar{u} \frac{\partial \bar{p}}{\partial x} - r (\bar{\tau}_{rx} - \bar{\rho}\bar{u}\bar{v}') \frac{\partial \bar{u}}{\partial r} = 0$$

(B.12)

The term $(\bar{\tau}_{rx} - \bar{\rho}\bar{u}\bar{v}') \frac{\partial \bar{u}}{\partial r}$ is the dissipation. Cebeci and Smith show

a nondimensional form of this equation in nonconservative form as

$$\rho^* \frac{\partial h^*}{\partial t} + \rho^* u^* \frac{\partial h^*}{\partial x} = Ec \left(\frac{\partial p^*}{\partial t} + u^* \frac{\partial p^*}{\partial x} \right) + \frac{1}{R_L} \frac{\partial}{\partial r} \left[\frac{\mu^*}{Pr} \frac{\partial h^*}{\partial r} - R_L \rho^* (\bar{h}v)^* \right] +$$

$$\frac{Ec}{R_L} \left[\mu^* \frac{\partial u^*}{\partial r} - R_L \rho^* (\bar{u}v)^* \right] \frac{\partial u^*}{\partial r} \quad (B.13)$$

The asterisk denotes nondimensional quantities (14:77). The Eckert number for pipe flow is defined as $E_c = \frac{u_c^2}{h_w}$ while the Reynolds number is defined as $R_L = \frac{u_c \rho L}{\mu}$. u_c denotes centerline velocity. Low fluid velocities produce a small E_c while R_L is large within the boundary layer approximation. The ratio $\frac{E_c}{R_L}$ is small and allows the dissipation terms in the energy equation to be neglected (14:78). All other terms are retained. Finally, assuming the variation in c_p due to turbulence is negligible, the terms \bar{h} and h' are written as $c_p \bar{T}$ and $c_p T'$ respectively. The system of equations becomes:

Continuity

$$\frac{\partial(r\bar{\rho})}{\partial t} + \frac{\partial(r\bar{\rho}\bar{u})}{\partial x} = 0 \quad (B.14)$$

x-momentum

$$\frac{\partial}{\partial t}(r\bar{\rho}\bar{u}) + \frac{\partial}{\partial x}[r(\bar{\rho}\bar{u}\bar{u} + \bar{p})] + \frac{\partial}{\partial r}[r(-\bar{\tau}_{xr} + \bar{\rho}\bar{u}v')] = 0 \quad (B.15)$$

Energy

$$\frac{\partial}{\partial t}(r\bar{\rho}c_p \bar{T}) - \frac{\partial}{\partial t}(r\bar{p}) + \frac{\partial}{\partial x}(r\bar{\rho}\bar{u}c_p \bar{T}) + \frac{\partial}{\partial r}[r(\bar{q}_r + \bar{\rho}c_p \bar{u}T')] - r\bar{u}\frac{\partial \bar{p}}{\partial x} = 0 \quad (B.16)$$

The Navier-Stokes equations are in a simplified form suitable for deriving the damped-wave equations.

The continuity equation may be expanded to produce the following:

$$\frac{\partial \bar{\rho}}{\partial t} + \bar{\rho} \frac{\partial \bar{u}}{\partial x} + \bar{u} \frac{\partial \bar{\rho}}{\partial x} = 0 \quad (\text{B.17})$$

Expressions for $\frac{\partial \bar{\rho}}{\partial t}$ and $\frac{\partial \bar{\rho}}{\partial x}$ can be obtained from the equation of state:

$$\frac{\partial \bar{\rho}}{\partial t} = \bar{\rho} \left(\frac{1}{\bar{p}} \frac{\partial \bar{p}}{\partial t} - \frac{1}{\bar{T}} \frac{\partial \bar{T}}{\partial t} \right) \quad (\text{B.18})$$

$$\frac{\partial \bar{\rho}}{\partial x} = \bar{\rho} \left(\frac{1}{\bar{p}} \frac{\partial \bar{p}}{\partial x} - \frac{1}{\bar{T}} \frac{\partial \bar{T}}{\partial x} \right) \quad (\text{B.19})$$

Equations (B.18) and (B.19) may be written in a more compact form by recognizing that $\frac{dp}{p} = d(\ln[p])$:

$$\frac{\partial \bar{\rho}}{\partial t} = \bar{\rho} \left(\frac{\partial(\ln[\bar{p}])}{\partial t} - \frac{1}{\bar{T}} \frac{\partial \bar{T}}{\partial t} \right) \quad (\text{B.20})$$

$$\frac{\partial \bar{\rho}}{\partial x} = \bar{\rho} \left(\frac{\partial(\ln[\bar{p}])}{\partial x} - \frac{1}{\bar{T}} \frac{\partial \bar{T}}{\partial x} \right) \quad (\text{B.21})$$

Substitution of Eqs (B.20) and (B.21) into the the continuity equation produces the following result:

$$\bar{\rho} \left[\frac{\partial \bar{T}}{\partial t} + \bar{u} \frac{\partial \bar{T}}{\partial x} \right] = \bar{\rho} \frac{\partial \bar{u}}{\partial x} + \bar{\rho} \left[\frac{\partial}{\partial t} \ln[\bar{p}] + \bar{u} \frac{\partial}{\partial x} \ln[\bar{p}] \right] \quad (\text{B.22})$$

The energy equation, Eq (B.16), can be written as

$$rc_p \bar{\rho} \left(\frac{\partial \bar{T}}{\partial t} + \bar{u} \frac{\partial \bar{T}}{\partial x} \right) - \frac{\partial(r\bar{p})}{\partial t} - r\bar{u} \frac{\partial \bar{p}}{\partial x} + \frac{\partial}{\partial r} \left(\bar{q}_r + \bar{\rho} c_p \bar{vT}' \right) = 0 \quad (B.23)$$

or more compactly to produce

$$rc_p \bar{\rho} \left(\frac{\partial \bar{T}}{\partial t} + \bar{u} \frac{\partial \bar{T}}{\partial x} \right) - \frac{\partial}{\partial t} \left(\bar{p} r \ln[\bar{p}] \right) - r\bar{u} \bar{p} \frac{\partial(\ln[\bar{p}])}{\partial x} + \frac{\partial}{\partial r} \left(\bar{q}_r + \bar{\rho} c_p \bar{vT}' \right) = 0 \quad (B.24)$$

Equation (B.22) can be used to replace the first term of Eq (B.24):

$$rc_p \bar{\rho} \bar{T} \left[\frac{\partial \bar{u}}{\partial x} + \left(\frac{\partial(\ln[\bar{p}])}{\partial t} + \bar{u} \frac{\partial(\ln[\bar{p}])}{\partial x} \right) \right] - \frac{\partial}{\partial t} \left(\bar{p} r \ln[\bar{p}] \right) - r\bar{u} \bar{p} \frac{\partial(\ln[\bar{p}])}{\partial x} + \frac{\partial}{\partial r} \left(\bar{q}_r + \bar{\rho} c_p \bar{vT}' \right) = 0 \quad (B.25)$$

The relations $p = \rho RT$, $R = c_p - c_v$, $\gamma = \frac{c_p}{c_v}$ may be used to simplify

Eq (B.25):

$$r\gamma \frac{\partial \bar{u}}{\partial x} + r \frac{\partial(\ln[\bar{p}])}{\partial t} + r\bar{u} \frac{\partial(\ln[\bar{p}])}{\partial x} + \frac{(\gamma - 1)}{\bar{p}} \frac{\partial}{\partial r} \left(\bar{q}_r + \bar{\rho} c_p \bar{vT}' \right) = 0 \quad (B.26)$$

The momentum equation Eq (B.15) is rewritten using the relations

$p = \rho RT$, and $c^2 = \gamma RT$.

$$r \frac{\partial \bar{u}}{\partial t} + \frac{c^2}{\gamma} \frac{\partial}{\partial x} \left(r \ln[\bar{p}] \right) + r\bar{u} \frac{\partial \bar{u}}{\partial x} + \frac{c^2}{\bar{p}\gamma} \frac{\partial}{\partial r} \left[r(-\bar{\tau}_{xr} + \bar{\rho} u v') \right] = 0 \quad (B.27)$$

The desired form of the damped wave equations is obtained by isolating the friction and heat transfer terms on the right hand side of the equations:

$$\frac{\partial(\text{Ln}[\bar{p}])}{\partial t} + \frac{\partial \bar{u}}{\partial x} + \bar{u} \frac{\partial(\text{Ln}[\bar{p}])}{\partial x} = - \frac{(\gamma - 1)}{\bar{p}} \frac{1}{r} \frac{\partial}{\partial r} [r(\bar{q}_r + \bar{\rho} c_p \bar{v} T')] \quad (\text{B.28})$$

$$\frac{\partial \bar{u}}{\partial t} + \frac{c^2}{\gamma} \frac{\partial(\text{Ln}[\bar{p}])}{\partial x} + \bar{u} \frac{\partial \bar{u}}{\partial x} = \frac{c^2}{\bar{p} \gamma} \frac{1}{r} \frac{\partial}{\partial r} [r(\bar{\tau}_{xr} - \bar{\rho} u v')] \quad (\text{B.29})$$

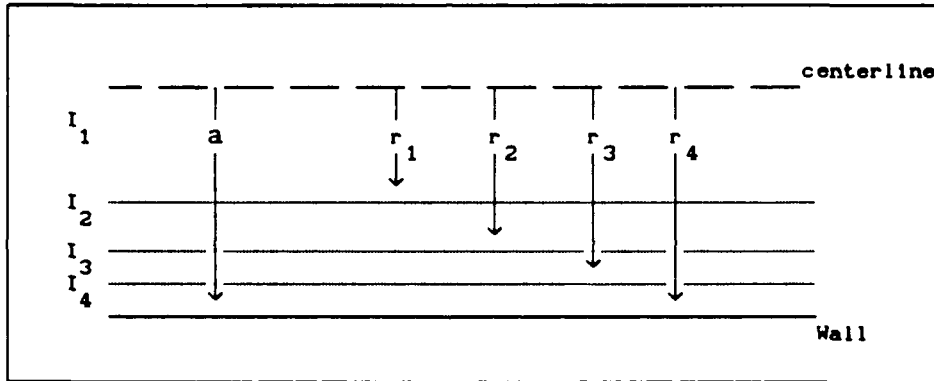


Fig. B.1 Partitioning of Flow

For each flow interval, averaged temperature and averaged velocity functions are defined for each region shown in Figure (B.1):

$$T_n(x, t) = \frac{1}{\Delta A_n} \int_{r_{n-1}}^{r_n} T(x, r, t) 2\pi r dr \quad (\text{B.30})$$

$$u_n(x, t) = \frac{1}{\Delta A_n} \int_{r_{n-1}}^{r_n} u(x, r, t) 2\pi r dr \quad (\text{B.31})$$

These averaged functions are incorporated into Eqs (B.28) and (B.29) as follows:

$$\begin{aligned} & \frac{1}{\Delta A_n} \int_{r_{n-1}}^{r_n} \frac{\partial u}{\partial t} 2\pi r dr + \frac{1}{\Delta A_n} \int_{r_{n-1}}^{r_n} \frac{c^2 \partial(\ln[p])}{\gamma \partial x} 2\pi r dr + \\ & \frac{1}{\Delta A_n} \int_{r_{n-1}}^{r_n} u \frac{\partial u}{\partial x} 2\pi r dr = \frac{1}{\Delta A_n} \int_{r_{n-1}}^{r_n} \frac{c^2}{p\gamma} \frac{\partial}{\partial r} [r(\tau_{xr} - \overline{\rho u v})] \end{aligned} \quad (B.32)$$

All variables are time-averaged except u' and v' . Evaluation of the integrals produces

$$\begin{aligned} \frac{\partial u}{\partial t}_n + \frac{c^2 \partial(\ln[p])}{\gamma \partial x} + \frac{\partial}{\partial x} \left(\frac{u^2}{2} \right)_n &= \frac{2\pi c^2}{\gamma p \Delta A_n} \left[r_n (\tau_{xr} - \overline{\rho u v})_{r=r_n} - \right. \\ & \left. r_{n-1} (\tau_{xr} - \overline{\rho u v})_{r=r_{n-1}} \right] \end{aligned} \quad (B.33)$$

In Eq (B.33), c^2 has been assumed to be constant over the line cross section and is taken as $\sqrt{\gamma RT}$. Here T is the average fluid temperature taken over the cross section and $\gamma = 1.4$. Some studies suggest values of γ less than 1.4 to provide better agreement with measured results since these smaller values of γ account for heat transfer to the pipe walls (19:11-12). Heat transfer to the pipe walls is already accounted for by use of the energy equation with the damped wave equations. As a result, the adiabatic speed of sound is used and γ is set at 1.4. The use of the average temperature of the cross

section to determine c is justified from the assumption of uniform pressure over the cross section. Also, the temperature variation over the cross section away from the wall will not be large.

In order to solve for u_n in Eq (B.33), the assumption that $(u^2)_n$ can be approximated by $(u)_n^2$ must be made. For a uniform velocity profile this is exactly true but for nonuniform velocity profiles, this can only be considered as an approximation. However, the velocity profiles will be shown to be relatively flat away from line wall. Also, the flow interval near the wall, where the largest velocity gradients exist, contains only a small portion of the flow energy. As a result, approximating $(u^2)_n$ by $(u)_n^2$, should not introduce a significant error in the results for the overall flow. The equation for averaged velocity function may now be written as

$$\frac{\partial u_n}{\partial t} + \frac{c^2}{\gamma} \frac{\partial(\ln p)}{\partial x} + u_n \frac{\partial u_n}{\partial x} = \frac{2\pi c^2}{\gamma p \Delta A_n} \left[r_n (\bar{\tau}_{xr} - \overline{\rho u v})_{r=r_n} - r_{n-1} (\bar{\tau}_{xr} - \overline{\rho u v})_{r=r_{n-1}} \right] \quad (B.34)$$

In a similar manner the equation for $\ln(p)$ is obtained in terms of averaged variables:

$$\frac{\partial(\ln[p])}{\partial t} + u_{av} \frac{\partial(\ln[p])}{\partial x} + \gamma \frac{\partial u_{av}}{\partial x} = - \frac{2\pi a(\gamma - 1)}{\Delta A p} (\bar{q}_r + \overline{\rho v c_p T})_{r=a} \quad (B.35)$$

where $u_{av} = \frac{1}{\Delta A} \int_0^a u 2\pi r dr$ and $\Delta A = \int_0^a 2\pi r dr$.

The friction term on the right hand side of the Eq (B.34) is written as

$$F_n = \frac{2\pi c^2}{\gamma p \Delta A_n} \left[(\mu_T)_{r=r_n} r_n \left(\frac{\partial u}{\partial r} \right)_{r=r_n} - (\mu_T)_{r=r_{n-1}} r_{n-1} \left(\frac{\partial u}{\partial r} \right)_{r=r_{n-1}} \right] \quad (B.36)$$

The heat transfer term in the Eq (B.35) is written as:

$$H_{av} = \frac{2(\gamma - 1)}{a p} k_T \left(\frac{\partial T}{\partial r} \right)_{r=a} \quad (B.37)$$

The variables μ_T and k_T are the sum of the molecular and turbulent viscosity and heat conduction coefficients, respectively. Values for μ_T are found using a suitable turbulence model and values for k_T are based on the Reynolds analogy.

Neither Eq (B.34) or (B.35) provides a means for finding T_n , thus a third equation, the energy equation, is required to find T_n . The energy equation Eq (B.16) is rewritten as

$$r \frac{\partial T}{\partial t} + r u \frac{\partial T}{\partial x} - \frac{c^2}{\gamma c_p} \frac{\partial}{\partial t} (r \ln[p]) - \frac{c^2}{\gamma c_p} r u \frac{\partial (\ln[p])}{\partial x} = \frac{c^2}{\gamma c_p} \frac{\partial}{\partial r} \left(r k_T \frac{\partial T}{\partial r} \right) \quad (B.38)$$

Applying the definition of the average temperature function to the Eq (B.38) produces

$$\begin{aligned} \frac{\partial T_n}{\partial t} + u_n \frac{\partial T_n}{\partial x} - \frac{c^2}{\gamma c_p} \frac{\partial}{\partial t} (\ln[p]) - \frac{c^2}{\gamma c_p} u_n \frac{\partial (\ln[p])}{\partial x} = \\ \frac{2c^2}{\gamma c_p (r_n^2 - r_{n-1}^2)} \left[r_n k_T(r_n) \left(\frac{\partial T}{\partial r} \right)_{r=r_n} - r_{n-1} k_T(r_{n-1}) \left(\frac{\partial T}{\partial r} \right)_{r=r_{n-1}} \right] \end{aligned} \quad (B.39)$$

The terms $\frac{\partial(\ln[p])}{\partial x}$ and u_n are obtained from solution of Eqs (B.34) and (B.35). The term $(u T)_n$ in Eq (B.39) is assumed to be approximated by $u_n T_n$ with the same reasoning used in the approximation of $(u^2)_n$ in Eq (B.34). This term is representative of the average amount of enthalpy transported by convection in the interval I_n .

APPENDIX C

Velocity Profile Approximation by Piecewise Continuous Polynomials

Piecewise continuous polynomials are used in Chapter II to reduce the number of grid points required in the radial direction to obtain an accurate numerical solution for transient flow in a fluid transmission line. The polynomials used to approximate the velocity profile in each of the radial intervals dividing the flow are shown in Eq (C.1)

(70:591):

$$u(x, r, t) \cong \begin{cases} p_1(x, r, t) = a_1 + b_1 r + c_1 r^2 & r \in I_1 \\ p_n(x, r, t) = a_n + b_n (r - r_{n-1}) + c_n (r - r_{n-1})^2 + \\ \quad + d_n (r - r_{n-1})^3 & r \in I_n \end{cases} \quad (C.1)$$

For $n = 1 \cdots M$, this system of equations contains $4M-1$ unknown coefficients. These coefficients must be evaluated at each time step and axial station.

Application of the definition of the averaged velocity function to Eq (C.1) produces M equations:

$$u_1(x, t) = a_1 + \frac{2}{3} b_1 r_1 + \frac{1}{2} c_1 r_1^2 \quad (C.3a)$$

$$u_n = a_n + b_n \left[\frac{2}{3} \frac{\delta_n^2}{r_n + r_{n-1}} + \frac{r_{n-1} \delta_n}{r_n + r_{n-1}} \right] + c_n \left[\frac{1}{2} \frac{\delta_n^3}{r_n + r_{n-1}} + \frac{2}{3} \frac{r_{n-1} \delta_n^2}{r_n + r_{n-1}} \right] + d_n \left[\frac{2}{5} \frac{\delta_n^4}{r_n + r_{n-1}} + \frac{1}{2} \frac{r_{n-1} \delta_n^3}{r_n + r_{n-1}} \right] \quad n = 1 \dots M \quad (C.3b)$$

The piecewise defined polynomials as well as their first and second derivatives are required to be continuous at the boundary between each flow interval. These conditions produce an additional $3M-3$ equations:

$$a_{n+1} = a_n + b_n \delta_n + c_n \delta_n^2 + d_n \delta_n^3 \quad (C.4)$$

$$b_{n+1} = b_n + 2c_n \delta_n + 3d_n \delta_n^2 \quad (C.5)$$

$$2c_{n+1} = 2c_n + 6d_n \delta_n \quad (C.6)$$

The assumption of no slip at the wall produces

$$0 = a_M + b_M (r_M - r_{M-1}) + c_M (r_M - r_{M-1})^2 + d_M (r_M - r_{M-1})^3 \quad (C.7)$$

and the assumption of axisymmetric parallel flow $\left. \frac{\partial u}{\partial r} \right|_{r=0} = 0$ is applied at the centerline:

$$b_1 = 0 \quad (C.8)$$

producing two more conditions. Equations (C.3) through (C.8) provide a system of $4M-1$ independent equations to solve for the $4M-1$ coefficients

in Eq (C.1).

The above equations need not be solved as they appear, but may be used to provide a set of linear dependence relationships (70:592).

Note that $d_1 = 0$ since the equation in the center interval is quadratic. With $d_1 = 0$, Eq (C.6) produces the relation $c_1 = c_2$ when $n = 1$. Equation (C.6) is solved for d_n to give

$$d_n = \frac{1}{3\delta_n}(c_{n+1} - c_n) \quad n = 2, 3, \dots, M-1 \quad (C.9)$$

By substituting Eq (C.8) into Eq (C.5) an expression for b_{n+1} is produced:

$$b_{n+1} = b_n + \delta_n(c_n + c_{n+1}) \quad n = 1, 2, \dots, M \quad (C.10)$$

For specific values of n , Eq (C.10) can be written as

$$\begin{aligned} b_2 &= 0 + \delta_1(c_1 + c_2) \\ b_3 &= b_2 + \delta_2(c_2 + c_3) = \delta_1(c_1 + c_2) + \delta_2(c_2 + c_3) \\ b_4 &= b_3 + \delta_3(c_3 + c_4) = \delta_1(c_1 + c_2) + \delta_2(c_2 + c_3) + \delta_3(c_3 + c_4) \\ &\vdots \\ &\vdots \end{aligned} \quad (C.11)$$

A recursion relationship for b_{n+1} in terms of c_n can be developed from Eq (C.11) by inspection:

$$b_{n+1} = \sum_{k=1}^n \delta_k c_k + \sum_{k=2}^{n+1} \delta_{k-1} c_k \quad (C.12a)$$

or equivalently

$$b_n = \sum_{k=1}^{n-1} \delta_k c_k + \sum_{k=2}^n \delta_{k-1} c_k \quad n = 2, 3, \dots, M \quad (C.12b)$$

Equation (C.4) may also be written for specific values of n . In addition, this result may be written in terms of c_n only, if Eqs (C.9) and (C.11) are used to eliminate the coefficients b_n and d_n :

$$\begin{aligned} a_2 &= a_1 + b_1 \delta_1 + c_1 \delta_1^2 + d_1 \delta_1^3 = a_1 + c_1 \delta_1^2 \\ &\quad (b_1=0) \quad (d_1=0) \\ a_3 &= a_2 + b_2 \delta_2 + c_2 \delta_2^2 + d_2 \delta_2^3 \\ &= a_1 + c_1 \delta_1^2 + \delta_2 [\delta_1 (c_1 + c_2)] + \delta_2^2 c_2 + \delta_2^3 \left[\frac{1}{3\delta_2} (c_3 - c_2) \right] \\ a_4 &= a_3 + b_3 \delta_3 + c_3 \delta_3^2 + d_3 \delta_3^3 \\ &= a_1 + c_1 \delta_1^2 + \delta_2 [\delta_1 (c_1 + c_2)] + \delta_2^2 c_2 + \frac{1}{3} \delta_2^2 (c_3 - c_2) + \\ &\quad \delta_3 [\delta_1 (c_1 + c_2) + \delta_2 (c_2 + c_3)] + \delta_3^2 c_3 + \delta_3^3 \left[\frac{1}{3\delta_3} (c_4 - c_3) \right] \\ &= a_1 + \delta_1 (\delta_1 c_1) + \delta_2 (\delta_1 c_1) + \delta_2 (\delta_1 c_1) + \delta_2 (\delta_2 c_2) + \\ &\quad \delta_3 (\delta_1 c_1) + \delta_3 (\delta_1 c_2) + \delta_3 (\delta_2 c_2) + \delta_3 (\delta_2 c_3) + \\ &\quad \delta_3 (\delta_3 c_3) + \frac{\delta_2^2}{3} (c_3 - c_2) + \frac{\delta_3^2}{3} (c_4 - c_3) \end{aligned} \quad (C.13)$$

By inspection of Eq (C.13), the pattern formed by the δ_n and c_n

coefficients produces a general expression for a_n :

$$a_n = a_1 + \sum_{j=1}^{n-1} \delta_j \sum_{k=1}^j \delta_k c_k + \sum_{j=2}^{n-1} \delta_j \sum_{k=2}^j \delta_{k-1} c_k + \frac{1}{3} \sum_{j=2}^{n-1} \delta_j^2 (c_{j+1} - c_j) \quad (C.14)$$

Note that a_n is in terms of δ_n and c_n except for the term a_1 .

Substitution of Eq (C.7) for a_n on the right-hand side of Eq (C.14) evaluated at $n = M$ results in the following:

$$\left[a_1 + \sum_{j=1}^{M-1} \delta_j \sum_{k=1}^j \delta_k c_k + \sum_{j=2}^{M-1} \delta_j \sum_{k=2}^j \delta_{k-1} c_k + \frac{1}{3} \sum_{j=2}^{M-1} \delta_j^2 (c_{j+1} - c_j) \right] + \delta_M \left[\sum_{k=1}^{M-1} \delta_k c_k + \sum_{k=2}^M \delta_{k-1} c_k \right] + \delta_M^2 c_M + \delta_M^3 d_M = 0 \quad (C.15)$$

Equation (C.15) is solved for a_1 to produce

$$a_1 = - \left[\sum_{j=1}^M \delta_j \sum_{k=1}^j \delta_k c_k + \sum_{j=2}^M \delta_j \sum_{k=2}^j \delta_{k-1} c_k + \frac{1}{3} \sum_{j=2}^{M-1} \delta_j^2 (c_{j+1} - c_j) + \delta_M^3 d_M \right] \quad (C.16)$$

Substitution of Eq (C.16) into Eq (C.14) produces

$$a_n = \left[\sum_{j=1}^{n-1} \delta_j \sum_{k=1}^j \delta_k c_k - \sum_{j=1}^{M-1} \delta_j \sum_{k=1}^j \delta_k c_k - \delta_M \sum_{k=1}^M \delta_k c_k - \delta_M^2 c_M \right] +$$

$$\left[\sum_{j=2}^{n-1} \delta_j \sum_{k=2}^j \delta_{k-1} c_k - \sum_{j=2}^{M-1} \delta_j \sum_{k=2}^j \delta_{k-1} c_k - \delta_M \sum_{k=2}^M \delta_{k-1} c_k \right] +$$

$$\left[\frac{1}{3} \sum_{j=2}^{n-1} \delta_j^2 (c_{j+1} - c_j) - \frac{1}{3} \sum_{j=2}^{M-1} \delta_j^2 (c_{j+1} - c_j) \right] - \delta_M^3 d_M \quad (C.17)$$

The terms in the brackets may be combined to produce

$$a_n = - \sum_{j=n}^M \delta_j \sum_{k=1}^j \delta_k c_k - \sum_{j=n}^M \delta_j \sum_{k=2}^j \delta_{k-1} c_k - \frac{1}{3} \sum_{j=n}^{M-1} \delta_j^2 (c_{j+1} - c_j) - \delta_M^3 d_M \quad (C.18)$$

The recursion relationships for all the unknown coefficients of the piecewise defined polynomials of are summarized below:

$$a_n = - \sum_{j=n}^M \delta_j \sum_{k=1}^j \delta_k c_k - \sum_{j=n}^M \delta_j \sum_{k=2}^j \delta_{k-1} c_k - \frac{1}{3} \sum_{j=n}^{M-1} \delta_j^2 (c_{j+1} - c_j) - \delta_M^3 d_M \quad n = 1, 2, \dots, M \quad (C.18)$$

$$b_1 = 0 \quad (C.8)$$

$$b_n = \sum_{k=1}^{n-1} \delta_k c_k + \sum_{k=2}^n \delta_{k-1} c_k \quad n = 2, 3, \dots, M \quad (C.12b)$$

$$d_1 = 0 \quad (C.19)$$

$$d_n = \frac{1}{3\delta_n} (c_{n+1} - c_n) \quad n = 2, 3, \dots, M-1 \quad (C.9)$$

All polynomial coefficients are now expressed in terms of c_2, c_3, \dots, c_M and d_M , which must be determined from values of the averaged velocities. This is accomplished using Eqs (C.2) and (C.3)

which describe the averaged velocity in each interval:

$$\begin{aligned}
 a_1 + \frac{2}{3} \delta_1 b_1 + \frac{1}{2} \delta_1 c_1 &= u_1 \\
 a_2 + m_{b_2} b_2 + m_{c_2} c_2 + m_{d_2} d_2 &= u_2 \\
 &\vdots \\
 &\vdots \\
 &\vdots \\
 a_n + m_{b_n} b_n + m_{c_n} c_n + m_{d_n} d_n &= u_n
 \end{aligned} \tag{C.20}$$

where

$$\begin{aligned}
 m_{b_1} &= \frac{2}{3} \delta_1 \\
 m_{c_1} &= \frac{1}{2} \delta_1^2 \\
 m_{d_1} &= 0 \\
 m_{b_n} &= \frac{2}{3} \frac{\delta_n^2}{r_n + r_{n-1}} + r_{n-1} \frac{\delta_n}{r_n + r_{n-1}} \\
 m_{c_n} &= \frac{1}{2} \frac{\delta_n^3}{r_n + r_{n-1}} + \frac{2}{3} r_{n-1} \frac{\delta_n^2}{r_n + r_{n-1}} \\
 m_{d_n} &= \frac{2}{5} \frac{\delta_n^4}{r_n + r_{n-1}} + \frac{1}{2} r_{n-1} \frac{\delta_n^3}{r_n + r_{n-1}}
 \end{aligned} \tag{C.21}$$

Notice that coefficients m_{b_n} , m_{c_n} , and m_{d_n} in Eq (C.21) depend only on the known values of r_1 through r_n which are the locations of the flow intervals. These values of r_1 through r_n are selected at the beginning and never change over the course of the solution. Also, the

values of u_n are considered known since they are provided by the solution of the damped wave equations or as part of the set of initial conditions.

The coefficients a_n , b_n , and d_n in Eq (C.20) can be expressed in terms of c_1, c_2, \dots, c_M and d_M . For a circular line with four intervals, Eqs (C.2) and (C.3) may be written as

$$\begin{aligned}
 & c_2 [-\delta_1 (\delta_1 + \delta_2 + \delta_3 + \delta_4) - \delta_2 (\delta_2 + \delta_3 + \delta_4) - \delta_1 (\delta_2 + \delta_3 + \delta_4) - \frac{1}{3} \delta_2^2 + \frac{1}{2} \delta_1^2] + \\
 & c_3 [-\delta_3 (\delta_3 + \delta_4) - \delta_2 (\delta_3 + \delta_4) - \frac{1}{3} (\delta_2^2 - \delta_3^2)] + c_4 [-\delta_4^2 - \delta_4 \delta_3 - \frac{1}{3} \delta_3^2] + \\
 & d_4 (-\delta_4^3) = u_1
 \end{aligned} \tag{C.22a}$$

$$\begin{aligned}
 & c_2 [2\delta_1 m_{b_2} + m_{c_2} \frac{m_d}{3\delta_2} - 2\delta_1 (\delta_2 + \delta_3 + \delta_4) - \delta_2 (\delta_2 + \delta_3 + \delta_4) + \frac{1}{3} \delta_2^2] + \\
 & c_3 [\frac{m_d}{3\delta_2} - \delta_3 (\delta_3 + \delta_4) - \delta_2 (\delta_3 + \delta_4) - \frac{1}{3} (\delta_2^2 - \delta_3^2)] + c_4 [-\delta_4 (\delta_3 + \delta_4) - \frac{1}{3} \delta_3^2] + \\
 & d_4 (-\delta_4^3) = u_2
 \end{aligned} \tag{C.22b}$$

$$\begin{aligned}
 & c_2 [m_{b_3} (2\delta_1 + \delta_2) - 2\delta_1 (\delta_3 + \delta_4) - \delta_2 (\delta_3 + \delta_4)] + \\
 & c_3 [m_{b_3} \delta_2 + m_{c_3} \frac{m_d}{3\delta_3} - \delta_3 (\delta_3 + \delta_4) - \delta_2 (\delta_3 + \delta_4) + \frac{1}{3} \delta_3^2] + \\
 & c_4 [\frac{m_d}{3\delta_3} - \delta_4^2 - \delta_4 \delta_3 - \frac{1}{3} \delta_3^2] + d_4 (-\delta_4^3) = u_3
 \end{aligned} \tag{C.22c}$$

$$c_2 [m_{b_4} (2\delta_1 + \delta_2) - \delta_4 (2\delta_1 + \delta_2)] + c_3 [m_{b_4} (\delta_2 + \delta_3) - \delta_4 (\delta_3 + \delta_2)] +$$

$$c_4 [m_4 \delta_3 + m_4 - (\delta_4^2 + \delta_4 \delta_3)] + d_4 [m_4 - \delta_4^3] = u_4 \quad (C.22d)$$

In the above equations, all expressions in the square brackets are in terms of δ_1 through δ_4 , or equivalently, r_1 through r_4 . The value of these bracketed terms are known and behave as constants once the locations of the interval boundaries have been selected. Let l_1 , m_1 , p_1 , and q_1 represent the bracketed terms in Eq (C.22) which multiply c_2 , c_3 , c_4 , and d_4 respectively. Equations (C.22a-d) are now written in matrix form as

$$\begin{bmatrix} l_1 & m_1 & p_1 & q_1 \\ l_2 & m_2 & p_2 & q_2 \\ l_3 & m_3 & p_3 & q_3 \\ l_4 & m_4 & p_4 & q_4 \end{bmatrix} \begin{bmatrix} c_2 \\ c_3 \\ c_4 \\ d_4 \end{bmatrix} = \begin{bmatrix} u_1 \\ u_2 \\ u_3 \\ u_4 \end{bmatrix} \quad (C.23)$$

The unknowns, c_2 , c_3 , c_4 , and d_4 , are obtained by solving Eq (C.23):

$$\begin{bmatrix} c_2 \\ c_3 \\ c_4 \\ d_4 \end{bmatrix} = \begin{bmatrix} l_1 & m_1 & p_1 & q_1 \\ l_2 & m_2 & p_2 & q_2 \\ l_3 & m_3 & p_3 & q_3 \\ l_4 & m_4 & p_4 & q_4 \end{bmatrix}^{-1} \begin{bmatrix} u_1 \\ u_2 \\ u_3 \\ u_4 \end{bmatrix} \quad (C.24)$$

This velocity profile approximation may be extended to any number of intervals. The method for determining the unknown coefficients in the temperature profile polynomials is exactly the same as shown above.

The profile of $T - T_w$ is used instead of T to produce a value of zero at the wall.

APPENDIX D

Unsteady Turbulent Friction Model

From an analogy with laminar flow, the eddy viscosity formulation of Boussinesq has the form (61:180):

$$\tau_{\text{Turb}} = -\overline{\rho uv} = \mu_{\text{Turb}} \frac{\partial u}{\partial y} \quad (\text{D.1})$$

Prandtl suggested the mixing length formulation:

$$\tau_{\text{Turb}} = -\overline{\rho uv} = \rho \ell_m^2 \left| \frac{\partial u}{\partial y} \right| \frac{\partial u}{\partial y} \quad (\text{D.2})$$

where ℓ_m is some effective interaction distance between eddies. A relationship for ℓ_m as a function of the dependent variables is required to calculate τ_{Turb} . The eddy viscosity and the mixing length formulations are essentially equivalent since inspection of Eqs (D.1) and (D.2) shows

$$\mu_{\text{Turb}} = \rho \ell_m^2 \left| \frac{\partial u}{\partial y} \right| \quad (\text{D.3})$$

The steady state model for apparent viscosity may be used as a starting point in developing a model capable of describing transient effects. Very near the wall, viscous shear dominates producing an approximately linear velocity profile: $\tau_w = \mu \frac{\bar{u}}{y}$ for $0 \leq y^+ \leq 5$ and

$u^+ = y^+$, where $y^+ = \frac{yu_*}{\nu}$, $u^+ = \frac{\bar{u}}{u_*}$, and $u_* = \sqrt{\frac{\tau_w}{\rho}}$. Further from the wall both viscous and turbulent shear become important but the flow is still dominated by the pipe wall. The velocity profile in this logarithmic overlap region found at $50 \leq y^+ \leq 500$ is

$$u^+ = \frac{1}{\kappa} \ln(y^+) + C \quad (D.4)$$

The region described by $5 \leq y^+ \leq 70$ may be considered as a transition region over which an expression must connect the velocity profiles from the viscous sublayer and the inner layer. The linear velocity profile of the viscous sublayer must blend smoothly into the logarithmic velocity profile of the inner part of the inner layer (61:182).

Van Driest developed a means of describing the shear stress in this transition region (61:183). The shear stress can be expressed in the transition region as:

$$\tau + \tau_{\text{Turb}} = \mu \frac{\partial u}{\partial y} - \overline{\rho u v} = \tau_w \quad (D.5)$$

where τ is the laminar shear stress. In the logarithmic part of this transition region the turbulent shear stress dominates so that

$\tau_{\text{Turb}} \gg \tau$ and $\tau_w \approx \tau_{\text{Turb}}$. Applying the eddy viscosity formulation to τ_{Turb} , Eq (D.1) can be written as

$$\mu_{\text{Turb}} \frac{\partial u}{\partial y} = \tau_w \quad (D.6)$$

Additionally, the derivative of the log law in this region produces

$$\frac{\partial u}{\partial y} = u_* \frac{1}{\kappa y} \quad (D.7)$$

Substituting Eq (D.7) into Eq (D.6) produces an expression for the eddy viscosity:

$$\mu_{\text{Turb}} = \kappa \rho u_* y = \kappa \rho \sqrt{\frac{\tau_w}{\rho}} y \quad (D.8)$$

Van Driest represented the damping of turbulent eddies due to the presence of a rigid wall by an oscillating wall in a fluid at rest. This problem had previously been solved by Stokes (61:93). Van Driest applied the factor $1 - \exp(-\frac{y}{A})$, based on Stokes' solution, to obtain the damping effect of the wall. The result of Eqs (D.6) and (D.8) is used with Eq (D.5) to produce

$$\tau + \tau_{\text{Turb}} = \tau_w = \mu \frac{\partial u}{\partial y} + \rho \kappa^2 y^2 \left[1 - \exp\left(-\frac{y}{A}\right) \right]^2 \left| \frac{\partial u}{\partial y} \right| \frac{\partial u}{\partial y} \quad (D.9)$$

Van Driest found that $A = \frac{26\nu}{u_*}$ and $\kappa = 0.40$ accurately represented data in the wall region.

The Van Driest mixing length model for the entire inner region is

$$\ell_m = \kappa \left[1 - \exp\left(-\frac{yu_*}{26\nu}\right) \right] y \quad (D.10)$$

An expression for the eddy viscosity is found by comparison of Eq (D.10) with Eqs (D.1) and (D.2):

$$\mu_T = \rho \kappa^2 \left[1 - \exp \left(\frac{-yu_*}{26\nu} \right) \right]^2 y^2 \left| \frac{\partial u}{\partial y} \right| \quad (D.11)$$

This eddy viscosity model is valid only for fully-developed, steady, turbulent flow. The effect of the unsteadiness resulting from transient flow disturbances produced by traveling pressure waves must be included in this model to make it suitable for the purposes of this study. Cebeci accounts for unsteady effects by using τ_s instead of τ_w in the calculation of u_* (12:2153). The variable τ_s represents the shear stress evaluated at the edge of the viscous sublayer rather than at the wall. This is justified on the physical grounds that the random velocity fluctuations, damped according to the mechanism of the Stokes layer, do not extend all the way to the wall but disappear at the viscous sublayer. Cebeci approximated the momentum equation in the immediate vicinity of the wall of a flat plate to include only the effect of the pressure gradient (12:2153):

$$\frac{\partial \tau_s}{\partial y} = \frac{\partial p}{\partial x} \quad (D.12)$$

Tellonis recommends the unsteady velocity term be included in the approximation of the momentum equation by modifying Eq (D.12) (66:233):

$$\rho \frac{\partial u}{\partial t} = - \frac{\partial p}{\partial x} + \frac{\partial \tau_s}{\partial y} \quad (D.13)$$

τ_s is found by integrating from the wall to to the edge of the viscous sublayer denoted by y_s^+ . Cebeci chose $y^+ = 11.8$ as the boundary between the viscous sublayer and the log law layer based on the intersection of the log-law equation and the equation of the viscous sublayer for steady flow. The expressions $u^+ = \frac{1}{\kappa} \ln(y^+) + C$ and $u^+ = y^+$ are equal at $y^+ = y_s^+$. The intersection of the two equations can easily be seen in the universal wall law plot for a turbulent boundary layer on a smooth, solid surface (73:476).

Transforming Eq (D.13) to cylindrical coordinates for pipe flow and integrating from the edge of the viscous sublayer to the wall produces

$$\int_{r_s}^a \frac{\partial(r\tau)}{\partial r} dr = \int_{r_s}^a \rho \frac{\partial u}{\partial t} r dr + \int_{r_s}^a \frac{dp}{dx} r dr$$

Note that the coordinate y in Eq (D.13), measured out from the wall, has been replaced by the coordinate r whose origin is now at the center of the fluid line. Assuming that $\rho(p, T_w) = \rho_w$ near the wall, integration of the above equation produces:

$$a\tau_w - r_s\tau_s = \rho_w \int_{r_s}^a \frac{\partial u}{\partial t} r dr + (a - r_s) \frac{dp}{dx}$$

or solving for τ_s :

$$\tau_s = \frac{1}{r_s} \left[a\tau_w + (r_s - a) \frac{dp}{dx} + \rho_w \int_{r_s}^a \frac{\partial u}{\partial t} r dr \right] \quad (D.14)$$

The term, $\rho_w \int_{r_s}^a \frac{\partial u}{\partial t} r dr$, in Eq (D.14) must be evaluated.

The inner boundary, r_{n-1} , of the region containing the viscous sublayer is chosen to be less than r_s , where $r_s = a - y_s$ and $y_s = \frac{\nu y}{u_s}$. The velocity profile in this region is approximated by the piecewise continuous polynomials as

$$u(r) = a_M + b_M(r - r_{M-1}) + c_M(r - r_{M-1})^2 + d_M(r - r_{M-1})^3 \quad (D.15)$$

Equation (D.15) is the cubic velocity profile approximation used in Chapter II. For r_s contained in the interval adjacent to the wall, integration of this velocity profile function from r_s to the wall produces

$$\begin{aligned} \int_{r_s}^{r_M} u_M r dr &= \frac{a_M}{2} (r_M - r_s^2) + b_M \left\{ \frac{1}{3} \left[(r_M - r_{M-1})^3 - (r_s - r_{M-1})^3 \right] + \right. \\ &\quad \left. \frac{r_{M-1}}{2} \left[(r_M - r_{M-1})^2 - (r_s - r_{M-1})^2 \right] \right\} + c_M \left\{ \frac{1}{4} \left[(r_M - r_{M-1})^4 - (r_s - r_{M-1})^4 \right] + \right. \\ &\quad \left. \frac{r_{M-1}}{3} \left[(r_M - r_{M-1})^3 - (r_s - r_{M-1})^3 \right] \right\} + d_M \left\{ \frac{1}{5} \left[(r_M - r_{M-1})^5 - (r_s - r_{M-1})^5 \right] + \right. \\ &\quad \left. \frac{r_{M-1}}{4} \left[(r_M - r_{M-1})^4 - (r_s - r_{M-1})^4 \right] \right\} \quad (D.16) \end{aligned}$$

Equation (D.14) can now be evaluated at each time step as the equations developed in Chapter II and III are solved numerically. Once τ_s is found, the unsteady value for the Van Driest damping factor A is easily calculated at each time step:

$$A = \frac{26\nu}{u_s} \quad (D.17)$$

where $u_s = \sqrt{\frac{\tau_s}{\rho}}$. The expression for the mixing length for pipe flow can be written from Eq (D.10):

$$\ell = 0.41(a - r) \left\{ 1 - \exp \left[\frac{-(a - r)}{A} \right] \right\} \quad (D.18)$$

This expression for the mixing length is an extension of the model developed by Cebeci in which Van Driest's damping factor is modified to include the effect of the time varying velocity in addition to the time varying pressure gradient (65:1000).

The Clauser eddy viscosity model is assumed to hold in the outer layer for flat plate flow:

$$\epsilon_o = \rho \kappa_2 U_c \delta^*$$

where $\kappa_2 = 0.0168$ and δ^* is the displacement thickness. The eddy viscosity is assumed to be constant across the outer layer. White points out that the outer layer is commonly neglected in pipe flow

since it has little effect on the analysis and the lack of intermittence in duct flow produces greatly increased turbulence at the centerline as compared to flow over a flat plate (73:473). As a result, Eq (D.11) will be used to calculate eddy viscosity from the wall to the centerline of the transmission line with no special expression governing the outer layer.

APPENDIX E

Development of Modal Superposition

Separation of Variables

To find the modal representation of Eq (90) f is expressed as the product of mode shapes $G_i(x)$ times modal general coordinates $\xi_i(t)$ (31:429). Thus f is written as

$$f = \sum_{i=0}^{\infty} G_i(x) \xi_i(t) \quad (E.1)$$

This technique is commonly applied to linear partial differential equations and is known as separation of variables, the product method, or Fourier's method (53:50). Homogeneous boundary conditions are required for this method to work. Substitution of Eq (E.1) into Eq (90) produces

$$\frac{\rho}{A\xi_i} \frac{\partial^2 \xi_i}{\partial t^2} + \frac{\rho F}{A\xi_i} \frac{\partial \xi_i}{\partial t} - \frac{\rho c^2}{AG_i} \frac{\partial^2 G_i}{\partial x^2} = 0 \quad (E.2)$$

The forcing function on the right-hand side of Eq (88) has been set to zero so that the modal frequencies can be found (32:82). In the absence of a forcing function, $\frac{\partial f}{\partial x}$ must vanish at each end of the line as a result of Eq (87). Since $\left. \frac{\partial p}{\partial t} \right|_{x=0}$ and $\left. \frac{\partial p}{\partial t} \right|_{x=L}$ are zero, separation of variables requires the following to be true:

$$\frac{1}{\xi_1} \left[\frac{\partial^2 \xi_1}{\partial t^2} + F \frac{\partial \xi_1}{\partial t} \right] = \frac{c^2}{G_1} \frac{\partial^2 G_1}{\partial x^2} = -\omega^2 \quad (\text{E.3})$$

Equation (E.3) provides an expression for the mode shapes:

$$c^2 \frac{\partial^2 G_1}{\partial x^2} + G_1 \omega_1^2 = 0 \quad (\text{E.4})$$

The boundary conditions for Eq (E.4) are

$$\frac{\partial f}{\partial x}(0, t) = 0 \quad (\text{E.5a})$$

$$\frac{\partial f}{\partial x}(L, t) = 0 \quad (\text{E.5b})$$

A general solution is assumed for $G_1(x)$:

$$G_1(x) = B \cos\left(\frac{i\pi x}{L}\right) + D \sin\left(\frac{i\pi x}{L}\right) \quad (\text{E.6})$$

The boundary conditions of Eq (E.5) require that $D = 0$. Assuming $B = 1$ the substitution of Eq (E.6) into Eq (E.2) and Eq (E.2) into Eq (E.1) produces

$$\frac{\rho}{A} \cos\left(\frac{i\pi x}{L}\right) \frac{\partial^2 \xi_1}{\partial t^2} + \frac{\rho F}{A} \cos\left(\frac{i\pi x}{L}\right) \frac{\partial \xi_1}{\partial t} + \frac{\rho c^2 i^2 \pi^2}{AL^2} \cos\left(\frac{i\pi x}{L}\right) \xi_1 = \frac{\dot{e}_1 + \dot{e}_2}{L} \quad (\text{E.7})$$

The orthogonality of the mode shapes may be used by, first, multiplying both sides of Eq (E.7) by $\cos\left(\frac{j\pi x}{L}\right)$ and then integrating over x from 0 to L . The dependence on x is removed from Eq (E.7):

$$\frac{\rho L}{2A} \frac{\partial^2 \xi_1}{\partial t^2} + \frac{\rho L F}{2A} \frac{\partial \xi_1}{\partial t} + \frac{\rho c^2 l^2 \pi^2}{2AL} \xi_1 = \dot{e}_1 + \dot{e}_2 (-1)^1 \quad (E.8)$$

Integration over time produces

$$\frac{\rho L}{2A} \frac{\partial \xi_0}{\partial t} + \frac{\rho L F}{2A} \xi_0 = e_1 + e_2 \quad (E.9)$$

$$\frac{\rho L}{2A} \frac{\partial \xi_1}{\partial t} + \frac{\rho L F}{2A} \xi_1 + \frac{\rho c^2 l^2 \pi^2}{2AL} \int_0^t \xi_1 dt = e_1 + e_2 (-1)^1 \quad (E.10)$$

Karnopp points out that Eq (E.9) represents the line as a single, lumped inertia while Eq (E.10) represents a collection of modal oscillators (31:439).

Residual Compliance

The residual compliance is calculated from Eq (E.10) at steady state with the mass and resistance elements suppressed (32:84). First, define two new variables; $q_1 = \int_0^t \xi_1 dt$ and $p_1 = \int_0^t e_1 dt$ where q_1 and p_1 represent the generalized displacement and the generalized momentum of the 1th mode, respectively. Equations (E.9) and (E.10) may be rewritten in terms of these new variables:

$$\frac{\rho L}{2A} \frac{\partial^2 q_0}{\partial t^2} + \frac{\rho L F}{2A} \frac{\partial q_0}{\partial t} = e_1 + e_2 \quad (E.11a)$$

$$\frac{\rho L}{2A} \frac{\partial^2 q_1}{\partial t^2} + \frac{\rho L F}{2A} \frac{\partial q_1}{\partial t} + \frac{\rho c^2 l^2 \pi^2}{2AL} q_1 = e_1 + e_2 (-1)^1 \quad (\text{E.11b})$$

At frequencies above ω_0 the stiffness term $\left[\frac{\rho c^2 l^2 \pi^2}{2AL} \right]^{-1}$ in Eq (E.11b) dominates the transient response:

$$q_1 = \frac{2AL}{\rho c^2 l^2 \pi^2} \left[e_1 + e_2 (-1)^1 \right] \quad (\text{E.12})$$

This expression may be thought of in terms of the displacement of a spring due to the application of a force displacement = force/stiffness. Using Eqs (E.1), (E.6) and the definition of q_1 where $q_1 = \int^t \xi_1 dt$, Eq (E.12) produces the following:

$$\begin{aligned} \int^t f_{s1} dt &= \sum_{i=0}^{\infty} G_i(0) q_1(t) = \sum_{i=0}^{\infty} (1)^i \frac{2AL}{\rho c^2 l^2 \pi^2} \left[e_1 + e_2 (-1)^1 \right] \\ \int^t f_{s2} dt &= \sum_{i=0}^{\infty} G_i(L) q_1(t) = \sum_{i=0}^{\infty} (-1)^i \frac{2AL}{\rho c^2 l^2 \pi^2} \left[e_1 + e_2 (-1)^1 \right] \end{aligned} \quad (\text{E.13})$$

Equation (E.13) may be written in the following form:

$$\begin{bmatrix} c_{11} & c_{12} \\ c_{21} & c_{22} \end{bmatrix} \begin{bmatrix} e_1 \\ e_2 \end{bmatrix} = \frac{2AL}{\rho c^2 \pi^2} \begin{bmatrix} \sum_{i=0}^{\infty} \frac{1}{i^2} & \sum_{i=0}^{\infty} \frac{1}{i^2} (-1)^i \\ \sum_{i=0}^{\infty} \frac{1}{i^2} (-1)^i & \sum_{i=0}^{\infty} \frac{1}{i^2} \end{bmatrix} \begin{bmatrix} e_1 \\ e_2 \end{bmatrix} \quad (\text{E.14})$$

Inspection of Eq (E.14) produces the residual compliance matrix. Since this residual compliance will be used to represent modes with frequencies greater than ω_0 , let i in Eq (E.14) become $n+j$ where n is the highest mode retained. The residual compliance is now written as

$$C_{eq} = \begin{bmatrix} c_{11} & c_{12} \\ c_{21} & c_{22} \end{bmatrix} = \frac{2AL}{\rho c^2 \pi^2} \begin{bmatrix} \sum_{j=1}^{\infty} \frac{1}{(n+j)^2} & \sum_{j=1}^{\infty} \frac{(-1)^j}{(n+j)^2} \\ \sum_{j=1}^{\infty} \frac{(-1)^j}{(n+j)^2} & \sum_{j=1}^{\infty} \frac{1}{(n+j)^2} \end{bmatrix} \quad (E.15)$$

Complementary Equations

The same electrical analogies used in developing Eq (106), (107), (111), and (112) are used to develop a complementary system of equations. Development of this system of equations is summarized below:

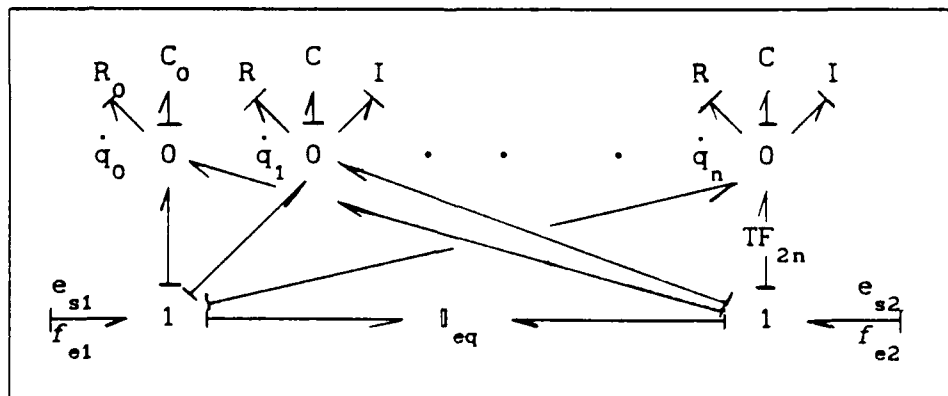


Fig. E.1. Bond Graph for Equations (E.16) and (E.17) with Flow Inputs at Each End

The variables i_{11} are elements of the residual inertance I_{eq} which is obtained in the same manner as the residual compliance C_{eq} :

$$I_{eq} = \begin{bmatrix} i_{11} & i_{12} \\ i_{21} & i_{22} \end{bmatrix} = \frac{2\rho L}{\pi^2 A} \begin{bmatrix} \sum_{j=1}^{\infty} \frac{1}{(n+j)^2} & \sum_{j=1}^{\infty} \frac{(-1)^{n+j}}{(n+j)^2} \\ \sum_{j=1}^{\infty} \frac{(-1)^{n+j}}{(n+j)^2} & \sum_{j=1}^{\infty} \frac{1}{(n+j)^2} \end{bmatrix} \quad (E.21)$$

The elements of the R, K, and M matrices are calculated as follows:

Table E.1
Inertia, Capacitance, and Resistance Parameters

	I_1	C_1	R_1
$i=0$	∞	$\frac{AL}{\rho c^2}$	$\frac{LAF}{\rho c^2}$
$i=1, 2,$	$\frac{2\rho L}{i^2 \pi^2 A}$	$\frac{AL}{2\rho c^2}$	$\frac{LAF}{2\rho c^2}$

As shown in Chapter V, it is possible to more accurately determine the M, K, and R matrices as well as a G matrix to account for heat transfer effects. Equations (E.19a,b) are written in terms of frequency dependent parameters:

$$L I \frac{\partial^2 q_0}{\partial t^2} + L R \frac{\partial q_0}{\partial t} = 0 \quad (E.22a)$$

$$\frac{L}{2} I \frac{\partial^2 q_1}{\partial t^2} + \frac{L}{2} R \frac{\partial q_1}{\partial t} + \frac{L}{2} \left(\frac{l^2 \pi^2}{L^2} \frac{1}{C} + \frac{R G}{C} \right) q_1 = 0 \quad (\text{E.22b})$$

The complementary formulation for Eqs (E.17) and (E.18) are written as

$$L C_0 \frac{\partial^2 q_0}{\partial t^2} + L \left(G_0 + \frac{R_0 C_0}{I_0} \right) \frac{\partial q_0}{\partial t} = 0 \quad (\text{E.23a})$$

$$\frac{L}{2} C_1 \frac{\partial^2 q_1}{\partial t^2} + \frac{L}{2} \left(G_1 + \frac{R_1 C_1}{I_1} \right) \frac{\partial q_1}{\partial t} + \frac{L}{2} \left(\frac{l^2 \pi^2}{L^2} \frac{1}{I_1} + \frac{R_1 G_1}{I_1} \right) q_1 = 0 \quad (\text{E.23b})$$

Tables E.2 and E.3 replace Tables 3 and E.1 respectively for Eqs (E.22a,b) and (E.23a,b).

Modal Frequencies

The modal frequencies for the systems shown in Figures 3, 4, E.1, and E.2 may be approximated from the two systems of modal equations and output relations developed above. The transmission line configuration shown in Figure 12 is used as an example. Neglecting the damping terms, Eqs (106) and (107) are combined and written as

$$M \frac{d^2 q}{dt^2} + K q - H^T [e_{s1}, e_{s2}] = 0 \quad (\text{E.24})$$

Table E.2

Inertia, Capacitance, and Resistance Parameters

	I_1	C_1	R_1
$i=0$	LI_0	∞	$L \left(\frac{I_0 G_0}{C_0} + R_0 \right)$
$i=1, 2,$	$\frac{L}{2} \frac{-I_1}{I_1}$	$\frac{\ell \left(1^2 \pi^2}{2 \left(\frac{C_1 L^2}{C_1} + \frac{R_1 G_1}{C_1} \right)} \right)$	$\frac{L}{2} \left(\frac{I_1 G_1}{C_1} + R_1 \right)$

Table E.3

Inertance, Capacitance, and Resistance Parameters

	I_1	C_1	R_1
$i=0$	∞	LC_0	$\left\{ L \left(\frac{R_0 C_0}{I_0} + G_0 \right) \right\}^{-1}$
$i=1, 2,$	$\frac{L}{2} \left(\frac{1^2 \pi^2}{C_1 L^2} + \frac{R_1 G_1}{I_1} \right)^{-1}$	$\frac{L}{2} \frac{-C_1}{C_1}$	$\left\{ \frac{L}{2} \left(\frac{R_1 C_1}{I_1} + G_1 \right) \right\}^{-1}$

With $e_{e1} = 0$ and $f_{e2} = 0$, Eq (5.30) produces

$$e_{s2} = - \frac{1}{c_{22}} L_2 H q \quad (E.25)$$

Substitution of Eq (E.25) into Eq (E.24) with $e_{e1} = 0$ produces

$$\frac{d^2 \mathbf{q}}{dt^2} + \mathbf{M}^{-1} \left(\mathbf{K} \mathbf{q} - \mathbf{H}^T \left[0, -\frac{1}{c_{22}} \mathbf{L}_2 \mathbf{H} \mathbf{q} \right] \right) = 0 \quad (\text{E.26})$$

Assuming a solution of the form $q_1 = \sin(\omega_1 + \theta)$ for Eq (E.26) produces

$$\left\{ \omega_1^2 \mathbf{I} - \mathbf{M}^{-1} \left(\mathbf{K} + \mathbf{L}_2 \mathbf{H}^T \frac{1}{c_{22}} \mathbf{L}_2 \mathbf{H} \right) \right\} \mathbf{q} = 0 \quad (\text{E.27})$$

where \mathbf{I} is the identity matrix in this case. The modal frequencies may be determined by setting the determinant of the bracketed term of Eq (E.27) to zero and solving for ω_1 . Similar expressions may be developed for other transmission line configurations.

Bibliography

1. Abbot, M. B. The Method of Characteristics. New York: American Elsevier, 1966.
2. Anderson, D. A., J. C. Tannehill and R. H. Pletcher. Computational Fluid Mechanics and Heat Transfer. New York: McGraw-Hill, 1984.
3. Benson, R. S., R. D. Garg and D. Woolatt. "A Numerical Solution of Unsteady Flow Problems," International Journal of Mechanical Sciences, 6: 117-144 (1964).
4. Blevins, R.D. Applied Fluid Dynamics Handbook. New York: Van Nostrand Reinhold, 1984.
5. Braden, R. P. "Fluid Line Dynamics with Through Flow and Finite Amplitude Disturbances," PhD thesis, Oklahoma State University, July 1973.
6. Bradshaw, P., D. H. Feriss and N. D. Altwell. "Calculation of Boundary Layer Development Using the Turbulent Energy Equation," Journal of Fluid Mechanics, 28: 593-616 (1967).
7. Brown, F. T., "The Transient Response of Fluid Lines," Journal of Basic Engineering, Trans. ASME, Series D, 84(3): 547-553 (December 1962).
8. Brown, F. T. "A Unified Approach to the Analysis of Uniform One-Dimensional Distributed Systems," Journal of Basic Engineering, Trans. ASME, Series D, 89(2): 423-432 (June 1967).
9. Brown, F. T. "A Quasi Method of Characteristics with Application to Fluid Lines with Frequency Dependent Wall Shear and Heat Transfer," Journal of Basic Engineering, Trans. ASME, Series D, 91(2): 217-227 (June 1969).
10. Brown, F. T. "Wave Propagation in Tubes with Turbulent Flow - 1. Analytical Models," Fluid Transmission Line Dynamics. New York: ASME Special Publication, 1981.
11. Brown, F. T., D. L. Margolis and R. P. Shah. "Small-Amplitude Frequency Behavior of Fluid Lines with Turbulent Flow," Journal of Basic Engineering, Trans. ASME, Series D, 91(4): 678-693 (December 1969).
12. Cebeci, T. "Behavior of Turbulent Flow near a Porous Wall with Pressure Gradient," AIAA Journal, 8(12): 2152-2156 (December 1970).

13. Cebeci, T. "Calculation of Compressible Turbulent Boundary Layers with Heat and Mass Transfer," AIAA Journal, 9(6): 1091-1097 (June 1971).
14. Cebeci, T. and A. M. O. Smith. Analysis of Turbulent Boundary Layers. New York: Academic Press, 1974.
15. Chakravarthy, S. R., D. A. Anderson and M. D. Salas. "The Split-Coefficient Matrix Method for Hyperbolic Systems of Gasdynamic Equations," AIAA Paper No 80-0268, Pasadena, California, (1980).
16. Chaudhry, M. H. and M. Y. Hussaini. "Second-Order Explicit Finite-Difference Methods for Transient Flow Analysis," Numerical Methods for Fluid Transient Analysis, edited by C. S. Martin and M. H. Chaudhry. New York: ASME Special Publication, 1983.
17. Chipman, R. A. Theory and Problems of Transmission Lines. New York: McGraw-Hill, 1968.
18. Conte, S. D. and C. deBoor. Elementary Numerical Analysis. New York: McGraw-Hill, 1980.
19. Funk, J. E. and T. R. Robe. "Transients in Pneumatic Transmission Lines Subjected to Large Pressure Changes," ASME Paper No 69-FLCS-42 (1969).
20. Funk, J. E. and D. J. Wood. "Frequency Response of Fluid Lines with Turbulent Flow," Journal of Fluids Engineering, Trans. ASME, Series I, 96(4): 365-369 (December 1974).
21. Gabutti, B. "On Two Upwind Finite_Difference Schemes for Hyperbolic Equations in Non-Conservative Form," Computers and Fluids, 11: 207-230 (1983).
22. Goodson, R. E. and R. G. Leonard. "A Survey of Modeling Techniques for Fluid Line Transients," Journal of Basic Engineering, Trans. ASME, Series D, 94(2): 474-482 (June 1972).
23. Holmboe, E. L. and W. T. Rouleau. "The Effect of Viscous Shear on Transients in Liquid Lines," Journal of Basic Engineering, Trans. ASME, Series D, 89(1): 174-180 (March 1967).
24. Hullender, D. A. "Time Domain Simulation of Fluid Transmission Lines Using Minimum Order State Variables," Fluid Transmission Line Dynamics, Volume II, edited by M. E. Franke and T. M. Drzewiecki. 78-97. New York: ASME Special Publication, 1983.
25. Hsu, C. Y. and D. A. Hullender. "Modal Approximations for the Fluid Dynamics of Hydraulic and Pneumatic Transmission Lines," Fluid Transmission Line Dynamics, Volume II, edited by M. E. Franke and T. M. Drzewiecki. 51-77. New York: ASME Special Publication, 1983.

26. Iberall, A. S. "Attenuation of Oscillatory Pressures in Instrument Lines," Journal of Research, National Bureau of Standards, 45: 85-108 (1950).
27. Isaacson, E. and Keller, H. B. Analysis of Numerical Methods, New York: John Wiley and Sons, 1966.
28. Kantola, R. "Transient Response of Fluid Lines Including Frequency Modulated Inputs," Journal of Basic Engineering, Trans. ASME, Series D, 93(2): 274-282 (June 1971).
29. Karam, J. T. and M. E. Franke. "The Frequency Response of Pneumatic Lines," Journal of Basic Engineering, Trans. ASME, Series D, 90(2): 371-378 (June 1967).
30. Karam, J. T. and R. G. Leonard, Jr. "A Simple Yet Theoretically Based Time Domain Model for Fluid Transmission Line Systems," Journal of Fluid Engineering, Trans. ASME, Series I, 95(4): 498-504 (December 1973).
31. Karnopp, D. "Lumped Parameter Models of Acoustic Filters Using Normal Modes and Bond Graphs," Journal of Sound and Vibration, 42(4): 437-446 (October 1975).
32. Karnopp, D. and R. Rosenberg. Analysis and Simulation of Multiport Systems. Cambridge: The M.I.T. Press, 1968.
33. Katz, S. "Transient Response of Terminated Pneumatic Transmission Lines by Frequency Response Conversion," ASME Paper No 75-WA/FLCS-4 (1975).
34. Katz, S., A. Hausner and N. A. Eisenberg. "The Effect of Throughflow on Signal Propagation in Fluid Lines," presented at: Harry Diamond Laboratories Fluidic State-of-the-Art Symposium 30 Sep-4 Oct 1974, 269-297, Adelphi, Md.
35. Kirmse, R. E. "Investigations of Pulsating Turbulent Pipe Flow," Journal of Fluids Engineering, Trans. ASME, Series I, 101: 436-442 (December 1979).
36. Kirshner, J. M. and S. Katz. Design Theory of Fluidic Components. New York : Academic Press Inc., 1975.
37. Krishnaiyer, R. and T. J. Lechner, Jr. "An Experimental Evaluation of Fluidic Transmission Line Theory." Advances in Fluidics. Edited by F.T. Brown et al. 367-389. New York: American Society of Mechanical Engineers, 1967.
38. Lapidus, A. "Shock Calculation by Second-Order Finite Differences," Journal of Computational Physics, 2:154-177 (1967).

39. Launder, B. E. "Turbulence Models: Present Status and Future Prospects," Reviews in Viscous Flow, Proceedings of the Lockheed-Georgia Company Viscous Flow Symposium, June 22-23 1976: 415-445, (LG77ER0044).
40. Lebrun, M. "Normal Modes in Hydraulic Lines," Proceedings of the American Control Conference, June 6-8 1984, Vol 1. 458-467. New York: IEEE, 1984.
41. Manning, J. R. "Computerized Method of Characteristics Calculations for Unsteady Pneumatic Line Flows," Journal of Basic Engineering, Trans. ASME, Series D, 90(2): 231-240 (June 1968).
42. Margolis, D. L. "Bond Graphs for Distributed System Models Admitting Mixed Causal Inputs," Journal of Dynamic Systems, Measurement, and Control, Trans. ASME, 102: 94-100 (June 1980).
43. Margolis, D. L. and F. T. Brown. "Measurement of the Propagation of Long-Wavelength Disturbances Through Turbulent Flow in Tubes," Journal of Fluids Engineering, Trans. ASME, Series I, 98(1): 70-78 (March 1976).
44. Mercier, O. L. and D. Wright. "A Dynamic Modeling Method of Unsteady Flows in Long Fluid Lines with Turbulent Bulk Velocities," Journal of Fluids Engineering, Trans. ASME, Series I, 95(3): 459-466 (September 1973).
45. Moore, E. F. and M. E. Franke. "Approximations for Frequency Dependent Attenuation in Circular and Noncircular Lines with Turbulent Mean Flow," Unpublished Paper.
46. Moretti, G. "The λ -Scheme," Computers and Fluids, 7: 191-205 (1979).
47. Morris, N. F. "The Use of Modal Superposition in Nonlinear Dynamics," Computers and Structures, 7: 65-72 (1977).
48. Nee, V. W. and S. G. Kovaszny. "Simple Theory of Turbulent Shear Flows," The Physics of Fluids, 12(9): 473-484 (1969).
49. Nichols, N. B. "The Linear Properties of Pneumatic Transmission Lines," Transactions of the Instrument Society of America, 1: 5-14 (January 1962).
50. Oldenburger, R. and R. E. Goodson. "Simplification of Hydraulic Line Dynamics by Use of Infinite Products," Journal of Basic Engineering, Trans. ASME, Series D, 86(1): 1-10 (March 1964).
51. Orner, P. A. "Linear Dynamic Modeling of Flowing Fluid Lines," Journal of Basic Engineering, Trans. ASME, Series D, 91(4): 740-749 (December 1969).

52. Pletcher, J. H., Jr. "An Analytical and Experimental Study of Aircraft Hydraulic Lines Including the Effect of Mean Flow," PhD thesis, Air Force Institute of Technology, 1979.
53. Powers, D. L., Boundary Value Problems. New York: Academic Press, 1972.
54. Reddy, V., J. B. McLaughlin and R. J. Nunge. "A Numerical Study of Pulsed Turbulent Pipe Flow," Journal of Fluids Engineering, Trans. ASME, Series I, 107: 205-211 (June 1985).
55. Rohmann, C. P. and E. C. Grogan. "On the Dynamics of Pneumatic Transmission Lines," Trans. ASME, 79: 853-874 (1957).
56. Romaniuk, M. S. and D. P. Telionis. "Turbulence Models for Oscillating Boundary Layers," Paper No 79-0069, 17th Aerospace Sciences Meeting, New Orleans, La., 15-17 January, 1979.
57. Rubesin, M. W. "A One-Equation Model of Turbulence For Use with the Compressible Navier-Stokes Equations," NASA TM-X-73-128 (1976).
58. Rubesin, M. W. and W. C. Rose. "The Turbulent Mean-Flow, Reynolds Stress, And Heat Flux Equations in Mass Averaged Dependent Variables," NASA TM-X-62,248 (1973).
59. Sandoz, S. A. "Intermediate Amplitude Response of Fluidic Transmission Lines," PhD thesis, Stanford University, March 1973.
60. Sandoz, S. A. and J. R. Manning. "Modeling of Fluidic Transmission Lines for Intermediate Amplitude Signals," Fluidics Quarterly, 6(2): 1-11 (1974).
61. Schetz, J., Foundations of Boundary Layer Theory for Momentum, Heat, and, Mass Transfer. Englewood Cliffs: Prentice Hall, 1984.
62. Schmidtberg, R. and T. Pal. "Solving Vibration Problems Using Modal Analysis," Sound and Vibration, Instrumentation Reference Issue, 16-21 (March 1986).
63. Shih, C. C. "Attenuation Characteristics of Nonlinear Pressure Waves Propagating in Pipes," Proceedings 1973 Symposium on Finite Amplitude Wave Effects in Fluids, Copenhagen, Denmark 20-22 August 1973: 81-87, Guildford, Surrey England: IPC Sci. Technol. Press (1974).
64. Streeter, V. L. and E. B. Wylie. Hydraulic Transients. New York: Mc-Graw-Hill, 1967.
65. Telionis, D. P. "On the Dynamics of Eddy Viscosity Models for Turbulent Boundary Layers," Archives of Mechanics, 28: 997-1010 (1976).

66. Telionis, D. P. Unsteady Viscous Flows. New York: Springer Verlag, 1981.
67. Telionis, D. P. and D. T. Tsahalis. "Unsteady Turbulent Boundary Layers and Separation," AIAA Journal, 14(4): 468-474 (April 1976).
68. Thompson, J. G. and Kohr, R. H. "Modeling and Compensation of Nonlinear Systems Using Sensitivity Analysis," Journal of Basic Engineering, Trans. ASME, Series D, 90(2): 187-194 (June 1968).
69. Trikha, A. K. "An Efficient Method for Simulating Frequency-Dependent Friction in Transient Liquid Flow," Journal of Fluids Engineering, Trans. ASME, Series I, 98(1): 97-105 (March 1975).
70. Tsao, S. "Numerical Solutions of Transients in Pneumatic Networks - Transmission-Line Calculations," Journal of Applied Mechanics, Trans. ASME, Series D, 92(4): 588-595 (September 1968).
71. Tsang, S. H. L., M. W. Benson and R. H. Granberg. "The Open and Blocked Distributed Air Transmission Lines by the Fast Fourier Transform Method," Journal of Dynamic Systems, Measurement, and Control, 107: 213-219 (September 1985).
72. Vliegenthart, A. C. "The Shuman Filtering Operator and the Numerical Computation of Shock Waves," Journal of Engineering Mathematics, 4(4): 341-348 (October 1970).
73. White, F. M. Viscous Fluid Flow. New York: McGraw-Hill, 1974.
74. Wood, D. J. and J. E. Funk. "A Boundary-Layer Theory for Transient Viscous Losses in Turbulent Flow," Journal of Basic Engineering, Trans. ASME, Series D, 92(4): 865-873 (December 1970).
75. Wylie, E. B. and V. L. Streeter. Fluid Transients. New York: McGraw-Hill, 1978.
76. Yoshioka, M. "Transient Phenomena in Pneumatic Transmission Lines: Part I - Model Comparison on the Basis of Step Response of Semi-Infinite Lines," The Journal of Fluid Control/Fluidics Quarterly, 14: 1-17 (1983).
77. Yoshioka, M. "Transient Phenomena in Pneumatic Transmission Lines: Part II - Step Response of Throat-Terminated Transmission Lines," The Journal of Fluid Control/Fluidics Quarterly, 14: 18-34 (1983).
78. Yoshioka, M. "Transient Phenomena in Pneumatic Transmission Lines: Part III - Dynamics of Volume-Terminated Transmission Lines," The Journal of Fluid Control/Fluidics Quarterly, 14: 35-48 (1983).

79. Yoshioka, M. "Transient Phenomena in Pneumatic Transmission Lines: Part IV. A Basic Approach to Transient Phenomena in Branched Lines," The Journal of Fluid Control/Fluidics Quarterly, 15: 5-21 (1983).
80. Yoshioka, M. "Transient Phenomena in Pneumatic Transmission Lines: Part V. Non-Reflection Matching of Branched Transmission Lines," The Journal of Fluid Control/Fluidics Quarterly, 15: 22-40 (1983).
81. Yoshioka, M. "Transient Phenomena in Pneumatic Transmission Lines: Part VI. Step Response of Branched Transmission Lines with Volume Terminations," The Journal of Fluid Control/Fluidics Quarterly, 15: 41-63 (1983).
82. Zielke, W. "Frequency-Dependent Friction in Transient Pipe Flow," Journal of Basic Engineering, Trans. ASME, Series D, 90(1): 109-115 (March 1968).

Vita

Captain Wayne P. Chepren [REDACTED]
[REDACTED]
[REDACTED]

[REDACTED] in 1970 [REDACTED] attended Worcester Polytechnic Institute, from which he received a Bachelor of Science in Mechanical Engineering in June 1974. Upon graduation, he worked for Stone and Webster Engineering and Maseonellan, International in quick succession, returning to Worcester Polytechnic Institute where he received his Master of Science in Mechanical Engineering in June 1979. Following a lengthy vacation, he received a commission in the USAF through OTS and served as a project officer on the Peacekeeper Missile Program until entering the Air Force Institute of Technology, in June 1984. He is presently chief of the Environmental Sciences Branch of the Engineering and Services Laboratory, Headquarters, Air Force Engineering and Services Center, Tyndall AFB, Florida.

[REDACTED] [REDACTED]
[REDACTED]

UNCLASSIFIED

SECURITY CLASSIFICATION OF THIS PAGE

REPORT DOCUMENTATION PAGE

Form Approved
OMB No. 0704-0188

1. REPORT SECURITY CLASSIFICATION UNCLASSIFIED			1b. RESTRICTIVE MARKINGS		
2a. SECURITY CLASSIFICATION AUTHORITY			3. DISTRIBUTION / AVAILABILITY OF REPORT Approved for public release; distribution unlimited		
2b. DECLASSIFICATION / DOWNGRADING SCHEDULE					
4. PERFORMING ORGANIZATION REPORT NUMBER(S) AFIT/DS/ENY/89-2			5. MONITORING ORGANIZATION REPORT NUMBER(S)		
6a. NAME OF PERFORMING ORGANIZATION School of Engineering		6b. OFFICE SYMBOL (If applicable) AFIT/EN		7a. NAME OF MONITORING ORGANIZATION	
6c. ADDRESS (City, State, and ZIP Code)				7b. ADDRESS (City, State, and ZIP Code)	
8a. NAME OF FUNDING / SPONSORING ORGANIZATION		8b. OFFICE SYMBOL (If applicable)		9. PROCUREMENT INSTRUMENT IDENTIFICATION NUMBER	
8c. ADDRESS (City, State, and ZIP Code)				10. SOURCE OF FUNDING NUMBERS	
				PROGRAM ELEMENT NO.	PROJECT NO.
11. TITLE (Include Security Classification) FLUID TRANSMISSION LINE DYNAMICS FOR SIGNALS OF FINITE AMPLITUDE					
PERSONAL AUTHOR(S) Wayne P. Chepren, B.S., M.S., Capt, USAF					
13a. TYPE OF REPORT PhD Dissertation		13b. TIME COVERED FROM _____ TO _____		14. DATE OF REPORT (Year, Month, Day) 1989 December	
15. PAGE COUNT 279					
16. SUPPLEMENTARY NOTATION					
17. COSATI CODES			18. SUBJECT TERMS (Continue on reverse if necessary and identify by block number) Fluid Transmission Line Finite Amplitude Signal Modal Superposition Finite Difference		
FIELD	GROUP	SUB-GROUP			
20	04				
19. ABSTRACT (Continue on reverse if necessary and identify by block number) Chairman of the Advisory Committee: Milton E. Franke Professor Department of Aeronautics and Astronautics					
20. DISTRIBUTION / AVAILABILITY OF ABSTRACT <input checked="" type="checkbox"/> UNCLASSIFIED/UNLIMITED <input type="checkbox"/> SAME AS RPT <input type="checkbox"/> DTIC USERS			21. ABSTRACT SECURITY CLASSIFICATION UNCLASSIFIED		
22a. NAME OF RESPONSIBLE INDIVIDUAL Milton E. Franke, Professor			22b. TELEPHONE (Include Area Code) (513)255-2362		22c. OFFICE SYMBOL ENY

UNCLASSIFIED

The transient response of a straight, cylindrical, fluid transmission line to a finite-amplitude pressure input is studied numerically to identify deviations from linear behavior. A nonlinear, finite-difference method is developed to predict the changes in the shape of a pressure wave as it propagates. The finite-difference algorithm is also applied to a linearized version of the governing equations to generate a basis against which to identify nonlinear behavior. The finite-difference method accounts for viscous losses and heat transfer. An algebraic model for calculating eddy viscosity in transient, turbulent flows is included.

Numerical simulations of a semi-infinite transmission line are performed using trapezoidal and half-sinusoidal pulses as well as a terminated-ramp as input pressure signal waveforms. Significant differences between linear and nonlinear results are found, even for input signals with maximum pressures less than two percent of the initial, undisturbed pressure.

Results are also obtained for lines of finite length with a blocked, volume terminated, or open end, opposite the end where the input signal is applied. The transient response to a terminated-ramp input pressure waveform is studied for this case. Good agreement with published results is obtained.

An engineering model is developed using the method of modal superposition. The modal model is modified to include frequency-dependent parameters for viscous and heat transfer losses. Results produced by the modal model for finite-length lines agree well with results from the finite-difference model and published data. All features present in the transient pressure and velocity waveforms produced at each end of the simulated transmission line by the finite-difference model are closely tracked by the modal model results.

UNCLASSIFIED